Supersonic Flight Characteristics of a Winged Re-Entry Vehicle

Gjalt Annega

Technische Universiteit Delft

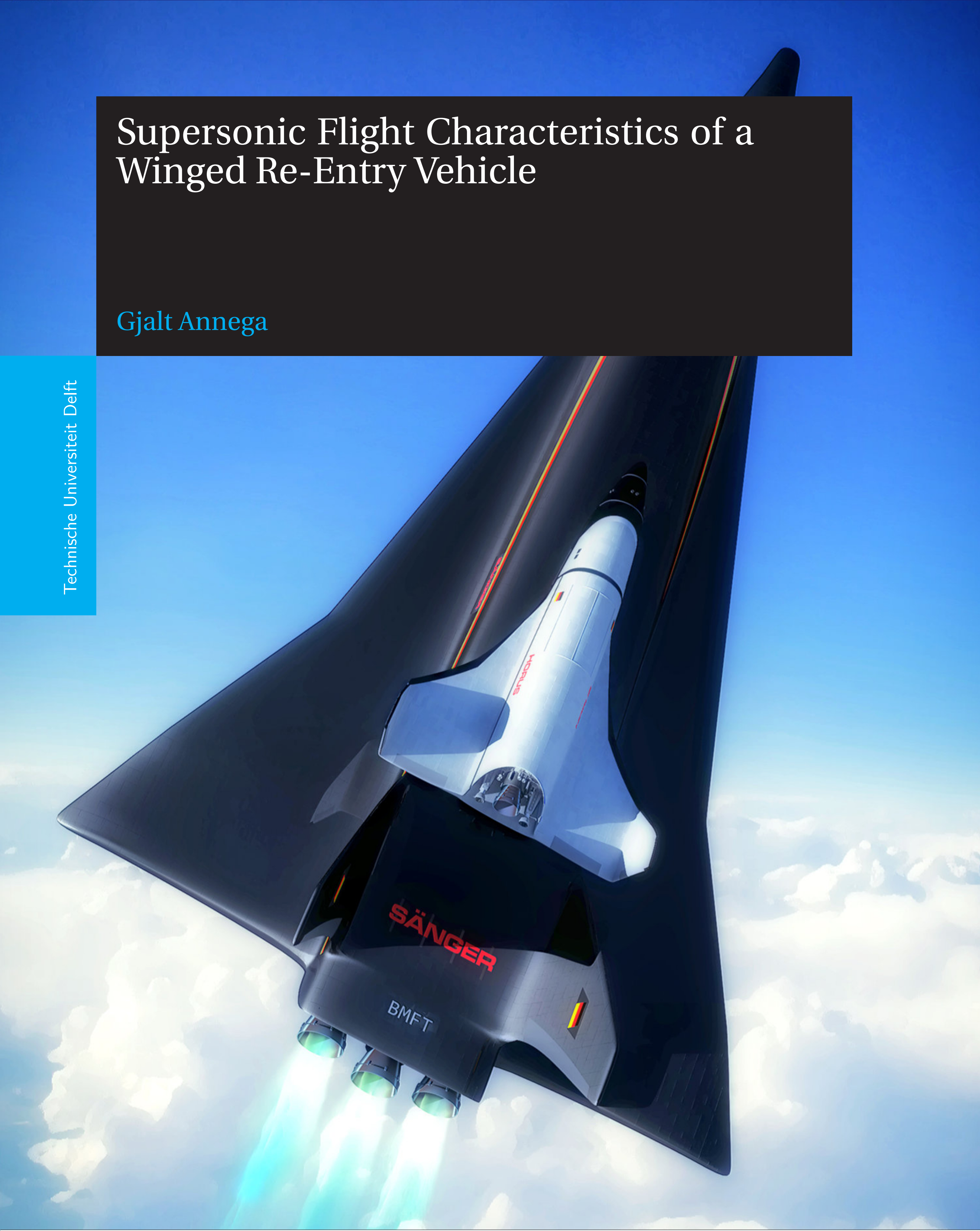

TU Delft Delft University of Technology

Challenge the future

DELFT UNIVERSITY OF TECHNOLOGY

FACULTY OF AEROSPACE ENGINEERING

ASTRODYNAMICS AND SPACE MISSIONS

Supersonic Flight Characteristics of a Winged Re-Entry Vehicle

Author:
Gjalt ANNEGA

Supervisors:
Dr. Ir. Erwin MOOIJ
Ir. Kees SUDMEIJER

February 27, 2017

Front cover image credit: T.G. Graham
Front cover model credit: N. Stevens

Acknowledgements

I would like to acknowledge and thank some people here. First of all I would like to thank my supervisors Erwin Mooij and Kees Sudmeijer for their patience, interesting conversations and for keeping an eye on the goal of graduation. I would also like to thank Rafael Molina for the hours he spent helping me understand the software and theory, the many visits I could make to ESTEC and giving me the feeling of having understood something new every time after a meeting. This thesis would also not have come to its current form without the help of Eddy van den Bos in creating the HORUS models and Relly for her great support in anything a student could need.

I would also like to thank my parents for their support throughout this journey and being a listening ear. Another thank you goes out to my friends for pulling me through to the end. Finally a thank you to the other students throughout the years for the fun, talks and interesting thoughts.

Abstract

Spaceplane designers need to be able to rapidly obtain estimations of aerodynamic and stability parameters throughout the re-entry flight. This aids with design changes and trade-offs regarding the stability characteristics of the design. This software was developed with a focus on stability analysis in the Terminal Area Energy Management phase (TAEM), the penultimate phase of the return to Earth.

For the HORUS spaceplane, a design study by MBB in the 1980s, the stability coefficients are known down to a Mach number of 1.2 and the dynamic stability characteristics down to a Mach number of 2.5. In this thesis a method is developed to calculate the aerodynamic forces and moments on a spaceplane. This method consists of two parts, an inviscid Euler code for the flow field away from the spaceplane and a viscous boundary layer code for the flow at the surface. The boundary layer code is based on the axisymmetric analogue, which uses a coordinate to transform a complex body into a series of axisymmetric bodies as long as the cross-flow between the streamlines is negligible. Using the Mangler transformation, these axisymmetric bodies can be transformed to flat plates, upon which momentum thickness and skin friction equations can be used. The inviscid Euler code calculates the pressure forces and moments, while the viscous boundary layer code calculates the forces and moments due to friction drag.

The combined pressure (inviscid) and friction (viscous) forces and moments on the HORUS are then used for stability analysis at Mach numbers of 2, 1.2 and 0.8, adding to the existing dataset. The stability analysis focuses on the stability coefficients (static stability) and motion characteristics (dynamic stability) around the trim condition at the aforementioned Mach numbers. For the dynamic stability an eigenvalue and eigenvector analysis is performed to investigate which motions are present in the lower Mach regimes, whether these motions are stable and how the vehicle behaves during these motions.

It is shown that the forces on the vehicle are simulated very well using this methods, as well as the longitudinal pitch moments. For the moments and derivatives regarding roll and yaw the simulated values differ significantly from the reference values. The simulations also show the large influence on the center of mass position on the stability of the HORUS, slight changes can turn an unstable motion in a stable motion and vice versa. Finally, the simulations show that the HORUS generally becomes more stable at lower Mach numbers, which indicates that the TAEM is not the critical phase regarding design for a stable spaceplane.

Contents

1 Introduction **17**

2 Mission Heritage **21**

2.1 Stability and performance of previous spaceplanes . . . 21
2.1.1 Space Shuttle . . . 21
2.1.2 Hermes . . . 27
2.1.3 Sänger/HORUS . . . 29
2.2 Existing research on aerodynamic simulation . . . 31
2.2.1 Aerodynamic simulation options . . . 31
2.2.2 Semi-empirical methods for the skin friction . . . 33
2.2.3 Boundary layer simulation . . . 33
2.2.4 Determining the skin friction . . . 36
2.3 System & Mission requirements . . . 36
2.3.1 Mission (results and analysis) requirements . . . 36
2.3.2 System requirements . . . 37

3 Flight Mechanics, Stability & Control **39**

3.1 Reference Frames . . . 39
3.1.1 Rotating Planetocentric Reference Frame F_C . . . 39
3.1.2 Body-fixed Reference Frame F_b . . . 39
3.1.3 Aerodynamic Reference Frame F_a . . . 41
3.2 Re-entry vehicle equations of motion . . . 41
3.2.1 Choice of method . . . 42
3.2.2 Conventions & assumptions . . . 42
3.2.3 Spaceplane treatment equations of motion . . . 43
3.3 Static stability & control . . . 46
3.3.1 Stability coefficients . . . 46
3.3.2 Control derivatives . . . 47
3.4 Dynamic stability & control . . . 48
3.4.1 Solution of the Equations of Motion . . . 48
3.4.2 Analysis of stability using the damping ratio . . . 51
3.4.3 Eigenvector analysis . . . 52
3.5 Application to stability analysis . . . 53

4 Aerodynamics **55**

4.1 Introduction . . . 55
4.2 Environment . . . 55
4.2.1 Wind . . . 57
4.3 Assumptions and validity . . . 58
4.4 Governing equations and principles . . . 59
4.5 Inviscid flow field - Euler equations . . . 60
4.5.1 Subsonic flow . . . 61
4.5.2 Transonic flow . . . 62
4.5.3 Supersonic flow . . . 66

4.6 Viscous flow field - Boundary layer . . . 68
4.6.1 Simplifying the boundary layer - the axially symmetrical analogy . . . 69
4.6.2 Compressible boundary layer . . . 71
4.7 Comparison of Parhizkar's and Hamilton's method . . . 77
4.8 A phase portrait method for determining stagnation lines . . . 81
4.8.1 Theory . . . 81
4.8.2 Implementation . . . 83

5 Simulation **85**
5.1 Software architecture . . . 85
5.2 Model, mesh and preparatory steps . . . 85
5.3 Euler . . . 88
5.4 Boundary layer simulation . . . 93
5.5 Result generation . . . 99
5.6 Simulation plan . . . 99

6 Verification and validation **103**
6.1 Verification . . . 103
6.1.1 Initialization module . . . 103
6.1.2 Stagnation module . . . 104
6.1.3 Backtracing module . . . 106
6.1.4 Propagation module . . . 106
6.2 Validation . . . 110
6.2.1 Rationale . . . 110
6.2.2 Euler code validation . . . 111
6.2.3 Accuracy of transition prediction . . . 115
6.2.4 Boundary layer development . . . 115
6.3 Comparison of simulated data to existing HORUS data . . . 121
6.3.1 Clean configuration coefficient comparison . . . 121
6.3.2 Body flap analysis . . . 124
6.3.3 Elevon deflection analysis . . . 124
6.3.4 Rudder deflection analysis . . . 124
6.3.5 Dynamic stability calculations . . . 124

7 Results & Analysis **127**
7.1 Experimental setup . . . 127
7.2 Horus Aerodynamic analysis . . . 128
7.2.1 High supersonic flow field . . . 128
7.2.2 Low supersonic / transonic flow field . . . 128
7.2.3 High subsonic flow field . . . 131
7.2.4 Errors in the flow field solution . . . 132
7.3 Stability results . . . 132
7.3.1 Trim . . . 136
7.3.2 Influence of the skin friction . . . 136
7.3.3 Static stability . . . 137
7.3.4 Dynamic stability . . . 141
7.3.5 Summary of stability situation for all simulated cases . . . 159
7.4 Sensitivity analysis . . . 159
7.4.1 High supersonic (Mach 2) . . . 159
7.4.2 Low supersonic (Mach 1.2) . . . 161

8 Conclusions & Recommendations **167**
8.1 Conclusions 167
8.2 Recommendations 170

Bibliography **173**

9 Appendix A: stability matrix coefficients **177**

10 Appendix B: validation stability and control coefficients **183**

List of Symbols

Term	**Description**	**Units**
Latin Symbols		
a	Speed of sound	m/s
b	Reference length	m
b	Sutherland Constant	$\frac{\mathrm{kg}}{\mathrm{ms}\sqrt{\mathrm{K}}}$
C_f	Skin friction coefficients	m
C*	Chapman-Rubesin parameter	-
C_h	Stanton number	-
cp	Specific heat	J/kg-K
c	Width (wingspan)	m
D	Drag force	N
F	Force	N
g	Gravitational acceleration	m/s^2
H	Enthalpy	J
h	Streamline metric coefficient	m/s
L	Length	m
H	Shape factor	-
I	Moment or product of inertia (depending on subscript)	kg m^2
k	Thermal conductivity	W/m-K
L	Lift force	N
m	Mass	kg
M	Mach number	-
M	Moment (with subscript x, y, z in Chapter 3)	Nm
P	Period of the motion	s
Pr	Prandtl number	-
p	Pressure	m^2
p	Roll rate	rad/s
q	Dynamic pressure	N/m^2
$\dot{q}$	Heat-transfer rate	J/s
q	Pitch rate	rad/s
r	Local radius of model	m
R	Radius from Earth Center	m
Rec	Recovery factor	-
Re	Reynolds number	-
r	Yaw rate	rad/s
s	Streamline distance	m
S	Side force	N
S	Surface area	m^2
S	Sutherland Temperature	K
T	Temperature	K
$T_{1/2}$	Half (+) or double (-) time	s
t	Time	s

Term	**Description**	**Units**
u	Velocity component in X-direction	m/s
V	Velocity	m/s
v	Velocity component in Y-direction	m/s
w	Velocity component in Z-direction	m/s
Y	Distance from surface in boundary layer	m
y_{cg}	Y-location of the center of gravity	m
z	Norm of the eigenvector	-

Coefficients		
C_D	Drag coefficient	-
C_{D_α}	Coefficient of drag w.r.t. angle of attack	rad^{-1}
C_{l_β}	Coefficient of roll moment w.r.t. the sideslip angle	rad^{-1}
$C_{l_{\delta_a}}$	Coefficient of roll moment w.r.t. the aileron deflection	rad^{-1}
$C_{l_{\delta_r}}$	Coefficient of roll moment w.r.t. the rudder deflection	rad^{-1}
C_L	Lift coefficient	-
C_{L_α}	Coefficient of lift w.r.t. angle of attack	rad^{-1}
C_{m_α}	Coefficient of the pitch moment w.r.t. to the angle of attack	rad^{-1}
C_{n_β}	Coefficient of the yaw moment w.r.t. the sideslip angle	rad^{-1}
$C_{n_{\delta_a}}$	Coefficient of yaw moment w.r.t. the aileron deflection	rad^{-1}
$C_{n_{\delta_r}}$	Coefficient of roll moment w.r.t. the rudder deflection	rad^{-1}
C_{S_β}	Coefficient of side force w.r.t. sideslip angle	rad^{-1}
C_S	Side force coefficient	-
C_X	Coefficient for force in X-direction	-
C_{X_u}	Coefficient of the force in X-direction w.r.t. to the velocity u	(m/s)$^{-1}$
C_Z	Coefficient for force in Z-direction	-

Greek Symbols		
α	Angle of attack	rad
β	Cross-streamline coordinate	-
β	Sideslip angle	rad
δ	Geocentric latitude	rad
ϵ	Distance from stagnation point for ϵ-curve	-
η	Imaginary part of an eigenvalue	-
γ	Ratio of specific heats	-
γ	Flight path angle	rad
λ	Eigenvalue	-
μ	Dynamic viscosity	kg/m·s
ω_n	Natural frequency	rad/s
Ω_t	Earth rotation rate	rad/s
ϕ	Roll angle	rad
ψ	Yaw angle	rad
ρ	Density	kg/m^3
σ	Bank angle	rad
$\dot{\tau}$	Rate of change of the geocentric longitude	rad/s
θ	Momentum thickness	m
θ_{arg}	Argument of the eigenvector	°
θ	Pitch angle	rad
ξ	Real part of an eigenvalue	-

Term	Description	Units
ζ	Damping ratio	-
Subscripts & superscripts		
a	Aerodynamic Reference Frame	-
aw	Value for an adiabatic wall	-
b	Body Reference Frame	-
.	Time derivative	-
e	Value at the outer edge of the boundary layer	-
L	Laminar boundary layer	-
c	Planetocentric Reference Frame	-
0	Reference state value	-
T	Turbulent boundary layer	-
w	Value at the wall in the boundary layer (inner edge)	-
’	Reference value	-
∞	Free-stream value	-
θ	Value based on momentum thickness	-
$\perp$	Perpendicular	-
*	Value at Eckert reference temperature	-
x, y, z	In X-direction, Y-direction or Z-direction	-

Acronyms

ACM Aerodynamic Configured Missile.

AoA Angle of attack.

APAS Aerodynamic Preliminary Analysis System.

ARM Aperiodic Roll Motion.

ATP Authority To Proceed.

c.g. Center of gravity.

c.o.m. Center of Mass.

CDR Critical Design Review.

ECI Earth-Centered Inertial.

FESTIP Future European Space Transportation Investigation Programme.

FLO Former Lateral Oscillation.

FSPO Former Short-Period Oscillation.

HASA Hypersonic Aerospace Sizing Analysis (for the Preliminary Design of Aerospace Vehicles).

HM Height Mode.

HORUS Hypersonic ORbital Upper Stage.

L/D Lift-to-Drag Ratio.

LEO Low Earth Orbit.

LO Lateral Oscillation.

MNT Modified Newtonian Theory.

OAE Once Around Earth.

OMS Orbital Maneuvering System.

PDR Preliminary Design Review.

PM Phugoid Motion.

PRR Preliminary Requirements Review.

RCS Reaction Control System.

SM Static Margin.

SOH Sub-Orbital Hopper.

SPO Short-Period Oscillation.

SSO Space Shuttle Orbiter.

SSTO Single Stage To Orbit.

TAEM Terminal Area Energy Management.

TPS Thermal Protection System.

TSTO Two Stage To Orbit.

UNLATCH3 Unstructured Langley Approximate Three-Dimensional Convective Heating version 3.

1
INTRODUCTION

The last few years there have been quite some changes in the space launch market. With the success of SpaceX and the upcoming launches of Blue Origin, the launch costs are set to decrease significantly. These launch costs will become even lower when these launchers are proven to be reusable, which will likely happen in the coming years. This means that many new opportunities arise in space, from asteroid mining to space tourism and off-planet living. However, not all these missions are efficiently fulfilled by capsule-based spacecraft, which are often used on the type of launchers used today. Controlled return in the atmosphere by a winged vehicle would lower loads (higher comfort) and make landing at predetermined landing spots achievable. The Space Shuttle Orbiter provided these capabilities and had a large cargo capacity for launch to Low Earth Orbit (LEO). However, due to its high cost and complexity, it never was the success that was envisioned when the project first started. The system has been retired in 2011.

Advances in materials science and computing have opened new possibilities for lower cost, reusable spaceplanes. Better Thermal Protection System materials should lead to lower refurbishment requirements after every flight. Improved computing power makes rapid design iterations possible that explore a wider range of options. Regarding developments in actual operational spaceplanes, the classified X-37 spaceplane has been launched on 4 missions already and is thought to be fully automated. Non-orbital spaceplanes such as Virgin Galactic's SpaceShipTwo are getting ready for deployment, entering the nascent tourism market.

For effective design of these spaceplanes it is important that the impact of design changes on the aerodynamic and stability performance of the spaceplane can be determined quickly. Faster iteration cycles on the design give the possibility to expand the range of options tested. Because of their high computing and time requirements, full-feature aerodynamic codes including all effects generally fail the criterion for fast iteration. Simpler, faster codes are needed for this purpose.

This thesis investigates and applies methods combining inviscid flow field calculations with viscous boundary layer calculations. This approach promises sufficient accuracy to separate stable from unstable designs and is faster than the complex codes often used by aerodynamicists. Aerodynamic methods used for modern design such as for the Orion Multi-Purpose Crew Vehicle [Schuster, 2008] generally use inviscid models for the inviscid flow regime and Navier-Stokes solutions for other flow regimes. Examples of the inviscid models can be found in [Aftosmis *et al.* , 2000] and [Bibb *et al.* , 1997]. Examples of Navier-Stokes models can be found in [Buning *et al.* , 1988], [Frink, 1998] and [Anderson & Bonhaus, 1994]. This means there is a niche in design software for a combination of inviscid calculations for the majority of the flow field and viscous boundary layer calculations close to the vehicle.

The main method that will be used, worked out by papers such as [Hamilton *et al.* , 2009] and

[Parhizkar & Karimian, 2009], uses a mathematical transformation such that complex shapes can be treated as a set of axisymmetric bodies, as originally invented by [Cooke, 1961]. The goal of this thesis is to investigate whether this method can be used to produce stability parameters for the spaceplane and assess its stable and unstable motions. To limit the scope of the research, only the stability and aerodynamics in the Terminal Area Energy Management (TAEM) phase will be determined, which is the phase between the hot part of re-entry and the operations just before landing.

The stability will be investigated using stability coefficients for the static stability analysis and eigenvalue/eigenmotion analysis for the dynamic stability. There is relatively little modern research on static stability as in most cases the complete dynamic stability is already determined. As dynamic stability is a sufficient condition for static stability, the separate determination of static stability is not always necessary. It does have its place in preliminary studies, such as [Kawato *et al.* , 2002] and can be determined using aerodynamic simulations or wind tunnel tests. The static stability coefficients will be determined in this thesis, as they can be calculated from equilibrium aerodynamic simulations.

The dynamic stability in modern design in generally determined using both CFD simulations and wind tunnel tests [Potturi & Peroomian, 2016], [Teramoto *et al.* , 2001]. For the CFD analysis a time-stepping Navier-Stokes simulation is often used, allowing for the determination of motion at every timestep. For the wind tunnel tests a forced oscillation can be used, making the model pitch with respect to the airflow using actuators and a sting. Because a time-dependent aerodynamic simulation would exceed the scope of this thesis, the dynamic stability analysis will be based on eigenvalue analysis, which allows for an analytic estimate of the most important dynamic motions.

The specific spaceplane used for this study will be the HORUS-2B7. It was part of the Saenger-II launch system which was designed in Germany in the 1980s and early 1990s. The system consisted of a hypersonic carrier plane and a rocket spaceplane, the latter being called the Hypersonic ORbital Upper Stage (HORUS). The whole system was envisioned to take of from a runway, accelerate to a velocity of Mach 6 at which point the upper stage HORUS was released. This upper stage would then start its rocket engines and accelerate to orbit. After its mission it could return to a runway due as a gliding aircraft in the lower reaches of the atmosphere. In 1994 the project was canceled due to the projected development cost [Wade, 2016].

The purpose of the aforementioned TAEM phase is to take the spaceplane from the end of the hypersonic phase to the start of the landing phase by aligning the spacecraft correctly with the runway with the correct amount of energy (meaning the correct velocity and altitude). As an example, the Space Shuttle Orbiter TAEM deals with Mach numbers ranging from high supersonic (3.2 for aborted launch, 2.5 for normal landing) to low subsonic. The corresponding altitudes are 26 kilometers above the Earth's surface at the start of the TAEM down to 3 kilometers at landing [Moore, 1991]. While there may still be some degree a heating of the air around the vehicle in the TAEM, the thermal regime is not as critical as it is in the hypersonic reentry phase. The requirements to prevent stall are not as critical in the TAEM phase as in the landing phase.

All the above will need to be covered by the research question. The main research question is:

Can a method based on the axisymmetric analogue predict the performance and stability coefficients of the HORUS spaceplane accurately enough to determine which motions are stable and unstable in the supersonic regime?

The subquestions that will help to answer the main question are:

1. Can boundary layer development be accurately predicted using the axisymmetric analogue?

2. Can the boundary layer skin friction be successfully determined from the boundary layer development?
3. Can a complex model like the HORUS spaceplane be treated as a model for the axisymmetric analogue?
4. Using a combined inviscid flow field and viscous boundary layer model, can predictions for performance and stability be made outside the known range and if yes, what do these predictions show?
5. Is the skin friction contribution to the performance and stability coefficients significant?
6. Can predictions for performance and stability be made outside the known range and if yes, what do these predictions show?
7. What motions can be identified for the HORUS-2B, which of those motions are stable in the TAEM and what does this mean for the overall stability?

The report has been divided in eight chapters excluding the introduction:

1. After the introduction, Chapter 2 deals with mission heritage, what research has already been done and how it is relevant to this research. The goal of this section is to create the context for this research in light of previous research.
2. Chapter 3 deals with the flight mechanics, stability and control of relevant for the TAEM. The equations of motion will be derived and linearized, after which the stability and control effectivity coefficients are discussed. The chapter ends with the choice of coefficients to be determined.
3. Chapter 4 deals with the aerodynamic theory and its application to this specific case. A derivation of the equations for the inviscid flow field and the boundary layer is shown, the axisymmetric analogue is explained, the methods of [Hamilton *et al.* , 2009] and [Parhizkar & Karimian, 2009] are introduced and different methods to find the skin friction are discussed. This chapter will also include a method for determining the stagnation lines which are of importance for spaceplanes with leading edges.
4. Chapter 5 deals with the simulation, which explains the steps needed to obtain the required results and the implementation of the discussed theories.
5. Chapter 6 is about the verification and validation of the results. This will be done using results for different models which were obtained through computations are wind tunnel tests.
6. Chapter 7 shows the results for the HORUS model. The obtained results will also be analyzed, discussed and compared to earlier results.
7. Chapter 8 gives the conclusions to the research question and the methods used. Recommendations for further research and improvements will also be given.

2

Mission Heritage

This chapter will focus on past work in the field and analysis of other spaceplanes to get a view of what this thesis builds on. The first section investigates the stability and performance of previous spaceplanes. The second section discusses existing aerodynamic research that relates to this thesis. The final section formulates the mission and system requirements for the thesis and software.

2.1. Stability and performance of previous spaceplanes

2.1.1. Space Shuttle

The Space Shuttle program was initiated in the late 1960s [Williamson, 1996] as the next generation space-transportation system. Several concepts were proposed but in the end the choice was made for a semi-reusable system. This system allowed the aircraft-like orbiter and the first stage solid rocket booster to be reused, while the external fuel tank was discarded. The aerodynamic design has been described in [Bornemann & Surber, 1978], on which the following discussion is based (unless indicated otherwise).

Design of the Space Shuttle Orbiter

The evolution of the Space Shuttle Orbiter (SSO) design is shown in Figure 2.1. The initial Authority To Proceed (ATP) design incorporated a 50° swept delta wing which provided a touchdown speed of 77.2 m/s. The size of the elevons could trim the vehicle at hypersonic velocities at angles of attack from 20° to 50° for a Center of Mass (c.o.m.) range of 3% of the body length. Through a series of further design changes such as the Preliminary Requirements Review (PRR) design and the Preliminary Design Review (PDR) design, the final Critical Design Review (CDR) design was obtained. The nose shape was changed from blunt to a parabolic cross section prevent early flow transition and in turn reduce lower body surface temperatures. The wing/fuselage fairings along the bottom of the orbiter were changed to have a thermodynamically smooth lower surface with minimum reverse curvature, the latter to prevent flow separation. The leading edge sweep was changed to 45/81° because a refairing into the modified nose was needed. Further configuration refinements led to a reduced CoM design range of 2.5% body length. Other changes between the versions can be found in [Bornemann & Surber, 1978]. A more detailed look at the final aerodynamic design reveals the reasons for the design choices that were made. The landing speed was one of the important criteria, as this puts a lower boundary on the subsonic lift-to-drag ratio. The wing was sized to provide a 88 m/s touchdown speed at an angle of attack of 15°. The double delta wing configuration with a leading edge sweep of 45° was chosen through a trade-off between aerothermodynamic effects and aerodynamic performance. The goal was a wing that was as small as possible and an optimized leading edge that would allow the thermal protection system to be used for 100 consecutive flights before a major rework. The wing design combined with the moderately low fineness ratio (approximately five) body provided an acceptable trim and stability range over the flight number Mach range, see Figure 2.2. The figure shows the boundaries regarding the stability for a range of Mach numbers, while also showing the safe center of mass range throughout the whole re-entry and landing trajectory.

The fuselage design was a function of the payload to be carried, the crew housing and the maneuvering control systems. The nose and forebody design, including aspects such as nose camber, cross section and the sloping forebody sides, was selected to improve hypersonic pitch trim and directional stability. Together with the wing-body blending it also helped reduce the entry heating on the body sides. Finally, the vertical tail was sized to a requirement for the yaw moment due to sideslip C_{n_β} = 0.0013 at low speed, an angle of attack of 13° and a CoM located at the aft limit. The tail has a reference area of 38.39 m^2 and the rudder is split so it can act both as rudder by being deflected to one side or as speed brake/stabilizing device by being deflected to both sides symmetrically. Next the performance of the the SSO will be discussed, which of course is a result of the design choices discussed above.

Performance of SSO

To obtain a complete picture of the stability and performance of the SSO, both the longitudinal and the lateral characteristics will be discussed. The focus will be on the coefficients most important for stability such as the coefficients of pitch moment with respect to the angle of attack C_{m_α}, roll moment with respect to the sideslip angle C_{l_β} and yaw moment with respect to the sideslip angle C_{n_β}.

Longitudinal characteristics

The main focus of the longitudinal characteristics is on the pitch coefficient and the trim capabilities. Figure 2.3 shows the primary parameters for the aerodynamic performance and longitudinal stability of the Space Shuttle Orbiter. The pitch moment coefficient graph shows that at nearly all Mach numbers the slope $\frac{dC_m}{d\alpha}$ (i.e. $C_{m_{alpha}}$) is negative, indicating positive static stability. Only at very low Mach numbers below M = 0.25 and high angles of attack above α = 20° does longitudinal static instability occur.

The relation between the elevon deflection angle and the pitch moment coefficient is shown in Figure 2.4. On the left side is a graph for the effect at Mach 0.6 and an angle of attack (α) of 5°. The plotted response indicates that deflection changes between -10° and -30° are the most effective, while positive deflections have almost no effect as the elevon is in the wake of the spacecraft. This means that if possible the trim should be set such that the elevon deflection is in the range -10° to -30°. At Mach 3 and an angle of attack of 15° the plot is much more linear, with a slightly higher effect for positive elevon deflections. The cause of the difference in behavior is because of the different Mach numbers and angles of attack, meaning the flow over the control surface is quite different between both situations.

The static trim capability, which is the range of angles of attack for which the SSO can fly in longitudinal equilibrium is shown in figure 2.5. The lines indicate what angle of attack can be trimmed at each center of gravity position for the given control surface deflections and Mach numbers. This means that the area enclosed by the lines (generally below) is the area of attainable trims. A margin of error is also included as a reserve for aerodynamic uncertainties, misalignments etc. The figure indicates there is a relatively wide trim margin over the range of Mach numbers and the CoM range is chosen conservatively.

Lateral characteristics

The main focus for the lateral characteristics is on the lateral stability derivatives and control effectiveness. As a complete analysis of all lateral derivatives of the SSO would be too extensive, so the most important derivatives will be discussed.

Figure 2.6 shows two very important stability criteria, the yaw coefficient derivative (upper graph) and roll coefficient derivative (lower graph) with respect to the sideslip angle. For good stability, C_{n_β} should be positive while C_{l_β} should be negative [Marzocca, 2003]. According to Figure 2.6 for the SSO C_{n_β} is negative for Mach numbers higher than 1.7 and positive for lower Mach numbers. This means the yaw moment response to a sideslip angle is not stable for higher Mach numbers. As long as the motion is slow this is should not pose a problem for the pilot or controller, but as [Bornemann & Surber, 1978] does not give the eigenvalues for the motion it can not be verified if this is the case. The coefficient C_{l_β} is negative for every Mach number, which means the Orbiter has static stability for the roll moment coefficient with respect to the sideslip angle.

Figure 2.7 and 2.8 show the effectiveness of the aileron and rudder for a range of Mach numbers from 0.2 to 20. The figures show that the aileron and rudder are generally effective regarding their primary effect (positive $C_{l_{\delta_a}}$ and $C_{n_{\delta_r}}$). However, above approximately Mach 2.5 the value of these derivatives is positive but small, which means that while the correct moment is generated, it is small. This means that for higher Mach numbers maneuvering is slow unless additional control mechanisms are used. The secondary effect $C_{n_{\delta_a}}$ is the yaw moment due to elevon/aileron deflection. Below Mach 1.5 a positive deflection causes a positive yaw moment, which is the behavior most aircraft show. The derivative reverses its behavior above Mach 1.5 which means a negative moment is created. The pilot or controller should take this reversal into account to correct for the unintended yaw moment. The roll moment due to rudder deflection coefficient $C_{l_{\delta_r}}$ (which is a secondary effect) is positive for all Mach numbers, with lower coefficient values for higher Mach numbers. The values of the secondary effects are significant compared to the primary effects, which means the roll-yaw coupling and yaw-roll coupling need special attention in the design.

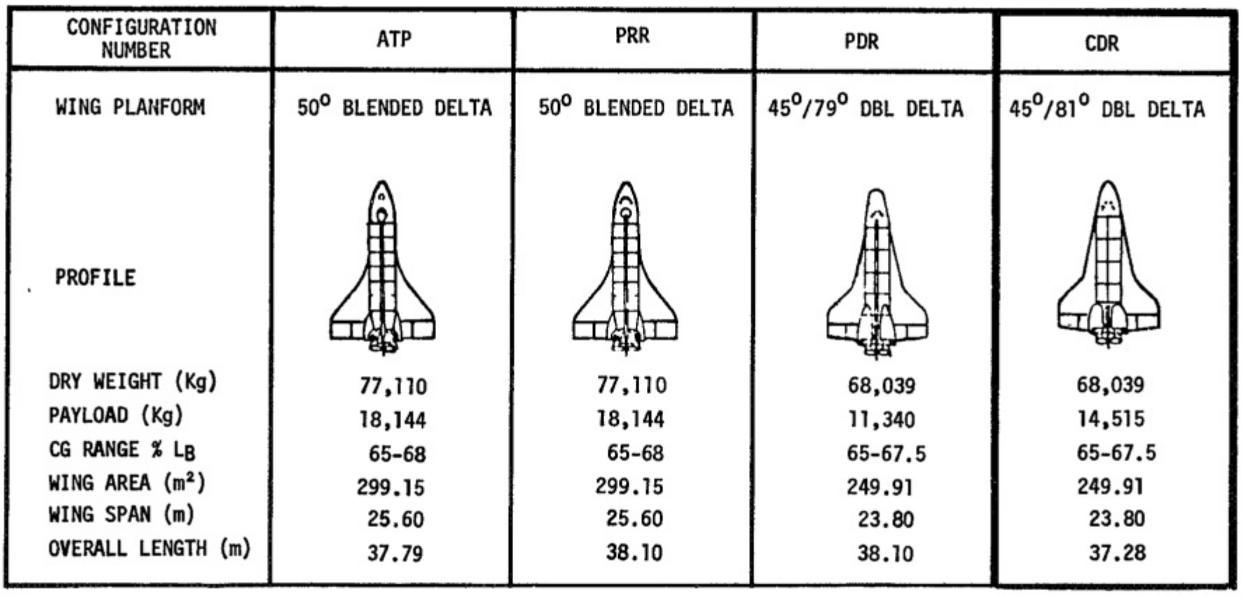

CONFIGURATION NUMBER	ATP	PRR	PDR	CDR
WING PLANFORM	50° BLENDED DELTA	50° BLENDED DELTA	45°/79° DBL DELTA	45°/81° DBL DELTA
PROFILE				
DRY WEIGHT (Kg)	77,110	77,110	68,039	68,039
PAYLOAD (Kg)	18,144	18,144	11,340	14,515
CG RANGE % LB	65-68	65-68	65-67.5	65-67.5
WING AREA (m²)	299.15	299.15	249.91	249.91
WING SPAN (m)	25.60	25.60	23.80	23.80
OVERALL LENGTH (m)	37.79	38.10	38.10	37.28

Figure 2.1: Evolution of the Space Shuttle Orbiter shape throughout the design process [Bornemann & Surber, 1978].

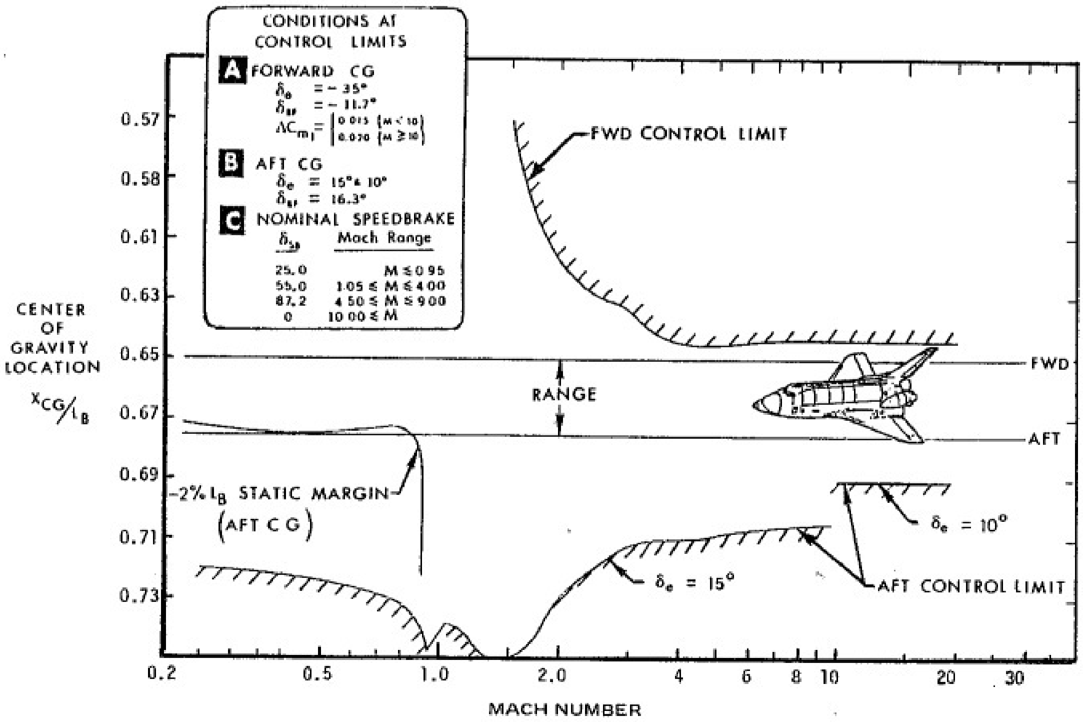

Figure 2.2: The center of gravity location limits as a function of Mach number [Bornemann & Surber, 1978].

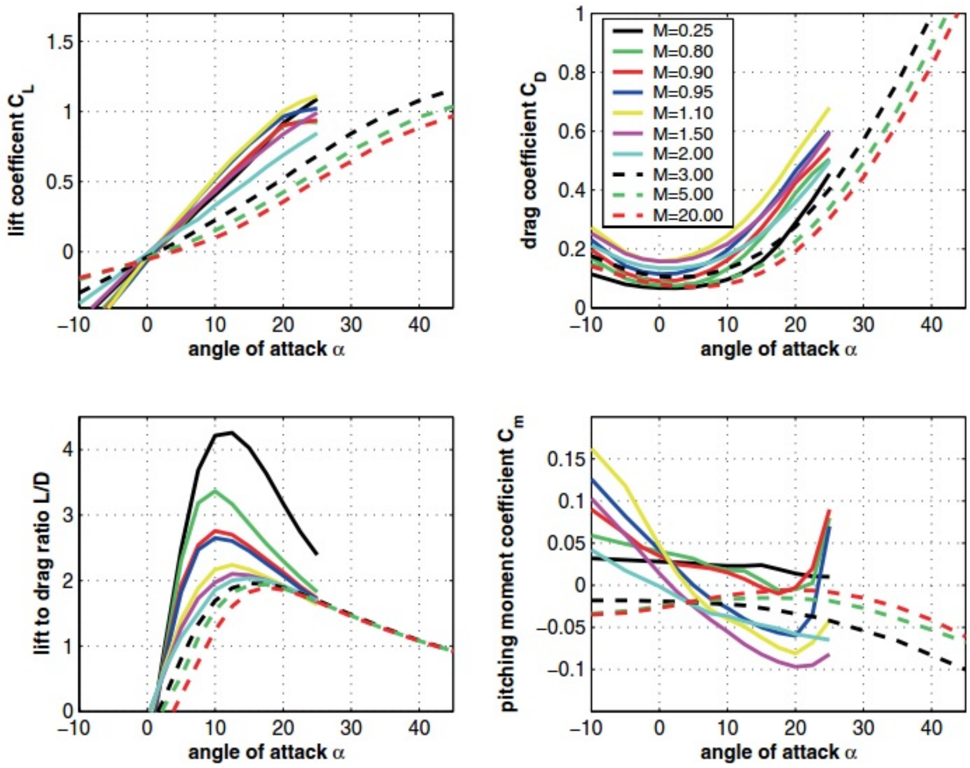

Figure 2.3: Aerodynamic data of the Space Shuttle Orbiter, [Hirschel & Weiland, 2009].

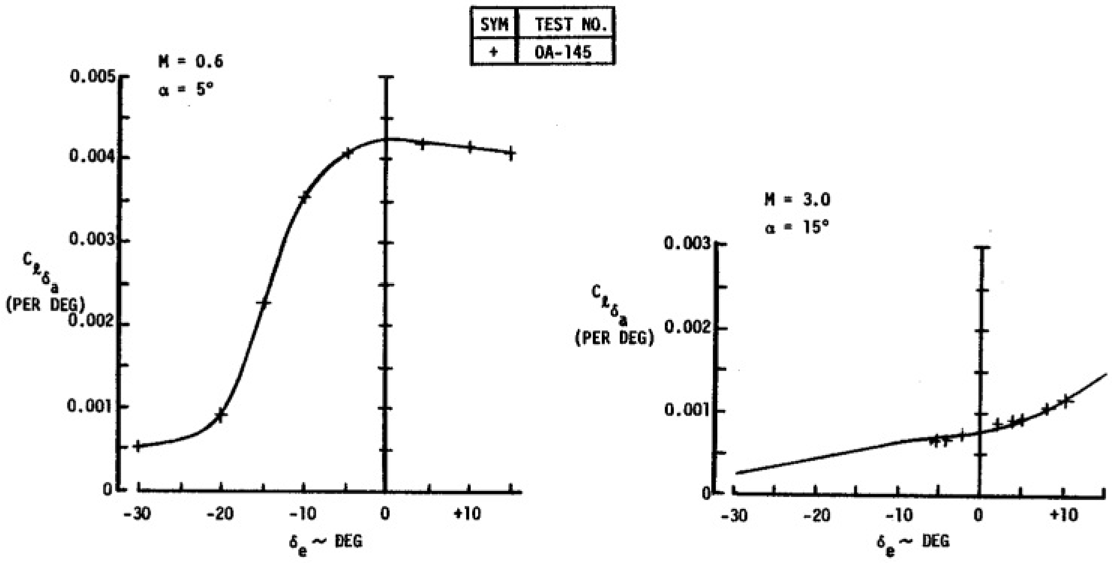

Figure 2.4: Effect of elevon deflection on aileron roll derivative for the SSO [Bornemann & Surber, 1978].

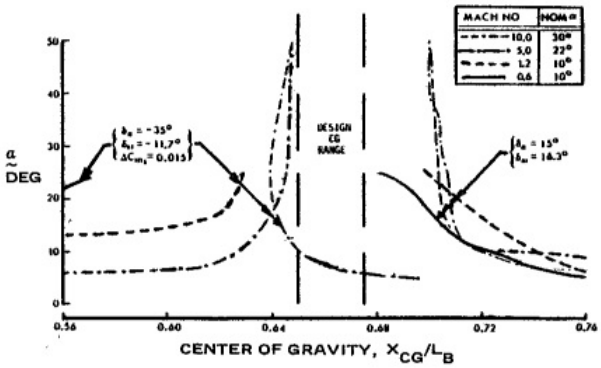

Figure 2.5: Space Shuttle Orbiter trim capabilities [Bornemann & Surber, 1978].

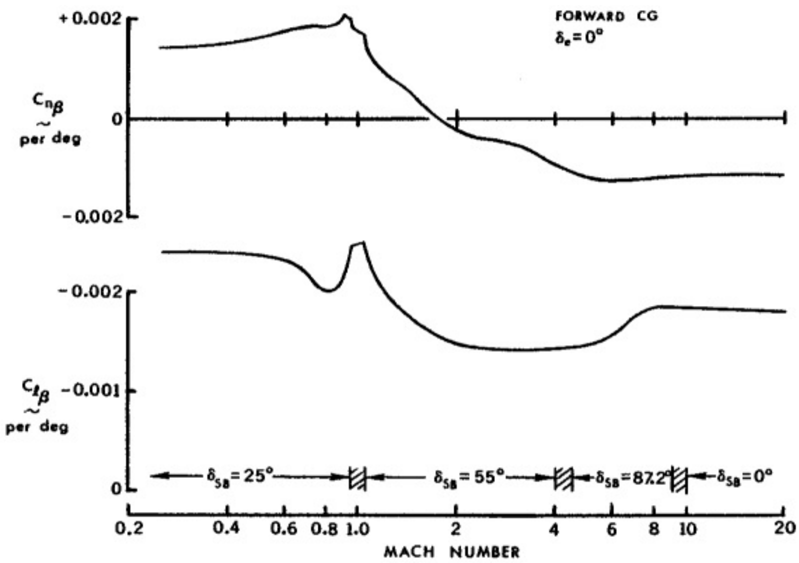

Figure 2.6: Lateral directional stability derivatives of the Space Shuttle Orbiter [Bornemann & Surber, 1978].

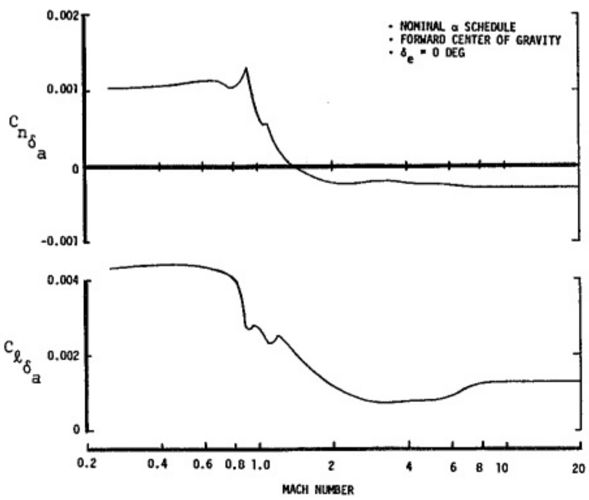

Figure 2.7: Space Shuttle Orbiter aileron effectiveness [Bornemann & Surber, 1978].

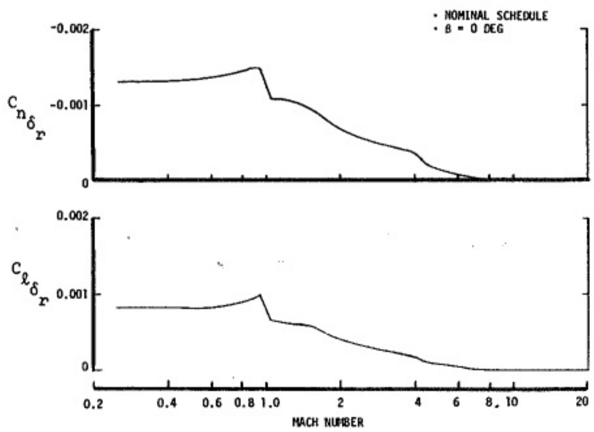

Figure 2.8: Space Shuttle Orbiter rudder effectiveness [Bornemann & Surber, 1978].

2.1.2. HERMES

The Hermes spaceplane project was initiated in the late 1970s by the French space agency CNES in the form of a study concerning a mini-shuttle to be launched on top of an Ariane rocket [Coué, 2003]. The project was adopted by ESA in November 1987 with the goal of independent access to space for Europe. Two competing concepts were delivered by Aerospatiale and Dassault, with the Aerospatiale concept winning the competition. Dassault was selected to provide the aerodynamic design for the shuttle. Between 1988 and 1990 the initial pre-development phase was planned, but this actually took until the end of 1991. Although the original goal was a payload of 4500 kg with a crew of 4-6, due to changes regarding crew safety this was reduced to 3000 kg and 3 crew members [ESA, 2011]. In the following discussion a look will be taken at the changes that were made to the design in a design phase by Dassault between March 1990 and March 1991, going from the 0.0 to the 1.0 shape. The information and images below are from [Raillon *et al.* , 1992] unless indicated otherwise.

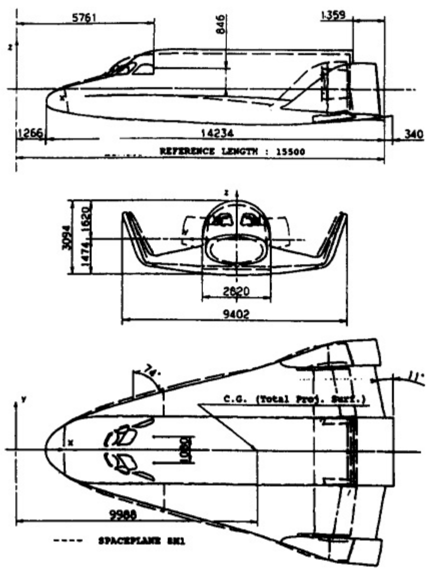

Figure 2.9: Final shape of the Hermes spaceplane [Raillon *et al.* , 1992].

The main features for the aerodynamic concept were defined after a trade-off of the options for these main features. The shape of the wing could either be a single delta wing or a double delta wing . The double delta wing has the advantage of offering better subsonic stability. However, it presents challenges regarding the leading edge temperature where the bow shock interacts, being 200° K higher than for the Space Shuttle Orbiter. Therefore the choice was made to use the single delta wing. This choice also led to the use of winglets instead of a central fin, as the winglets help to reduce the subsonic instability. The winglets also allow improved control at high angles of attack, useful, during hypersonic atmospheric entry. A potential drawback of the winglets was the interaction between the bow shock and the upper part of the winglets. This interaction is generally not strong enough to cause issues and the angle of attack can be increased to prevent the interaction from happening.

The dimensioning of the Hermes spaceplane had to take many different phases and aerodynamic regimes into account. First of all, being launched on top of an Ariane rocket (similar to the X-20 Dyna-Soar, [Boeing, 2017]), the design of the spaceplane had to be able to cope with high dynamic pressures and mechanical loads during launch, as well as high aerodynamical instability. This put a major constraint on wing span, which in turn has effect on the subsonic performance when landing. The Hermes needed a certain Lift-to-Drag Ratio (L/D) for its cross range in the hypersonic regime and a certain L/D for an acceptable landing speed in the subsonic regime. Because of the relatively low cross-range requirement of 1500 km, the hypersonic L/D was not the limiting case for the aerodynamic design. The 1.0 shape gives an L/D of 5.15 in the subsonic regime, though in the worst case scenario with uncertainties this is only 4.6. To allow for the lower subsonic L/D the approach can be modified to cope with a lower L/D.

The thermal constraints imposed by hypersonic entry into the atmosphere from orbit and emergency launch abort re-entries were also an important consideration. The nose and control surface heat flux requirements were dictated by hot re-entry phase as temperatures will be highest in that phase. The temperature requirements on the windward tiles were imposed by emergency launch abort where flow transition and/or turbulence is occurring. The thermal limits on the control surfaces also impose limits on the deflection of those surfaces in hot conditions, as higher deflections lead to higher temperatures.

For a good overview of the limiting cases for the longitudinal center of gravity location over the complete Mach regime Figure 2.10 is useful. The limiting cases were the controllability requirement regarding pitch up deflections in the rarefied flow regime and the required maximum negative static margin of 4% in the subsonic phase. This negative stability margin means that the spaceplane is unstable, but with the indicated range the required reaction time is around 0.5 seconds, which is deemed acceptable. This means center of mass locations between 58.5% and 61% of the reference length of the vehicle were acceptable in the nominal case. However, due to uncertainties the exact CoM range is not known. The authors of the paper suggest an initial CoM of 60% together with an entry angle of attack of 40° for the first flight as a safe bet. The range can then be refined based on data from that first flight. The most important predicted aerodynamic coefficients of the HERMES are shown in Figure 2.11.

The pitching moment coefficient graph in the lower right of Figure 2.11 shows that in the transonic/low supersonic regime the Hermes is statically stable for the primary longitudinal coefficient (negative $\frac{dC_m}{d\alpha}$) up to an angle of attack of 10°). For higher angles of attack the coefficient becomes positive, which means the static unstability. For the Mach numbers of 2 and 2.5 the craft is statically unstable for all angles of attack.

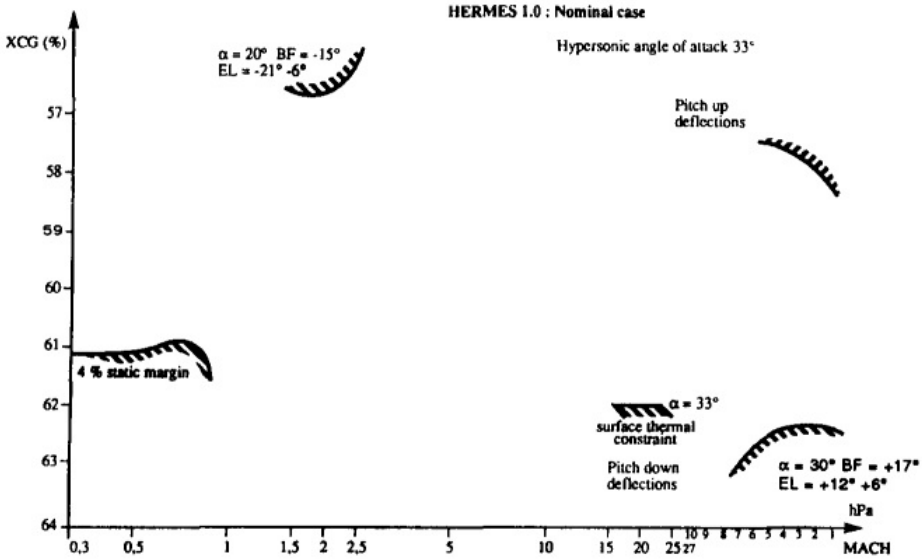

Figure 2.10: Hermes' center of gravity location limitations for the complete Mach regime [Raillon *et al.* , 1992].

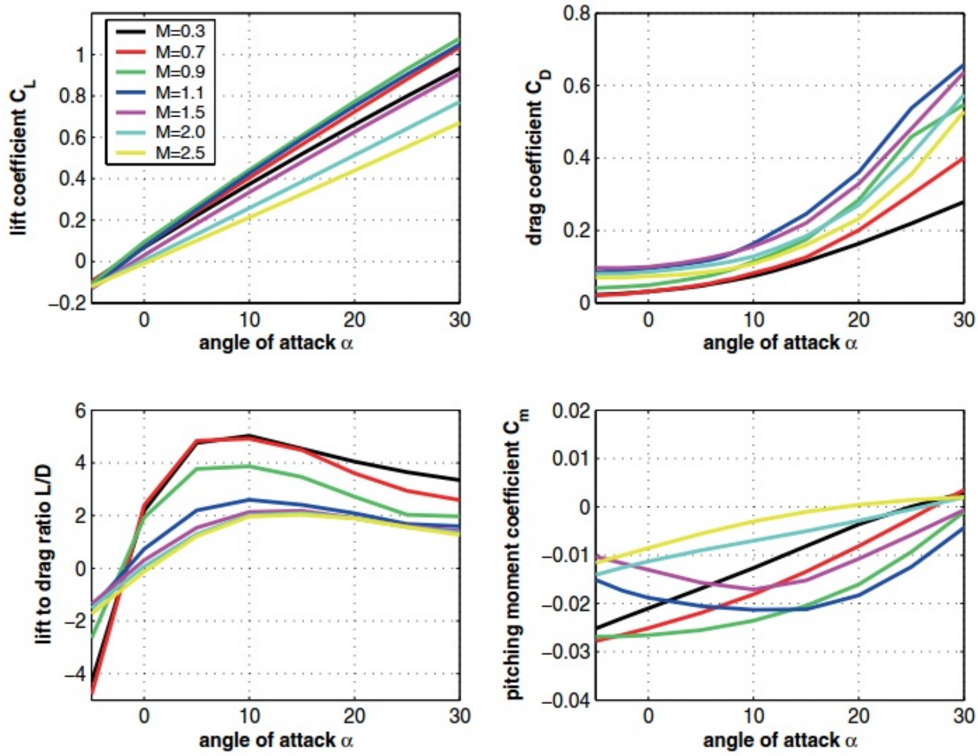

Figure 2.11: Aerodynamic data of the HERMES as a function of angle of attack and Mach number, [Hirschel & Weiland, 2009].

2.1.3. SÄNGER/HORUS

The Sänger II spaceplane concept was a proposed two-stage spaceplane concept. The first first stage would be a hypersonic carrier aircraft that would bring the launch system to an altitude of 35 km with a velocity of Mach 6.6 [Koelle & Kuczera, 1992]. At that point the second stage (also called HORUS) would be released, ignite its rocket engines and boost into orbit. The planned payload that could be put into orbit was around 7000 kg including crew provisions, with a total launch mass of the HORUS second stage of 112,000 kg [Koelle & Kuczera, 1992].

The information and images below are from [Cucinelii & Müller, 1988] unless indicated otherwise. The HORUS-2B concept has gone through at least seven iterations, HORUS 2B-1 through HORUS 2B-7. The first iteration was designed for a high lift to drag ratio in the hypersonic range and an acceptable lift to drag ratio in the subsonic range. To achieve this the body was heavily cambered, which is visible in the deviation of the lower side of the body from the straight line above it in Figure 2.12. Other features of this iteration were the variable geometry wings and small nose radius. The strongly cambered body led to a very strong pitch-down moment at all velocities, thus the body chamber was reduced. Furthermore, the small nose radius led to too high heat fluxes so the nose was rounded and shortened. While the moments and heat fluxes were in the acceptable range due to these changes the lift to drag ratio decreased significantly.

The extendable wing tips were changed to fixed wings to reduce complexity and allow for the use of tip fins and trailing edge controls. The trailing edge controls were deemed necessary for lateral control (i.e., pitch) and moment equilibrium. The tip fins also allow for fin rudders, which, together with the fins themselves, improve directional stability at high angles of attack (during reentry) and low speed performance. The cranked wing (change of sweep along the span of the wing) is supposed to achieve a maximum lift to drag ratio of 4 during the landing phase while keeping the wing area

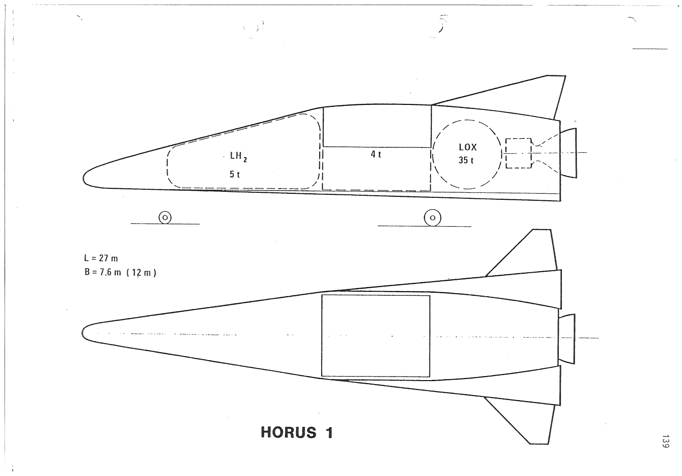

Figure 2.12: First iteration of the HORUS, outer surface [Cucinelii & Müller, 1988]

small, reducing drag. The downside is that the effect of the crank on local overheating is not taken into account yet and might be a problem. A feature that is found in the fourth iteration but not in the final seventh iteration are the extendable canards. While they would have helped reducing some problems with pitching moment they were again deemed too complex.

In the final design (see Figure 2.14 for the CATIA model) the entire trailing edge including the body lower side is designed as control surface. The body flap, located on the lower side of the body, plays an important role in pitch trim. The tip rudders can only be moved outboard to reduce complexity. By moving the rudders symmetrically they can act as speed brakes, when deflecting only one rudder they can be used for lateral control. Finally, the body of the seventh iteration was made convex to obtain good behaviour of the longitudinal and lateral moments.

The choices made for the final design have a large impact on the performance and stability of the HORUS spacecraft. The influence of the design choices will be discussed now, focusing on the fuselage, wings and control surfaces.

FUSELAGE

The design of the front of the vehicle is most important during the hot, hypersonic reentry phase. While a thermal protection system can handle quite high temperatures, most of the energy created during this phase needs to be kept away from the vehicle, explaining the need for a blunt nose. While a blunt nose is not optimal for the aerodynamic performance in the TAEM, its size is dictated by the thermal requirements.

The rest of the fuselage is designed such that it stays out of the shockwave during the hot phase, to fit all the required payload and systems and to minimize the contribution to drag. From a stability viewpoint the interesting features of the fuselage are the shape of the underside of the fuselage and the drag coefficient of the fuselage. The shape of the underside of the fuselage has influence on the lift of the whole vehicle, a curved underside will give a different lift profile than a flat underside. As the HORUS has wings which provide the major part of the lift, the body lift is not so significant for the total lift. By minimizing the drag coefficient of the fuselage in all directions, the range of the vehicle can be optimized and the influence of disturbances minimized.

WINGS

Again the design of the wings is greatly influenced by the thermal requirements of the hot hypersonic phase. While large, thinner wings would be better from a TAEM flight performance point of view, the short, stubby wings with large leading edges deal much better with the high thermal and structural loads a spaceplane experiences. The other reason is that the HORUS had to fit on top of the carrier aircraft, also putting a limit on the wingspan. As the aerodynamic center of the wing is much further back from the center of mass compared to conventional aircraft, disturbances will have a much larger influence on the stability. As one of the winglets may be in the wake of the fuselage for sideways disturbances, for severe sideways disturbances the usable winglet surface area is much smaller than the total winglet surface area.

CONTROL SURFACES

The HORUS has a different set of control surfaces from most conventional aircraft. This is because they have to fit a design optimized for reentry, which all but excludes the use of separate horizontal stabilizers with elevators.
The body flap's main function is to trim the aircaft and keep it at the required angle of attack. It also shields the backside of the vehicle from the heated air during the hot phase. The body flap is sized to achieve pitch trim, which is why it is almost as large as the elevons together (8.5 m^2 versus 9.2 m^2. This together with its position further to the back provides a similar control level as the elevons.

The elevons function as both elevators and ailerons. These functions can be combined only to a limited degree at the same time, which shows the importance of the body flap trimming. Due to the small distance of the elevons to the center of mass compared to conventional aircraft, they occupy a rather large part of the planform of the HORUS to ensure a sufficient degree of control.

The rudders are located in the winglets, which is why there are two of them. The position of the rudders away from the symmetry plane can help or oppose the rudder control, because a deflection also increases the drag on the winglet, creating a moment along the Z-axis. For outboard deflections the drag supports the moment that the rudder is supposed to make, while for inboard deflection it opposes it. Because the rudders are not aligned vertically but also have a horizontal component, the coupling between rudder deflection and roll will be stronger.

2.2. EXISTING RESEARCH ON AERODYNAMIC SIMULATION

Aerodynamicists today have very advanced aerodynamic simulations at their disposal. Even though full Navier-Stokes solutions are out of reach for high Reynolds numbers, in most cases researchers can now approximate flight parameters with good accuracy. For example, a comparison of around 30 methods for simulating high subsonic flows showed that the standard deviation for the drag coefficient differed only 3% in value from the average outcome [Vassberg *et al.* , 2010]. The same comparison also shows that not all parameters can be estimated with high accuracy, as the pitch moment standard deviation was 40% off compared to the average. For supersonic simulation the results are still good, but the error in drag coefficient grows to about 10% at the design lift coefficient [Umeda *et al.* , 2007]. High accuracy models do come at the cost of high computational power requirements. depending on parameters such as the time step, grid resolution and the type of effects modeled the run time can range from minutes to days. While long run times is acceptable for designers looking to validate their final design, this is not so useful for the design process itself. Quick solutions are needed for this that are *sufficiently* accurate, as opposed to as accurate as possible. In this context this means that the stability of motions needs to be determined correctly, as well the order of magnitude of the time periods associated with the motions.

To design a fast code for aerodynamic results it is very useful to look at the past, as computers were not fast or widespread. This will show several methods and simplifications that with limited computational power can obtain good results under a certain set of assumptions.

2.2.1. AERODYNAMIC SIMULATION OPTIONS

The goal of making an engineering design code that runs on a personal computer limits the choices for the aerodynamic simulation method. A full Navier-Stokes simulation at the Mach and Reynolds numbers that occur during re-entry or the TAEM phase is simply not feasible if rapid solutions are

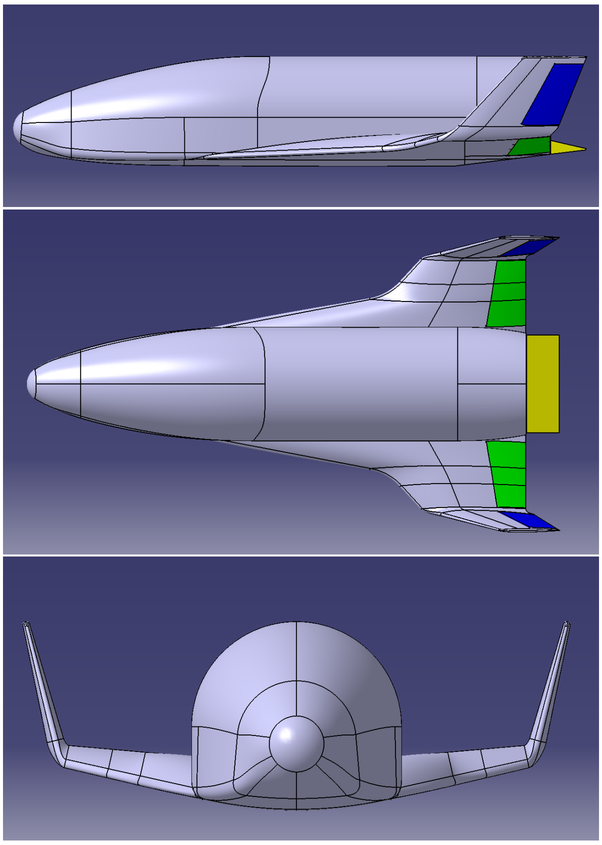

Figure 2.13: Side, top and front view of the CATIA model of the HORUS-2B7. The rudders are in blue, the elevons in green and the body flap in yellow.

needed, as indicated by the need for a supercomputer to compute a channel flow at a Reynolds number of 5000 [Moser, 2013]. Certain effects can be neglected to speed up computations such as the viscosity of the flow, which leads to an inviscid flow solution. An inviscid-only solution alone will not be satisfactory, as this neglects the skin friction which could have significant effect at subsonic Mach numbers near the end of the TAEM phase. This means that a method to determine the skin friction is necessary, which is then added to the drag calculated by the inviscid solution. The two main options are then concerned with different methods of determining the skin friction:

1. Inviscid flow field solution with semi-empirical methods for the skin friction determination. During design of the SSO different methods were used that used a combination of theory and empirical data to obtain an estimate of the skin friction.

2. Inviscid flow field solution with a boundary layer simulation. The boundary layer simulation includes viscous effects for the region very close to the surface of the vehicle. By making this division between the viscous and inviscid region, the skin friction can be calculated with a stronger theoretical basis.

2.2.2. SEMI-EMPIRICAL METHODS FOR THE SKIN FRICTION

AERODYNAMIC PRELIMINARY ANALYSIS SYSTEM (APAS)

During the design of the Space Shuttle Orbiter the aerodynamics of the vehicle needed to be simulated with the limited computing resources available at the time. To achieve this the scientists and engineers had to find methods that were fast and reasonably accurate. The resulting software was called APAS and was prepared for the Langley Research Center by Rockwell international [Bonner *et al.* , 1981].

For the aerodynamic simulation Rockwell used potential flow theory for the subsonic and supersonic flight phases [Bonner *et al.* , 1991]. Potential theory can be applied using a vortex panel method, which combines panels with different flow types to approximate the flow. Examples of panel flow types are sources, sinks, vortices and uniform flows. The strength of the panel method is that these flows can be linearly added, which gives many possibilities to model three-dimensional vehicles. It also requires only a small number of panels to approximate the flow (a few hundred), while boundary layer methods require many more elements. The advantage of using a low number of panels is that the number of required computations is limited. The downside of using such a small number,however, is that more subtle shape variations are lost. It is also important to note that potential theory assumes an irrotational flow. A flow will only stay irrotational in an inviscid flow field, meaning that as soon as viscous effects are taken into account the potential flow assumptions break down.

The scientists at Rockwell solved this by first applying potential theory and then using semi-empirical methods and a component buildup approach to estimate the skin friction. For laminar flow the Blasius solution with an Eckert compressibility correction was used, while for turbulent flow the compressible turbulent flat plate flow method of Van Driest was used [Bonner *et al.* , 1991]. The roughness of the surface was also taken into account using tabulated data on the roughness of several materials. Finally, to correlate the flat plate results to the actual body with finite thickness the experimentally determined equations from Horner were used.

2.2.3. BOUNDARY LAYER SIMULATION

The boundary layer is the area in which viscous effects are significant, which is usually a thin layer near the surface of the vehicle. This region is dominant regarding friction effects (friction further away from the vehicle is negligible) and the resulting heating. To deal with the complex shapes and curvatures of an actual spacecraft coordinate transformations can be used, of which some examples will be discussed.

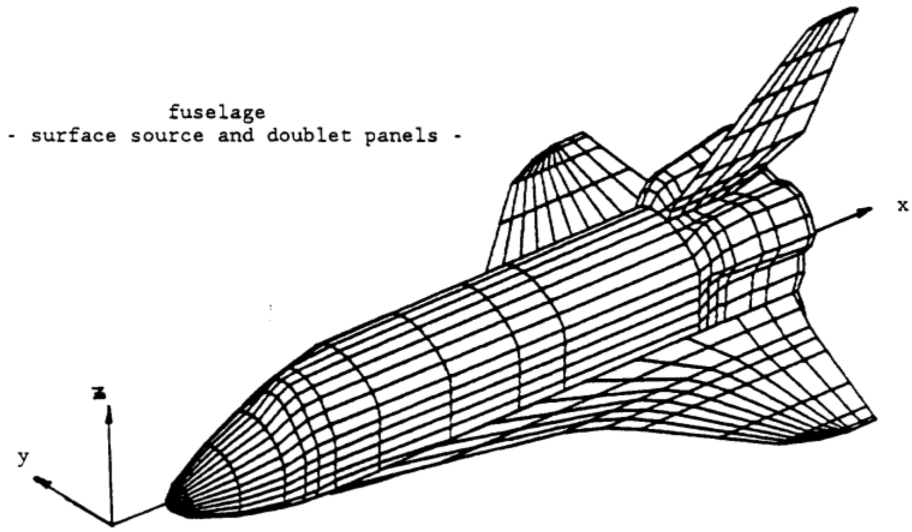

Figure 2.14: Panel representation of the Space Shuttle Orbiter, as used for the potential flow simulation of the vehicle [Bonner *et al.* , 1981].

AXISYMMETRIC ANALOGUE

The axisymmetric analogue is a method to mathematically transform the boundary layer equations for an arbitrary body to those of an axisymmetric body [Cooke, 1961]. To obtain the transformed equations the equations of motion for the flow are written in boundary layer form.

It is only valid when the crossflow between adjacent streamlines is small and can be neglected, which is the case when their sideways curvature is small (meaning the radius of the curvature is large). The effect of this assumption is that adjacent streamlines can be considered to be on an axisymmetric body with an equivalent radius r. In essence the complex body is replaced by a collection of equivalent axisymmetric bodies. Cooke also derives equations for determining the equivalent radius r, but these are relatively complex and have been simplified by other authors, such as Hamilton and Parhizkar (where they rename it to the metric coefficient h. Cooke goes even further is his paper by applying the Mangler transformation. This transformation allows the equations for an axisymmetric body to be written as if they were for a flat plate. The end result is that flat plate boundary layer methods such as the Blasius equation can be used.

UNSTRUCTURED GRIDS AND STAGNATION POINT SINGULARITY

Cooke's method has been used by many different authors for simplified boundary layer calculations. A recent example using this method is based on using an unstructured grid in combination with heating calculations based on the axisymmetric analogue. [Hamilton *et al.* , 2009]. The referenced paper explains an improved method for determining heating on an unstructured grid. Hamilton determines the equivalent radius for Cooke's transformation by using the derivative of the sideways position (y) with respect to β, the cross-streamline coordinate. The initial value of this derivative is determined on the so-called ϵ-curve, a concept introduced in an earlier paper by the same authors [Hamilton *et al.* , 2006]. Due to the nature of the stagnation point it acts as a singularity in the flowfield, which causes problems for the aerodynamic equations at the stagnation point. To circumvent this a curve is created at a very small distance ϵ from the stagnation point. The points on the curve are non-singular and the values for the aerodynamic properties can be determined from the stagnation point values using some assumptions that only hold when ϵ is small:

- Insignificant variation of the density and viscosity within the ϵ-curve.

- Approximately linear variation of the velocity and equivalent radius along a streamlin from the stagnation point within the ϵ-curve.

By determining the initial equivalent radius and derivative of y with respect to β on the epsilon curve and then propagating these along the streamlines, the equivalent radius on every point on the body is determined. Using the equivalent radius the momentum thickness and heating rate at every point on the body can then be determined using Zoby's method [Zoby *et al.* , 1981], which will be discussed below. Before the treatment of Zoby's method, a simpler method to determine the equivalent radius as found by Parhizkar et al. will be explained [Parhizkar & Karimian, 2009].

ALTERNATIVE METHOD TO DETERMINE THE METRIC COEFFICIENT

In their paper, Parhizkar et al. identify the issues with the existing methods for determining the metric coefficient (equivalent radius) as either complex to implement or only applicable to simple models. The starting point of the paper is the 2006 paper of Hamilton et al. [Hamilton *et al.* , 2006] and the paper of Parhizkar et al. does not take into account the paper of Hamilton et al. of the same year, 2009. Parhizkar's main criticisms of the method Hamilton proposed in his 2006 paper are that it is a complex method and that it is not efficient for complex geometries because of the forward propagation. Parhizkar et al. propose two measures to deal with these issues:

- For any point at which the heating needs to be calculate, propagate the adjacent streamline backwards in time towards the ϵ-curve. After the backwards propagation intersects the ϵ-curve, propagate the properties on the adjacent streamline forward.

- Instead of determining the initial metric coefficient on the ϵ-curve and then propagating it, determine the metric coefficient locally. This is done by comparing the perpendicular distance between the streamlines to the distance between two points at the same streamwise distance from the ϵ-curve on those same adjacent streamlines. This way, no integration of metric coefficient variables is necessary and only knowledge of the streamwise distance of points on the streamlines is needed.

Parhizkar et al. also refer to [Zoby *et al.* , 1981] for the calculation of the momentum thickness and heating rate using the metric coefficient. Therefore the paper of Zoby et al. will be discussed next.

MOMENTUM THICKNESS AND HEATING RATE CALCULATION

To determine the actual momentum thickness of the boundary flow, both Hamilton and Parhizkar refer to a paper by Zoby, Moss and Sutton [Zoby *et al.* , 1981]. The paper presents equations for dealing with a range of flows, including reacting and non-reacting flows, constant-entropy and variable-entropy edge conditions, and hypersonic flows.

Three cases are treated in Zoby's paper: stagnation point heating, laminar flow heating and turbulent flow heating. For the heating in the stagnation point for air the equation of Cohen [Cohen & Reshotko, 1956] is used, which relates the heating rate to the Prandtl number, stagnation point and wall enthalpy, density, viscosity and acceleration of the flow.

The other two cases are of particular interest for this research, as they detail how to calculate the momentum thickness which is needed to determine the heating rate. The equation for laminar momentum thickness a modified version of the Blasius momentum thickness equation, taking into account Eckert's reference enthalpy and the divergence of streamlines caused by the curvature of the body. The equation for the heating rate is similar to the equation for stagnation point heating discussed above, except for different coefficients, the Eckert reference enthalpy correction and the dependence on the momentum thickness Reynolds number. The equations for the turbulent momentum thickness and heating rate are similar in principles to those for the laminar case with some key differences. The major difference is that the coefficients are different and variable, depending on the velocity profile in the boundary layer. By making the guessed velocity profile dependent on the momentum thickness Reynolds number, qualitative differences between flows at different Reynolds numbers can be accounted for. The momentum thickness Reynolds number and guessed velocity profile are interdependent however, which necessitates an iterative process to find the correct values. Zoby gives an empirical relation for an axisymmetric nozzle wall, but this is not an accurate relation for the research in this report.

In conclusion, the paper of Zoby acts as the bridge between Cooke's method of transforming the aerodynamic equations to axisymmetric/flat plate equations and the calculation of the heating rate and skin friction, which will be discussed further in this chapter.

2.2.4. DETERMINING THE SKIN FRICTION

A method is needed to determine the skin friction from the momentum thickness. In this section a short summary of these methods is given, while Chapter 4 includes a more extensive treatment.

Blasius flat plate solution

Blasius was a student of the famous aerodynamicist Ludwig Prandtl. He found a solution for laminar boundary flow past a flat plate [Blasius, 1950] that has been used in many approximations. It is assumed that the displacement thickness is small (which is true for large Reynolds numbers) which leads to a constant value for the velocity and a zero velocity derivative. While an exact analytical solution is not available, it can easily be approximated by analytical series or a simple computer program. The Blasius solution is not as accurate for boundary layers with a pressure gradient or thick boundary layers.

Reynolds analogy

Osborne Reynolds postulated that there is a relation between the heat transfer and the wall stress, namely that they are proportional. This can be used to calculated friction forces if the heating is known. The relation will only hold if the velocity and temperature are similar in behaviour, varying wall temperatures or strong pressure gradients will reduce the accuracy of the solution. The advantage is that it is applicable to a wider range of shapes than flat plates and that the heating results from [Zoby *et al.*, 1981] can be used for the calculation. A further discussion of the Reynolds analogy can be found in [White, 2005].

Van Driest flat plate

Van Driest's flat plate theory [van Driest, 1956] is based on the Kármán integral relation. This integral relation also returns later in this thesis in the relation for the momentum thickness. Van Driest used assumption for the density and velocity profiles and integrated that over the thickness of the boundary layer. Because of the complicated outcome, this was then approximated using a series form, which made it much easier to handle. It is applicable for compressible, turbulent boundary flow, which is generally the hardest flow to predict.

2.3. SYSTEM & MISSION REQUIREMENTS

Before starting with the theoretical part of this thesis the system & mission requirements should be determined. The system requirements detail what the code (system) should be able to do. In the case of this thesis the mission requirements detail the requirements for results and the analysis of the results.

2.3.1. MISSION (RESULTS AND ANALYSIS) REQUIREMENTS

These are the top-level requirements for the thesis and revolve around answering the research question. The requirements are:

- An analysis regarding the static stability of the HORUS at different Mach numbers should be performed, resulting in a summary of stable and unstable coefficients.

- An analysis regarding the dynamic stability of the HORUS at different Mach numbers should be done which will give a first estimation of the evolution of the dynamic motion. A full analysis of the time-dependent motions of the HORUS is outside the scope of this research.

- An analysis regarding the total stability picture of the HORUS at different Mach numbers is needed as a judgment of what the stable and unstable motions mean for the flight characteristics.

2.3.2. SYSTEM REQUIREMENTS

These requirements flow from the mission requirements as they are needed to satisfy the mission requirements. These requirements relate to the output, accuracy of the results and the usability of the software.

USER AND INPUT REQUIREMENTS

- The software should be automated as much as possible while retaining the possibility of detailed control. A lack of automation will increase the time needed for a simulation and also increase the chance of user errors.

- To incorporate a wide range of operating circumstances the user should be able to modify as many of the input variables as possible. This also means that the user needs to be given options for the mode or assumptions the simulation uses.

- The simulation should be able to work with both symmetric (half) models as well as asymmetric full models. The only requirement for the model is that it is singular enclosed volume (no gaps or multiple volumes) and there are no errors in the model (intersections of elements, unconnected or underconnected elements).

OUTPUT REQUIREMENTS

- The aerodynamic modules of the code should provide the skin friction drag, the pressure drag, the total forces in each direction of the reference frame and the total moments in each direction of the reference frame.

- The static stability module should at least provide the static stability and control coefficients used in [Mooij, 1995].

- The dynamic stability module should provide the eigenvalues at the stability matrix and relevant derivative parameters including, but not limited to, motion amplitude half time, damping ratio, motion period and natural frequency.

VERIFICATION AND VALIDATION REQUIREMENTS

- Each module should be verified using analytical solutions or simple example cases. This means the code should be as modular as possible, such that each module can be verified separately.

- The output mentioned before should be validated using experimental or computational reference cases where available and possible.

- The stability and control coefficients should be validated against the data from [Mooij, 1995]. From this comparison an estimate of the differences between the data from the current simulation and the reference values can be made.

The requirements will come return in most chapters to make sure they are satisfied.

3

Flight Mechanics, Stability & Control

This chapter will deal with the theory surrounding flight mechanics and stability. Although control analysis and design is outside the scope of this thesis, it will be discussed briefly as it is closely related to the stability. As noted in the requirements, the software needs to be able to give predictions for a range of parameters regarding the static and dynamic stability of the vehicle. Furthermore, the requirements further state that an analysis regarding the static and dynamic stability of the HORUS spaceplane is required. This chapter is structured as follows. Section 3.1 discusses the relevant reference frames that will be used in this thesis. Section 3.2 deals with the equations of motion, the method through which they are derived and the resulting stability matrix. Section 3.3 discusses the static stability of the spaceplane and the relevant coefficients. Section 3.4 details the concepts regarding the dynamic stability of the vehicle. The final section is Section 3.5 which discusses how the concepts of this chapter will be applied to the stability analysis.

3.1. Reference Frames

To properly discuss flight mechanics it is important to clearly define the reference frames that are used. For a choice of reference system it should first be clear what the scope of the investigation is. In the case of the current research the focus is on the flow around the vehicle and the resulting effects on the stability and control of the vehicle at non-orbital velocities. The important reference frames for this study are the planetocentric reference frame for the derivation of the equations of motion, the body-fixed reference frame and the aerodynamic reference frame. These reference frames will now be briefly discussed.

3.1.1. Rotating Planetocentric Reference Frame F_C

This reference frame is fixed to the Earth but rotates with the rotation of the Earth. The origin of the frame is in the center of mass of the Earth. The X_C-axis passes through the Greenwich meridian, the Y_C-axis lies in the equatorial plane and is perpendicular to the X_C-axis and finally the Z_C-axis is in the direction of the spinning axis of the Earth. The Planetocentric Reference Frame is shown in Figure 3.1.

3.1.2. Body-fixed Reference Frame F_b

The body-fixed reference frame is a reference frame connected to the body of the vehicle. It remains fixed to the craft in all cases. The choice of axes is rather arbitrary, an often used definition can be found in Figure 3.2. It has its origin in the center of mass, the X_b-axis pointing to the nose in the

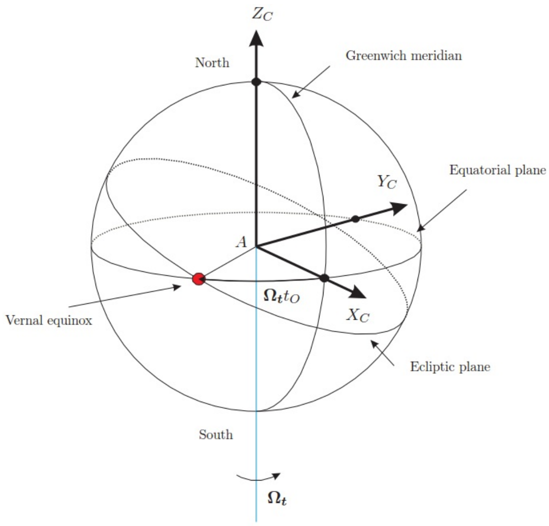

Figure 3.1: Planetocentric Reference Frame (F_C) definition [Mulder *et al.* , 2013].

plane of symmetry, the Z_b-axis pointing downwards in the plane of symmetry and the Y_b-axis completing the right-handed axis system. In the figure the roll angle (ϕ), pitch angle (θ) and yaw angle (ψ) are also indicated. As the axis directions can be arbitrarily chosen as long as an orthogonal ref-

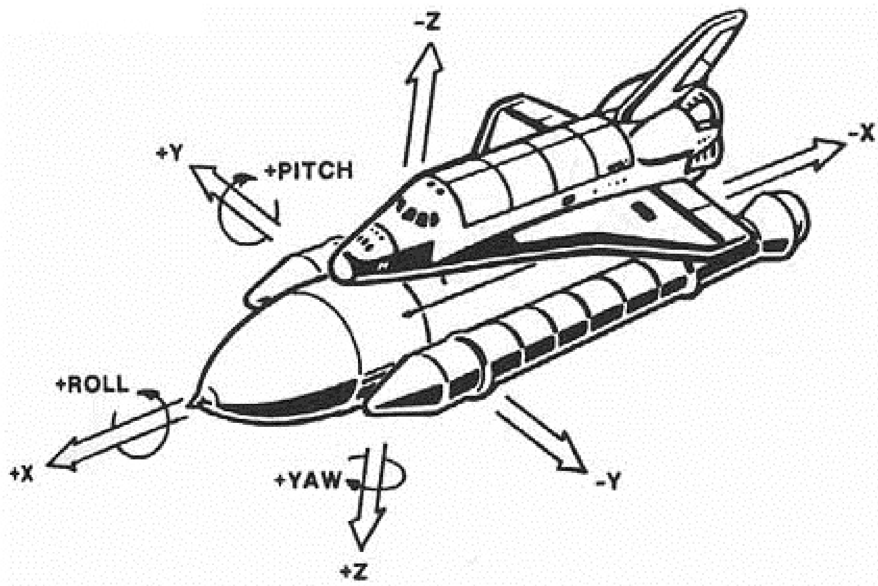

Figure 3.2: Body-fixed reference frame (F_b) definition [J.Erickson, 1986]

erence frame results, there are also other options. Two of these that will be used are the stability reference frame and a body-fixed reference frame with origin at the tip of the nose pointing backwards. For the stability reference frame the axes are chosen to point in the direction of a reference flight condition. If the aircraft is perturbed the axes keep pointing at the reference flight condition, in effect rotating with respect to the body. The stability reference frame will be used to study the stability after perturbations. The nose-based body-fixed reference frame has the x-axis pointing to the back of the spacecraft, z-axis pointing to the upper side of the spacecraft and the y-axis completing the right-handed reference frame. This frame is used for the 3D-model, meshing and Euler simulation.

3.1.3. AERODYNAMIC REFERENCE FRAME F_a

The aerodynamic reference frame has its origin in the center of mass of the spaceplane. The X_a-axis points in the direction of the velocity vector of the vehicle. The Z_a-axis is in the symmetry plane and the Y_a-axis completes the right-handed coordinate system. This system is very useful to study the aerodynamics of the vehicle. The aerodynamic velocity V_a can be expressed in the aerodynamic reference frame:

$$\mathbf{V}_a^a = \begin{bmatrix} u_a^a \\ v_a^a \\ w_a^a \end{bmatrix} = \begin{bmatrix} V_a \\ 0 \\ 0 \end{bmatrix} \tag{3.1}$$

It is more convenient to express it in the body reference frame, as this is often used in the literature (for example, [White, 2005]):

$$\mathbf{V}_a^b = \begin{bmatrix} u_a^b \\ v_a^b \\ w_a^b \end{bmatrix} = \begin{bmatrix} u \\ v \\ w \end{bmatrix} \tag{3.2}$$

where u, v and w are the velocity in the direction of the axes of the body-fixed reference frame and V_a is the scalar velocity in the aerodynamic reference frame (not a vector because the aerodynamic reference frame always points in the direction of the velocity). The aerodynamic reference frame is shown in Figure 3.3.

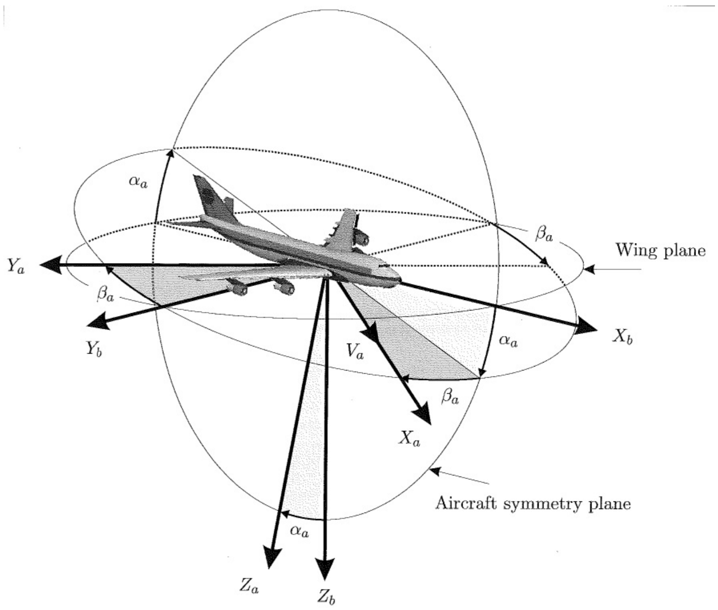

Figure 3.3: Aerodynamic reference frame (F_a) definition [Mulder *et al.* , 2013].

3.2. RE-ENTRY VEHICLE EQUATIONS OF MOTION

The goal in this section is to obtain the equations of motion using the assumptions in Section 3.2.2, from which the stability and control matrices should follow. The first step is to define how the vehicle will be treated and what assumptions can be used, which will be done next.

3.2.1. CHOICE OF METHOD

There are two major options for the derivation of the equations of motion, treating the HORUS as a re-entering spacecraft or as an aircraft. The choice will have an effect on further assumptions that can be made and the validity of the results. First the characteristics of the two methods will be summarized after which the choice and the reasons for it will be discussed.

Aircraft treatment

This method is often used for research into the stability of aircraft and it has been shown to work well for a range of subsonic aircraft. The assumptions necessary for this type of treatment such as the lack of Mach dependence and flat Earth assumption break down at high velocities and altitudes, making it impossible to extend simulations and results to higher Mach numbers and/or altitudes. Furthermore, the derivation is aimed at conventionally configured airliners, which has an effects on the assumptions that are made regarding the shape. The advantage is that the motions can be simply separated into longitudinal and lateral motions for the stability analysis. Furthermore the number of coefficients needed for the stability matrices is also smaller because of number of variables are neglected.

Spacecraft treatment

The spacecraft treatment has a number of advantages for re-entering spaceplanes. First of all it uses C_L and C_D (aerodynamic reference frame) instead of C_X and C_Z (body reference frame), which makes analysis of the aerodynamic performance much easier. Due to the assumptions made, this method is also valid for higher Mach numbers and altitudes than those in this thesis. Furthermore, the effect of yaw thrusters can be easily taken into account, which is important for the TAEM as for the HORUS they are used down to Mach 1. An important disadvantage is that the dependency of the drag coefficient on height is neglected, which is very reasonable to do for Mach numbers above Mach 1.5, but not always valid below Mach 1.5. This should be kept in mind when dealing with motions that have a large variation is altitude. However, this effect is also not taken into account in the aircraft method, so it should not matter for the trade-off.
In the end, the choice is made for the equations derived for re-entry vehicles (spacecraft treatment). This was done because of the unconventional shape of HORUS compared to airliners, the high altitudes and velocities that occur during the TAEM and because the reference data for the HORUS was calculated based on equations derived using the spacecraft method. Furthermore, it allows for the inclusion of Mach effects on the parameters, which could play a significant role in the TAEM. In the next section the conventions and assumptions for this treatment will be discussed briefly.

3.2.2. CONVENTIONS & ASSUMPTIONS

For a proper treatment of stability it should be clear what the naming and direction conventions are. There will also be certain assumptions that will be used for the derivations which need to be mentioned. Many of the assumptions will also be discussed in following sections when they play a role in the derivation. The conventions and assumptions will be described below:

- Several different notations for derivatives will be used. In subscript notation, the non-subscript letters or symbols are the variables of which the derivative is taken while the subscript letters are the variables with respect to which the derivative is taken. For example, in subscript notation X_u means that the derivative of X with respect to u is taken. Not all subscripts in this chapter indicate derivatives, the interpretation is given where necessary.

- For the type of spaceplanes in this report there are three relevant control surfaces: the body flap, elevons and rudders. For the body flap, a downward deflection is considered positive. For both elevons a downward deflection is taken as the positive direction. Finally, for both rudders a clockwise deflection when looking at the top of the vehicle is considered to be the positive direction.

- Different forces are indicative of different reference frames. For example, the lift and drag forces are relevant in the aerodynamic reference frame, while the forces in X- and Z-direction are relevant for the body reference frame.

- Taking the Space Shuttle as an example, the TAEM starts at Mach 2.5 (762 m/s) at an altitude of approximately 25,300 m and about 96 km from the runaway [NASA, 2002] and ends less then 6.5 minutes later when the landing starts [Harwood, 2006]. The mentioned Mach number of 2.5 is relative to the air surrounding the vehicle. As the atmosphere rotates with approximately the same angular velocity as the Earth, it can be concluded that the rotation term can be safely neglected as long as an aerodynamic or body-fixed reference frame is used and the assumption is made that there is no wind.

- To simplify the equations the assumption of a perfectly spherical, non-rotating Earth will be made. For the kinematic attitude equations it will also be assumed that the vehicle trajectory is parallel to the equator and does not change.

- For HORUS, I_{xy} and I_{yz} are assumed to be zero as the craft has a symmetry plane. Another simplification will be that $I_{xz} \approx 0$, which is the case when the craft is approximately rotationally symmetric along the X_b axis.

- For the dynamic stability analysis, the spacecraft is assumed to be flying in trimmed condition. This cancels a number of terms concerned with the pitching moment. This may not always be strictly true in all results due to the lack of exact a priori knowledge of what the required state for the trimmed condition is.

3.2.3. SPACEPLANE TREATMENT EQUATIONS OF MOTION

Using the treatment and assumptions discussed before the equations of motion can be derived. Because there are many excellent sources for such a derivations such as [Vinh, 1981] or [Mooij, 1997], it will not be repeated here. In essence the derivation starts with equations that relate the complete set of forces and fictitious forces (due to using a non-inertial reference frame) to the translational accelerations of the vehicle. The same is done for the rotations, moments and rotational accelerations. The assumptions are applied to obtain simplified equations of motion. The resulting equations are then linearized, which means only linear effects will be studied. To do this it is assumed that close to a reference state the response to a disturbance is linear and that higher-order effects can be neglected. The resulting simplified, linearized equations can be found in Equations (3.3) through (3.11).

These 9 equations are the 9 uncoupled, first-order differential equations that can be used to describe the response to disturbances from the reference state.

$$\Delta\dot{V} = -\frac{\Delta D}{m} + 2\frac{g_0}{R_0}\sin\gamma_0\Delta R - g_0\cos\gamma_0\Delta\gamma \tag{3.3}$$

$$\begin{aligned}\Delta\dot{\gamma} = \left(-\dot{\gamma}_0 + \frac{2V_0}{R_0}\cos\gamma_0\right)\frac{\Delta V}{V_0} + \left(\frac{2g_0}{R_0} - \frac{V_0^2}{R_0^2}\right)\frac{\cos\gamma_0}{V_0}\Delta R - \left(\frac{V_0^2}{R_0} - g_0\right)\frac{\sin\gamma_0}{V_0}\Delta\gamma \\ -\frac{L_0}{mV_0}\sin\sigma_0\Delta\sigma + \frac{\cos\sigma_0}{mV_0}\Delta L - \frac{\sin\sigma_0}{mV_0}\Delta S\end{aligned} \tag{3.4}$$

$$\Delta\dot{R} = \sin\gamma_0 \Delta V + V_0 \cos\gamma_0 \Delta\gamma \tag{3.5}$$

$$\Delta\dot{p} = \frac{\Delta M_x}{I_{xx}} \tag{3.6}$$

$$\Delta\dot{q} = \frac{\Delta M_y}{I_{yy}} \tag{3.7}$$

$$\Delta\dot{r} = \frac{\Delta M_z}{I_{zz}} \tag{3.8}$$

$$\begin{aligned}\Delta\dot{\alpha} = \Delta q - \frac{1}{mV_0}\Delta L - \frac{g_0}{V_0}\cos\gamma_0 \sin\sigma_0 \Delta\sigma + \left(\frac{L_0}{mV_0^2} - \frac{g_0}{V_0^2}\cos\gamma_0\cos\sigma_0\right)\Delta V \\ - \frac{g_0}{V_0}\sin\gamma_0\cos\sigma_0\Delta\gamma - \frac{2g_0}{R_0 V_0}\cos\gamma_0\cos\sigma_0\Delta R\end{aligned} \tag{3.9}$$

$$\begin{aligned}\Delta\dot{\beta} = \sin\alpha_0\Delta p - \cos\alpha_0\Delta r - \frac{\Delta S}{mV_0} - \frac{g_0}{V_0}\cos\gamma_0\cos\sigma_0\Delta\sigma + \frac{g_0}{V_0^2}\cos\gamma_0\sin\sigma_0\Delta V \\ + \frac{2g_0}{R_0 V_0}\cos\gamma_0\sin\sigma_0\Delta R + \frac{g_0}{V_0}\sin\gamma_0\sin\sigma_0\Delta\gamma\end{aligned} \tag{3.10}$$

$$\begin{aligned}\Delta\dot{\sigma} = -\cos\alpha_0\Delta p - \sin\alpha_0\Delta r - \left(\frac{L_0}{mV_0} - \frac{g_0}{V_0}\cos\gamma_0\cos\sigma_0\right)\Delta\beta + \frac{L_0}{mV_0}\sin\sigma_0\Delta\gamma \\ + \frac{\tan\gamma_0}{mV_0}\left(\sin\sigma_0\Delta L + \cos\sigma_0 L_0\Delta\sigma + \cos\sigma_0\Delta S - \frac{L_0}{V_0}\sin\sigma_0\Delta V\right)\end{aligned} \tag{3.11}$$

The reference states in the linearized equations are known from the nominal trajectory except for p_0, q_0 and r_0. These can be calculated from Equations (3.12) through (3.14).

$$p_0 = c_1 \sin\alpha_0 + c_2\cos\alpha_0 \tag{3.12}$$

$$q_0 = \frac{L_0}{mV_0} - \frac{g_0}{V_0}\cos\gamma_0\cos\sigma_0 \tag{3.13}$$

$$r_0 = -c_1\cos\alpha_0 + c_2\sin\alpha_0 \tag{3.14}$$

with

$$c_1 = \frac{g_0}{V_0}\cos\gamma_0\sin\sigma_0 \tag{3.15}$$

$$c_2 = \frac{L_0}{mV_0}\tan\gamma_0 sin\sigma_0 \tag{3.16}$$

The equations of motion can be cast in state-space form, resulting in a 9x9 stability matrix and a 9x6 control matrix. As higher order effects are neglected (for example, the effect of the roll rate on the angle of attack) many entries of the resulting matrix will be zero. Before obtaining the final matrix the force and moment variations need to be evaluated. For example, the change in drag force can be expressed as the sum of all the contributions to the drag. Neglecting the small contribution of control surfaces and the altitude variation to the total drag the simplified Equation (3.17) is obtained.

$$\Delta D = \frac{\partial D}{\partial M}\Delta M + \frac{\partial D}{\partial \alpha}\Delta\alpha \tag{3.17}$$

This is done for all forces and moments, for more information see [Mooij, 1997]. This notation gives to the stability coefficients, which express the variation of one parameter as a result of a variation of a state variable. The forces and moments are non-dimensionalized by a relevant non-dimensionalization term. For example, the drag can be non-dimensionalized as follows:

$$C_D = \frac{D}{\frac{1}{2}\rho V^2 S} \tag{3.18}$$

The resulting equation for the change in moment coefficient can be found in Equation (3.19). The coefficients will be the basis for the static stability analysis.

$$\Delta C_D = C_{D_M}\Delta M + C_{D_\alpha}\Delta\alpha \tag{3.19}$$

The final matrix equation can be found in Equation (3.20). The formulas for the coefficients can be found in Appendix 9.

$$\begin{pmatrix} \Delta\dot{V} \\ \Delta\dot{\gamma} \\ \Delta\dot{R} \\ \Delta\dot{p} \\ \Delta\dot{q} \\ \Delta\dot{r} \\ \Delta\dot{\alpha} \\ \Delta\dot{\beta} \\ \Delta\dot{\mu} \end{pmatrix} = \begin{bmatrix} a_{VV} & a_{V\gamma} & a_{VR} & 0 & 0 & 0 & a_{V\alpha} & 0 & 0 \\ a_{\gamma V} & a_{\gamma\gamma} & a_{\gamma R} & 0 & 0 & 0 & a_{\gamma\alpha} & a_{\gamma\beta} & a_{\gamma\mu} \\ a_{RV} & a_{R\gamma} & 0 & 0 & 0 & 0 & 0 & 0 & 0 \\ 0 & 0 & 0 & 0 & 0 & 0 & 0 & a_{p\beta} & 0 \\ a_{qV} & 0 & 0 & 0 & 0 & 0 & a_{q\alpha} & 0 & 0 \\ 0 & 0 & 0 & 0 & 0 & 0 & 0 & a_{r\beta} & 0 \\ a_{\alpha V} & a_{\alpha\gamma} & a_{\alpha R} & 0 & a_{\alpha q} & 0 & a_{\alpha\alpha} & 0 & a_{\alpha\mu} \\ a_{\beta V} & a_{\beta\gamma} & a_{\beta R} & a_{\beta p} & 0 & a_{\beta r} & 0 & a_{\beta\beta} & a_{\beta\mu} \\ a_{\mu V} & a_{\mu\gamma} & 0 & a_{\mu p} & 0 & a_{\mu r} & a_{\mu\alpha} & a_{\mu\beta} & a_{\mu\mu} \end{bmatrix} \begin{pmatrix} \Delta V \\ \Delta\gamma \\ \Delta R \\ \Delta p \\ \Delta q \\ \Delta r \\ \Delta\alpha \\ \Delta\beta \\ \Delta\mu \end{pmatrix}$$
$$+ \begin{bmatrix} 0 & 0 & 0 & 0 & 0 & 0 \\ 0 & 0 & 0 & 0 & 0 & 0 \\ 0 & 0 & 0 & 0 & 0 & 0 \\ 0 & b_{pa} & 0 & b_{px} & 0 & 0 \\ b_{qe} & 0 & 0 & 0 & b_{qy} & 0 \\ 0 & b_{ra} & b_{rr} & 0 & 0 & b_{rz} \\ 0 & 0 & 0 & 0 & 0 & 0 \\ 0 & 0 & 0 & 0 & 0 & 0 \\ 0 & 0 & 0 & 0 & 0 & 0 \end{bmatrix} \begin{pmatrix} \Delta\delta_e \\ \Delta\delta_a \\ \Delta\delta_r \\ \Delta M_{T,x} \\ \Delta M_{T,y} \\ \Delta M_{T,z} \end{pmatrix} \tag{3.20}$$

3.3. STATIC STABILITY & CONTROL

In this section the coefficients relevant to the stability analysis performed in this thesis will be discussed. Their meaning and preferred sign for stability (where applicable) will also be treated. Only coefficients for first-order effects will be discussed and higher-order effects are neglected in the stability analysis.

3.3.1. STABILITY COEFFICIENTS

DRAG FORCE COEFFICIENTS

C_{D_α}

This coefficient deals with the effect of the angle of attack on the drag force (along the X-axis of the aerodynamic frame). A pure change in angle of attack is obtained by varying the velocity along the Z-axis. The expected sign of this coefficient is positive, as the drag coefficient increases with angle of attack and the coefficient is designated as being positive in the negative X_a-direction.

C_D

This is the drag coefficient in the reference condition, which represents the force along the X-axis in the aerodynamic reference frame. It is generally more useful than C_X in the stability reference frame because it indicates whether the vehicle is in equilibrium (constant velocity) or accelerating. Again, the sign will be positive due to the definition of this coefficient in the aerodynamic reference frame.

LIFT FORCE DERIVATIVES

C_{L_α}

This coefficient indicates the effect of the angle of attack on the lift coefficient. The expected sign of this coefficient depends on the angle of attack, before stall occurs it will be positive, while post-stall it will be negative. Similar to the drag coefficient, the lift coefficient is defined as being positive in the direction of the negative Z-axis in the aerodynamic reference frame.

C_L

This is the lift coefficient, which represents the force along the Z-axis in the aerodynamic reference frame. It is generally more useful than C_Z in the stability reference frame because it indicates whether the vehicle is in equilibrium or accelerating perpendicular to the flow direction. The expected sign depends on the geometry of the vehicle and the angle of attack. For HORUS, the lift coefficient is negative at zero angles of attack (so a positive angle of attack is necessary to generate lift).

MOMENT AROUND Y-AXIS (M)

C_{m_α}

This is one of the most important stability coefficients as it expresses the effect of the angle of attack on the pitching moment. If stability is not achieved for coefficient then an increase in the angle of attack increases the pitching moment, which in turn increases the angle of attack again. Without control input this would then reinforce itself and at a certain angle of attack stall occurs, leading to a drop in the lift force which can be very dangerous. It is thus paramount that $C_{m_\alpha} < 0$. The way to achieve this is to have the aerodynamic center behind the center of mass.

The aerodynamic center is the point on the vehicle around which a change in lift does not produce a change of moment. In other words, it can be considered as the point in which changes in lift force work. If the aerodynamic center is located behind the center of mass, this means that an increase in angle of attack will produce an increase in lift (when not in stall conditions), which then in turn means a moment is created which is opposite to the angle of attack.

FORCE ALONG Y-AXIS

C_{S_β}

C_{S_β} concerns the the effect of a sideslipping motion on the lateral force. Due to the choice of coordinate system, the lateral force is negative for positive sideslip angles, thus $C_{S_\beta} < 0$. The design of the vehicle can influence the value of this derivative by the size and sideways drag coefficient of the fuselage and vertical surfaces, which in the case of HORUS are the winglets.

MOMENT AROUND X-AXIS (L)

C_{l_β}

This coefficient deals with the effect of the sideslip angle on the roll moment. For stability, a negative sign of this coefficient is desirable, because in that case the sideslip generates an opposite moment. The largest contributions to C_{l_β} are the dihedral and sweep angle of the wing, and the wing-fuselage interaction on the flow. It is one of the primary lateral stability coefficients, because a negative value of this coefficient ensures a moment occurs that works in the direction of a level spaceplane after a sideslip disturbance.

MOMENT ALONG Z-AXIS (N)

C_{n_β}

This coefficient is about the effect of the sideslip angle on the yaw moment. Also known as the static directional or weathercock stability, a positive sign is desirable because this makes the vehicle 'resist' (opposite moment) a change in sideslip angle. The tailplanes have a significant stabilizing effect on this type of stability, as do swept wings at high angles of attack.

3.3.2. CONTROL DERIVATIVES

The control-related stability derivatives deal with the derivatives of forces and moments following from deflections of the control surfaces. Because in vehicles such as the HORUS the functions of elevator and aileron are combined in an elevon, these coefficients will be discussed together.

ROLL MOMENT

$C_{l_{\delta_e}}$

This is the aileron effectivity, i.e. how large a moment along the X-axis a deflection of the elevon creates. This coefficient represents one of the primary functions of the elevon, initialing a rolling motion. Due to the choice of axes, this coefficient is negative. It is important to note that it is dependent on C_L for higher Mach numbers, so the coefficient has to be determined at different Mach numbers. According to [Cucinelii & Müller, 1988], negative deflections (upwards) have a larger effect of the roll moment than positive deflections.

PITCH MOMENT

$C_{m_{\delta_e}}$

This coefficient is the rudder effectivity, i.e. how large a moment along the Y-axis a symmetric deflection of the elevon creates. As this is one of the primary functions of the elevon, it needs to be designed for carefully and have a negative sign. The larger the coefficient, the more sensitive the vehicle is to pitch input. According to [Cucinelii & Müller, 1988], this coefficient should increase for decreasing Mach numbers, at least in the supersonic regime.

$C_{m_{\delta_b}}$

Very similar to the coefficient $C_{m_{\delta_e}}$, it has a negative value. The body flap is usually not used as control but as a trimming surface. This coefficient is important in determining the conditions in which the vehicle can and cannot be trimmed. However, in the TAEM the body flap is kept at a deflection of $-20°$, which means this coefficient is of less importance for that regime.

YAW MOMENT

$C_{n_{\delta_r}}$
This is the rudder effectivity, i.e. how large a moment along the Z-axis a deflection of the rudder creates. This coefficient represents one of the primary functions of the rudder, initialing a yawing motion. Due to the choice of axes, this coefficient is negative. An interesting characteristic is that according to [Cucinelii & Müller, 1988] there is only a Mach number dependence of this coefficient for low rudder deflections, while for deflections higher than 25° there is no Mach number dependence.

3.4. DYNAMIC STABILITY & CONTROL

Now that the static stability derivatives, requirements and characteristics have been investigated the dynamic stability of the vehicle should be investigated. If a vehicle is dynamically stable it means that in trying to return to its initial state the amplitude of the deviation decreases. Thus, the dynamic stability is a requirement in addition to static stability, which only requires a reaction in opposite direction of the disturbance without regard to the magnitude of that reaction.

3.4.1. SOLUTION OF THE EQUATIONS OF MOTION

In the state-space form the equations of motion can be summarized with Equation (3.21).

$$\dot{\mathbf{x}} = A\mathbf{x} + \Delta\mathbf{f_c} \tag{3.21}$$

Where $\mathbf{x}$ is the state vector, A is the system matrix in which the entries are calculated using the stability derivatives, $\Delta\mathbf{f_c}$ is the control vector and $\dot{\mathbf{x}}$ is the resulting motion. When analyzing the stability of uncontrolled motion (stick-free), the control forces are zero, leading to:

$$\dot{\mathbf{x}} = A\mathbf{x} \tag{3.22}$$

This is a first order differential equation. The general solution to this type of equation
The general form for solution of the equilibrium equations of symmetric motions is:

$$\mathbf{x}(t) = \boldsymbol{\mu} e^{\lambda t} \tag{3.23}$$

where $\boldsymbol{\mu}$ is the eigenvector, λ is the eigenvalue and t is the time. Because of the linearity of the system, the total solution can be written as the sum of the individual parts:

$$\mathbf{x}(t) = \sum_i \boldsymbol{\mu}_i e^{\lambda_i t} \tag{3.24}$$

This means the motion of the vehicle only has positive dynamic stability if all the components do. The condition for positive dynamic stability of each component motion is:

$$\lim_{t\to\infty} \mathbf{x}(t) = 0 \tag{3.25}$$

Outside of the trivial solution ($\boldsymbol{\mu} = 0$) this means that $\lambda < 0$ for stable motions. Determining the complete motion of the vehicle is outside the scope of this thesis, but by investigating the eigenvalues and eigenvectors a first impression of the dynamic stability can be obtained. Depending on the specific component motion, the eigenvalue can either be real or complex. The effect of this distinction will be discussed next.

REAL EIGENVALUES

If the eigenvalue only has a real part, this means the motion is not periodic. As mentioned before, for positive stability the eigenvalue needs to be negative. The speed at which the vehicle returns to the reference state for a given negative, real eigenvalue can be expressed using the half amplitude time T_{half} or the exponential time constant τ:

- The time to damp to half amplitude, T_{half}, is self-explanatory in its meaning.

  $$x(t+T_{1/2}) = \frac{1}{2}x(t) = e^{\lambda(t+T_{1/2})} = \frac{1}{2}e^{\lambda t}$$

  Which leads to:

  $$T_{1/2} = \frac{\ln\frac{1}{2}}{\lambda}$$

  In case of positive eigenvalues, instead of the half amplitude time T_{half} the doubling time T_{double} can be used. This will come out of the half time equations as a negative value.

- Exponential time constant τ, the time interval in which the exponent decreases by 1 and the exponential function itself thus decreases by a factor of $\frac{1}{e}$. This means:

  $$x(t+\tau) = \frac{1}{e}x(t) = e^{\lambda(t+\tau)} = \frac{1}{e}e^{\lambda t}$$

  Which can be solved to yield:

  $$\tau = -\frac{1}{\lambda}$$

The general shape of the responses is shown in Figure 3.4. The graphs show the trend of the response for a negative real eigenvalue to go to zero and for a positive real eigenvalue to go to infinity. Clearly, the left case is preferable from a vehicle stability point of view.

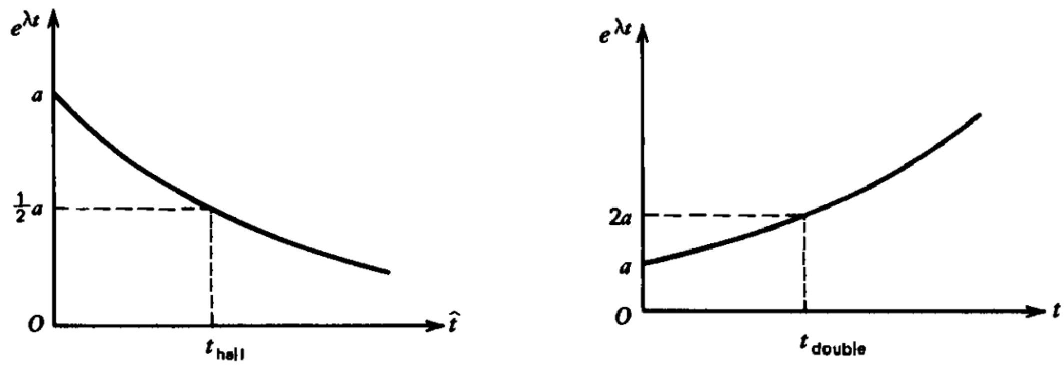

Figure 3.4: General response shape for negative (left) and positive (right) real eigenvalues [Etkin, 1996].

Complex eigenvalues
If the eigenvalue is a complex value there is a real and an imaginary part. As for real (non-complex) eigenvalue discussed before, the sign of the real part of the complex eigenvalue determines whether the response tends to return to the equilibrium position. The imaginary part of the eigenvalue indicates the response in periodic in nature.

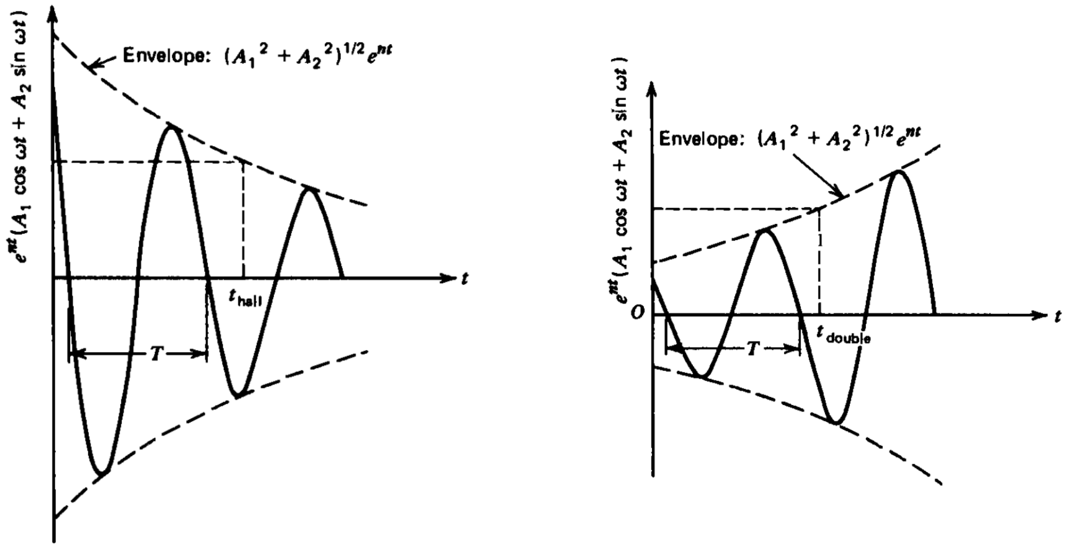

Figure 3.5: General response shape for negative (left) and positive (right) complex eigenvalues [Etkin, 1996].

The general shape of the responses is shown in Figure 3.5. The graphs show the periodic nature of the response. Similar to the real eigenvalues, the trend of the response for a negative complex eigenvalue is to go to zero and for a positive complex eigenvalue to go to infinity.

The complex eigenvalues are always conjugate pairs, meaning the real part is the same but the sign of the complex part changes:

$$\lambda_{c_{1,2}} = \xi_c \pm j\eta_c \qquad j = \sqrt{-1} \tag{3.26}$$

The resulting response equation for example value x_1 is given in Equation (3.27).

$$x_1(t) = a_1 e^{(\xi + j\eta)t} + a_2 e^{(\xi - j\eta)t} \tag{3.27}$$

Exploiting Euler's formula (Equation (3.28)) relating complex functions to trigonometric functions, a form of the response equation is obtained in which the periodic nature is more explicit (Equation (3.29)).

$$e^{jx} = \cos x + j \sin x \tag{3.28}$$

$$x_1(t) = e^{\xi t}\left(A_1 \cos(\eta t) + A_2 \sin(\eta t)\right) \tag{3.29}$$

in which:

$$A_1 = (a_1 + a_2) \qquad A_2 = j(a_1 - a_2)$$

The period of the oscillation follows from the imaginary part η of the two eigenvalues. When the argument of the harmonic function has increased by 2π a time P has elapsed:

$$\eta_c P = 2\pi \rightarrow P = \frac{2\pi}{\eta_c} \tag{3.30}$$

The amplitude of the oscillation, also known as the envelope, is given by:

$$A_{env} = \sqrt{A_1^2 + A_2^2} e^{\xi t``} \tag{3.31}$$

It can be seen from this equation that only the real part of the eigenvalues determines the amplitude and thus the convergence to zero. Similar variables can be used to describe the damping of the motion compared to real eigenvalues. The only difference is that the contributions of the real and imaginary part need to be separated.

- time to damp to half amplitude, same as for real eigenvalues, but with λ_c replaced by ξ_c:

$$T_{1/2} = \frac{\ln \frac{1}{2}}{\xi}$$

- The damping ratio ζ describes the decay of the oscillations. It can be determined using:

$$\zeta = -\frac{\xi}{\sqrt{\xi^2 + \eta^2}}$$

  The denominator of the equation is also known as the natural frequency ω_n, so $\omega_n = \sqrt{\xi^2 + \eta^2}$. The damping ratio can thus also be written as:

$$\zeta = -\frac{\xi}{\omega_n} \tag{3.32}$$

3.4.2. ANALYSIS OF STABILITY USING THE DAMPING RATIO

The damping ratio is very useful for stability analysis, as the type of response behaviour can be quickly predicted from the value of ζ:

$\zeta > 1$
For this damping ratio the eigenvalues are both real and negative, leading to a damped, aperiodic motion. Higher values of ζ lead to higher damping, reducing the halving time.

$\zeta = 1$
For this damping ratio the roots of the characteristic equation are equal, leading to a single eigenvalue. For this damping ratio the motion is critically damped, which means there are no oscillations.

$0 < \zeta < 1$
The motion is periodic and damped because the eigenvalues are complex and the real part is negative. Higher values of ζ lead to higher damping.

$\zeta = 0$
For this damping ratio the stability is neutral, meaning that the amplitude of the motion does not change from the initial amplitude.

$-1 < \zeta < 0$
For damping ratios lower than zero the stability is negative, meaning that the motion diverges due to positive real parts of the complex eigenvalue. The divergence is periodic.

$\zeta < -1$
This indicates a periodic, diverging motion due to real, positive eigenvalues. The more negative the value of ζ is, the faster the motion diverges.

In summary, the equilibrium is stable if all real eigenvalues and real parts of the complex eigenvalues are negative. In the complex plane this translates to the requirement that all points should be on the left side of the imaginary axis.

3.4.3. EIGENVECTOR ANALYSIS

The eigenvalue analysis discussed in the previous section gives answers about whether is stable and how long it takes to decay or grow. It does not however give insight in the type of motion that occurs, which is where an eigenvector analysis comes in. Each of the eigenvalues will have a corresponding eigenvector with as many entries as there are eigenvalues. The largest values in the eigenvector will dominate and thus characterize the motion. For this it is useful to express the eigenvectors in a norm z and an argument θ_{arg}. These can be calculated using Equations

$$z = \sqrt{\xi^2 + \eta^2} \tag{3.33}$$

$$\theta_{arg} = \arctan \frac{\eta}{\xi} \tag{3.34}$$

By using the norm to determine the largest contributors in an eigenvector the corresponding eigenmotion of the vehicle can be identified. According to [Mooij, 1997] 6 typical motions can be expected:

1. **Short period Oscillation:** The short period motion is characterized by relatively large changes in angle of attack and high pitch rates. If the motion is short and well-damped the difference in height and velocity is insignificant (generally true for conventional aircraft), while in the case the motion is longer and less well-damped it could play a role (generally higher up in the atmosphere for spaceplanes). According to [Mooij, 1997] for the HORUS below a Mach number of 3 and a bank angle of 55° this mode changes into two separate, aperiod modes of which one is stable and the other is unstable.

2. **Phugoid:** The phugoid motion is also a longitudinal motion, but in this case the height and velocity vary while the angle of attack is relatively constant. This means that in essence this is an exchange between potential and kinetic energy. The motion is generally slower than the short period oscillation and unstable.

3. **Lateral oscillation:** The lateral oscillation is for conventional aircraft often highly damped and fast. For the initial stages of re-entry of HORUS this mode is unstable, but it should be stable in the TAEM. Major components of this motion are the yaw rate and the roll rate, although the latter does not influence the motion much.

4. **Aperiodic roll motion:** There are two aperiod roll modes, a fast and a slow roll mode which both have the bank angle as the main contributor. It is expected to be stable in most of the flight regime, which includes the TAEM.

5. **Spiral mode:** This lateral mode is mainly created by a yawing motion, though there is some contribution of a rolling motion. The sideslip angle is nearly zero. This is generally a very slow motion that is aperiodic and can either be stable or unstable. It is generally expected to be present when flying with a non-zero bank angle.

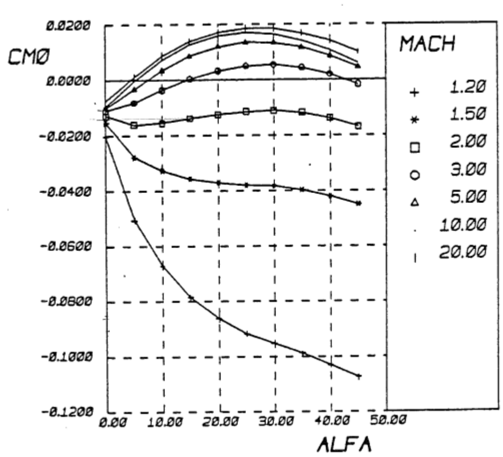

Figure 3.6: Clean pitching moment for HORUS [Cucinelii & Müller, 1988].

6. **Height mode:** This final mode has the altitude as a main contributor and is a lightly damped aperiodic motion with the altitude changes as dominant factor. It is not expected to be visible in the TAEM, because it generally occurs in the hypersonic phase.

With the information about the different modes that can occur the eigenvectors can be analyzed. For a spaceplane that is easy to fly not all modes need to stable, but those with short doubling times and periods may make control of the vehicle difficult. The next section discusses some extra aspects of the stability analysis.

3.5. APPLICATION TO STABILITY ANALYSIS

The theory necessary for a proper stability analysis has been discussed in the chapter. The question remains how to apply this theory to satisfy the requirement

While in this chapter the theory behind determining stability has been discussed, the way in which this can be implemented has been absent. The equations use derivatives of forces and moments with respect to control variables such as angles and angular velocities. As exact derivatives are not possible using numerical methods a finite difference calculation needs to be used. An example equation is shown in Equation (3.35).

$$C_{m_\alpha} = \frac{C_{m,\alpha_2} - C_{m,\alpha_1}}{\alpha_2 - \alpha_1} = \frac{\Delta C_m}{\Delta \alpha} \tag{3.35}$$

Choosing an appropriate angle of attack step depends on two contradictory requirements. On the one hand the change in the coefficient needs be significantly larger than the errors and variability of the simulation to make it stand out from the noise. On the other hand the linearity of the response is only valid for small deviations. While a complete analysis of the optimal step is outside the scope of this thesis, a good estimate can be made by looking at the choices made by other authors. For the angle of attack step [Cucinelii & Müller, 1988] is used as a reference. As shown in Figure 3.6 the step for the data in the report is 5°. As the results in this thesis will be compared to those in [Cucinelii & Müller, 1988], it is reasonable to choose the same step. The sideslip angle step of 2° is mentioned in [Mooij, 1995] as the maximum sideslip angle for which linearization is valid.

In order to investigate the sensitivity of the obtained stability picture there are two error sources that need to be taken into account. The first is that circumstances are different than expected. For example, the vehicle may be lower or slower than it should be according to the reference trajectory or the center of mass may be in a different location due to how the spacecraft is packed. If the stability situation changes significantly with these variations in circumstances there may be some hidden problems with the stability. The second error source is the accuracy of the simulation itself. It is possible that a simulated stability coefficients is significantly different from the reference value. As it is not clear how accurate the reference data in [Cucinelii & Müller, 1988] is, it cannot be assumed that that data is correct. To investigate the influence of these variations a Monte Carlo simulated with a randomized variation can shed light on the sensitivity of certain motions to errors in the data.

The stability analysis outcomes will be judged mostly on whether the motion is stable or unstable and what the corresponding half/doubling time is. In general, a stable motion will not present a problem though lower half times are better from a stability point of view than higher half times. If the motion is unstable the doubling time plays an important role. While automated controllers can take care of motions that diverge quickly, this is not the case for human pilots. According to [Hosman & Stassen, 1999], the response time of pilots for roll attitude and roll rate perception is just below 1 second. As a safe margin, any motion with a doubling time below 1 second will be critical, which means that the total stability is likely compromised without automated controller. Motions with doubling times on the order of a couple of seconds are judged as hazardous, because they require high concentration from a pilot. Motions with doubling times above 10 seconds are expected to be comfortably controllable by a human pilot.

Finally the equations for the dynamic stability analysis are based on the assumption there is longitudinal stability, meaning that the pitch coefficient must be zero. The control surface deflections at the required angle of attack of 10° were chosen to obtain this zero pitch moment using the graphs in [Cucinelii & Müller, 1988], but the trim situation should still be checked in the results.

4

Aerodynamics

4.1. Introduction

The stability and control of any flying vehicle is determined by the airflow around the vehicle. This raises the question of the quantitative and qualitative behaviour of the airflow in different flow regimes. The topic of aerodynamics is very expansive, so the first step should be to define the domain of interest. As the current study revolves around the airflow behaviour in the Terminal Area Energy Management (TAEM) phase, then this means that the literature about this phase will give a fair estimation of what to expect. The requirement that this chapter deals with is "The aerodynamic modules of the code should provide the skin friction drag, the pressure drag, the total forces in each direction of the reference frame and the total moments in each direction of the reference frame".

The reference for the flow regimes of interest is the Space Shuttle Orbiter. Data about the return landing of the SSO indicates that the TAEM phase starts at 25,000 m with a velocity of 760 m/s [Powers, 1986]. Using the US standard atmosphere [NASA, 1976], this corresponds to a Mach number of approximately 2.55 and a maximum Reynolds number of $7.7 \cdot 10^7$, meaning this is happening in the high supersonic range. For the SSO the TAEM phase ends at 3000 m [NASA, 2005] to 3700 m [Powers, 1986] with a velocity of 190 m/s [NASA, 2005]. This corresponds to a Mach number of about 0.58, squarely within the compressible region of subsonic flow. As the SSO slows down from the high supersonic velocities to the high subsonic velocities, this means it will also go through all the intermediate flow regimes. This means that the aerodynamically distinct phases that are of importance are compressible subsonic flow, transonic flow and supersonic flow.

The current chapter will treat the following topics. Section 4.2 discusses the aerodynamic environment in which the vehicle will be present. Section 4.3 treats the major assumptions used for the aerodynamic analysis. Section 4.4 deals with the governing equations and principles for aerodynamic analysis. Section 4.5 and 4.6 dive into more detail about the inviscid flow field and boundary layer, respectively. Section 4.7 discusses the differences in the methods proposed by [Hamilton *et al.*, 2009] and [Parhizkar & Karimian, 2009] for calculating boundary layer parameters. Finally, section 4.8 details a method to determine the location of stagnation lines.

4.2. Environment

To be able to apply the correct aerodynamic models, it is important to know what the aerodynamic environment will be and what effects can be expected in the flow. From the previously mentioned velocities and altitudes the boundaries of the encountered conditions can be determined. This will also allow the investigation of flow assumptions that could simplify the aerodynamics methods.

First the high altitude/high velocity assumptions will be checked. The atmospheric properties at the start of the TAEM for the Space Shuttle Orbiter can be found in table 4.1. The reason the Space

Parameter	Symbol	Value	Unit
Density	ρ	0.040	kg/m^3
Static temperature	T	217	K
Static pressure	p	2.48	kPa
Speed of sound	a	295	m/s
Mach number	M	2.57	-
Dynamic pressure	q	11	kPa
Total pressure	p_{tot}	47	kPa
Total temperature	T_{tot}	503	K

Table 4.1: Conditions at h = 25,000 m and V = 760 m/s [Glenn Research Center, 2013]

Shuttle Orbiter data was used was that real-life data of the re-entry profile was available, which is not available for HORUS.

One of the most common assumptions is for the gas to be perfect. This means that the gas particles only interact elastically when they collide, and there are not other interactions. [White, 2005] gives a graphical method to check this assumption. It plots the compressibility factor as a function of the reduced pressure and temperature. The perfect gas assumption is only true for $Z = 1$, i.e., when the perfect gas law $p = \rho RT$ holds. However, small deviations from 1 can be accepted as they will not have a major impact on the results.

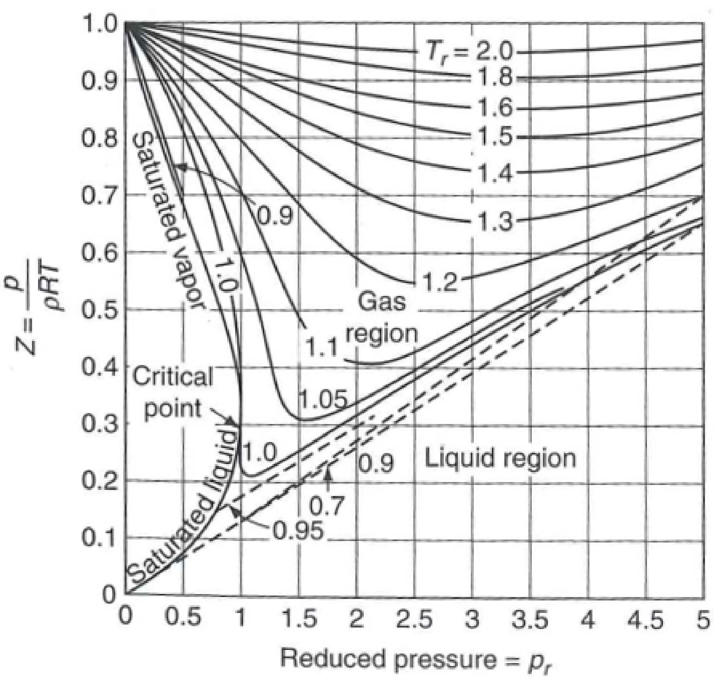

Figure 4.1: Compressibility factors for gases, [White, 2005].

For this method two new variables are defined:

- $T_r = \frac{T}{T_c}$ is the scaling temperature with T_c being the critical temperature
- $p_r = \frac{p}{p_c}$ is the scaling pressure with p_c being the critical pressure.

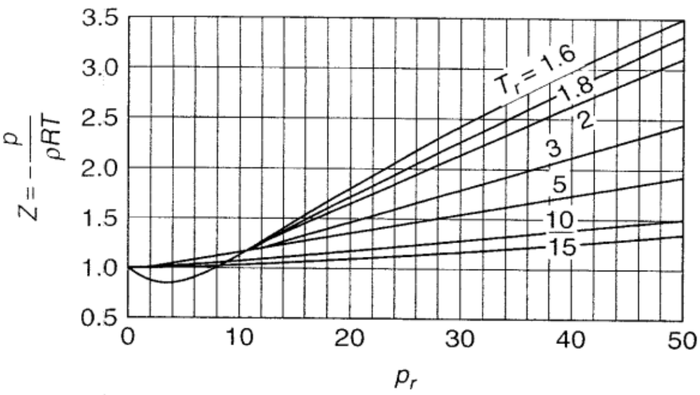

Figure 4.2: Compressibility factors for gases for higher scaling temperatures, [White, 2005].

Assuming the air composition at 25 kilometers altitude (stratosphere) is similar to the one at sea level [UCAR, 2003], the values for air are those in Table 4.2.

Parameter	Symbol	Value	Unit
Critical temperature	T_c	132.2	K
Critical pressure	p_c	$3.688 \cdot 10^6$	Pa

Table 4.2: Critical-point constants for air [White, 2005]

Checking Figure 4.1, it is clear that the combination of low T_r and increasing p_r present the biggest challenge. The lowest temperature encountered in the troposphere and stratosphere is approximately 210 K (figure 4.3), which gives $T_r = \frac{210}{132.2} \approx 1.59$. For $T_r \approx 1.6$ and deviations smaller than 5% percent from a perfect gas, the reduced pressure needs to be $p_r \leq 0.5$. The highest pressure occurs in the unrealistic scenario of the spaceplane still flying Mach 2.5 at sea level. In this case the highest expected total pressure $p_t = 1.73 \cdot 10^6 Pa$ (obtained from [Glenn Research Center, 2013] and [NASA, 2014], two online calculation tools) going through a normal shockwave. This value would result in $p_r = \frac{1.73 \cdot 10^6}{3.688 \cdot 10^6} \approx 0.47$, satisfying the requirement of $p_r \leq 0.5$ for $T_r = 1.6$. A final requirement is that $T_r \leq 15$ for the perfect gas law to be accurate, see Figure 4.2. Using the extreme of going Mach 2.5 at sea level again, this would result in a total temperature of 648 K ([Glenn Research Center, 2013]). Using this value $T_r = \frac{648}{132.2} \approx 4.9$, thus the maximum reduced temperature requirement is also met. It can be concluded that the perfect gas assumption is valid for the complete TAEM.

Another assumption is the use of an inviscid flow field. There are some caveats to this assumptions. First of all, it is not true close to the body where there is significant viscosity. This behaviour is captured by the viscous boundary layer. In the case of a separated boundary layer this assumption will not hold true either, because the boundary layer enters the domain of the inviscid flow.

4.2.1. WIND

One of the assumptions that is made in this report is that the influence of wind can be neglected. This can be checked by comparing the maximum average wind velocity at a certain altitude to the velocity at that altitude [Struzak, 2003]. It turns out that for all flight Mach numbers the maximum wind fraction of the total velocity is below 10%, barring extreme weather events.

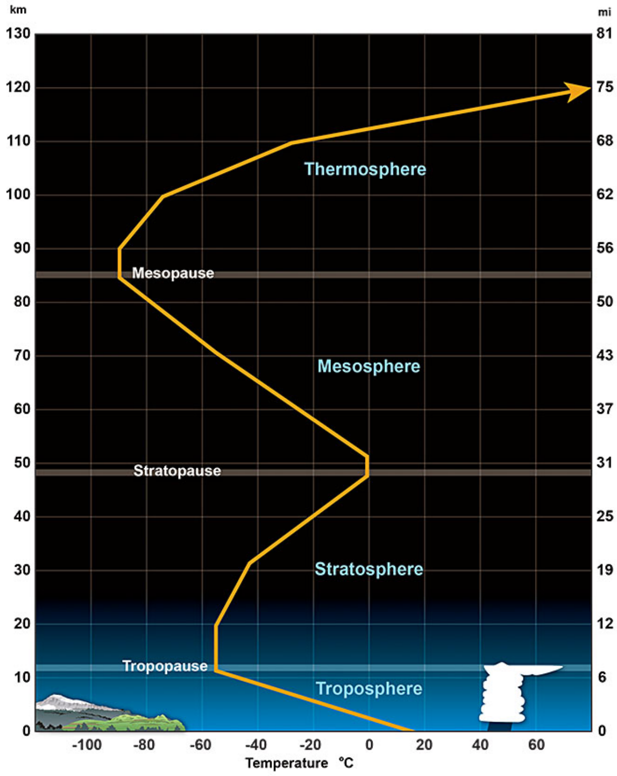

Figure 4.3: Temperature profile of the atmosphere, from [NOAA, 2013]

4.3. ASSUMPTIONS AND VALIDITY

The aerodynamics described in this chapter rely on a number of assumptions. While these generally will be mentioned when appropriate, the most important assumptions are summarized here for convenience.

No chemical reactions in the flow

The flow will not be chemically reactive. For the TAEM this is a fair assumption as the maximum Mach number will be between M=2.5 and M=3. This assumptions needs to be made to not invalidate the ideal gas law. In principle the methods can deal with a chemically reacting gas, but not in the current version of the code.

Flow is a continuum

The flow needs to be a continuum, molecular flow cannot be modeled in the current version. Assuming a continuum flow makes sure the ideal gas law is not invalidated. At the altitudes relevant for the TAEM (up to 30 km) the assumption of continuum flow can safely be made.

Ideal gas

While the above two assumption form part of the conditions for an ideal gas, there is also a requirement for the temperature not to be very low and the pressure not to be very high. The ideal gas assumption allows the use of the ideal gas law, which is used to relate the pressure, density and temperature.

Wall temperature

The current model suppose a fixed wall temperature at each location on the model. The default setting is a single wall temperature for the whole model, but options are included for the wall temperature to be equal to the adiabatic wall temperature (no heat flow) or to the temperature at the edge of the boundary layer (equilibrium temperature). This means effects of heating up of cooling off of the wall are not incorporated.

Attached boundary layer

The simulation can not deal with separated boundary layers. Usually when this happens a vortex will be created behind the separated boundary layer, making the influence of boundary layer separation even larger.

Thin boundary layer

The whole inviscid flow field with viscous boundary layer model rests on the assumption that the boundary layer has no significant thickness compared to the dimensions of the model and the flow field. This assumption is the reason why the inviscid values for the aerodynamic state variables (pressure, density etc.) on the surface can be taken as those at the edge of the boundary layer. A thick boundary layer also affects the invsicid flow field to such a degree that the apparent shape of the model changes.

No entropy swallowing

In flows with shocks a layer with a strong entropy layer gradient will form, known as the entropy layer. When this entropy layer interacts with the boundary layer, heating can be much higher than expected in a turbulent boundary layer [Kinney, 2011]. This will also influence the boundary layer thickness and thus the skin friction. These effects will not be taken into account in this research, as the modeling is far too complex for an engineering design code such as this.

4.4. GOVERNING EQUATIONS AND PRINCIPLES

The field of aerodynamics is ruled by three conservation equations: conservation of mass, conservation of momentum and conservation of energy. Even though there are only three equations (if the vector form is taken), there is no analytical solution to all of these equations making a numerical solution necessary for the most general cases. However, for higher Reynolds numbers the calculation time needed far exceeds present computing capabilities. To combat this problem, simplifications of these equations are a necessity.

The conservation of mass equation, more commonly known as the *continuity equation*, is expressed in Equation (4.1).

$$\frac{D\rho}{Dt} + \rho\nabla\cdot\mathbf{V} = 0 \tag{4.1}$$

The first term is the material (or particle) derivative of the density, with is the time rate change of the density in Euler form. In the second term the divergence of the velocity ($\nabla\cdot\mathbf{V}$) is a measure of the normal-strain rate of the volume, which is multiplied by the density. In essence, this equation indicates that the net result of all changes of mass flow must be zero, i.e., conservation.

The momentum conservation will be described using the Navier-Stokes equations, after which in subsequent sections the Euler equation will be derived from it. Historically the order was reversed, Leonhard Euler published his equations in 1757 while the Navier-Stokes equations expanded on them for a general description of the flow. This order is chosen to show the relation between these equations. The Navier-Stokes equations in vector form are given in Equation (4.2).

$$\rho\frac{D\mathbf{V}}{Dt} = \rho\mathbf{g} - \nabla p + \frac{\partial}{\partial x_j}\left[\mu\left(\frac{\partial v_i}{\partial x_j} + \frac{\partial v_j}{\partial x_i}\right) + \delta_{ij}\lambda\nabla\cdot\mathbf{V}\right] \tag{4.2}$$

Is essence the equation is a statement of Newton's second law, $F = m \cdot a$. The term on the left-hand side of the equation indicates the change in momentum. The first term on the right-hand side of the equation is the momentum change due to gravity. The second term indicates the contribution of a pressure gradient across the volume to the momentum change. The term between brackets describes the momentum change due to deformation of the fluid. The symbol δ_{ij} is the Kronecker function, attaining a value of 1 when $i = j$ and a value of 0 when $i \neq j$.

The equation for energy conservation is derived from the first law of thermodynamics, stating that the change of energy is the sum of the work and heat added to(or subtracted from) the system. The form shown in Equation (4.3) is from [White, 2005]

$$\rho\frac{Dh}{Dt} = \frac{Dp}{Dt} + \nabla\cdot(k\nabla T) + \Phi \tag{4.3}$$

The term on the left-hand side of the equation indicates the energy change in the system, expressed as the change in enthalpy. The first term on the right side is the contribution of pressure changes to the energy change of the system. The second term expresses the heat flow into or out of the system. The last term indicates the dissipation of energy due to viscous stresses. As dissipation cannot add energy to the system, it will always be positive in this equation. For a Newtonian fluid, the dissipation function is given by:

$$\Phi = \mu\left[2\left(\frac{\partial u}{\partial x}\right)^2 + 2\left(\frac{\partial v}{\partial y}\right)^2 + 2\left(\frac{\partial w}{\partial z}\right)^2 + \left(\frac{\partial v}{\partial x} + \frac{\partial u}{\partial y}\right)^2 + \left(\frac{\partial w}{\partial y} + \frac{\partial v}{\partial z}\right)^2 + \left(\frac{\partial u}{\partial z} + \frac{\partial w}{\partial x}\right)^2\right] + \lambda\left(\frac{\partial u}{\partial x} + \frac{\partial v}{\partial y} + \frac{\partial w}{\partial z}\right)^2 \tag{4.4}$$

As stated before, these equations are impossible to solve analytically in general and hard to solve numerically. In order to tackle the aerodynamics more effectively, Ludwig Prandtl proposed the boundary layer model at the start of the twentieth century. The model utilizes the fact that the majority of the viscous effects take place in a relatively small layer around the body, while for the rest of the flowfield the viscous effects can mostly be neglected. The assumptions hold only true when the boundary layer is small compared to the body and the rest of the flow or when the boundary layer is coupled to the inviscid flowfield. The reason is that a boundary layer acts as an extension of the body because it displaces the outer flow. In a coupled system this shape change is fed back into the inviscid flow field simulation and used for a new round of calculations. This also allows for the effects of boundary layer heating to be communicated to the inviscid solver. However, this coupling increases the computing effort significantly because of the required iterations. For thin boundary layers where the heating of the inviscid flow field is not important, the coupling and iterations can be left out.

4.5. INVISCID FLOW FIELD - EULER EQUATIONS

The term Euler equations often has different meanings. In essence it is the inviscid form of the Navier-Stokes equations. However, often the full set of continuity, momentum and energy equations for an inviscid flowfield is meant by the term Euler equations. This last definition will also be used throughout this study.

The continuity equation has no viscous terms and thus stays as it is. The momentum equation has one major viscous term, the one between brackets in Equation (4.2). Finally, the energy equation also has one viscous term, which is the very last one. Neglecting the viscous terms, the following system of equations for inviscid flows is obtained:

$$\frac{D\rho}{Dt} + \rho\nabla\cdot\mathbf{V} = 0 \tag{4.5}$$

$$\rho\frac{D\mathbf{V}}{Dt} = \rho\mathbf{g} - \nabla p \tag{4.6}$$

$$\rho\frac{Dh}{Dt} = \frac{Dp}{Dt} + \nabla\cdot(k\nabla T) \tag{4.7}$$

4.5.1. SUBSONIC FLOW

Generally the subsonic flow regime itself is divided into two separate areas, incompressible and compressible flow. While incompressible flow is much easier to work with due to the elimination of the density derivatives (because of constant density), it is only applicable up to a Mach number of 0.3. Above Mach 0.3 the flow is generally considered compressible, which means the fluid density changes throughout the flow.

The major difference between subsonic flow on the one hand and transonic and supersonic flow on the other hand is the absence of discontinuities in the form of shocks. Because the flow velocity is lower than the speed of sound, disturbances propagate in all directions. In the case of incompressible flow this would happen at the same velocity is all directions (from a Lagrangian point of view), while for compressible flow the velocities would be different.

If viscosity terms are neglected (as is the case for the Euler equations), the flow is isentropic, or in other words adiabatic and reversible. The first term means that no heat is added to the process. In a flow without external heating elements the only source of heat to the process is friction. Because viscosity is neglected there is no friction, which means there is no heat added to the system and the flow is adiabatic.

A reversible process is a process in which the entropy does not increase, which means that in an enclosed system with adiabatic walls the direction of the process can be reversed after any change of state. As the flow is subsonic there are no non-isentropic shockwaves and because there is no entropy added trough friction, the flow is also reversible.

Having shown that the subsonic flow without viscosity is isentropic, the isentropic flow equations can be used to relate different quantities throughout the flow.

$$\frac{p}{p_t} = \left(1 + \frac{\gamma-1}{2}M^2\right)^{\frac{-\gamma}{\gamma-1}} \tag{4.8}$$

$$\frac{T}{T_t} = \left(1 + \frac{\gamma-1}{2}M^2\right)^{-1} \tag{4.9}$$

Equations (4.8) and (4.9) relate the ratio of static pressure to total pressure to the Mach number and the ratio of specific heats. As the total temperature and pressure are constant throughout an isentropic flow, the static pressure and temperature can be calculated easily. The total pressure and temperature can be determined using Equations (4.10) and (4.11) respectively.

$$p_t = p + \frac{1}{2}\rho V^2 \tag{4.10}$$

$$\frac{T_t}{T} = 1 + \frac{\gamma - 1}{2} M^2 \tag{4.11}$$

Finally the actual subsonic flow field around a model will be shown, specifically the shell (similarity to an artillery shell) model shown in Figure 4.4. Figures 4.5 and 4.6 show the Mach number and pressure coefficient around the model at a Mach number of 0.6 and an angle of attack of 0°. The images contain only dimensionless coefficients in an inviscid flow field, meaning that the Mach number is the only relevant setting. As expected there are no visible shocks in either of the figures. This makes sense as the maximum indicated Mach number is 0.7, well below Mach 1. Figure 4.6 shows that changes in the slope of the model have an impact both upstream and downstream. For example, at the widest point of the model (where the favorable pressure gradient $\frac{dp}{dx} < 0$ changes to an adverse pressure gradient $\frac{dp}{dx} > 0$) the green low-pressure area extends both upstream and downstream. The reason for this is that information travels through the air at the speed of sound, and for a subsonic flow in equilibrium this means that information about the upcoming adverse pressure gradient can travel both upstream and downstream.

At both places where the favorable pressure gradient changes to an adverse pressure gradient (at the widest point of the model and a little behind the model), the local Mach number is higher than the free-stream Mach number. This means that if the free-stream Mach number becomes higher, these will be the first places to go supersonic.

The wake behind the model also contains vortices, as indicated by the bottom streamline in Figure 4.6. The flow turns inward directly behind the model, creating a high pressure area in the middle and a low pressure area a little further behind, indicates by the blue area. This area is where the wake drag emerges from, as the low pressure area in a way sucks the model backwards. Interestingly, when comparing both figures it emerges that the pressure coefficient goes back to the free-stream value much faster than the Mach number after the flow leaves the model.

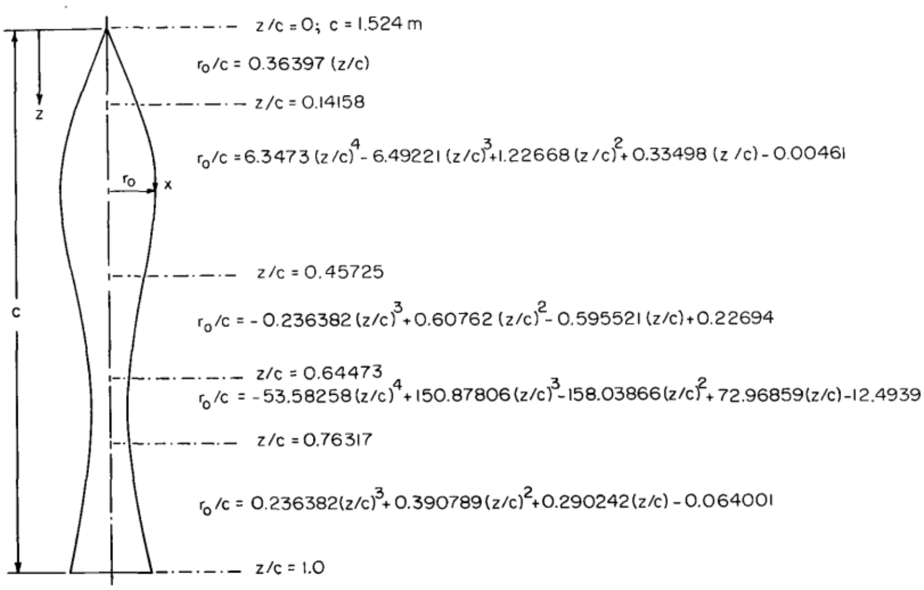

Figure 4.4: Model used for the simulation [Harris, 1971].

4.5.2. TRANSONIC FLOW

The transonic regime is the transition between subsonic and supersonic flow. It is characterized by parts of the flow that are subsonic and other parts that are supersonic. This means that the shock

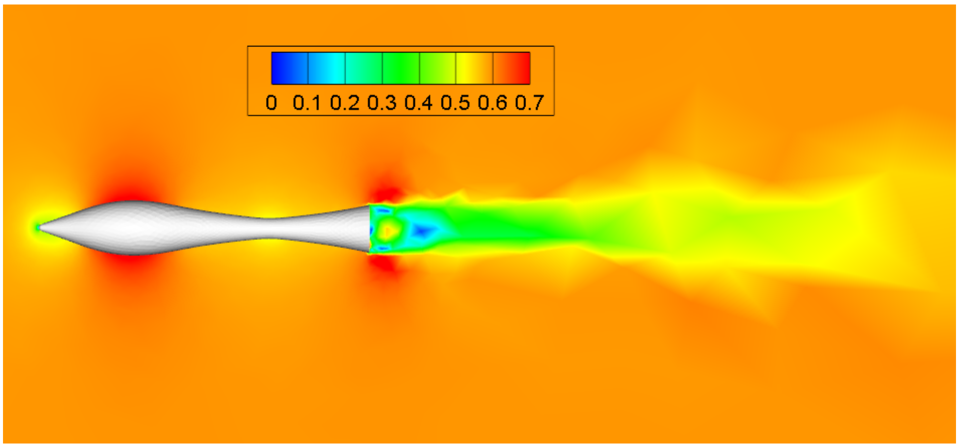

Figure 4.5: Euler solution (Mach number) of the shell model at a free-stream Mach number of 0.597

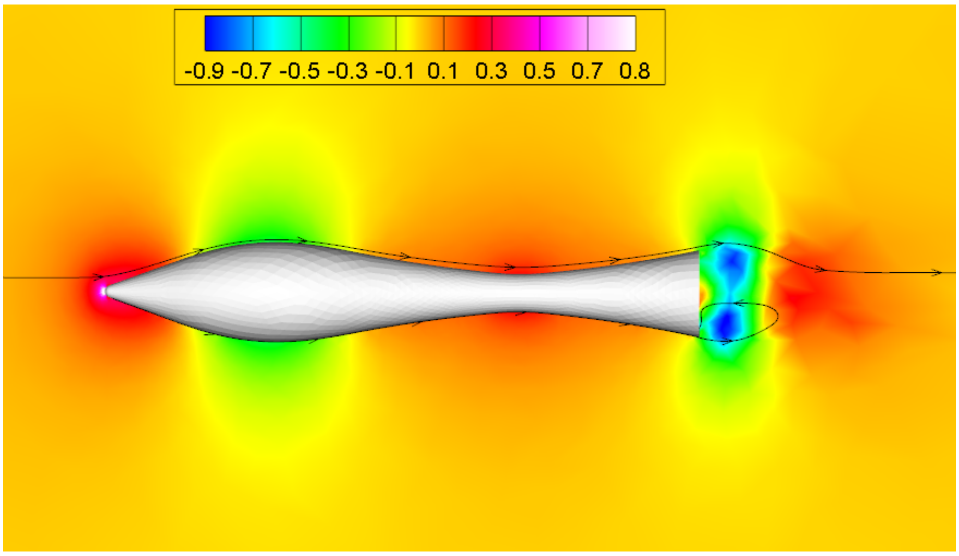

Figure 4.6: Euler solution (pressure coefficient) of the shell model at a free stream Mach number of 0.597

associated with the supersonic flow will occur somewhere on the body.

The occurrence of a shockwave on the vehicle leads to shock-boundary layer interaction. This leads to boundary layer behaviour that is difficult to simulate without dedicated methods. Due to the compression waves the pressure will increase and the skin friction will see a peak downwards [Gadd, 1962]. The flow field around a strong shock at Mach 5 is shown in Figure 4.7. The figure shows that within the boundary layer there can be large variations in Mach number when there is a shock-boundary layer interaction. This breaks down the assumptions about the velocity profile in the boundary layer that are used for the momentum thickness calculations (see also Section 4.6). Modeling these interactions is very complex and outside the scope of this thesis, therefore they will not be taken into account.

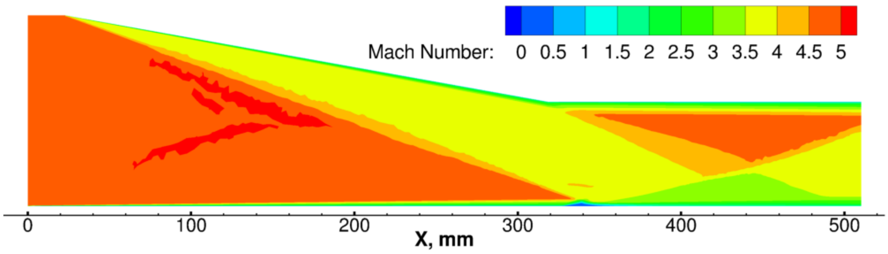

Figure 4.7: Flow field of a shock-boundary layer interaction at Mach 5. [Slater, 2015].

The inviscid flow field for Mach number and pressure coefficient distribution for the transonic regime are shown in Figures 4.8 and 4.9. For both these figures a Mach number of 1 and an angle of attack of 0° were used. Figure 4.8 shows there are significant supersonic and subsonic portions of the flow. At the tip there is a clear stagnation point, but a clear shock in front of the model does not appear. This is because the velocity component normal to an oblique shock will always be subsonic. This follows from the fact that the total Mach vector is equal to 1, so any component will be lower than 1. After the stagnation point the flow accelerates and goes supersonic slightly ahead of the point where the favorable pressure gradient changes to an adverse pressure gradient (where yellow changes to orange). Notice that the adverse pressure gradient starts behind the widest point due to the supersonic nature of that portion of the flow. Due to the adverse gradient the supersonic flow decelerates and at the point where it goes subsonic the first shock is found. The shock is nicely visible due to the sudden change (in color) for both the mach number and pressure. Only at the back of the model does the flow become supersonic again, but no clear shocks are visible. As for the streamlines, the same type of vortices occur in the wake of the vehicle, again creating a higher pressure region in the center at the back of the vehicle.

The figure also show why the transonic regime presents problems for the stability of the vehicle. Depending on the exact Mach number the location of the shock (where the pressure rapidly changes) moves. This means that the moments on the vehicle can also rapidly change in this regime. If the shock in on or close to a control surface this also influences the controllability of the vehicle.

The flow behavior for transonic flow (Figure 4.8) differs clearly from the subsonic case due to the shocks and expansion fans on the surface. The flow behaviour at the tip is similar to the subsonic case as there is no bow shock. Because of the negative pressure coefficient the flow accelerates to a supersonic Mach number through an expansion fan (weak shock) at the first curvature. When the pressure gradient becomes positive again, a compression shock occurs, clearly visible in both figures as the Mach number and pressure change rapidly. At the end of the model the flow accelerates to supersonic conditions again, after which it decelerates quickly to nearly atmospheric pressure and Mach number through a weaker shock. The low pressure area in the direct wake of the model that was seen in the subsonic case is again visible with the vortices showing up again too.

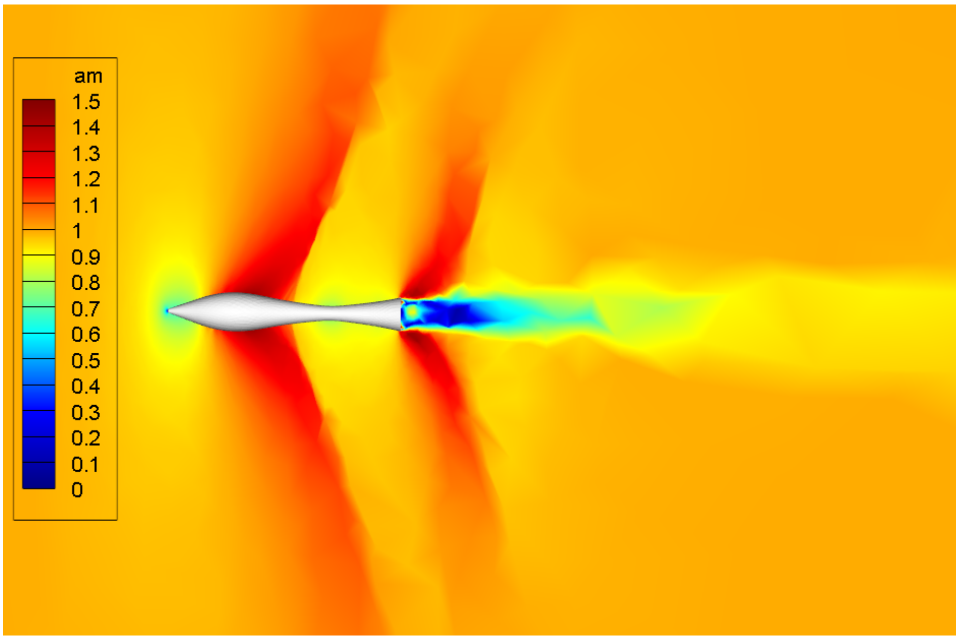

Figure 4.8: Euler solution (Mach number) of the shell model at a free-stream Mach number of 1

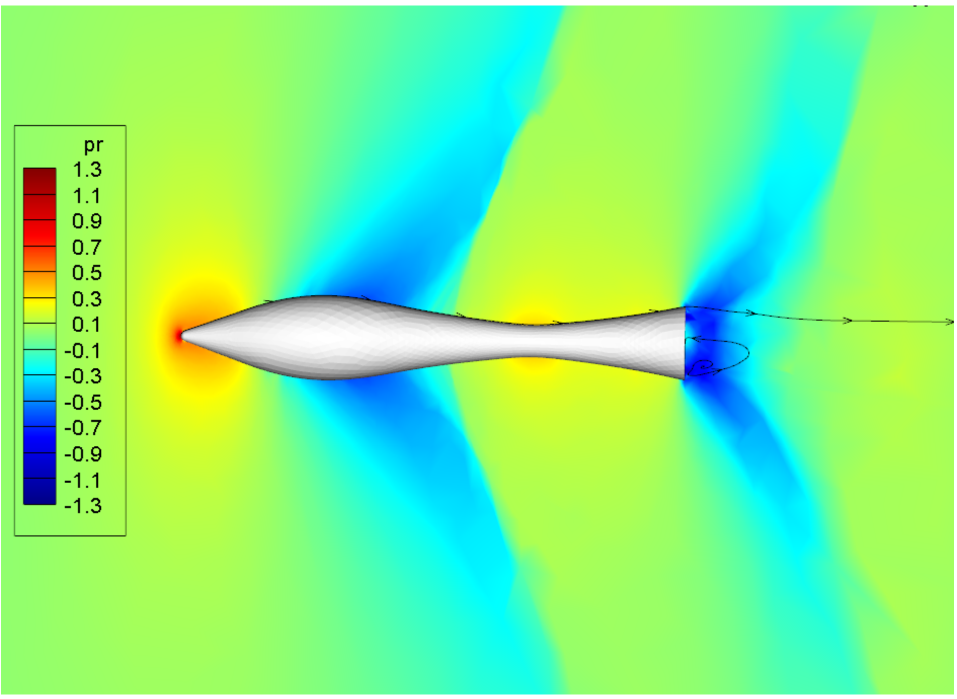

Figure 4.9: Euler solution (pressure coefficient) of the shell model at a free-stream Mach number of 1

4.5.3. SUPERSONIC FLOW

The final case is fully developed supersonic flow. When the flow is supersonic, the information about the body cannot travel upstream as the information only travels with the speed of sound. Instead, a discontinuous shock wave forms in front of the body. This will be the first point where the flow is influenced by the body.

In this case a detached shockwave will have formed at the nose of the vehicle, as well as possibly along the leading edges of other surfaces. These shockwaves increase the difficulty of finding proper solutions using the Euler equations, as they represent near discontinuities for the density, pressure and temperature of the flow. While for bodies with very sharp noses the shock may approximate an attached oblique shock, for most realistic bodies a detached bow shock will form. A normal shock will occur in front of the nose and the leading edges and this is the shock that the streamline to the stagnation point goes through. Around the rest of the vehicle a curved oblique shockwave will occur. Because of these shocks, the flow between the shock and the body will have different properties compared to the freestream flow. The most important for the current study is the streamline that goes through the normal part of the shockwave, as this is the stagnation streamline. For this part of the shock the normal shock wave relations can be used to determine the properties of the flow right behind the shock. The properties behind the normal shock are only influenced by the type of gas in the flow through the ratio of specific heats and by the Mach number. The equations are shown in Equations (4.12) through (4.15).

$$M_2^2 = \frac{(\gamma-1)M_1^2+2}{2\gamma M_1^2-(\gamma-1)} \tag{4.12}$$

$$\frac{\rho_2}{\rho_1} = \frac{(\gamma+1)M_1^2}{2+(\gamma-1)M_1^2} \tag{4.13}$$

$$\frac{p_2}{p_1} = \frac{2\gamma M_1^2-(\gamma-1)}{\gamma+1} \tag{4.14}$$

$$\frac{T_2}{T_1} = \frac{h_1}{h_2} = \frac{\left[2\gamma M_1^2-(\gamma-1)\right]\left[(\gamma-1)M_1^2+2\right]}{(\gamma+1)^2 M_1^2} \tag{4.15}$$

While the rest of the shock is curved, at any point the shock can be treated as a regular oblique shock wave by using the appropriate angle between the flow direction and the shock.

The flow behaviour for fully supersonic flow (Figure 4.10) is again quite different from the transonic flow. A detached bow shock has formed, leading to a high-pressure stagnation point (Figure 4.11) on the tip behind the normal shock. This strong shock extends to approximately two model diameters and beyond that the shock is weak or even non-existent. Along the model the flow is completely supersonic, except for the region immediately next to the stagnation point. This means no further shocks occur along the. The only other interesting feature is the wake. While the flow is subsonic directly behind the model with supersonic flow around it, there is no shock present. This is confirmed by the lack of a (near) discontinuity in the pressure in Figure 4.11. Compared to the transonic case there will be less uncertainty about the stability because there are shocks on the model itself.

The flow behind the shock wave is a subsonic flow with the boundary conditions imposed by the shock wave(s). This means that air properties can be calculated using the isentropic equations (Equation (4.8) and Equation (4.9)).

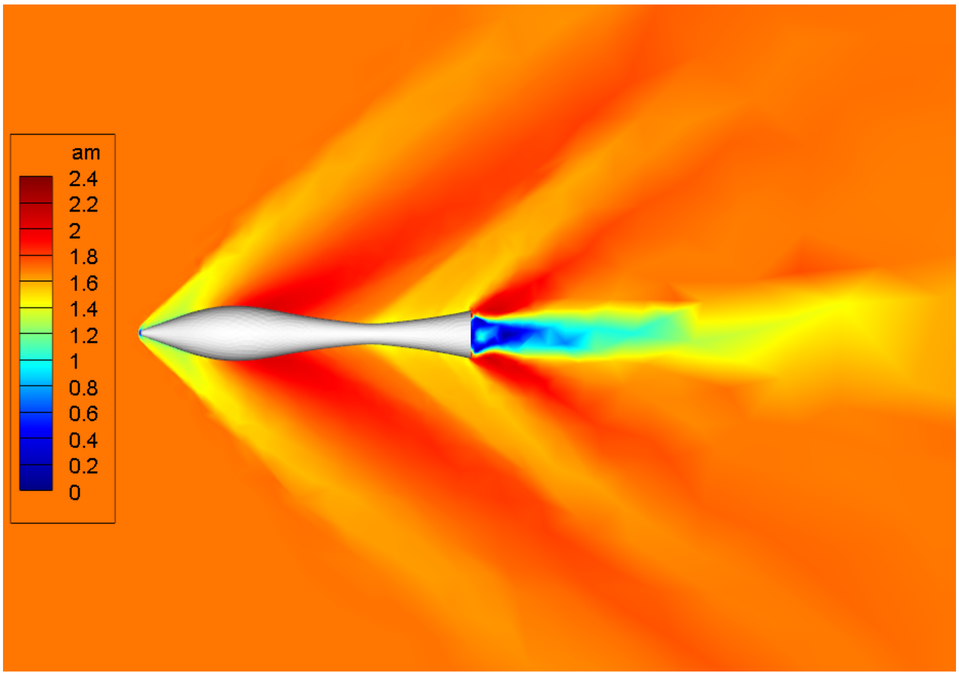

Figure 4.10: Euler solution (Mach number) of the shell model at a free-stream Mach number of 1.7

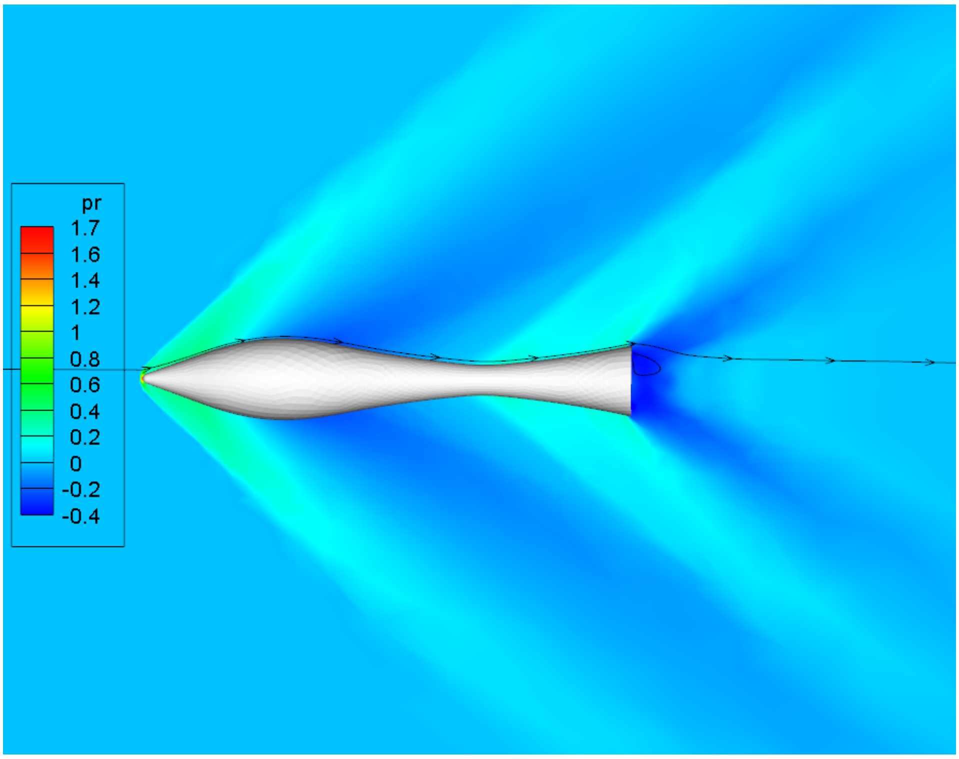

Figure 4.11: Euler solution (pressure coefficient) of the shell model at a free-stream Mach number of 1.7

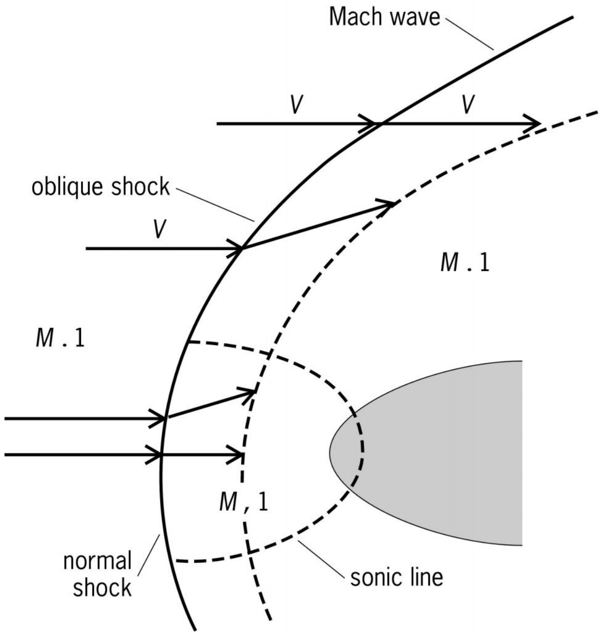

Figure 4.12: Diagram showing a detached bow shock. Indicated are the shock in front of the body acting as a normal shock and the curved oblique shock [McGraw-Hill Concise Encyclopedia of Physics, 2002].

4.6. VISCOUS FLOW FIELD - BOUNDARY LAYER

The viscous boundary layer determines the friction and heating on the vehicle itself. In the boundary layer cumulative parameters are of great importance, such as the momentum thickness. If a certain variable is cumulative, it means that it depends on the previous evolution of the parameter, i.e. it needs to be integrated with time or length. In order to facilitate this behaviour it is convenient to utilize streamlines.

Several parameters can be used to describe the boundary layer and its development, such as the shear-layer thickness, displacement thickness and momentum thickness. The shear-layer thickness indicates the region around the body in which the velocity is influenced by skin friction. It is generally defined as the height above the surface at which the velocity reaches 99% of the velocity of the inviscid flow field.

The displacement thickness indicates the distance the inviscid flow is displaced because of the presence of the boundary layer. To satisfy conservation of mass (same mass flow), the control volume needs to be larger to compensate for the lower velocities in the boundary layer. A representation of the shear-layer thickness and displacement thickness can be found in Figure 4.13. Using the assumption of constant density (incompressible flow) and defining the displacement thickness as the difference between the initial and final height of the control volume, $\delta^* = Y - H$, the formal definition of the incompressible displacement thickness is:

$$\delta^* = \int_0^{Y\to\infty} \left(1 - \frac{u}{V}\right) dy \tag{4.16}$$

Note that this equation requires the integration of the velocity profile in the boundary layer over the boundary layer thickness. This presents a problem as the velocity profile is not known a priori. This can be solved using guessed profiles, which will be touched upon later.

The third parameter is the momentum thickness and plays a large role in determining the heating rate and skin friction. The momentum thickness is a measure of the momentum loss through

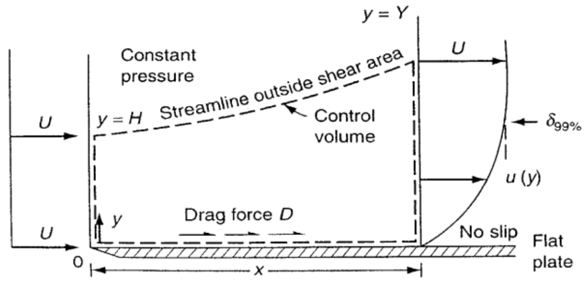

Figure 4.13: Definition of the shear-force thickness and displacement thickness over a flat plate [White, 2005].

friction in the boundary layer compared to the momentum outside the boundary layer. Again using the assumption of incompressible flow, the momentum thickness is given as:

$$\theta = \frac{D}{\rho U^2} = \int_0^{Y\to\infty} \frac{u}{U}\left(1 - \frac{u}{V}\right) dy \tag{4.17}$$

4.6.1. SIMPLIFYING THE BOUNDARY LAYER - THE AXIALLY SYMMETRICAL ANALOGY

To simplify the boundary layer computations the axial symmetrical analogy can be used. The goal of the axisymmetric analogue is to transform the body in a set of equivalent axially symmetrical bodies.

The first step is to change to the streamline coordinate system. This system is expressed in the coordinates ξ, η and ζ, where ξ is the coordinate along the streamline, η is the cross-stream coordinate (parallel to surface) and ζ is the outward normal from the surface. In this coordinate system, a line element is described by:

$$ds^2 = h_1^2 d\xi^2 + h_2^2 d\eta^2 + d\zeta \tag{4.18}$$

h_1 and h_2 are stretching factors, needed because the new coordinate system deals with curved surface. h_3 is not needed because it is normal to the streamline and thus not curved. Using the new coordinate system, the Navier-Stokes equations (Equation (4.2)), the continuity equation (Equation (4.1)) and energy equation (Equation (4.3)) can be rewritten.

It should be noted that the transformation to the Navier-Stokes equations in the streamline coordinate system starts from a slightly different form of the Navier-Stokes equation, which is equivalent but not equal to Equation (4.2). This can be found in Cooke [1961]. With the new coordinates the following equations are obtained:

$$\rho\left\{\frac{u}{h_1}\frac{\partial u}{\partial \xi} + \frac{v}{h_2}\frac{\partial u}{\partial \eta} + w\frac{\partial u}{\partial \zeta} + \frac{uv}{h_1 h_2}\frac{\partial h_1}{\partial \eta} - \frac{v^2}{h_1 h_2}\frac{\partial h_2}{\partial \xi}\right\} = -\frac{1}{h_1}\frac{\partial p}{\partial \xi} + \frac{\partial}{\partial \zeta}\left(\mu\frac{\partial u}{\partial \zeta}\right) \tag{4.19}$$

$$\rho\left\{\frac{u}{h_1}\frac{\partial v}{\partial \xi} + \frac{v}{h_2}\frac{\partial v}{\partial \eta} + w\frac{\partial v}{\partial \zeta} + \frac{uv}{h_1 h_2}\frac{\partial h_2}{\partial \xi} - \frac{u^2}{h_1 h_2}\frac{\partial h_1}{\partial \eta}\right\} = -\frac{1}{h_2}\frac{\partial p}{\partial \eta} + \frac{\partial}{\partial \zeta}\left(\mu\frac{\partial v}{\partial \zeta}\right) \tag{4.20}$$

$$0 = \frac{\partial p}{\partial \zeta} \tag{4.21}$$

$$\rho c_p\left\{\frac{u}{h_1}\frac{\partial T}{\partial \xi} + \frac{v}{h_2}\frac{\partial T}{\partial \eta} + w\frac{\partial T}{\partial \zeta}\right\} = \Phi + \frac{u}{h_1}\frac{\partial p}{\partial \xi} + \frac{v}{h_2}\frac{\partial p}{\partial \eta} + w\frac{\partial p}{\partial \zeta} + \frac{\partial}{\partial \zeta}\left(k\frac{\partial T}{\partial \zeta}\right) \tag{4.22}$$

$$\frac{1}{h_1 h_2}\left\{\frac{\partial}{\partial \xi}(\rho h_2 u) + \frac{\partial}{\partial \eta}(\rho h_1 v) + \frac{\partial}{\partial \zeta}(\rho h_1 h_2 w)\right\} = 0 \tag{4.23}$$

The first two equations are the momentum equations for the coordinates along the surface using the assumption of steady flow and neglecting gravity. The third equation is the boundary layer assumption that the pressure does not vary throughout the thickness of the boundary layer. The fourth equation is the energy equation and the fifth equation is the continuity equation.

The streamlines on the surface are now considered. This means that $\frac{\partial}{\partial \zeta} = 0$, $u = u_1$ and $v = v_1 = 0$, leading to the simplified versions of equations 4.19 and 4.20.

$$-\frac{1}{h_1}\frac{\partial p}{\partial \xi} = \frac{\rho_1 u_1}{h_1}\frac{\partial u_1}{\partial \xi} \qquad -\frac{1}{h_2}\frac{\partial p}{\partial \eta} = \frac{\rho_1 u_1^2}{h_1 h_2}\frac{\partial h_1}{\partial \eta} \tag{4.24}$$

Now rewriting for the element of length along a streamline:

$$\frac{1}{h_1}\frac{\partial}{\partial \xi} = \frac{\partial}{\partial s} \tag{4.25}$$

h_2 is renamed to r and can be calculated using Equation 4.30. Assuming v and its derivatives are small, the along-stream momentum, energy and continuity equation become:

$$\rho\left(u\frac{\partial u}{\partial s} + w\frac{\partial u}{\partial \zeta}\right) = \rho_1 u_1 \frac{\partial u_1}{\partial s} + \frac{\partial}{\partial \zeta}\left(\mu\frac{\partial u}{\partial \zeta}\right) \tag{4.26}$$

$$\rho c_p\left(u\frac{\partial T}{\partial s} + w\frac{\partial T}{\partial \zeta}\right) + \rho_1 u u_1 \frac{\partial u_1}{\partial s} = \frac{\partial}{\partial \zeta}\left(k\frac{\partial T}{\partial \zeta}\right) + \mu\left(\frac{\partial u}{\partial \zeta}\right)^2 \tag{4.27}$$

$$\frac{1}{r}\frac{\partial}{\partial s}(\rho r u) + \frac{\partial}{\partial \zeta}(\rho w) = 0 \tag{4.28}$$

The above equations are the equations of motion in the boundary layer over an axisymmetric body, taken along a given external streamline.

After u and w are found from the previous equations, v can be found from eq [4.13] as it has become linear:

$$\rho\left(u\frac{\partial v}{\partial s} + w\frac{\partial v}{\partial \zeta} + \frac{uv}{r}\frac{\partial r}{\partial s} + \kappa u^2\right) = \rho_1 \kappa u_1^2 + \frac{\partial}{\partial \zeta}\left(\mu\frac{\partial v}{\partial \zeta}\right) \tag{4.29}$$

where $\kappa = \frac{1}{h_1 r}\frac{\partial h_1}{\partial \eta}$

There is still the curvature r to be determined. This can be done using the following equation:

$$u_1\frac{\partial}{\partial s}\left(\log\frac{u_1^2 r^2}{g}\right) = 2\left(\frac{\delta \bar{U}}{\delta x} + \frac{\delta \bar{V}}{\delta y}\right) \tag{4.30}$$

with

$$u_1\frac{\partial}{\partial s} = \bar{U}\frac{\delta}{\delta x} + \bar{V}\frac{\delta}{\delta y} \tag{4.31}$$

$$\frac{\delta}{\delta x} = \frac{\partial}{\partial x} + \frac{\partial z}{\partial x}\frac{\partial}{\partial z} \tag{4.32}$$

$$\frac{\delta}{\delta y} = \frac{\partial}{\partial y} + \frac{\partial z}{\partial y}\frac{\partial}{\partial z} \tag{4.33}$$

$$g = 1 + \left(\frac{\partial z}{\partial x}\right)^2 + \left(\frac{\partial z}{\partial y}\right)^2 \tag{4.34}$$

with the equation of the surface being $z = z(x, y)$. In Cartesian coordinates Equation 4.30 then becomes:

$$\bar{U}\frac{\partial}{\partial x}\left(\log\frac{u_1^2 r^2}{1+z_x^2+z_y^2}\right) + z_x\frac{\partial}{\partial z}\left(\log\frac{u_1^2 r^2}{1+z_x^2+z_y^2}\right) + \bar{V}\frac{\partial}{\partial y}\left(\log\frac{u_1^2 r^2}{1+z_x^2+z_y^2}\right) + z_y\frac{\partial}{\partial z}\left(\log\frac{u_1^2 r^2}{1+z_x^2+z_y^2}\right)$$
$$= 2\left(\frac{\partial \bar{U}}{\partial x} + z_x\frac{\partial \bar{U}}{\partial z} + \frac{\partial \bar{V}}{\partial y} + z_y\frac{\partial \bar{V}}{\partial z}\right) \tag{4.35}$$

If z_x and z_y are small this changes to:

$$\bar{U}\frac{\partial}{\partial x}\left(\log(u_1 r)\right) + \bar{V}\frac{\partial}{\partial y}\left(\log(u_1 r)\right) = \frac{\partial \bar{U}}{\partial x} + \frac{\partial \bar{V}}{\partial y} \tag{4.36}$$

where use has been made of $\log(x^2) = 2\log(x)$.

The geodesic curvature of the curve ξ = constant given by

$$\frac{1}{h_1 h_2}\frac{\partial h_2}{\partial \xi} = \frac{1}{r}\frac{\partial r}{\partial s} \tag{4.37}$$

is a measure of the convergence or divergence of the streamlines. This means that if r increases downstream the neighboring streamlines have moved apart, thus a positive $\frac{\partial r}{\partial s}$ means diverging streamlines.

The transformations described above with the equivalent radius/metric coefficient are used in the boundary layer methods of [Hamilton *et al.* , 2009] and [Parhizkar & Karimian, 2009], which will be discussed further along in this chapter.

4.6.2. COMPRESSIBLE BOUNDARY LAYER

The incompressible boundary layer equations described in the previous section are only valid for low velocities. The flow regimes that are simulated in this study have Mach numbers from approximately 0.7 up to 3. For all these free-stream Mach numbers, the flow around the body will have sections with Mach numbers above the incompressible flow assumption cut-off, which is generally set at a Mach number of 0.2-0.3. This means the flow boundary layer needs to be treated as a compressible boundary layer. A different set of equations is needed, incorporating the changes in density.

$$\delta^* = \int_0^{Y\to\infty}\left(1 - \frac{\rho}{\rho_e}\frac{u}{V}\right)dy \tag{4.38}$$

$$\theta = \int_0^{Y\to\infty}\frac{\rho}{\rho_e}\frac{u}{U}\left(1 - \frac{\rho}{\rho_e}\frac{u}{V}\right)dy \tag{4.39}$$

LAMINAR BOUNDARY LAYER

The momentum thickness in case of a laminar boundary layer does not need any iteration. Looking at Equation (4.40), the laminar momentum thickness depends on the conditions at the edge of the boundary layer, the reference enthalpy, the local body radius and the distance from the streamline initial point. As it involves integration, the calculation should start at the initial point on the ϵ-curve and then propagate downstream. The ϵ-curve is a concept used by [Hamilton *et al.* , 2006] and [Parhizkar & Karimian, 2009] to prevent issues occurring with the streamlines close to the stagnation point. At the stagnation point, the velocity is approximately zero which would mean no streamline can propagate from the stagnation point. Therefore a curve is calculated a small distance ϵ from the stagnation point and propagation is started from there. This is further explained in Section 4.7.

$$\theta_L = 0.664\frac{\left(\int_0^S \mu^* \rho^* V_e h^2 ds\right)^{\frac{1}{2}}}{\rho_e V_e h} \tag{4.40}$$

In the above equation θ is the momentum thickness, μ is the dynamic viscosity, ρ^* the density at the reference enthalpy, ρ_e the density at the edge of the boundary layer, V_e the velocity at the edge of the boundary layer, r the local radius of the body and s the integration distance.

The edge conditions are known from the Euler solution. For the reference enthalpy condition, the relevant enthalpy needs to be determined first.

$$H_e = c_p T_e \tag{4.41}$$

For a flow in equilibrium, there is no heat transfer between wall and flow and as such the wall can be treated as an adiabatic wall. This means the wall temperature is equal to the adiabatic wall temperature, $T_w = T_{aw}$. In turn, the wall enthalpy is equal to the adiabatic wall enthalpy. The adiabatic wall enthalpy can be calculated using:

$$H_{aw} = H_e + 0.5RV_e^2 \tag{4.42}$$

H_{aw} represents the adiabatic wall enthalpy and Rec represents the recovery factor. The recovery factor depends only on the flow regime (laminar or turbulent) and the Prandtl number:

$$Rec_L = Pr^{\frac{1}{2}} \tag{4.43}$$

$$Rec_T = Pr^{\frac{1}{3}} \tag{4.44}$$

The Prandtl number itself can be calculated using Equation (4.45). For air, it is usually has a value around 0.7-0.8.

$$Pr = \frac{c_p \mu}{k} \tag{4.45}$$

Using the wall enthalpy and boundary layer edge enthalpy, the reference enthalpy H^* can be determined:

$$H^* = 0.50H_e + 0.50H_w + 0.22R\frac{V_e^2}{2} \tag{4.46}$$

With the reference enthalpy known ρ^* and μ^* can be calculated. First, T^* is determined using

$$T^* = \frac{H^*}{c_p} \tag{4.47}$$

Using the adiabatic assumption again, the ratio of densities can be expressed as a temperature ratio:

$$\rho^* = \rho_e \left(\frac{T^*}{T_e}\right)^{\frac{1}{\gamma-1}} \tag{4.48}$$

For the determination of μ^* Sutherland's law is used. The Sutherland Temperature S has a value of $110.4K$. The constant b incorporates the reference dynamic viscosity and reference temperature and has a value of $1.458 \cdot 10^{-6} \frac{kg}{ms\sqrt{K}}$

$$\mu^* = \frac{b \cdot \sqrt{(T^*)^3}}{T^* + S} \tag{4.49}$$

The momentum thickness gives the necessary information to determine the heating rate and skin friction around the vehicle. First the Reynolds number momentum thickness needs to be calculated:

$$Re_\theta = \frac{\rho \cdot V \cdot \theta}{\mu} \tag{4.50}$$

The laminar heat-transfer equation ([Zoby *et al.*, 1981]) is based on the Blasius flat plate heating equation, with an Eckert compressibility correction based on a reference enthalpy added:

$$\dot{q}_{w,L} = 0.22 \left(R_{\theta,e}\right)^{-1} \frac{\rho *}{\rho} \frac{\mu *}{\mu} \rho_e u_e \left(H_{aw} - H_w\right) Pr_w^{-0.6} \tag{4.51}$$

Determining the skin friction is the next step. Several methods exist that relate the skin friction and the momentum thickness either directly or indirectly. Two of these methods for a laminar, compressible boundary layer will be discussed below.

Blasius solution

A very simple method for determining the skin friction on a flat plate in compressible laminar flow is the Blasius solution with compressibility correction. The Blasius solution for incompressible flow over a flat plate is shown in Equation (4.52).

$$C_f = \frac{0.664}{\sqrt{Re_x}} \tag{4.52}$$

To add compressibility effects the reference temperature is used. This temperature can be calculated with empirical Equation (4.53).

$$\frac{T^*}{T_e} = 0.5 + 0.039 M_e^2 + 0.5 \frac{T_w}{T_e} \tag{4.53}$$

The reference temperature can be used to calculate the Chapman-Rubesin parameter, see Equation (4.54).

$$C^* = \frac{\rho^* \mu^*}{\rho_e \mu_e} \approx \left(\frac{T^*}{T_e}\right)^{-1/3} \tag{4.54}$$

The final compressibility corrected equation is shown in Equation (4.55)

$$C_f = \frac{0.664\sqrt{C^*}}{\sqrt{Re_x}} \tag{4.55}$$

A typical Blasius solution for skin friction on a laminar flat plate is shown in Figure 4.14. An important identifying feature of such a solution is the inverse square-root type shape, indicating that the local skin friction is highest in the first section of the flat plate, while flattening in the later sections.

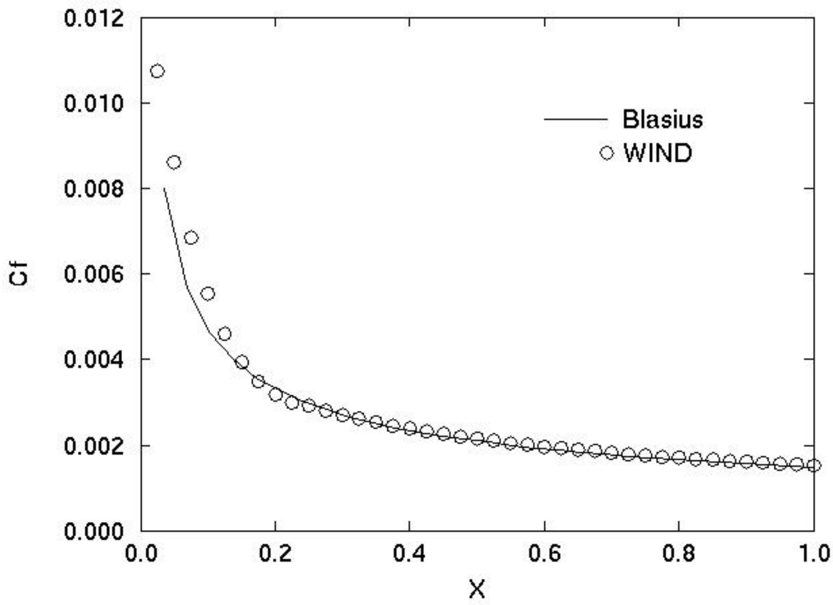

Figure 4.14: Typical Blasius skin friction development in laminar flow on a flat plate, [John W. Slater, 1999].

Reynolds analogy

The Reynolds analogy posits a relationship between the skin friction on the surface and the heating rate (or rather Stanton number). This function can be expressed as:

$$\frac{C_h}{C_f} = f\left(Pr, \frac{x}{L}, \text{geometry}\right) \tag{4.56}$$

The actual equation used in the simulation is based on the form given in [White, 2005] shown in Equation 4.57.

$$C_f = \frac{2\dot{q}_{w,T} Pr^{2/3}}{\rho_e u_e c_p (T_{aw} - T_w)} \tag{4.57}$$

The caveat is that this analogy fails if the flow is non-similar, the wall temperature and adiabatic wall temperature are very close or the wall temperature varies. As the axisymmetric analogue results in axisymmetric equations which fulfill the similarity requirements, this is not an obstacle that cannot be taken. The wall temperature requirement makes that only simulations with constant wall temperatures are allowed, which limits the simulation to simple models. Finally, the coefficient used in the Reynolds analogy depends strongly on the pressure distribution.

TRANSITION FROM LAMINAR TO TURBULENT FLOW

There is a large difference in momentum thickness, heating rate and friction between laminar and turbulent flow. To ensure a correct prediction of the actual values of these parameters it is important to know where flow transition takes place. With the methods in this research an approximation based on empirical equations is the best result possible. The method of choice is the method by [Wazzan *et al.* , 1981a], which is a so-called e^9 method, meaning that the total amplification of the Tollmien-Schlichting waves is approximately equal to e^9. The formula for this method is:

$$\log_{10}(Re_{x,tr}) \approx -40.4557 + 64.8066H - 26.7538H^2 + 3.3819H^3 \tag{4.58}$$

In this equation H is the shape-factor correlation, $H = \frac{\delta^*}{\theta}$, with δ^* being the displacement thickness.This means the shape factor is a measure of the displacement thickness with respect to the momentum thickness. As Equations (4.16) and (4.17) have already shown they are a function of the velocity profile only, so the shape factor itself is an indicator of the velocity profile throughout the boundary layer. The shape-factor correlation can for example be determined using the method of Thwaites [Thwaites, 1949]. However, because of the transformation to an equivalent flat plate that is being used here the shape factor for a laminar flat plate can be used, which is 2.7.

All the methods described above give the critical Reynolds number, i.e. the Reynolds number for which transition occurs. As the Reynolds number can be determined at any position along the vehicle after the appropriate transformations to a flat plate, the position of the critical point can be found iteratively. If the position of transition is approximately known the methods for laminar boundary layers can be used for the part of the vehicle in front of this point and methods for turbulent boundary layers can be used for the parts behind this point.

TURBULENT BOUNDARY LAYER

A similar method is used for the turbulent boundary layer. However, in this case the coefficients of the momentum thickness equations are not constant and also not explicit. The reason for this is that the momentum thickness depends on the momentum thickness Reynolds numbers through the coefficient N, while the Reynolds number is dependent on the momentum thickness. This means that in order to numerically solve the equations, iteration is necessary.

The general equation for the momentum thickness of a turbulent boundary layer is shown in Equation (4.59) [Zoby *et al.* , 1981].

$$\theta_T = \frac{\left(c_2 \int_0^S \rho^* u_e {\mu^*}^m r^{c_3} dS\right)^{c_4}}{\rho_e u_e r} \tag{4.59}$$

The equation for the coefficient N depends on the momentum thickness Reynolds number $R_{\theta,e}$, but an exact equation is not available. Therefore Zoby et al. use an empirical equation obtained from axisymmetric nozzle-wall data, see Equation (4.60).

$$N = 12.67 - 6.5\log(R_{\theta,e}) + 1.21\left(\log(R_{\theta,e})\right)^2 \tag{4.60}$$

An equation based axisymmetric nozzle-wall data may not be accurate for the external flow along models on which the axisymmetric analogue is applied. To account for these types of flows, [Hamilton *et al.* , 2009] supplies a table of momentum thickness Reynolds numbers and the corresponding value for N.

The coefficients that depend on N are given by Equation (4.61) through 4.66

$$m = \frac{2}{N+1} \tag{4.61}$$
$$c_1 = \left(\frac{1}{c_5}\right)^{\frac{2N}{N+1}} \left[\frac{N}{(N+1)(N+2)}\right]^m \tag{4.62}$$
$$c_2 = (1+m)c_1 \tag{4.63}$$
$$c_3 = 1+m \tag{4.64}$$
$$c_4 = \frac{1}{c_3} \tag{4.65}$$
$$c_5 = 2.2433 + 0.93N \tag{4.66}$$

The equation for the heat flux is also modified by the coefficients for turbulent flow:

$$\dot{q}_{w,T} = c_1 \left(R_{\theta,e}\right)^{-m} \frac{\rho*}{\rho_e} \left(\frac{\mu*}{\mu_e}\right)^m \rho_e u_e \left(H_{aw} - H_w\right) \left(Pr_w\right)^{-0.4} \tag{4.67}$$

With the momentum thickness known from Equation (4.59), the skin friction can be determined. Below, two methods for determining the turbulent skin friction are discussed.

Simple method based on momentum thickness Reynolds number

A very simple method given by [Zoby *et al.* , 1981] relates the skin friction coefficient to the momentum thickness Reynolds number. In essence, it is a simplified version of the Kármán integral expression, with modifications to account for turbulent flow. The form given by Zoby can be seen in equation (4.68).

$$c_f = 2c_1 \left(\frac{1}{Re_{\theta,e}^m}\right) \tag{4.68}$$

While it incorporates turbulent effects through the use of the coefficients m and c_1, it is not clear how well it can deal with pressure gradients, as the term dealing with these gradients is missing. The reason may be that for the extra term knowledge of the shape factor is known, i.e. the ratio of displacement thickness to momentum thickness. While the momentum thickness is determined elegantly by Zoby, the displacement thickness is not which makes it impossible to determine the shape factor from the paper.

Van Driest method

The method of van Driest is considered to be one of the best simple engineering approximation for compressible, turbulent skin friction on a flat plate [White, 2005]. It is a semi-empirical method taking into account compressibility corrections. The equation for the skin friction is given in Equation (4.69) while the coefficients are given in Equations (4.70) through (4.74).

$$C_f \approx \frac{0.455}{S^2 \log^2\left(\frac{0.06}{S} Re_\theta \frac{\mu_e}{\mu_w} \sqrt{\frac{T_e}{T_w}}\right)} \tag{4.69}$$

$$a = \sqrt{\frac{\gamma - 1}{2} M_2^2 \frac{T_e}{T_w}} \tag{4.70}$$

$$b = \frac{T_{aw}}{T_w} \tag{4.71}$$

$$A = \frac{2a^2 - b}{(b^2 + 4a^2)^{1/2}} \tag{4.72}$$

$$B = \frac{b}{(b^2 + 4a^2)^{1/2}} \tag{4.73}$$

$$S = \frac{(T_{aw}/T_e - 1)^{1/2}}{sin^{-1} A + sin^{-1} B} \tag{4.74}$$

This equation should be very accurate for large range of turbulent Reynolds numbers, Mach numbers and wall temperatures for a flat plate with no pressure gradient. For conversion between between a cone and a plate, use can be made of a power law, where for turbulent flows the coefficient m is between $\frac{1}{8}$ and $\frac{1}{4}$. Equation (4.75) shows this relationship.

$$\frac{C_{f,cone}}{C_{f,plate}} \approx (2+m)^{m/(m+1)} \tag{4.75}$$

Putting the extremes of the range of values for m in the equation, it becomes clear that the skin friction of a cone in turbulent flow is only 10% to 15% higher than of a plate.

4.7. COMPARISON OF PARHIZKAR'S AND HAMILTON'S METHOD

Using the axisymmetric analogue, one of the most important steps is finding the equivalent radius used in the determination of the momentum thickness, as described by [Cooke, 1961] and discussed earlier in this chapter. Two methods have been investigated for their accuracy and speed, one method by [Hamilton *et al.* , 2009] and one by [Parhizkar & Karimian, 2009].

HAMILTON

The basic approach of Hamilton et al. is to determine the metric coefficient parameters on the ϵ-curve and then integrate it along the streamline, taking into account the shape of the vehicle and the velocity distribution.

The ϵ-curve is obtained by taking a point a distance of ϵ away from the stagnation point. From that point, the curve is created by propagating perpendicular to the velocity vector. The propagation continues until it reaches the symmetry plane or a full curve (360°) is obtained. The general equation for the metric coefficient is shown in Equation (4.76).

$$h = \frac{|\nabla F|}{F_x V}\left[w\left(\frac{\delta y}{\delta \beta}\right)_z\right] \tag{4.76}$$

In the above equation ∇F is the gradient of the surface function, F_x is the derivative with respect to x of the surface function, V is the local velocity in m/s and $w\left(\frac{\delta y}{\delta \beta}\right)_z$ is a factor that takes into account the curvature of the streamline throught the derivative. At this point it is also important to introduce the concept of the independent and dependent variables. Because the x, y and z-coordinates describe a known surface, only 2 of the 3 coordinates are actually independent. The third coordinate can be expressed as a function of the former two. The independent coordinates can be chosen freely for each element of the mesh, but the most effective approach is to take the two coordinates that change the most as independent coordinate, i.e. the coordinate that changes the least on the element is the dependent variable.

The surface is fit using the following equation

$$F(x,y,z) = a_1 y^2 + a_2 y + a_3 z^2 + a_4 z + a_5 x^2 + a_6 x + a_7 = 0 \tag{4.77}$$

Because of the zero in the equation it is possible to divide the whole equation by one of the coefficients, which means that only 6 of the 7 coefficients are independent. As long as $x = y = z = 0$ is not true, the coefficient a_7 can be set to 1. In case $x = y = z = 0$ is true, a_7 is set to 0. Using Equation (4.77) at the three vertices of an element gives three equations. Furthermore, using Equation (4.78) (derivation given in [Hamilton *et al.* , 2009]) again applied at the three vertices of an element, another three equation are obtained, which can be found in Equation (4.79) to Equation (4.81). These six equations together are then sufficient to solve for all the coefficients.

$$uF_x + vF_y + wF_z = 0 \tag{4.78}$$

$$F_x = 2a_5 x + a_6 \tag{4.79}$$
$$F_y = 2a_1 y + a_2 \tag{4.80}$$
$$F_z = 2a_3 z + a_4 \tag{4.81}$$

When all six coefficients are known, Equation (4.79), 4.80 and 4.81 can be used to determine F_x, F_y and F_z at every point on the surface as long as the element is known. The ∇ term can be determined simply using Equation (4.82).

$$\nabla F = \sqrt{F_x^2 + F_y^2 + F_z^2} \tag{4.82}$$

With the surface terms of each element known, the procedure can start. First the points on and the shape of the ϵ-curve needs to be determined. Hamilton proposes using two differential equations to numerically integrate the ϵ-curve. Equations 4.83 and 4.84 express the change of coordinates perpendicular to the streamlines.

$$\frac{dy}{dS_\perp} = \hat{e}_\perp \circ \hat{j} = \frac{w\left(F_x^2 + F_z^2\right) + vF_yF_z}{F_x V\,|\nabla F|} \tag{4.83}$$
$$\frac{dz}{dS_\perp} = \hat{e}_\perp \circ \hat{k} = -\frac{v\left(F_x^2 + F_y^2\right) - wF_yF_z}{F_x V\,|\nabla F|} \tag{4.84}$$

This method can be simplified however. First determine the perpendicular direction on the surface of the body by taking the cross-product. Then simply propagate in this direction with a small timestep. Because the propagation is always done on the element no propagation is necessary.

After the shape of the ϵ-curve has been determined the metric coefficient of each point on the epsilon needs to be determined. Because the epsilon curve is supposed to be equidistant from the stagnation point along the streamlines, a simple formula suffices, see Equation (4.85).

$$h = \frac{\Delta S_\perp}{\Delta\beta} \tag{4.85}$$

In essence, this equation calculates the metric coefficient by comparing the distance between two points to the angle change between two points. Using the initial metric coefficient, the initial curvature derivative can be calculated using an inversion of Equation (4.76), as shown in Equation (4.86).

$$w\left(\frac{\delta y}{\delta\beta}\right)_z = \frac{hF_xV}{|\nabla F|} \tag{4.86}$$

To find the curvature derivative along the streamline the differential equation shown in Equation (4.87) is integrated when stepping along the streamline.

$$\frac{D}{Ds}\left[w\left(\frac{\delta}{\delta\beta}\right)_z\right] = \frac{1}{V}\left[w\left(\frac{\delta}{\delta\beta}\right)_z\right]\left[\frac{\delta w}{\delta y} + \frac{\delta w}{\delta z}\right] \tag{4.87}$$

PARHIZKAR

The approach of Parhizkar is simpler than Hamilton's because of its local nature instead of propagated nature. Instead of using the metric coefficient h, Parhizkar et al. use the metric hd_β, which is the perpendicular distance between two adjacent streamlines. This distance is found as follows. First the streamwise distance of the node (p_i is Figure 4.15) to the ϵ-curve is calculated. Then, a streamline which is adjacent (i.e. very close) to the node streamline is determined. The point on the adjacent streamline which is the same streamwise distance from the ϵ-curve as the node is then found (intersection of the $h_\beta d_\beta$ line with the $\beta_l + d\beta$ line in Figure 4.15. The distance between these 2 points can be found by simply subtracting the coordinates. Next, calculate the angle between the main streamline and the line connecting the node to the equidistant point on the adjacent streamline, which will be γ. Finally, Parhizkar's. version of the metric coefficient is calculated using Equation (4.88).

$$hd_\beta = h_\beta d_\beta \sin\gamma \tag{4.88}$$

Parhizkar et al. argue that hd_β can simply be substituted in the equations for the momentum thickness given by Hamilton. The reasons are twofold: first, β is by definition constant along a streamline, so d_β is constant between streamlines. Second, the metric coefficient appears with the same power in the nominator and denominator in the equation for momentum thickness. Therefore the substitution is valid.

Judging from the method, Parhizkar makes the implicit assumption that the streamline and adjacent streamline are approximately parallel. This is because Equation (4.88) only is true if the angle between the adjacent streamline and the hd_β line is a right angle, which is only the case if the streamlines are assumed parallel (see also Figure 4.15). This means that the streamline density should be high on surfaces that are strongly curved, to satisfy the condition of near-parallelism.

Parhizkar also specifically mentions wings on a vehicle. Because the streamlines on a wing do not originate solely at the stagnation point (if at all) but also from the wing stagnation line, a different treatment is warranted. As a wing generally has very little curvature between streamlines, the flow is close to two-dimensional flow. In the convective heating equations of [Zoby *et al.* , 1981], the equations are equal to the ones for two-dimensional flow for a value of $h = 1$. Therefore, in the case of wings the metric coefficient is set to 1 by Parhizkar et al.

With the differences discussed, it is important to know how well both methods perform in the simulation. Therefore the methods will be compared in the next section.

COMPARISON

Figure 4.16 shows the momentum thickness for a shell calculated using both methods. The advantages and disadvantages of the current implementation are clear from the images and will be discussed. The first striking difference is the build-up of the momentum thickness. Parhizkar's curve increases very rapidly at the tip, then decreases somewhat and then increases to the same peak as Hamilton's curve. The momentum thickness is expected to build up gradually from zero at the tip of the model however, so this is not correct (see also section Validation). The cause of this behaviour can be found in the current implementation of the initial metric coefficient for Parhizkar's method, which gives wrong values for the metric coefficient at the start of the streamline. This means that using this method, all nodes located in the first 20% of the model would have too high values for the momentum thickness.

The second difference is the variation at the peak of the curve at 70% of the model. Both models show variation there, but the variation using Hamilton's method is much stronger. The reason for this variation is a strong variation in the metric coefficient at that point, either due to a change in curvature or due to inaccuracies in the Euler solution (which could be eliminated using more

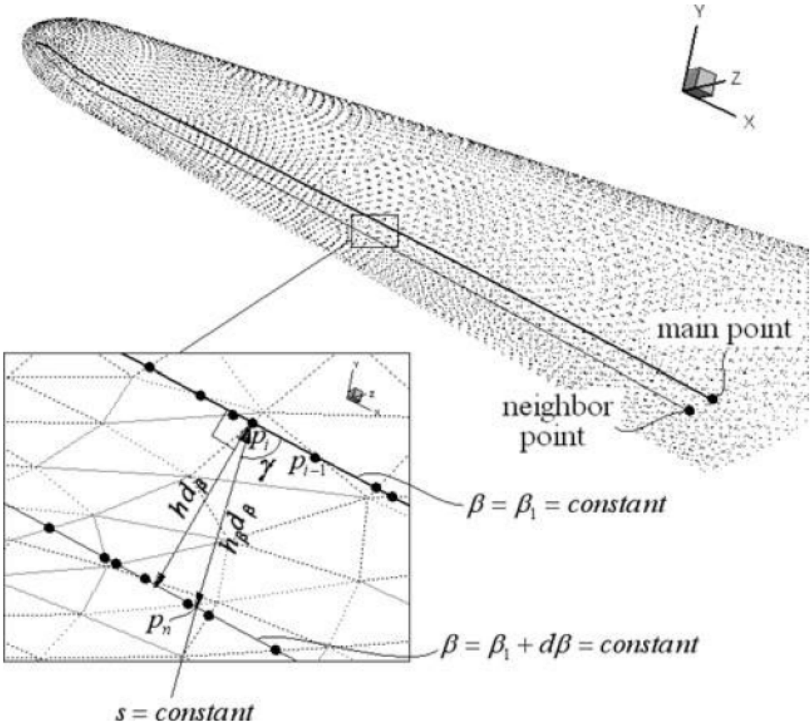

Figure 4.15: Method used to determine the metric coefficient [Parhizkar & Karimian, 2009].

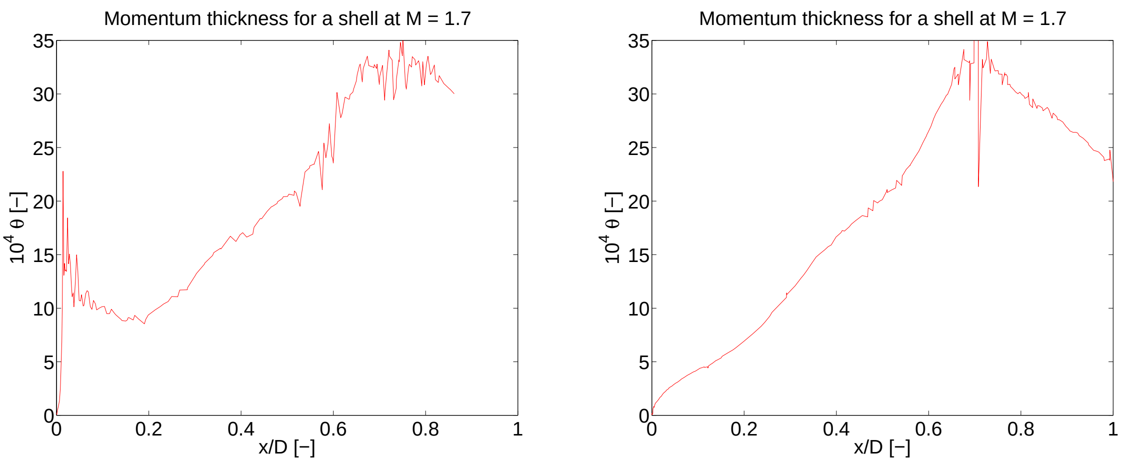

Figure 4.16: Comparison of the (non-normalized) momentum thickness calculated using Parhizkar's method (left) and Hamilton's method (right).

iterations). The difference between the methods is due to Hamilton's method propagation of the metric coefficient along the streamline, while Parhizkar's method determines it locally. This allows Parhizkar's method to balance the variation a bit in the nominator and denominator. The rapid variations only have impact on a very small section of the model, which limits the impact on the total friction solution.

The last difference is the smoothness outside of the peak. Hamilton's outcome is much smoother, again due to the metric coefficient being determined through an integral. This behaviour is better for moment prediction due to friction, as an oscillation around a mean value has a much bigger impact on the moments of the vehicle than the total forces.

There is another factor to consider. Hamilton's method needs the determination of a set of parameters on the epsilon curve in order to propagate the metric coefficient. Parhizkar's method does not need this, but does need an extra loop in the code to calculate the local metric coefficient using an adjacent streamline. This means that as it stands, Hamilton's method is generally faster.

In conclusion, in the current code Hamilton's method allows for better and faster predictions. The rapid variation at the peak of the curve will have limited influence due to the small area in which it occurs. Improvements could be made by averaging the metric coefficient or momentum thickness over a certain range to filter out the variations.

4.8. A PHASE PORTRAIT METHOD FOR DETERMINING STAGNATION LINES

For a proper treatment of the streamlines it is necessary to know where the streamlines originate from. This means the stagnation points and stagnation lines need to be determined. The method to do this is based on the phase portrait of the local flowfield, as explained in [Kenwright, 1998].

4.8.1. THEORY

The basis of the method are the phase portraits of the local flowfield around critical points. These are points where the velocity is zero, which means the velocity field around it depends on the gradient of the velocity. The type of critical points can approximately be determined by the eigenvalues and eigenvectors of the velocity gradient. For clarity, some examples of phase portraits are given in Figure 4.17.

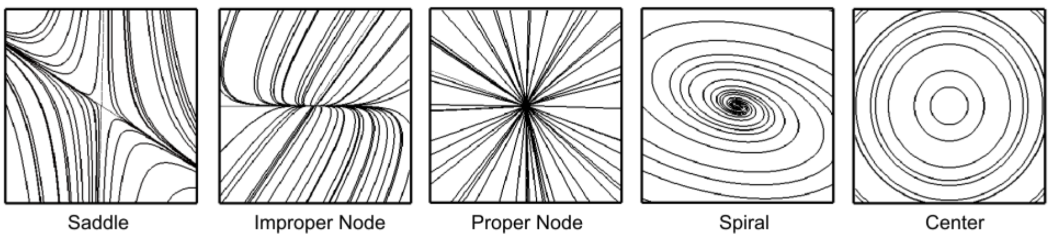

Figure 4.17: Five phase portraits that arise in linear vector fields [Kenwright, 1998].

The continuous linear vector field can be represented by Equation (4.89). It expresses the velocity as a factor of a constant contribution to the velocity, the x-position and the y-position. It should be noted that this is only valid in a two-dimensional basis. The coefficients are all constants.

$$\begin{bmatrix} \dot{x} \\ \dot{y} \end{bmatrix} = \begin{bmatrix} a_1 \\ a_2 \end{bmatrix} + \begin{bmatrix} b_1 & c_1 \\ b_2 & c_2 \end{bmatrix} \begin{bmatrix} x \\ y \end{bmatrix} \tag{4.89}$$

The values of the constants can be found by solving the matrix equation, which in analytical form is given in Equations 4.90 and 4.91.

$$\begin{bmatrix} a_1 \\ b_1 \\ c_1 \end{bmatrix} = \begin{bmatrix} 1 & x_1 & y_1 \\ 1 & x_2 & y_2 \\ 1 & x_3 & y_3 \end{bmatrix}^{-1} \begin{bmatrix} \dot{x}_1 \\ \dot{x}_2 \\ \dot{x}_3 \end{bmatrix} \tag{4.90}$$

$$\begin{bmatrix} a_2 \\ b_2 \\ c_2 \end{bmatrix} = \begin{bmatrix} 1 & x_1 & y_1 \\ 1 & x_2 & y_2 \\ 1 & x_3 & y_3 \end{bmatrix}^{-1} \begin{bmatrix} \dot{y}_1 \\ \dot{y}_2 \\ \dot{y}_3 \end{bmatrix} \tag{4.91}$$

To find the eigenvalues and eigenvectors of the field the derivative of Equation (4.89) is needed. After taking the derivative, Equation (4.89) can be substituted for $\dot{y}$ and $\dot{x}$ respectively. After some further manipulation and substitution Equation (4.93) is obtained.

$$\ddot{x} - (b_1 + c_2)\dot{x} + (b_1 c_2 - b_2 c_1)x = (a_2 c_1 - a_1 c_2) \tag{4.92}$$

$$\ddot{y} - (b_1 + c_2)\dot{y} + (b_1 c_2 - b_2 c_1)y = (a_1 b_2 - a_2 b_1) \tag{4.93}$$

The eigenvalues can found as the roots of the homogeneous part of this equation, i.e.

$$\lambda^2 - (b_1 + c_2)\lambda + (b_1 c_2 - b_2 c_1) = 0 \tag{4.94}$$

For a solution the determinant of the Jacobian matrix in Equation (4.89) needs to be non-zero. If this condition is met, the solution takes the following form:

$$\begin{bmatrix} x - x_0 \\ y - y_0 \end{bmatrix} = \begin{bmatrix} \xi_1 & \eta_1 \\ \xi_2 & \eta_2 \end{bmatrix} \begin{bmatrix} \alpha e^{\lambda t} \\ \beta e^{\mu t} \end{bmatrix} \tag{4.95}$$

The coordinates x_0 and y_0 are the coordinates of the critical point.

$$x_{cp} = x_0 = \frac{a_2 c_1 - a_1 c_2}{b_1 c_2 - b_2 c_1} \tag{4.96}$$

$$y_{cp} = y_0 = \frac{a_1 b_2 - a_2 b_1}{b_1 c_2 - b_2 c_1} \tag{4.97}$$

$$\begin{bmatrix} x \\ y \end{bmatrix} = \begin{bmatrix} \xi_1 & \eta_1 \\ \xi_2 & \eta_2 \end{bmatrix}^{-1} \begin{bmatrix} x \\ y \end{bmatrix} = \begin{bmatrix} \alpha e^{\lambda t} \\ \beta e^{\mu t} \end{bmatrix} \tag{4.98}$$

The eigenvectors and eigenvalues are already clear from this equation, as the eigenvectors are the columns of ξ and η and the eigenvalues are the exponents λ and μ. The transformed curves can be described by the following scalar function:

$$\Psi(x, y) = \frac{x^\mu}{y^\lambda} \quad \text{or} \quad \Psi(x, y) = -\frac{y^\lambda}{x^\mu} \tag{4.99}$$

$$\Psi(r, \theta) = r e^{\frac{\sigma}{\nu}\theta} \tag{4.100}$$

with $r = \sqrt{x^2 + y^2}$ and $\theta = tan^{-1}\left(\frac{y}{x}\right)$

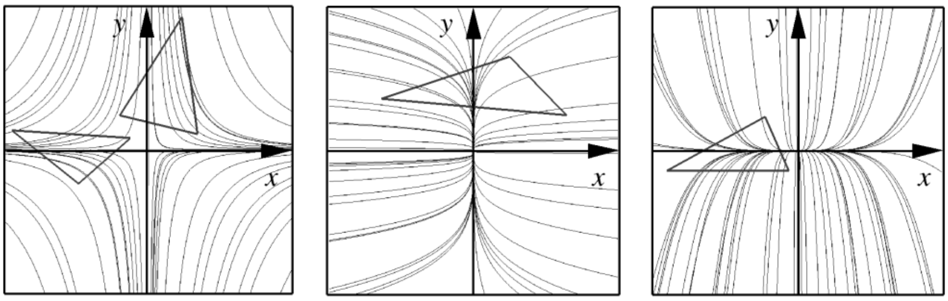

(a) Saddle: μ < 0 < λ (b) Repelling node: 0 < μ < λ (c) Attracting node: μ < λ < 0

Figure 4.18: The three phase portraits in which the curves asymptotically converge to the axes [Kenwright, 1998].

4.8.2. IMPLEMENTATION

[Kenwright, 1998] describes a step by step approach, which will be outlined now:

1. Project the velocity vectors at the vertices onto the plane of the element.
2. Change the coordinates and vectors of the triangle from a three-dimensional basis to a two-dimensional one, meaning that these are rewritten in two independent coordinates.
3. Calculate the coefficients using Equation (4.90) and 4.91.
4. Determine the discriminant of the Jacobian matrix of Equation (4.89) from the trace and the determinant, i.e. $\Delta = (b_1 + c_2)^2 - 4(b_1 c_2 - b_2 c_1$. If the discriminant is zero, it means the eigenvalues are complex numbers and the algorithm is stopped.
5. Evaluate the eigenvalues of the matrix using the characteristic equation. If an eigenvalue is zero it means that the phase portrait is a proper node, see also Figure 4.17.
6. Determine the eigenvectors by substituting the found eigenvalues for λ in the matrix. The eigenmatrix can be constructed by combining the eigenvectors in a matrix.
7. Transform each vertex of the triangle into so-called canonical coordinates using Equation (4.98). The x and y coordinates can be determined from Equations (4.96) and 4.97. Doing this projects the triangle on the phase plane.
8. Use the eigenvalues to test the type of phase portrait. There are three possibilities:
   - $\mu < 0 < \lambda$: Saddle
   - $0 < \mu < \lambda$: Repelling node
   - $\mu < \lambda < 0$: Attracting node

   An illustration of these options is shown in Figure 4.18.
9. Determine whether there is an attachment or a separation line.
   - Saddle or repelling node: if the line $x = 0$ intersects the triangle on the phase plane, calculate the 2 intersects and transform it to the 2D plane. In this case there is an attachment line.
   - Saddle or attracting node: if the line $y = 0$ intersects the triangle on the phase plane, calculate the 2 intersects and transform it to the 2D plane. In this case there is an separation line.

10. Transform the 2D coordinates back into 3D Cartesian coordinates.

After following this procedure the coordinates of the stagnation line are known. The implementation in the simulation will be discussed in the next chapter.

5
SIMULATION

This chapter explains the methods used to simulate the airflow around and stability of the vehicle. It differs from the theoretical chapters because it is concerned with implementation, not with theory. Because the code for the Euler simulation was not written by the author of this report, it will not be discussed extensively. Rather it will deal with the simulation of the boundary layer and its properties regarding momentum thickness, heat flux and skin friction.

5.1. SOFTWARE ARCHITECTURE

The general software architecture is shown is Figure 5.1. There are two subdivisions in the architecture, namely modules and functions. Functions group together steps that functionally belong to the same group. However, this does not mean that they are always grouped together in a piece of software as other architecture choices may have been made for software developed by other authors. This gives rise to the concept of modules, which are steps that are grouped together in a single software package. As an example, while the flow field meshing would functionally belong to the group of meshing functions, it has been packed together with the Euler solver.

In short, the following major steps are shown in the architecture:

1. Generating model and creating a surface mesh of this model and the corresponding flow field mesh around the model.
2. Solve the inviscid flow field which is used as input for the boundary layer simulation.
3. Integrate the boundary layer variables along the streamlines to obtain the skin friction at each node.
4. Determine the total forces and moments due to the skin friction and add these to the forces and moments due to the pressure distribution.
5. Calculate relevant stability coefficients and characteristics using the forces and moments on the model for different configurations.

The architecture will be further detailed in the rest of this chapter.

5.2. MODEL, MESH AND PREPARATORY STEPS

Before there can be any simulation, a number of preparatory steps are necessary to create the aerodynamic mesh and correctly set up the simulation. The process starts by creating a model, usually

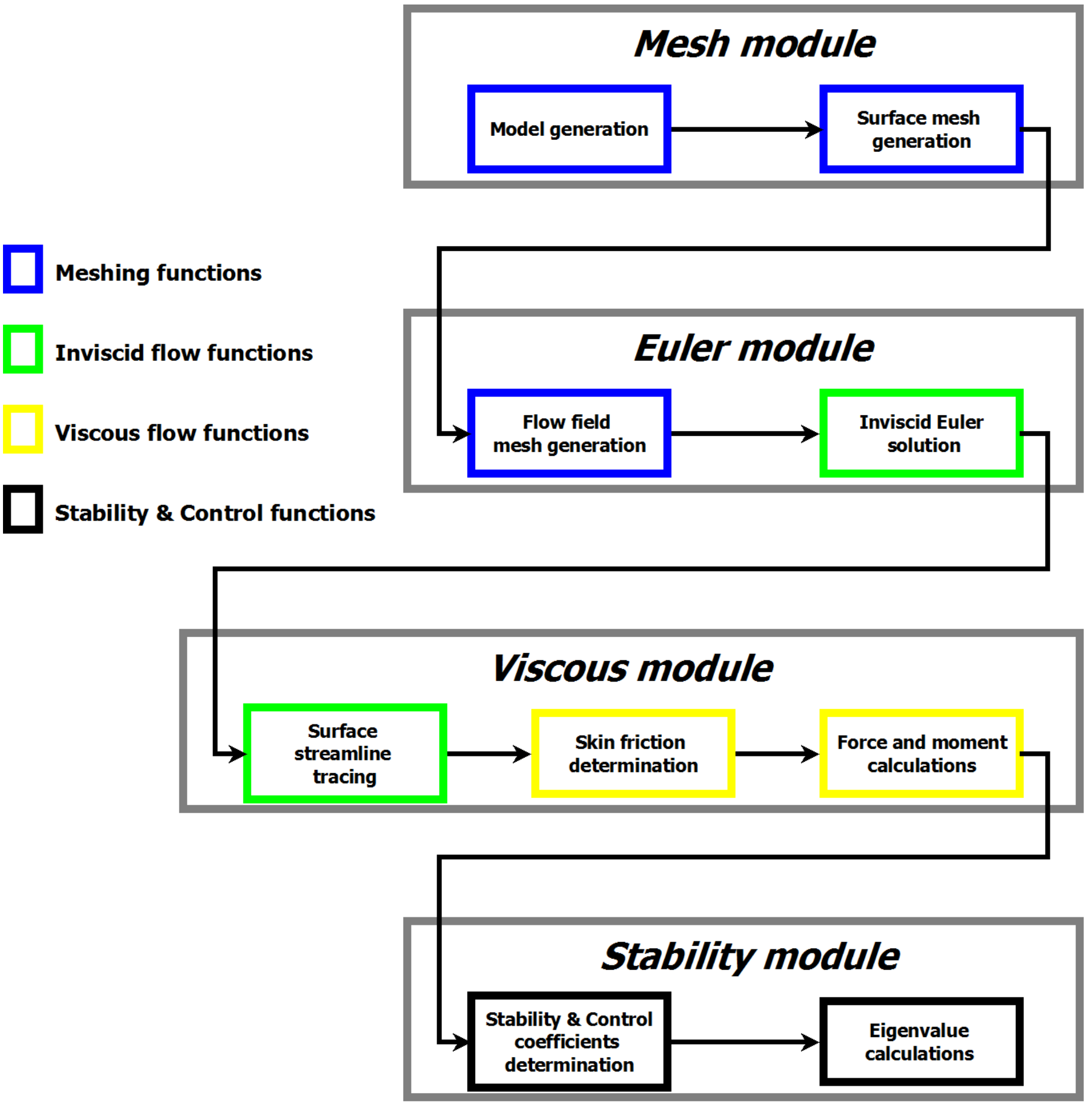

Figure 5.1: High-level software architecture.

in a CAD modeling program. After creating the model it needs to be loaded into meshing software such as GMSH. Formats such as step files, geometry files or IGES files can be used.

For a proper mesh it is important to carefully create the model and select the options for the mesher. For the mesher to produce a clean mesh, discontinuities in the surface curvature should be avoided and all surfaces should be nicely connected (which means no gaps or intersections). Figure 5.2 through 5.4 show what these problem areas look like. A curvature discontinuity happens when the surface curvature suddenly changes, which makes it difficult for the meshing software to connect elements properly. This problem can be minimized by using smaller elements and ensuring proper, continuous connection of surfaces in the model design. A surface intersection is an area where parts of the model pass through each other. A clean surface mesh is only obtained when no elements intersect and there are no elements inside the vehicle that the flow cannot reach. This issue can simply be prevented by proper shell design of the initial model.

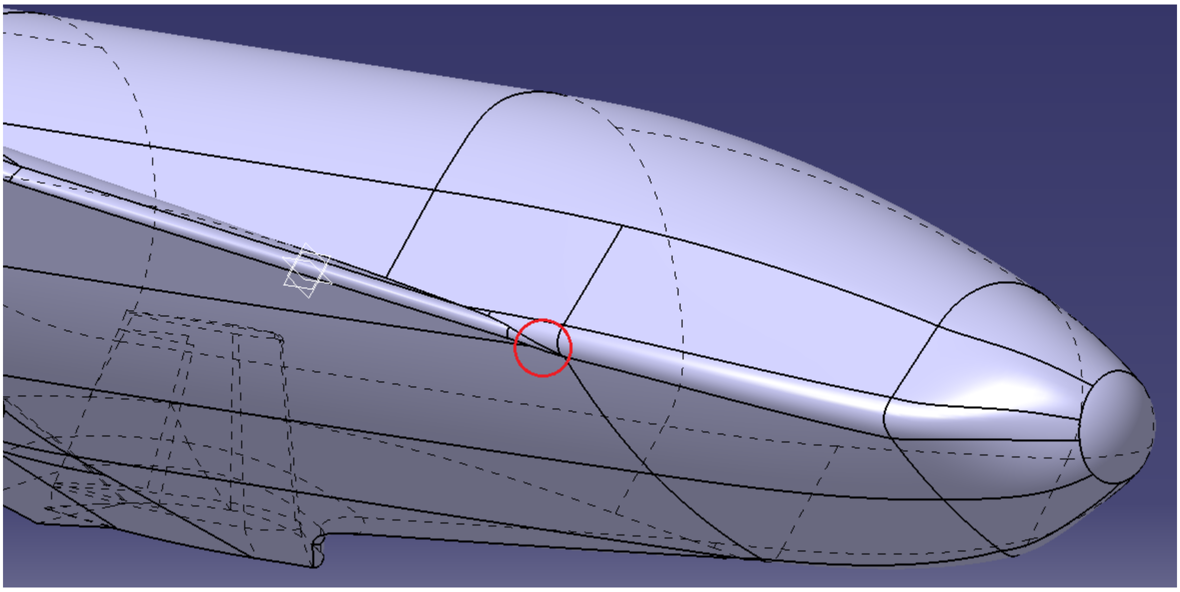

Figure 5.2: Curvature discontinuity.

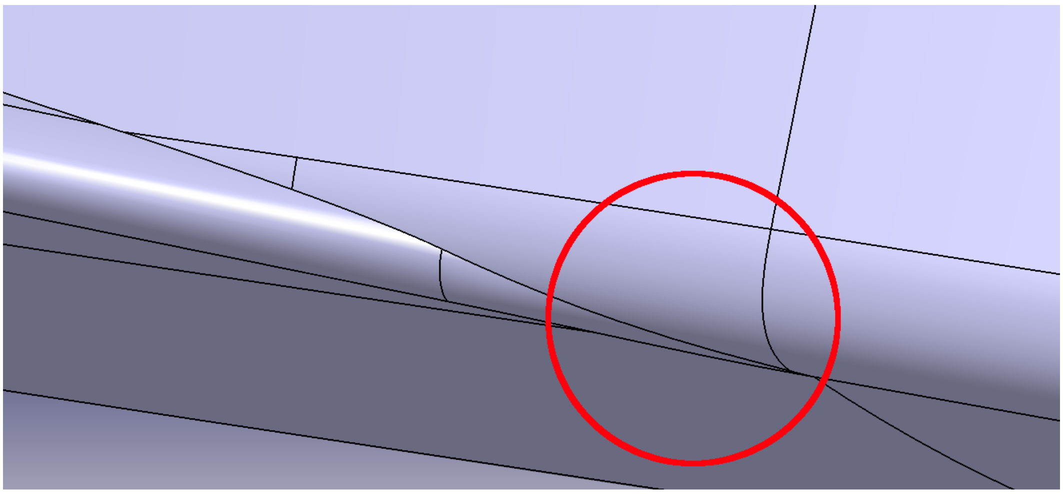

Figure 5.3: Detailed view of curvature discontinuity.

The next step is the mesh creation itself. Automated mesh generators have taken over a lot of

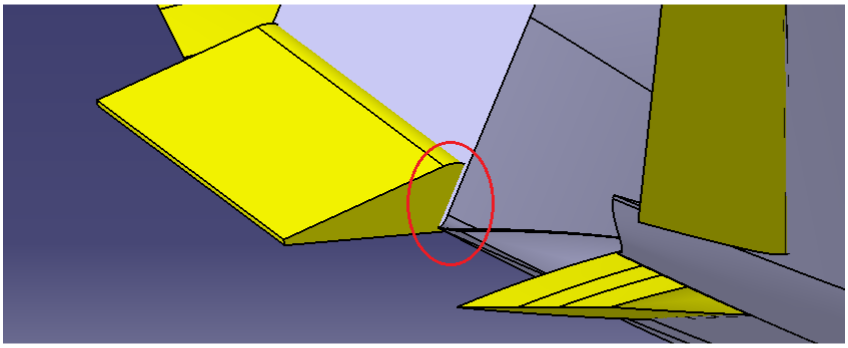

Figure 5.4: Surface intersection.

work. They are however far from perfect, as there may be unwanted concentrations of elements, gaps or intersecting elements. For the surface meshes in this thesis the open-source software called GMSH is used [Geuzaine & Remacle, 2009].

A further mesh optimization is performed using a piece of software called YAMS. This program gives the user a range of options regarding methods and parameters. Included methods are mesh optimization, mesh smoothing, mesh refinement or decimation using methods using Hausdorff distance or finite elements. The options that can be set concern edge detection, tolerances, mesh sizes and the relative size of elements. The output from YAMS is very dependent on the input, so mesh faults in the input will propagate. Examples of mesh faults can be found in Figure 5.6 and 5.8. The mesh fault in the wing leading edge was caused by using elements that were too large in combination with a high curvature. The mesh faults at the intersection of the fuselage with the body flap were the result of a very small edge between the body flap and the fuselage, which the optimizing software had difficulty with.

While this can be minimized by using a good model, it is hard to eliminate completely. Therefore the mesh needs to be checked afterwards for these errors. The software that checks for errors identifies nodes that are not in any element (orphan nodes) and elements that are not enclosed by 3 other elements (except those bordering the symmetry plane). It then removes the orphaned nodes and outputs the elements to be checked manually. For complex models manual adjustments are often necessary for a clean mesh.

After obtaining a clean mesh the simulation parameters need to be set. For the Euler simulation the only interesting parameter is the Mach number and the angle of attack because the simulation outputs dimensionless variables and the results are inviscid, meaning that there is no Reynolds number dependence. The boundary layer simulation needs the reference state variables of the air to convert the dimensionless values to actual forces and moments. A wall temperature is also needed as input to derive the state variables at the wall. The transition Reynolds number can be set a manual value or such that the internal method calculates it. The values for the timestep and the ϵ-curve step can also be changes, as well as the settings for the stagnation line and the location of the center of mass (for the moment calculations).

5.3. EULER

The next phase in the simulation procedure is the Euler simulation, which gives the inviscid flowfield on the surface of the model. Without going into too much detail, the steps in the Euler simulation will be explained. A flow diagram of the software can be found in Figure 5.9.

The first stage is concerned with creating the three-dimensional mesh of the flow field surrounding the model. At this point in the simulation symmetry conditions are not considered yet. The distance of the outer boundary from the model can be set, which is usually around 20 times the

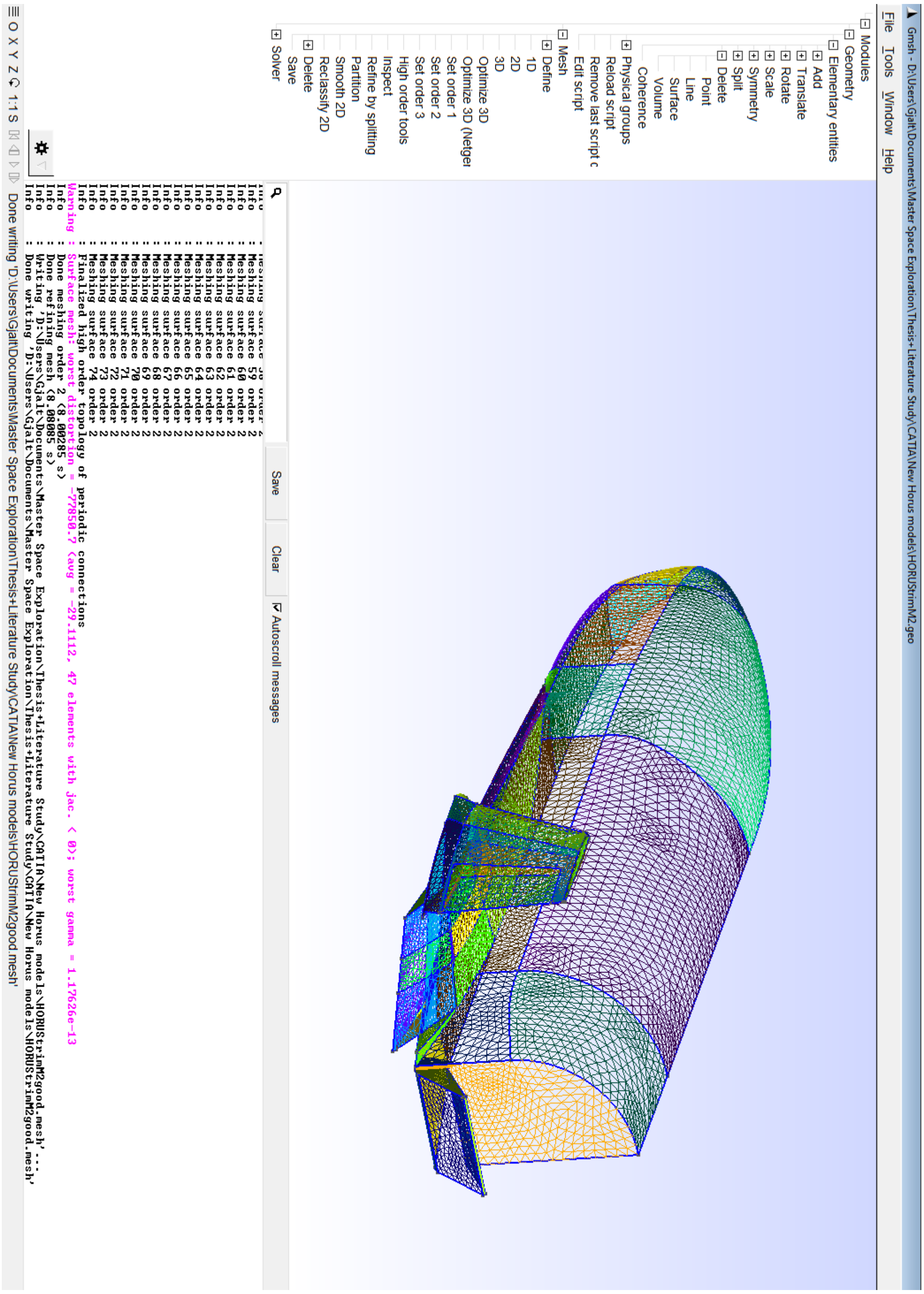

Figure 5.5: Typical mesh from GMSH.

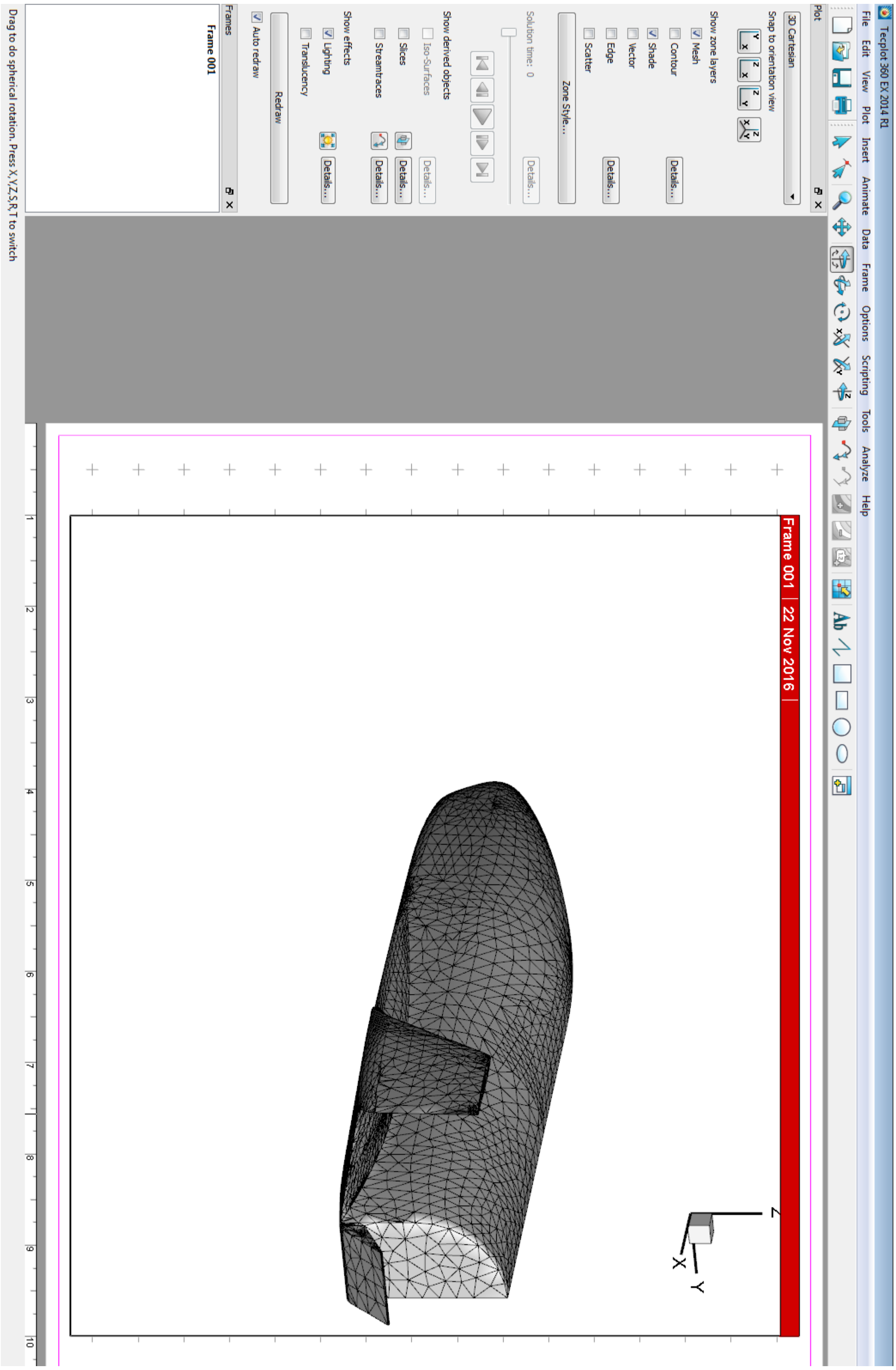

Figure 5.6: Typical output from YAMS.

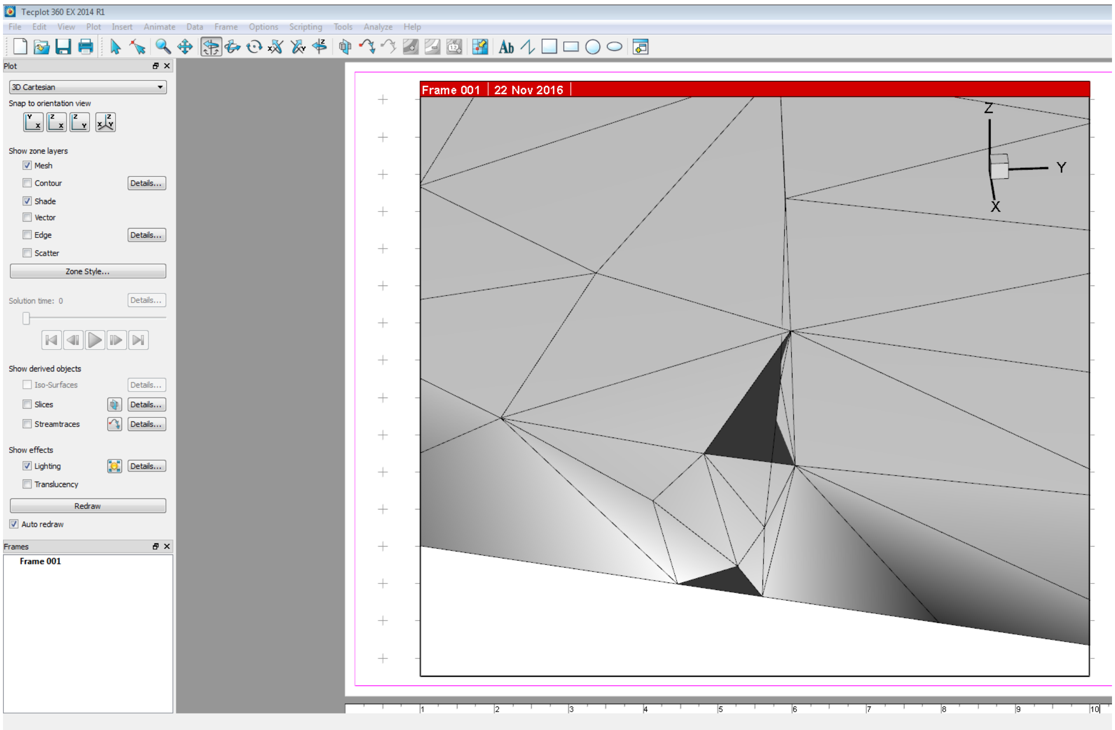

Figure 5.7: Detail of mesh fault in wing leading edge.

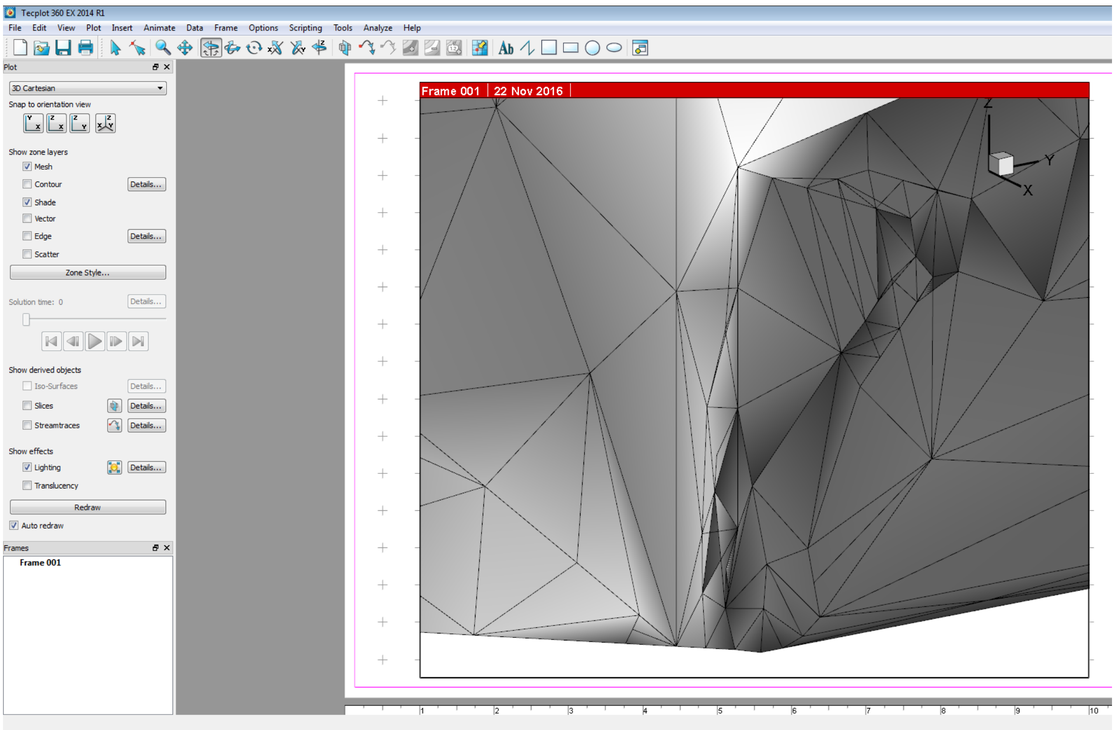

Figure 5.8: Detail of mesh faults at intersection of fuselage with body flap.

length of the vehicle (which is normalized to 1). Three separate substeps create the initial mesh, clean the mesh and smooth the results.

The second stage creates the first Euler solution of the flowfield. In this current version of the software there is no convergence criterion and the number of iterations is set manually. The convergence can be checked by investigating the convergence of the forces to a single value. The Euler solution code is the point where symmetry conditions are taken into account, if the model is set as symmetric, the flow field solution will only be calculated up to the symmetry plane, which reduces the number of calculations required. This is also the point where the Mach number, angle of attack and sideslip angle (if the symmetry condition is off) are taken into account.

The third stage adapts the mesh by moving the nodes, based on the Euler solution of the previous stage. The mesh nodes on the surface of the vehicle and of the far field are excluded from this. The clustering of nodes is based on the local density in the flow field, as higher density regions will need a tighter clustering of nodes to achieve the required resolution.

The fourth stage adds nodes to the mesh where smaller elements are needed. By choosing the lower and upper thresholds for where the changes occur specific areas can be refined, as well as the level of refinement. Care should be taken to not set the level of refinement too large (zoom level of above 1.2) as this might introduces anomalies.

The fifth stage stretches elements in areas where this leads to a better solution. For example, around the shockwave the elements can be stretched in the direction of the shock to capture the shock better. A lower threshold is set to prevent the whole field from being treated. The amount of stretching for supersonic flows can be very high (on the order of 100-1000x), while for subsonic flows it will be relatively modest. The stretch value that the Euler simulation asks for is the square of the actual required stretching, so a stretching factor of 100 should be input as $100^2 = 10,000$.

The sixth stage creates new mesh based on all the changes in the previous stages. Then the values of the parameters on the new mesh are determined by interpolating them from the old mesh. Using this new mesh, a new Euler solution can be obtained. If further refinement of the mesh is necessary, stage 3-6 can be repeated.

To represent shocks in an Euler solution there are two main methods: shock fitting and shock capturing. The first method calculates the flow field between the body and the shockwave from an initial dataline near the nose of the body. In order to do this however, the shape of the shockwave needs to be known or estimated a priori. This is fine for regular bodies with sharp noses, but not as effective for more complex bodies with multiple shocks and blunt noses.

The alternative method is shock capturing. This method calculates the much larger flow field around the body with the free-stream conditions as boundary condition. In principle the shock waves emerge naturally from these equations. However, because the equations cannot deal very well with discontinuities, the shocks will be smeared out over a number of nodes. Because of the larger flowfield that needs to be calculated, the computing requirements are also higher. Finally, the shock capturing method requires that the conservative form of the governing equations are used. Because the equations have already been written in Eulerian form (as opposed to the Langragian form).

The Euler code used for this research is based on the shock capturing moment, with as adaptive algorithm for the mesh to correctly size the elements to capture the shock. The chapter on validation also includes a section on the pressure calculated by the Euler simulation, to validate the correctness of the shock capturing.

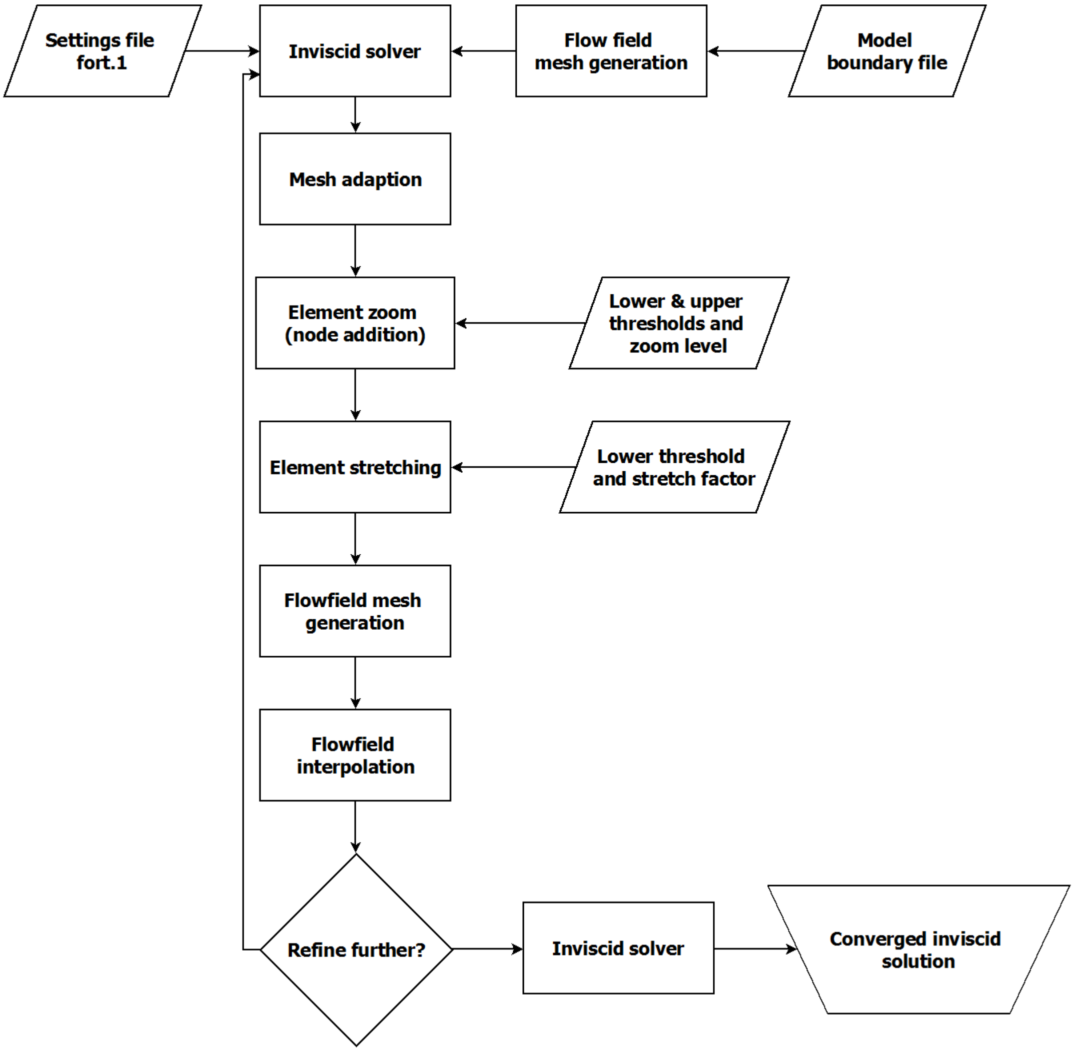

Figure 5.9: Flow diagram of the inviscid flow software.

5.4. BOUNDARY LAYER SIMULATION

The boundary layer is simulated using a method similar to the method described by [Hamilton *et al.*, 2009], though it will deviate from that method in certain regards. There are 5 phases in the simulation: the initialization, the epsilon curve determination, the backtracing, the forward propagation and the result aggregation. A flow diagram of the software can be found in Figure 5.10. The modules in the figure will be discussed below..

INITIALIZATION

The purpose of the initialization phase is to prepare all the data for the simulation. This means that all the mesh data from the Euler simulation is read from file, as are simulation parameters. From this data input derived parameters are calculated, such as plane equation coefficients, connections between elements, Hamilton element interpolation coefficients and derived parameters are calculated. The surface grid used in the Euler code is loaded with all the parameters at the nodes. This means that the position of each node is known, as well as the velocities, Mach number, density and

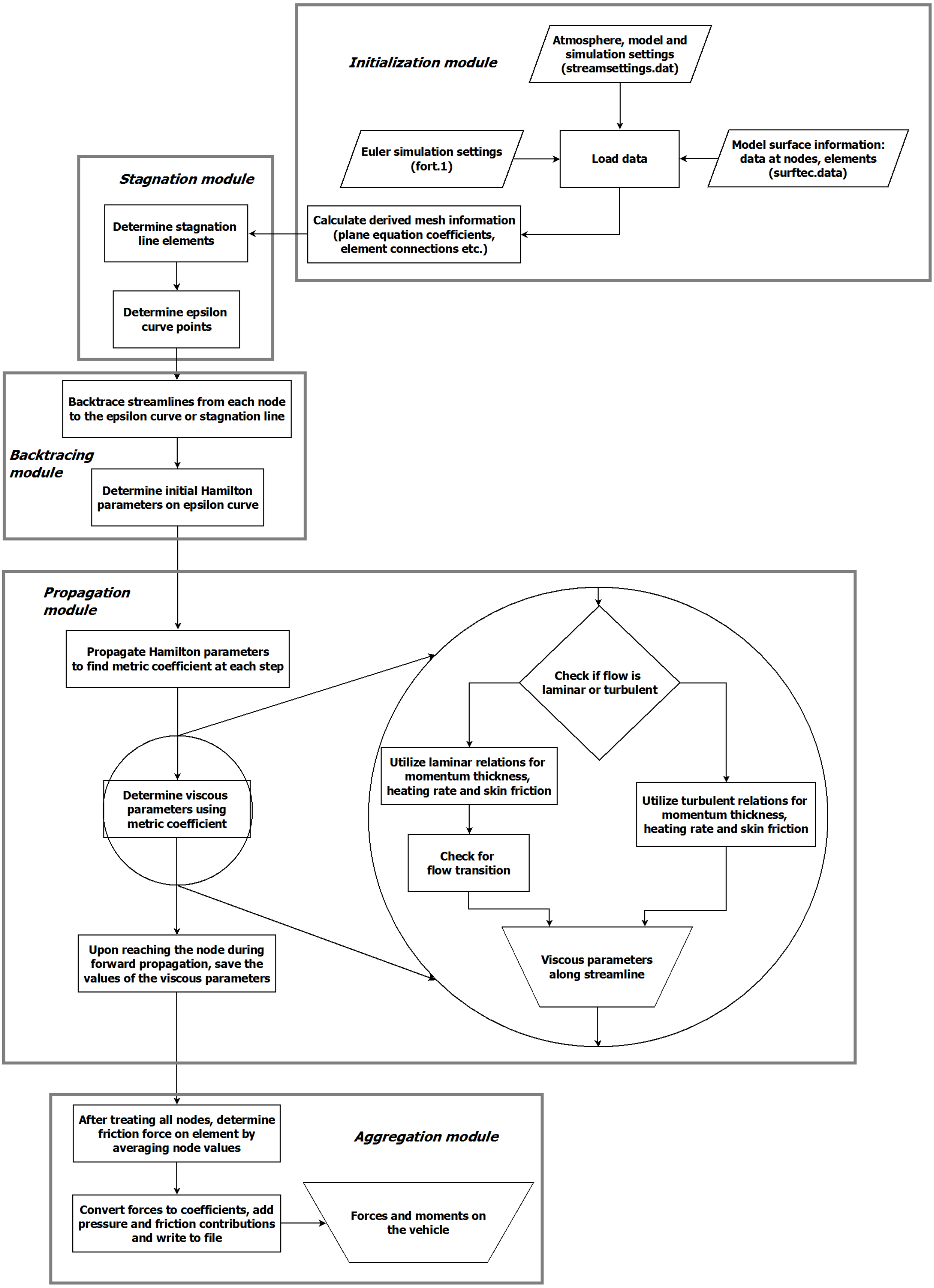

Figure 5.10: Flow diagram of streamline code.

pressure at each node. Because all the parameters in the surface grid are expressed as dimensionless variables there is need for a conversion. The coordinates also need to be transformed as the coordinates in the Euler simulation are scaled by the length, i.e. the maximum x-coordinate in the output is 1. The equations are given below:

$$x = x_{Euler} L \tag{5.1}$$
$$u = \frac{\frac{u_{Euler} V_\infty}{M_\infty}}{\sqrt{\gamma - 1}} \tag{5.2}$$
$$\rho = \rho_{Euler} \rho_\infty \tag{5.3}$$
$$p = p_\infty + 0.5 \rho_\infty V_\infty^2 p_{Euler} \tag{5.4}$$

EPSILON CURVE AND STAGNATION LINE

In the second phase the shape of the epsilon curve and its parameters are determined. Because the epsilon curve is centered around the stagnation point (i.e. point with highest pressure), this stagnation point needs to be determined first. Because an approximate location of the stagnation point is sufficient, the simulation loops through all the nodes to find the one with the highest pressure, without using interpolation. With the stagnation point known the initial point of the epsilon curve is placed on the grid at a distance of ϵ from the stagnation point, which is user-defined. It is recommend to choose a value for ϵ as small as possible without the curve creation crashing, though user trial & error is needed for this. From the initial point the subsequent points are determined by propagating perpendicular to the local velocity vector. As the local velocity vectors all point outward from the stagnation point, the curve will approximate a circle on a spherical nose. The propagation is done in both directions to obtain the complete curve and stops when the edge of the grid is reached (symmetrical half model) or when it has covered ±180 degrees (full model).

The stagnation line can be determined using the methods outlined in Section 4.8. Because the results are not always clean regarding a continuous line and ghost points, a few tricks are used. First of all, a lower limit is set on the eigenvalues for an element to be regarded as part of the stagnation line. The line itself is also not determined, but the elements that make up the stagnation line are. As soon as a streamline enters an element that is part of the stagnation line, that streamline is considered as originating from the stagnation line at that element.

BACKTRACING STREAMLINES

The third phase is the backtracing phase. Starting from each node the streamlines are traced back in time. In theory the backtracing should always end at the epsilon curve around the stagnation point or at a stagnation line. However, in cases of numerical inaccuracies or vortices on the leeward side of an object these backtraced streamlines may not reach these stagnation point or line, or it takes a very long time. Therefore the backtracing is also stopped when a streamline 'falls' of the object or after a maximum number of simulation steps.

One of the main challenges of the backtracing is how to ensure the streamline is properly propagated over the surface. This is challenging because it involves dealing with

One issue arises when a part of the model is convex and the propagation vector falls in the so-called deadzone. This is the zone above two convex elements in which the projection of a point on one of the two elements will always lie outside the element. This is because there is a projection deadzone (dashed area in refim:Deadzone) in which no matter which plane is chosen, the perpendicular projection always crosses the border. The solution (if the smallest angle between the planes is greater than 90°) is to use a double projection, as illustrated in Figure 5.12. Essentially, the first projection step projects the point to an area outside the deadzone. By detecting whether the projection falls inside or outside the intended element it can be determined whether a double projection is necessary.

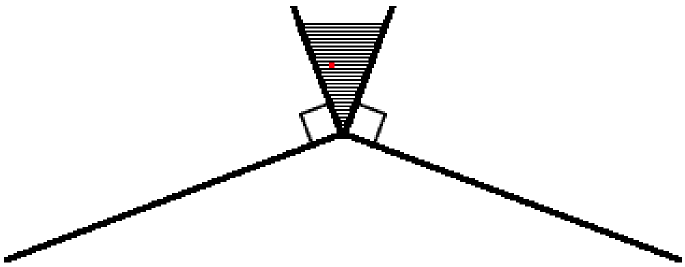

Figure 5.11: Projection deadzone for convex elements.

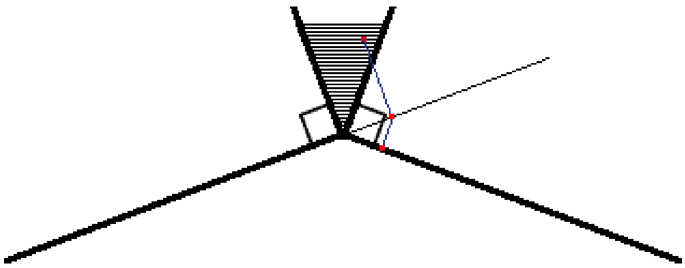

Figure 5.12: Double projection from deadzone for convex elements.

Another issue occurs at the starting/ending node for each streamline. Because the node is part of multiple elements, the element on which there should be propagated and projected is not known. To determine this element the following procedure is followed.

1. Determine the elements that the node is part of.

2. Determine shortest distance in element, which is the perpendicular distance between the node and the opposite side. Create a vector in the direction of the velocity vector with a length less than the minimum element distance.

3. Check whether the projected end point of the created vector falls within one of the elements.

4. If this is the case, determine whether there are multiple possible elements in which the projected point falls (can happen for concave surfaces). If this is the case, use the one with the shortest distance between the vector end point and the projected point.

5. If no element has been found, use the element to which the projected point is closest. Once this element has been found, propagate a minor step into the element and restart the propagation from there.

FORWARD PROPAGATION

There are two options in the simulation for the determination of the metric coefficient using Hamilton's of Parhizkar's method. After the metric coefficient has been determined by one of these methods, the local values of the momentum thickness, heating rate and skin friction are determined.

Hamilton

The method of Hamilton integrates the metric coefficient along a streamline, as was discussed in Section 4.7. In the numerical implementation the following steps are taken.

1. Calculate the initial Hamilton parameters such as h and $w\left(\frac{\partial}{\partial\beta}\right)$ for the streamlines originating from the ϵ-curve, see Section 4.7 for the equations.

2. For each streamline originating from the stagnation point/ϵ-curve, step forward through the previously determined streamline. Determine the velocity derivatives in all directions. This is done by keeping one variable constant and then following the elements until the required distance from the original point is reached. The velocity at the stepped point is determined and the derivative can be calculated as a difference equation, see Equation 5.5 for an example.

$$\left(\frac{du}{dx}\right)_y = \frac{u(x_{step,y}) - u(x_{original,y})}{x_{step,y} - x_{original,y}} \tag{5.5}$$

3. At each step the metric coefficient is updated using the equations shown in Section 4.7, for which the aforementioned velocity derivatives are necessary. For each streamline originating from a stagnation line, set the metric coefficient to 1.

Parhizkar

The method of Parhizkar determines the metric coefficient by calculating the perpendicular distance between two adjacent streamlines. This is implemented in the following way:

1. Pick subsequent point on streamline in forward propagation direction. The point coordinates are taken from the backtrace results, to make sure that the forward propagation would not result in a slightly different streamline compare to the backtrace. Save the streamwise distance of the point from the epsilon curve.

2. Take the adjacent streamline and cycle trough the points until the streamwise distance matches or is greater than the streamwise distance of the point on the original streamline. If the streamwise distance of the adjacent point is greater than the original point, interpolate to find the coordinates where the streamwise distances match.

3. Calculate the distance between the two points (indicated by $h_\beta d_\beta$). The left side of this factor (h_β) is the metric coefficient between two points on adjacent streamlines that are equidistant from the origin (ϵ-curve or stagnation line). The right side of this factor (d_β) is the derivative perpendicular streamline coordinate, which is constant along a streamline. Following that, determine the angle between the original streamline and the vector connecting the same-distance points on both streamlines. Then, use the equation from [Parhizkar & Karimian, 2009] to determine hd_β, which is used in determining the momentum thickness. In this factor h is the metric coefficient between two point on adjacent streamlines of which the vector between the two points is perpendicular to the main streamline.

Common

After the metric coefficient has been calculated, the steps are the same for both methods. These steps are:

1. Pick subsequent point on streamline in forward propagation direction. The point coordinates are taken from the backtrace results, to make sure that the forward propagation would not result in a slightly different streamline compare to the backtrace. Save the streamwise distance of the point from the epsilon curve.

2. If the transition condition has not been reached yet, the momentum thickness is calculated with the laminar boundary layer equations for the momentum thickness mentioned in [Zoby *et al.* , 1981].

3. If the flow is still laminar, check whether the transition condition has been reached. This condition can be specified in different ways. If the internal code is used, the method of [Wazzan *et al.* , 1981b] is used which compares the Reynolds number at that location to the local transition Reynolds number. The transition Reynolds number can also be specified in the settings file. In both cases, if the boundary layer Reynolds number exceeds the transition Reynolds number, the transition condition is set to true.

4. If the transition condition is true, the boundary layer momentum thickness is calculated using the turbulent boundary layer momentum thickness equations in [Zoby *et al.* , 1981]. For the calculation the parameter N needs to be determined, which is dependent on Re_θ. As Re_θ is dependent on the momentum thickness, which in turn depends on N, iteration is needed to determine N. [Zoby *et al.* , 1981] gives a curve fit for N, but because it is based on axisymmetric nozzle-wall data it is not valid for the simulation. Instead, the tabulation of [Hamilton *et al.* , 2009] is used, together with a curve-fit for the upper range and a floor of $N = 4$ for the lower range. The iteration procedure is considered complete if the momentum thickness Reynolds number does not vary significantly anymore.

5. In either of the cases of laminar or turbulent flow, the heat-transfer rate $\dot{q}_w$ is calculated using the previously obtained momentum thickness. The wall temperature is the other big factor influencing the heat-transfer rate besides the momentum thickness.

6. Using different methods, the skin friction is calculated from the momentum thickness, heat-transfer rate or local Reynolds number.

7. The process is repeated until the simulation is back at the node from which the backtracing began. Here, the value of the skin friction is recorded. This is the local skin friction at that particular node.

RESULT AGGREGATION AND COEFFICIENT CALCULATION

The final phase is the result aggregation phase. The goal of this phase is to combine the obtained results and transform them into the required coefficients. First, the contribution of the inviscid drag needs to determined. The Euler simulation force and moment results need to be converted to their corresponding coefficients, see Equations 5.6 through 5.8.

$$C_X = \frac{10 C_{X,Euler} L_{ref}^2}{S_{ref} M^2} \tag{5.6}$$

$$C_Z = \frac{10 C_{Z,Euler} L_{ref}^2}{S_{ref} M^2} \tag{5.7}$$

$$C_m = \frac{10 C_{m,Euler} L_{ref}^2}{S_{ref} M^2} \tag{5.8}$$

where $C_{X,Euler}$, $C_{Z,Euler}$ and $C_{m,Euler}$ are the outputs from the Euler simulation. With the inviscid coefficients known for the forces and moments of interest, the contributions of the skin friction need to be determined. Skin friction occurs because of a velocity difference between the surface of the vehicle and the flow outside the boundary layer, thus the direction of the skin friction is in the direction of the local velocity vector. Multiplying the skin friction value by normalized velocity components given the skin friction in the direction components. As the friction force depends on the area over which it acts, the values at the nodes of an element are averaged, after which this average is used for the whole area of the element. At this point the moment contribution of the skin friction of each element is also determined by multiplying the force components by the distances to the center of mass.

The friction symmetric coefficients are calculated using Equation

$$C_{X_f} = \frac{F_X}{\frac{1}{2}\rho V^2 S_{ref}} \tag{5.9}$$

$$C_{Z_f} = \frac{F_Z}{\frac{1}{2}\rho V^2 S_{ref}} \tag{5.10}$$

$$C_{m_f} = \frac{M_Y}{\frac{1}{2}\rho V^2 c_{ref}} \tag{5.11}$$

Note that all these coefficients are still in the vehicle reference frame with the origin at the center of mass, which is the same reference frame used by [Mooij, 1995].

5.5. RESULT GENERATION

To be able to make an assessment of the performance and longitudinal of the vehicle, the simulation needs to determine the relevant coefficients such as the moment coefficient, lift coefficient C_L and drag coefficient C_D. A MATLAB script is used for these calculations.

The first step is to load the data about the forces and moments. This output is given by the streamline code. The results for each particular Mach number are copied in a file called stability-mat.dat, which is ordered for angle of attack, sideslip angle and control angles. After loading the data, the forces need to be transformed to the aerodynamic reference frame. Because of the different conventions used, the side force and moment around Y-axis need to be reversed in direction, i.e., the sign changes.

The next step is to determine the force and moment derivatives. Because of the assumed linearity of the reponse, this is done by dividing the difference in force/moment by the difference in angle of attack/sideslip angle. With these derivatives the coefficients for the stability matrix are calculated. From this matrix the eigenvalues can be determined, which in turn lead to the period, half-time, natural frequency and damping ratio.

The final part is a sensitivity analysis. This is done using a Monte Carlo simulation using the difference in values from the simulations and the reference data. For each stability derivative a random value is chosen that lies between the simulation value and reference value. The period, half-time, natural frequency and damping ratio of each iteration is calculated and the results are aggregated in a histogram.

5.6. SIMULATION PLAN

In order to obtain insight in the stability and control of the HORUS vehicle, a range of simulations under different conditions is necessary. First it is important to define the goals of the simulation, from this the simulation plan flows naturally.

- Results in the subsonic, transonic and supersonic regimes. Where possible, Mach numbers equal to those in [Mooij, 1995] were chosen to verify results and increase confidence in the outcomes. The choice for the supersonic Mach number was 2, as this Mach number is tabulated in the reference and it is inside of the TAEM of the Space Shuttle Orbiter. For transonic flight, a Mach number of 1.2 was chosen, again because of the tabulation in [Mooij, 1995].

While this Mach number is on the high end of the transonic regime, this choice allows comparison to earlier obtained. The choice for the subsonic Mach number is 0.7, which was chosen to be below the critical Mach number (where local supersonic flow can occur) and above the lowest Mach number for which the Euler simulation is reliable ($M = 0.6$) while simultaneously being in reference [Cucinelii & Müller, 1988].

- A single, reasonable reference angles of attack with a deviation above and below. To keep the scope of the thesis limited a single reference state will be used from which deviations will be calculated. The deviation was picked as ±5° to make sure the differences can be clearly identified while the behaviour is still linear. The reference angle of attack was set at 10°, based on two arguments. The first is based on Figure 5.13, which shows the re-entry profile of the Space Shuttle Orbiter. The data in the figure indicates that for the part of the flight below approximately 30 km the angle of attack is between 5° and 15°. As the SSO has flown actual mission this is a reasonable range to pick the reference angle of attack from. The second reason follows from Figures 5.14 and 5.15 which show the elevon trim deflection for a range of angles of attack and Mach numbers. For a Mach number of 1.2, Figure 5.15 shows a flat line above an angle of attack of 15°, indicating that the combination of the maximum elevon deflection with the standard body flap deflection does not result in equilibrium. To investigate the effect of a disturbance in angle of attack, a change of ±5° is used to be able to discern significant effects. This leads to a reference angle of attack of 10° to ensure these disturbances can be simulated.

- A single reference sideslip angle with one deviation. The reference sideslip angle was set to zero degrees, because this is the reference state in symmetric flight. The deviation was set at 2° sideslip as this is approximately the maximum deflection in the linear range, a greater deflection will results in non-linear behavior.

- A limited set of control surface deflections for validation. Because of the amount of work required for each different deflection, the rudder and elevon deflections were limited to 0°, 5° and the trimmed deflection obtained from Figures 5.14 and 5.15. These deflections are large enough to create noticeable moment changes while still being reasonable values for the linear response assumption. The body flap deflections were chosen as 0° and -20°, the first being the clean configuration and the second being the control law for Mach numbers below $M = 1$. This same deflection is valid up to a Mach number of 2.

- Variations of the center of mass, altitude and Mach numbers around the reference values to investigate their influence on the stability. The Mach number step is set to 0.05 below the reference Mach number, which is used to incorporate the Mach dependency. For the center of mass location two values are used, one based on the reference length and one based on the full length of the HORUS. This leads to center of mass locations at 61% of the total vehicle length if the length is taken as 23 meter (reference length) and 56% of the total vehicle length if the length is taken as 25 meter (full length). Finally, for the Mach 2 case the effect of an altitude variation is investigated with an altitude step of 1 km below the reference altitude of 20 km.

In Table 5.1 the simulation plan is tabulated. It is based on consideration in the discussion above. As the reference angle of attack was determined to be 10°, the disturbances of ±10° lead to an angle of attack sweep of 5°, 10° and 15°. The sideslip angle sweep is done at the reference angle of attack and includes the sidesweep angles 0° and 2°. Regarding the control surface deflections, for the clean configuration simulation every control surface deflection is set to zero. The other deflection for the body flap is the default deflection during the TAEM (see also [Cucinelii & Müller, 1988]).

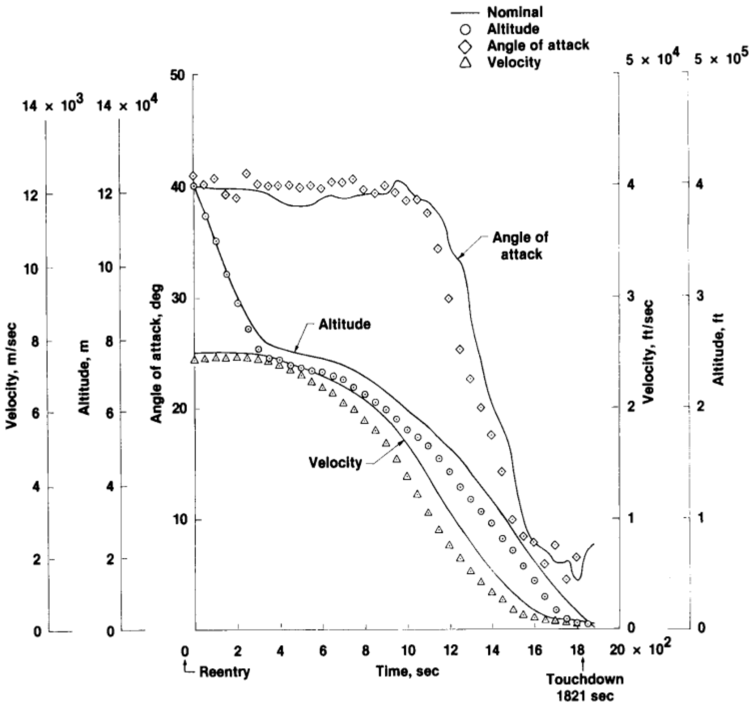

Figure 5.13: Re-entry data of STS-5 [Gong *et al.* , 1984].

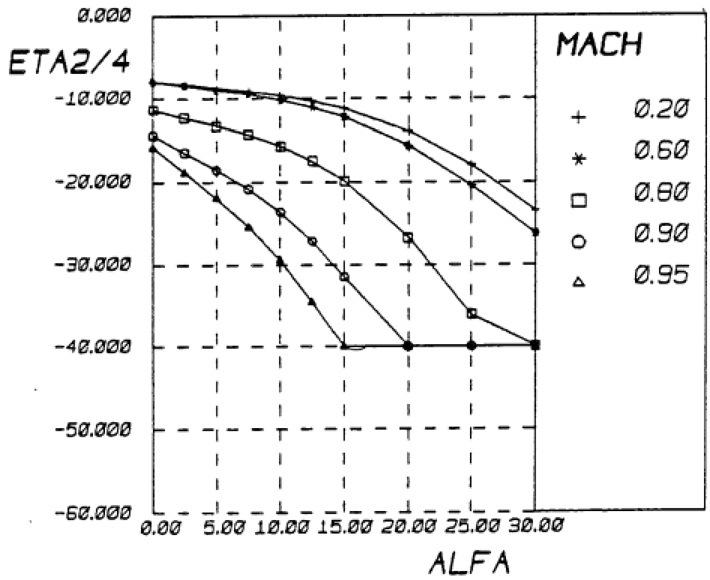

Figure 5.14: Subsonic elevon trim deflection for the HORUS [Cucinelii & Müller, 1988].

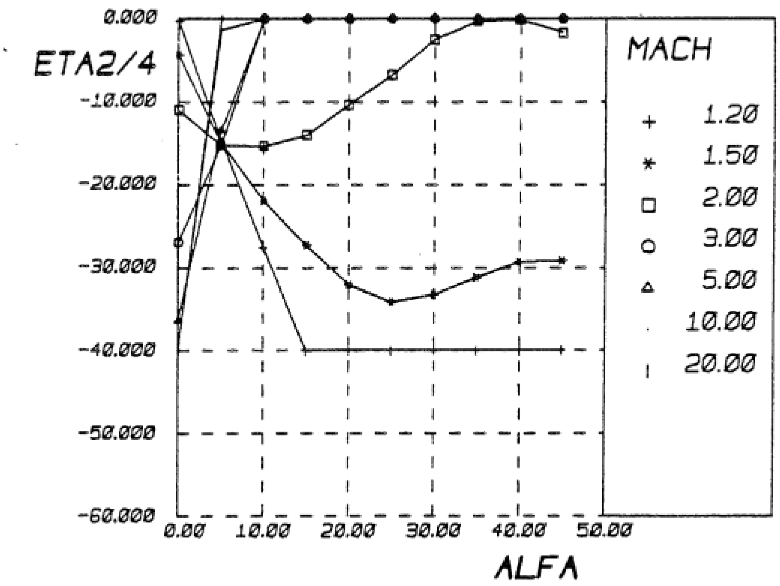

Figure 5.15: Supersonic elevon trim deflection for the HORUS [Cucinelii & Müller, 1988].

Mach number	α [°]	β [°] (at $\alpha = 10°$)	δ_{bf} [°]	δ_e [°]	δ_r [°]
0.8	5, 10, 15	0, 2	0, -20	0, 5, -16	0, 5
1.2	5, 10, 15	0, 2	0, -20	0, 5, -27.5	0, 5
2	5, 10, 15	0, 2	0, -20	0, 5, -16	0, 5

Table 5.1: Simulation plan for HORUS. All deflection are in degrees.

For both the rudder and elevon deflections of 5° are included for the validation of the control coefficients. Finally the last set of elevon deflection were based of the trim conditions for the relevant Mach numbers.

6

VERIFICATION AND VALIDATION

This chapter deals with the verification and validation of the simulation. Besides showing that the code performs as expected, this will also give an indication of the accuracy of the results. This chapter will satisfy the requirements regarding the verification of the modules, the validation against experimental or computational reference cases and validation against reference data for HORUS. The following definitions of verification and validation will be used: Verification is making sure the code performs as expected. Results from the simulation for simple test cases as compared to analytical results. Validation is comparing the outcomes of the simulation to other datasets, preferably from flight or wind tunnel measurements. When these are not available, results from validated simulations will also be accepted.

6.1. VERIFICATION

The first step in proving the correctness of the code is verification. To avoid creating a very large chapter that is filled with trivial verifications, only the most important verification steps will be shown here. The software architecture shown in the previous chapter is leading in the choice of relevant verifications for this report. For the initialization module the interpolation coefficient calculation verification will be treated. For the stagnation module the epsilon curve and stagnation line determination verification will be discussed. For the backtracing module the streamline tracing verification will be shown. For the propagation module the momentum thickness and skin friction is verified.

6.1.1. INITIALIZATION MODULE

INTERPOLATION COEFFICIENTS

As the variables are only calculated on the nodes, for any point between the nodes these variables need to be interpolated. As mentioned in [Hamilton *et al.* , 2009], when dealing with a surface only 2 of the 3 Cartesian coordinates are independent. The relation between the dependent and independent variables is given in Equation (6.1) and the coefficients are different for each element.

$$F(x, y, z) = a_1 y^2 + a_2 y + a_3 z^2 + a_4 z + a_5 x^2 + a_6 x + a_7 = 0 \tag{6.1}$$

To verify the calculation of coefficients one can simply fill in the coefficients and coordinates in Equation (6.1) and check that the answer is zero. An example is given in Table (6.1). The final result is very close to zero, though not actually zero. However, it is small enough to serve as a successful verification step.

Unit	Value
$\mathbf{a}_1$	48.08442
$\mathbf{a}_2$	8.93526
$\mathbf{a}_3$	11.66235
$\mathbf{a}_4$	-6.81634
$\mathbf{a}_5$	30.95546
$\mathbf{a}_6$	-34.10158
$\mathbf{a}_7$	1
x	0.199857
y	-0.374243
z	-0.139978
Outcome	-0.0057112

Table 6.1: Verification of coordinate coefficients

		u	v	w
Node 1	Input	1.87082875	7.48331499	1.87082875
	Interpolation	1.87082911	7.48331499	1.87082887
Node 2	Input	11.2249718	1.87082875	5.61248589
	Interpolation	11.2249718	1.87082863	5.61248589
Node 3	Input	3.74165750	3.74165750	3.74165750
	Interpolation	3.74165773	3.74165750	3.74165750

Table 6.2: Velocity interpolation verification

The velocity interpolation can be verified by checking whether the interpolated velocity on the nodes matches with the actual (input) velocity on those nodes. Table 6.2 shows the input velocity and the interpolated velocity. The interpolated values differ from the input values by less than 0.001%, indicating the velocity is successfully interpolated.

6.1.2. STAGNATION MODULE

STAGNATION LINE

To verify the determination of the stagnation line the simple case of a flat plate is used. For the velocity field the parametric equations shown in Equations (6.2) and (6.3) were used. Figure 6.1 shows the reference for how the velocity field and stagnation line should look. Figure 6.2 shows the simulated velocity field, stagnation line elements (blue dots) and stagnation line (red line). Comparing the figures, the stagnation line is in the exact same location while all the elements that the stagnation line goes through are marked with the blue dots. This shows that the stagnation line software is working correctly.

$$u = x \tag{6.2}$$

$$v = x + y \tag{6.3}$$

EPSILON CURVE

While the ϵ-curve could be created manually, the automated method provides a much quicker simulation process. Therefore, it is important that the automated process creates a good curve. The user can input the value of ϵ, so the method is scalable. In Figure 6.3 an ϵ-curve created by the code is shown, with a larger value for ϵ than usual to make it more visible. The curve is smooth,

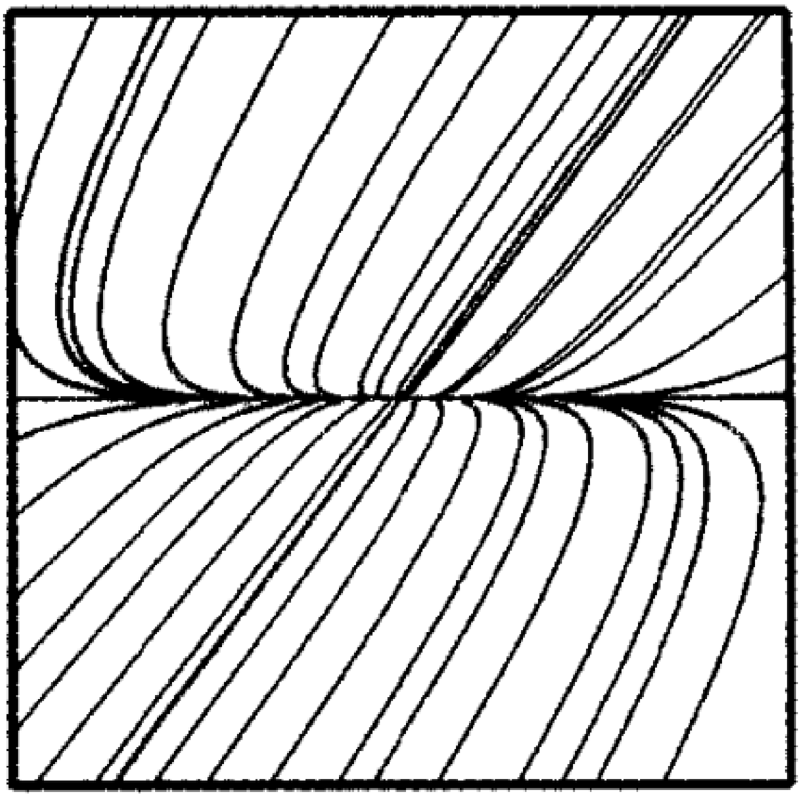

Figure 6.1: Reference flat plate velocity field and stagnation line [Kenwright *et al.* , 1999].

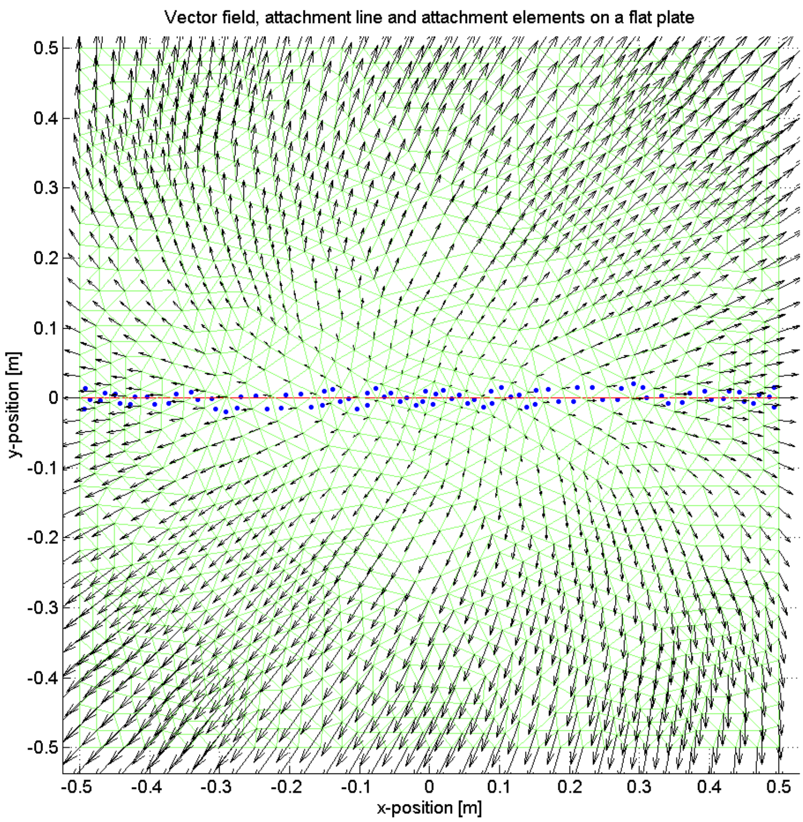

Figure 6.2: Simulated flat plate velocity field and stagnation line.

nearly circular and the streamline correctly originates from the curve (in other words, the backtrace terminates successfully) verifying this module works correctly.

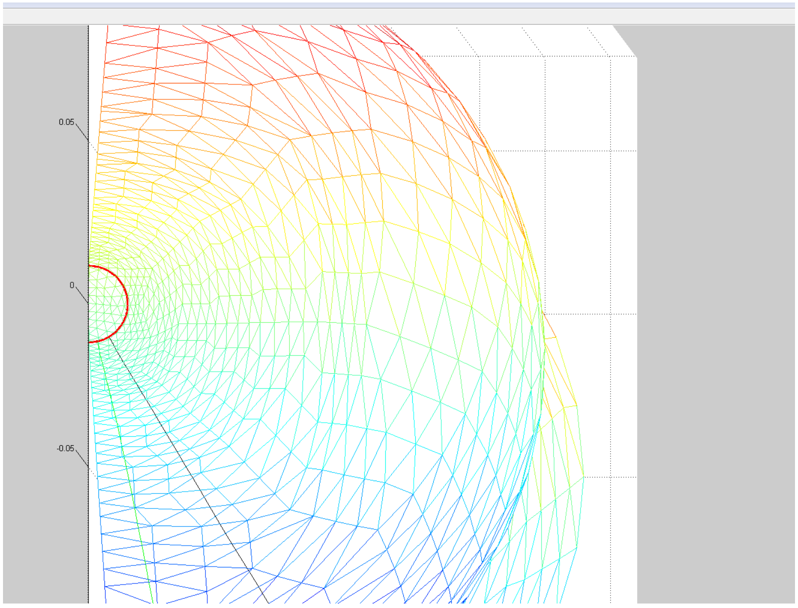

Figure 6.3: ϵ-curve created using the automated method, shell model at M = 1.7.

6.1.3. BACKTRACING MODULE

STREAMLINE

For the streamline verification a flat plate was used with the same velocity as for the verification of the stagnation line. A traced streamline is superimposed on the velocity field, as can be seen in Figure 6.4. The velocity field is the same as the one used for the stagnation line determination, see Equations (6.2) and (6.3).

The streamline should be parallel to the local velocity at each point. Figure 6.4 shows that this is the case. The accuracy of the streamline determination depends on the step size for the streamline tracing and the velocity field. For the current example the difference between the local velocity vector and the streamline direction is below 5%.

The streamlines for a more complex model are shown in 6.5. On the left side of Figure 6.5 is a figure given by [Hamilton *et al.* , 2009], showing the heating and streamlines on the spherecone model. On the right side of the figure is a plot of the streamlines on the simulated model. Because there is no streamline data in tabulated or graph form in the reference, a numerical assessment of the accuracy is not possible, though the accuracy should be better because of the small step size used for streamlines in the TECPlot software. This leaves visual comparison as the only available option. The same starting point and curvature can be observed for the reference case and the simulated case, which verifies the three-dimensional streamline tracing.

6.1.4. PROPAGATION MODULE

MOMENTUM THICKNESS VERIFICATION

Both the laminar momentum thickness and turbulent momentum thickness need to be verified. For both cases a flat plate is used as the test case. Table 6.4 gives the settings used for this case. The reason that the settings are different for the laminar and turbulent case is because the turbulent momentum thickness code is only accurate for momentum thickness Reynolds numbers (Re_θ) above 10^4. This will also become apparent in the results.

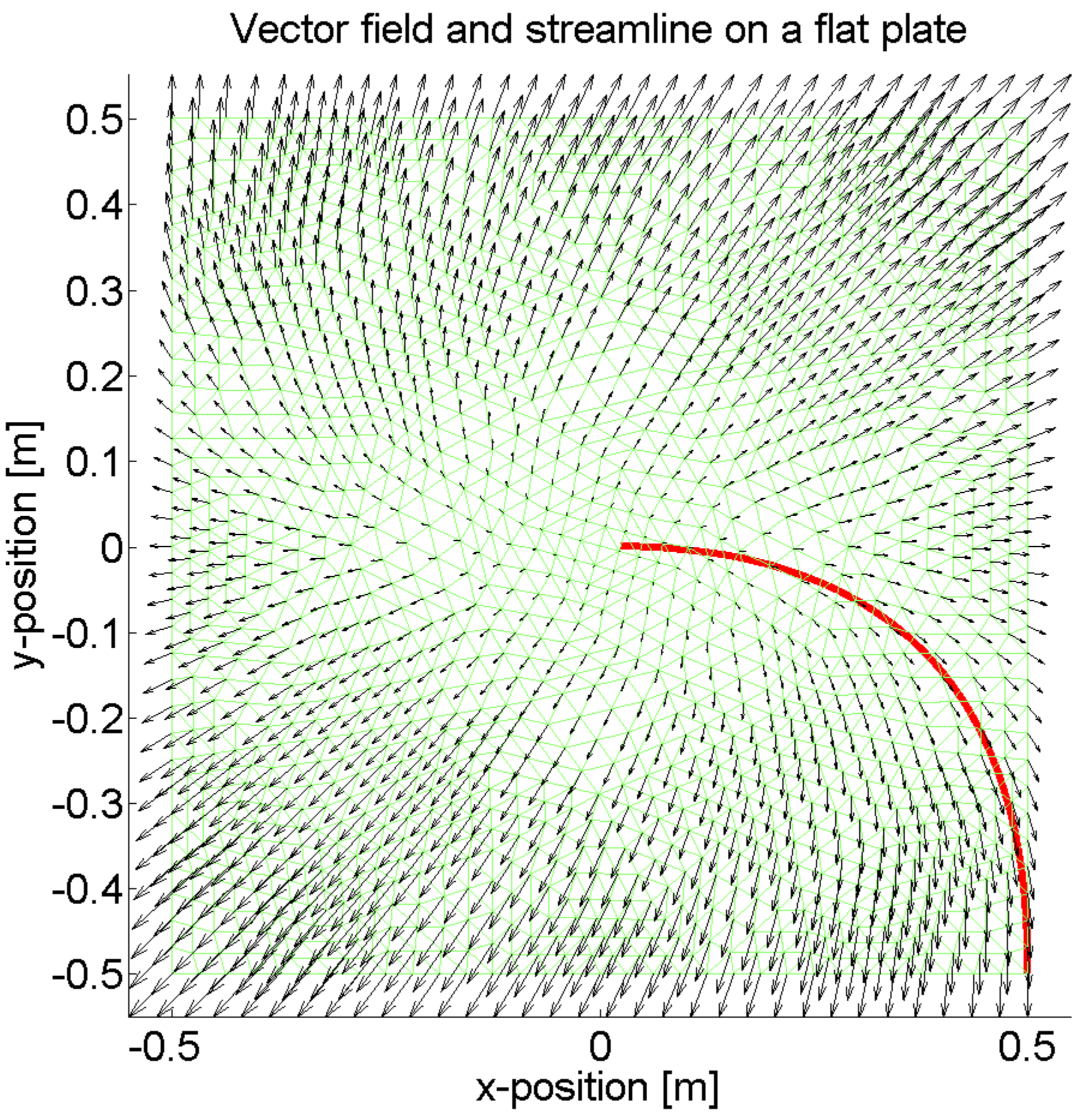

Figure 6.4: Simulated flat plate velocity field and streamline.

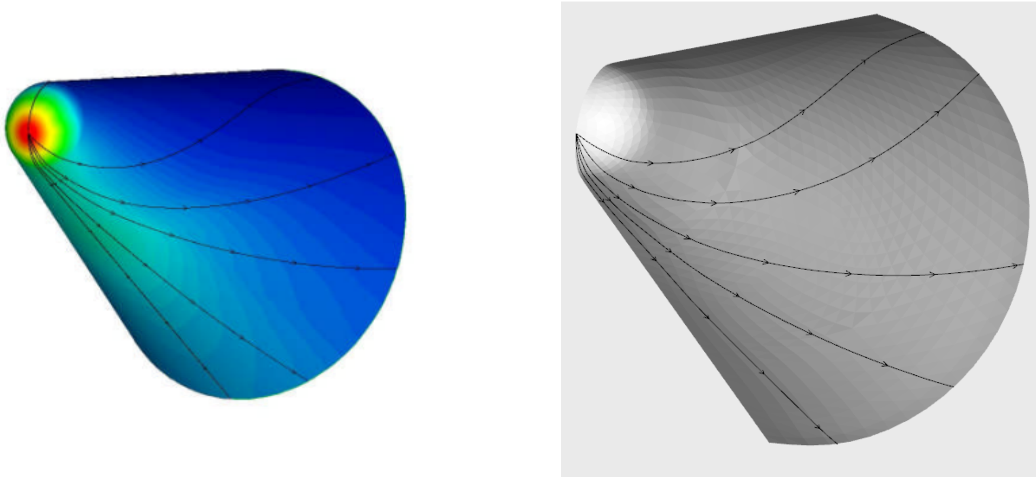

Figure 6.5: Visualization of the streamlines determined using TECPLOT from the data of the Euler simulation.

Figure 6.6 shows the laminar momentum thickness calculated using the code and calculated using the Blasius solution. As the method in the code is a modified Blasius method the results should be very close. The figure confirms this, showing that the reference data coincides with the simulated data at every location.

Figure 6.7 shows the turbulent momentum thickness calculated using the code and calculated using an engineering approximation for a turbulent Blasius solution. The approximation is from [Cimbala & Cengel, 2012] and the formula can be found in Equation (6.4).

$$\theta = \frac{0.037x}{Re_x^{1/5}} \tag{6.4}$$

The method in the simulation is a modified form of the Blasius equation for turbulent flow with coefficients that change depending on the local momentum thickness Reynolds number. This method is not mathematically equal to Equation (6.4) as the latter uses constant coefficients and is not related to the momentum thickness. Both methods should therefore not be expected to yield the exact same results. What is being verified in Figure 6.7 is whether the results are similar. The similarity is very clear in the first 30% of the plate length where the momentum thickness for both methods is almost equal, deviating at most by 5%. After 30% of the length the difference grows larger until the value obtained using Equation (6.4) is 30% higher than the value obtained from the simulation (i.e. Blasius with varying coefficients). While the match is not as good as hoped, it does at least verify the general shape of the solution as well as the range of values that can be expected. The real accuracy of the momentum thickness calculation will be determined in the validation section.

	Laminar	**Turbulent**
Mach number	1	10
p	1 Pa	100000 Pa
ρ	1 kg/m^3	0.1 kg/m^3
T_∞	1 K	287 K
T_w	1 K	287 K

Table 6.3: Simulation settings for the flat plate cases

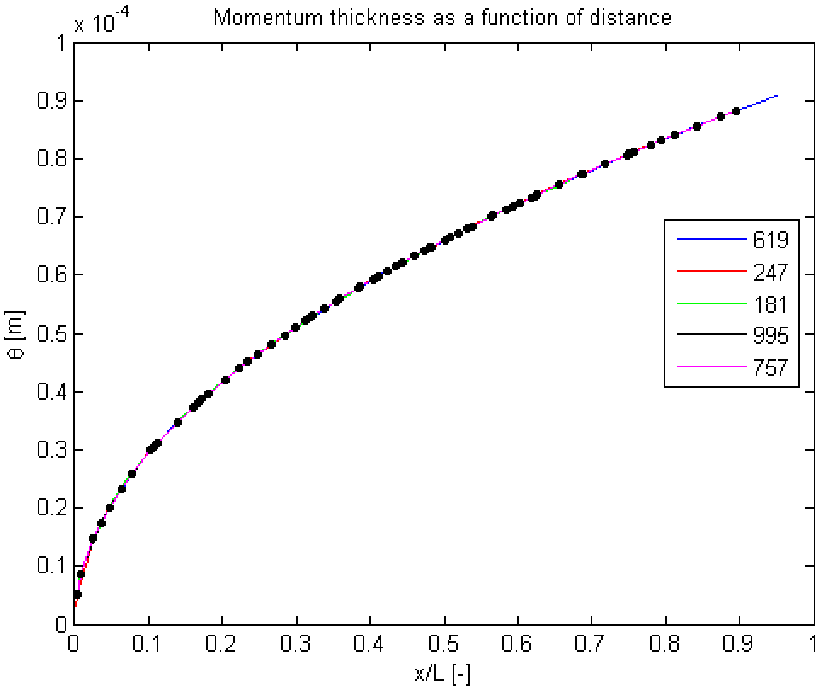

Figure 6.6: Laminar momentum thickness verification of simulation against Blasius value.

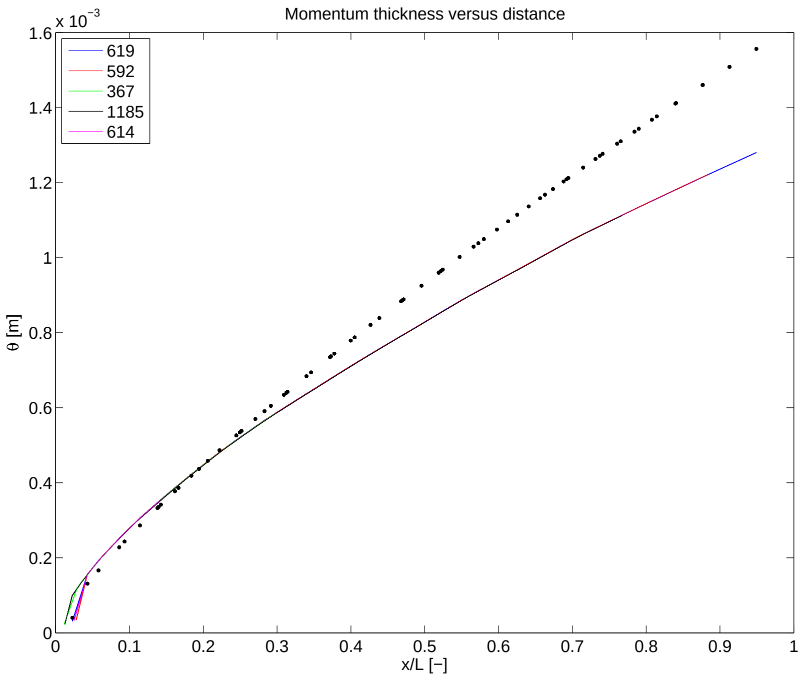

Figure 6.7: Turbulent momentum thickness verification of simulation against Blasius Engineering value.

SKIN FRICTION

The last verification that needs to be performed are the skin friction results. For the laminar skin friction, shown in Figure 6.8, the Blasius flat plate equation is used for both curves. The difference between the curves can be explained by the use of Eckert reference variables for compressible flow for the simulated curve, while the non-Eckert variables are used for the reference case. The difference is minor (less than 10% at maximum) and the shape is perfectly captured, which verifies the laminar skin friction results.

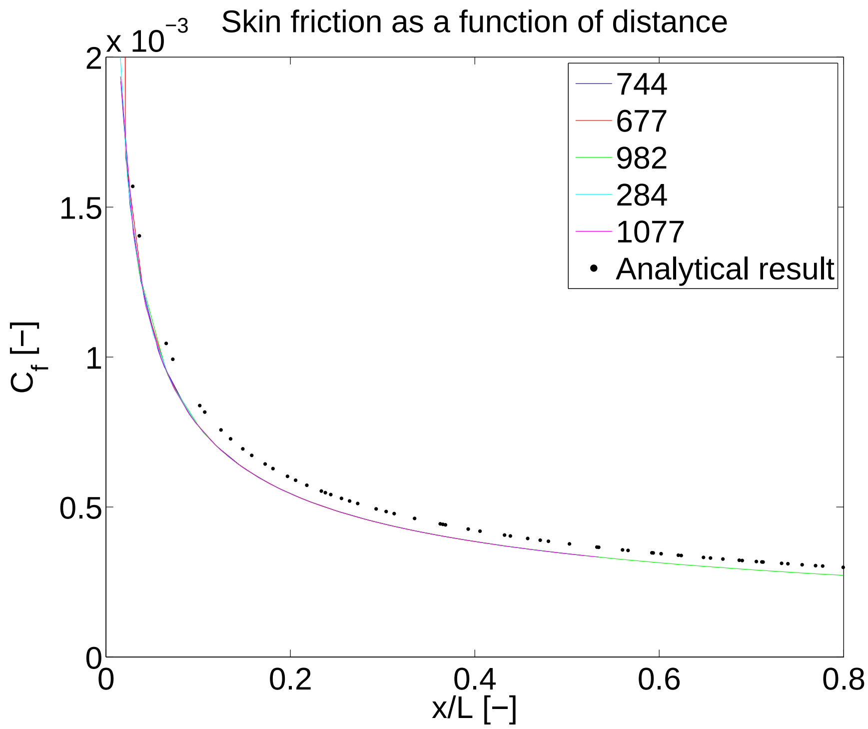

Figure 6.8: Laminar momentum thickness verification of simulation against Blasius value. The colored lines are different streamline results from the simulation while the dots are the values calculated by the simple Blasius equation for skin friction.

For the turbulent skin friction verification again used will be made of an engineering approximation from [Cimbala & Cengel, 2012], which is shown in Equation (6.5). The shape of the curve is very similar for both cases, though the analytical result is consistently 30% lower than the simulated result. The methods used for the analytical result and simulation are not mathematically equal (again constant coefficients versus variable coefficients) so there is also no expectation that the results are exactly the same. The real accuracy of the skin friction calculation will be determined in the validation section.

$$C_{f,x} = \frac{0.059}{Re_x^{1/5}} \tag{6.5}$$

6.2. VALIDATION

6.2.1. RATIONALE

It is important to define what parameters and calculations need to be checked for the validation process. The validation steps will be discussed now.

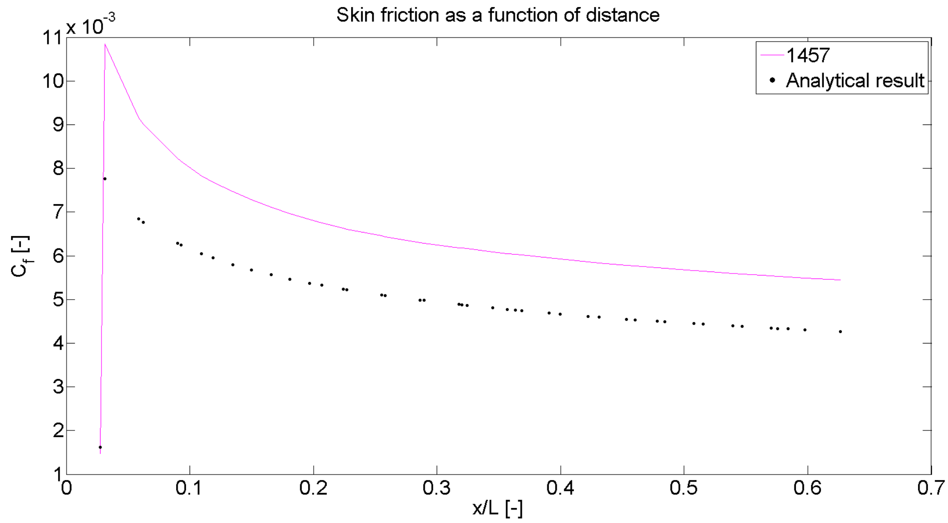

Figure 6.9: Laminar momentum thickness verification of simulation against Blasius Engineering value. The pink curve is the streamline result from the simulation while the dots are the values calculated by the Blasius approximation for skin friction.

The most important cases that need to be validated are: subsonic and supersonic flow & laminar and turbulent boundary layers. The variables that need to be validated are the pressure coefficient distribution, momentum thickness, heat flux and skin friction. However, due to interdependencies they do not need to be checked for all the cases.

The first step is to verify the outcome of the inviscid Euler simulation. The simplest way to do this is through the pressure coefficient distribution. The momentum thickness will be validated for both subsonic and supersonic flow. Regarding the use of a laminar or turbulent boundary the choices made in the reference cases will be used, as described in each subsection. As the skin friction reference data is from the same sources as the momentum thickness reference data this use of a laminar, turbulent or mixed boundary layer will again depend on the specific cases. The transition point from laminar flow to turbulent flow will also need to be validated, as this will influence the friction distribution on the vehicle. Finally, the calculated coefficient and eigenvalues will be validated against reference data from [Cucinelii & Müller, 1988] and [Mooij, 1997].

6.2.2. EULER CODE VALIDATION

The Euler code was supplied by Rafael Molina from ESA [Molina, 2014] and has been verified and validated by the author. However, it is still important to perform an acceptance test for the flow regimes of interest in this research.

The test case will be a test series in which roughened sphere-ellipsoid bodies were tested in a wind tunnel at Mach 3 [Deveikis & Walker, 1961]. This test case was chosen because it was performed at a Mach number that is in the relevant range for this thesis (high side of the supersonic regime) and because the experimental pressure data is readily available. Because a parametric equation for the complete length of the model is not given in the paper and the mentioned reference in the paper could not be retrieved, only the spheroid nose was modeled. This means that the results should only be compared for that section of the model. The general outline of the model is shown in Figure 6.10.

The primary acceptance test is done using pressure data. For the supersonic case the paper by [Deveikis & Walker, 1961] gives the pressure ratio of the local pressure versus the stagnation pressure of a Mach number of 3. The reference data is shown as circles in Figure 6.11. The blue line is the result from the simulation. The figure shows that the simulated pressure ratio in general matches well

	Laminar
Mach number	3.0
Reynolds number	$4.25 \cdot 10^6$
Stagnation temperature	616.5 K

Table 6.4: Simulation settings for the sphere at Mach 3, from [Deveikis & Walker, 1961].

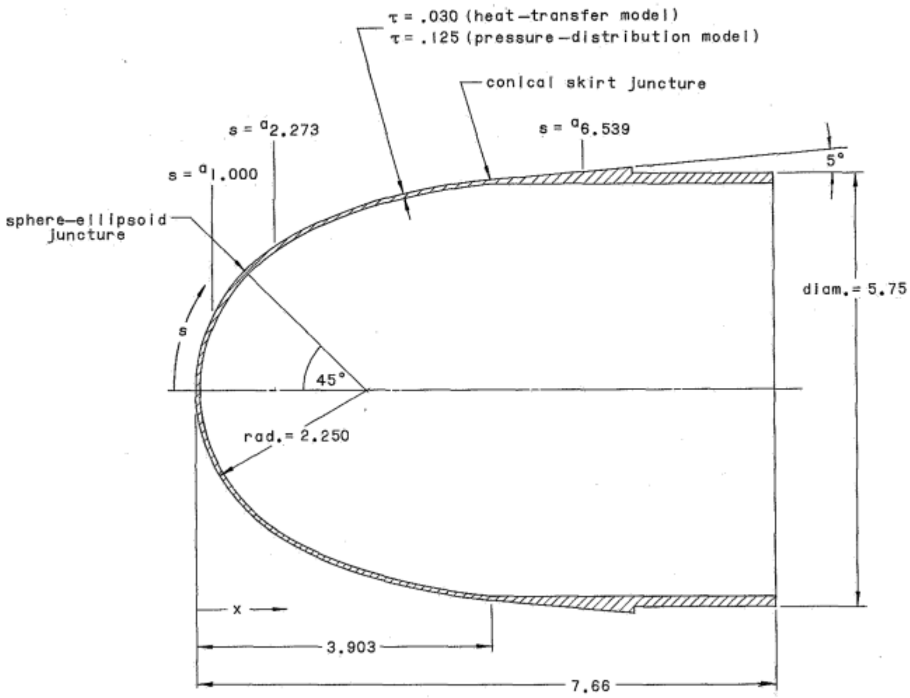

Figure 6.10: Model used in the wind tunnel test [Deveikis & Walker, 1961].

with the measured pressure ratio. At the stagnation point the pressure is slightly overestimated by approximately 2 %. At the measuring station at a surface distance of 40% of the model the pressure ratio is underestimated by about 5%. These results are good as the simulated and measured model are not exactly the same (the difference in shape beyond $\frac{s}{D} = 0.5$ will have some influence on the pressure ratio in compared range) and the pressure ratio at the stagnation point is assumed to be 1 for the simulation.

To verify the actual pressure, the stagnation point pressure from the simulation is compared to the theoretical stagnation pressure using the normal shock wave and isentropic equations. The simulation gives a stagnation point pressure of 460,185 Pa, while the analytical result is 463,303 Pa in the stagnation point. The difference is less than 1%, validating the stagnation point pressure.

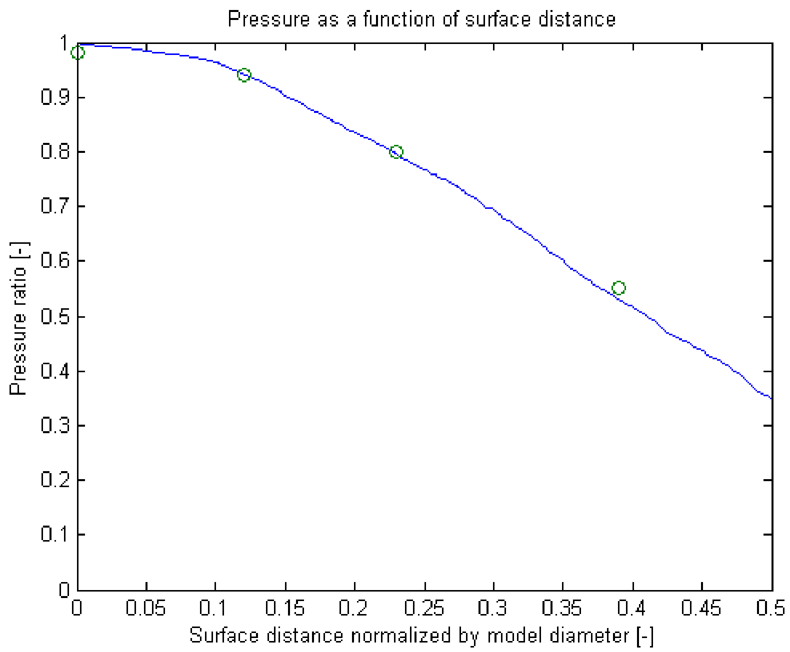

Figure 6.11: Pressure ratio as a function of the streamwise distance. The reference data is from [Deveikis & Walker, 1961].

For lower Mach numbers data from [Lam & Pollock, 1989] can be used for the acceptance test. Figure 6.12 shows the pressure coefficient as a function of the angle from the 'nose' of the sphere for a Mach number of 0.8. In the figure 5 streamlines are plotted (lines) as well as reference data from [Lam & Pollock, 1989]. The graph shows that at every station the simulated pressure is lower than the measured pressure. Put another way, for each pressure level the simulated point for that pressure occurs approximately 4° before it occurs in the measurement. The starting pressure coefficient is also lower in the simulation compared to the measurement.

Figure 6.13 shows a detail of the pressure coefficient versus the Mach number plot. In the figure 5 streamlines are plotted as well as the critical pressure coefficient at which the flow goes supersonic according to [Lam & Pollock, 1989]. The graphs intersect very close to Mach 1, which means the critical pressure coefficient is predicted very well.

In conclusion, for subsonic flow the simulated pressure coefficient has a maximum deviation of 0.15 from the measured value at the same location (70°). Putting it into terms of the angle, each simulated pressure coefficient level occurs approximately 4° earlier compared to the measured value. The maximum deviation for the critical pressure coefficient is approximately 0.0015.

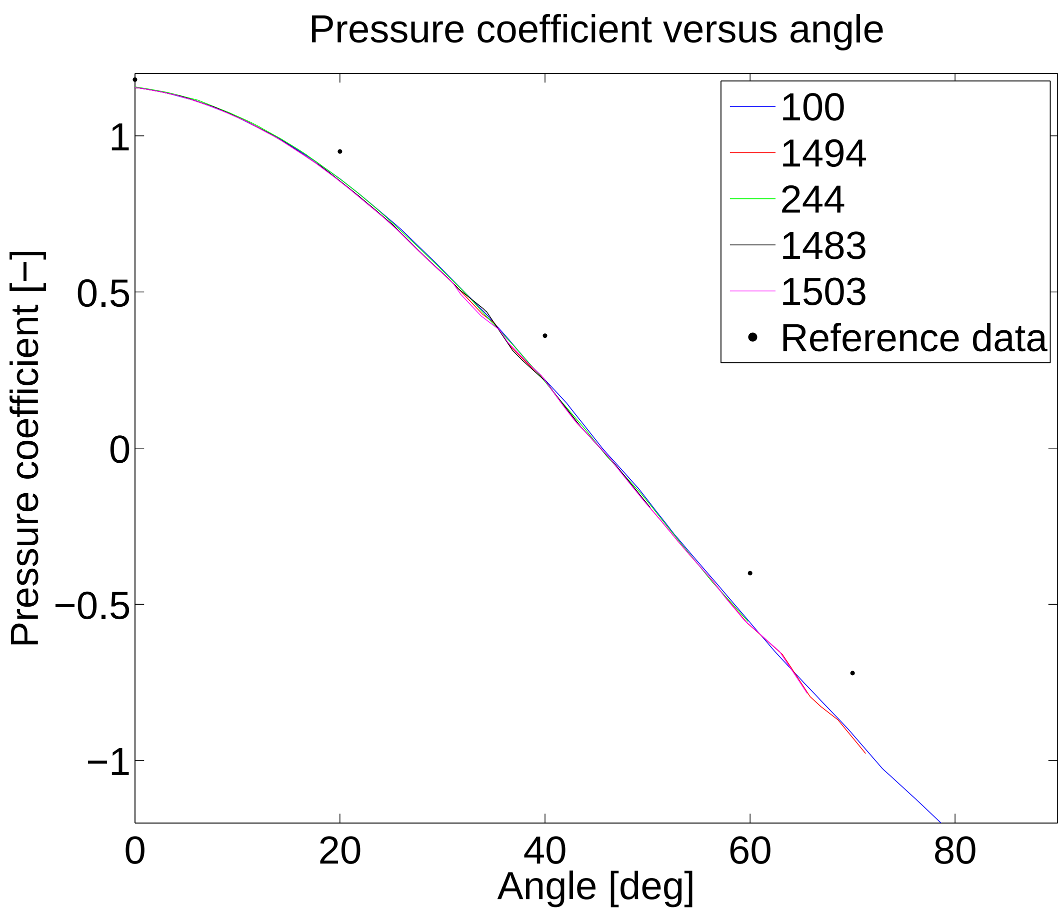

Figure 6.12: Pressure coefficient as a function of the streamwise angle around the sphere. The reference data is from [Lam & Pollock, 1989].

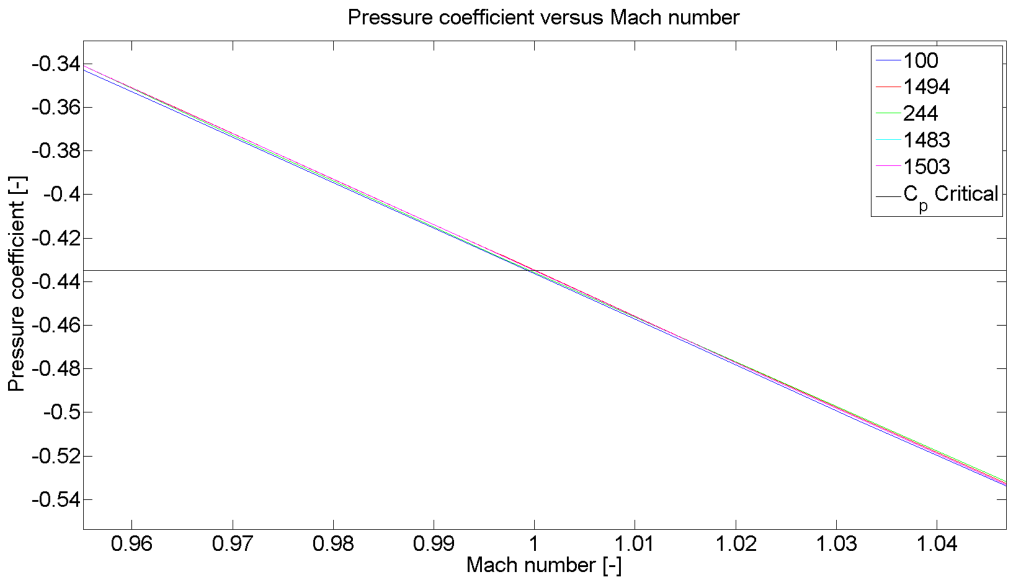

Figure 6.13: Pressure coefficient as a function of Mach number around the sphere. The reference data is from [Lam & Pollock, 1989].

6.2.3. ACCURACY OF TRANSITION PREDICTION

In the simulation Wazzan's engineering method is used to determine the location of the flow transition, see also Chapter Aerodynamics. Due to the large number of variables having an influence on the transition point such as the free stream flow turbulence, surface roughness, pressure distribution and Reynolds number, its exact location is hard to predict accurately for all cases. In this subsection it will be investigated how accurate the transition point determination is for a sphere at a Mach number of 3. The reference case that will be used is from [Deveikis & Walker, 1961]. In this paper the transition point is determined for three different surface roughnesses, ranging from 5 to 300 microinches. The variable used to show the change is based on the Stanton number, which is an indicator of the heat flux. In the simulation the heat flux is determined using a method based on the Blasius solution for laminar flow and based on the Reynolds analogy for turbulent flow.

Figure 6.14 shows the transition point comparison. The first thing to note is that the upper reference graph uses the Stanton number on the y-axis while lower graph of simulated data uses the momentum thickness on the y-axis. However, because of the dependency between momentum thickness and heating rate large changes in both variables happen at the same point along the streamline. Therefore the interesting part of the graphs is at what distance from the nose the change occurs.

The upper graph shows that for the model with the lowest surface roughness (squares in the graph) the heating rate starts growing rapidly at 25% s/D. This continues up to 40% s/D where the trend changes to a nearly linear one. What the graph shows is the whole transition region where the flow changes flow fully laminar to fully turbulent. Wazzan's methods gives only a single point where the transition occurs, which Figure 6.14 shows to be around 38% s/D. The difference of 2% in the distance from the nose is better than expected for an engineering approximation, validating the method for this case. It should be noted however that accurate prediction of the transition point is hard to do consistently with such engineering methods, so this result should not be taken as proof that the transition point will be predicted accurately for every model and pressure distribution.

6.2.4. BOUNDARY LAYER DEVELOPMENT

The determination of the turbulent momentum thickness is one of the core functions in the simulation. Good turbulent momentum thickness experimental data was obtained from [Harris, 1971] and [Winter *et al.* , 1970]. The experimental model is the same shell as was shown in Chapter 4 (in Figure 4.4). The simulated model is based on the experimental model, with the only difference being that the tip of the nose is rounded with a radius of 1% of the length of the model. This is done because the simulation expects a proper stagnation point. The mesh for the model is shown in Figure 6.15.

Figures 6.16 shows the comparison between the simulated momentum thickness and the reference momentum thickness ([Winter *et al.* , 1970]) for the model at a Mach number of 0.6. The simulation settings are based on the test conditions described in the paper and can be found in Table 6.4. The test included a tripping device such that the complete boundary layer is turbulent, so a turbulent model was used for the simulation also. The shape of the momentum thickness development is captured correctly, at least up to the point of maximum momentum thickness. The location of maximum momentum thickness is captured correctly at 70% of the model length for the subsonic case. As for the actual value of the momentum thickness, the value is about 15% to 20% higher over the whole range up to the point of maximum momentum thickness, with a maximum deviation of $5 \cdot 10^{-4} \frac{\theta}{L}$ at the top. After the maximum momentum thickness the reference data falls much quicker than the simulated data, giving rise to differences in value of over 50%. This means the prediction is good for situation where the momentum thickness increases but not very accurate when it decreases.

Figures 6.18 shows the comparison between the simulated momentum thickness and the reference momentum thickness ([Harris, 1971]) for the model at a Mach number of 1.7. Except the Mach

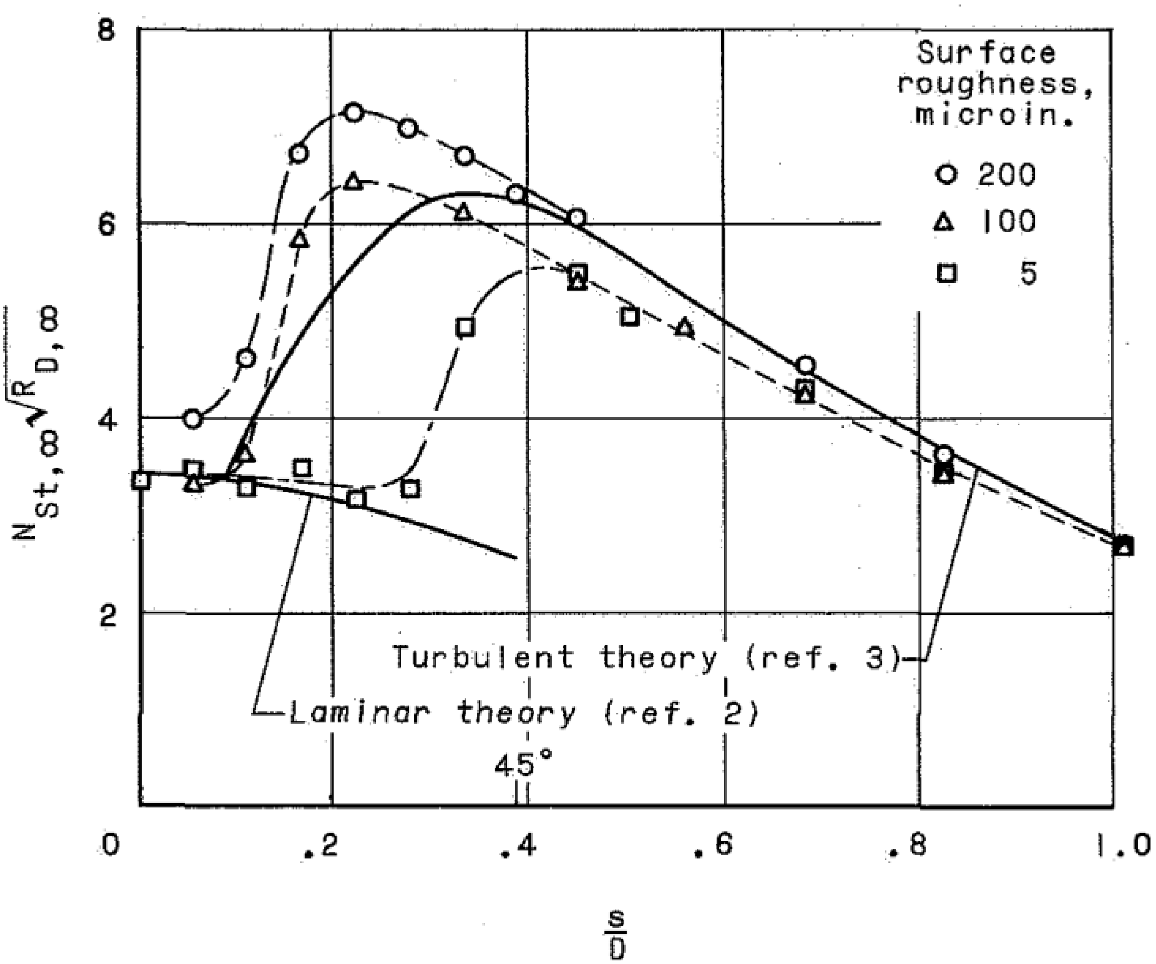

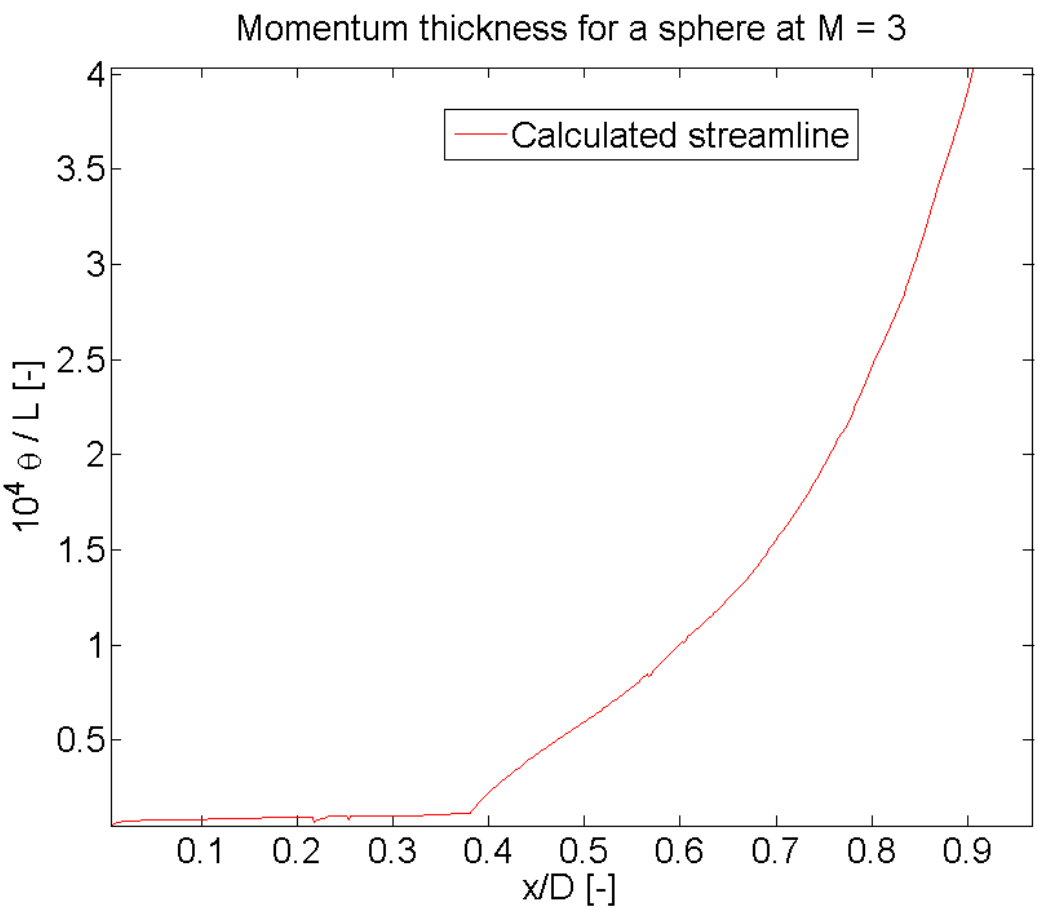

Figure 6.14: Comparing the laminar to transition location [Deveikis & Walker, 1961].

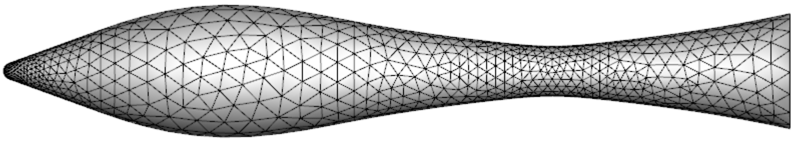

Figure 6.15: Mesh used for the simulation.

number and test atmosphere variables the testing conditions are the same. Again the shape and location of maximum momentum thickness are predicted correctly. The difference in values between the simulated and reference data is higher (compared to the subsonic case), with the latter being 50% lower than the former at the first measuring station. The absolute difference stays approximately constant at $5 \cdot 10^{-4} \frac{\theta}{L}$, the same difference as for the subsonic case. At the point of maximum momentum thickness the reference data value is 25% lower than the simulated value. Behind the point of maximum momentum thickness the absolute difference again increases.

Regarding the large oscillations at the point of maximum momentum thickness, this is due to the neck of the model at this location. The changing conditions at this point combined with an Euler solution that could use some refinement means that there are some Mach number variations there that may not be completely realistic. Furthermore, the velocity derivative calculations of the boundary layer code deal better with flat or concave surfaces compared to convex surfaces. Also, while the local momentum thickness change very rapidly, the trend is not impacted which means that these oscillations will not have influence the majority of the streamline.

The influence of changing the input variables on the outcome has also been investigated, see Figure 6.17 and the red and green graph in Figure 6.18. The changes made to the input variables can be found in Table 6.6. In general the increased values are 10% than the nominal values, with the exception of the time step (10× lower than the nominal time step for both cases) and the wall temperature (100 K higher in the supersonic case to make the influence clearer). Both graphs show that an increase in density decreases momentum thickness, though a 10% increase in ρ translates in a much smaller decrease in the momentum thickness. This means the solution is not very sensitive to changes in density.

Figure 6.17 also shows that an increase in pressure increases the momentum thickness. The effect is greater compared to the change in density, meaning the sensitivity of the momentum thickness to the pressure is higher. Finally, the smaller timestep (which was combined with the increased pressure) does not change the value of the momentum thickness but enlarges the errors in the solution. The reason for this is that a larger timestep acts as an averaging function, lowering these oscillations.

The yellow line in Figure 6.18 shows that an increase in wall temperature decreases the momentum thickness. As a wall temperature increase of 35% only results in a momentum thickness decrease of 10%-15%, the sensitivity is not very high. Figure 6.18 also shows that the sensitivity of the momentum thickness to changes in density is higher for the higher Mach number case, which indicates that the density start to increase in importance for those higher Mach numbers.

SKIN FRICTION

The turbulent skin friction is the final streamline variable to be validated. [Winter *et al.* , 1970] and [Harris, 1971] are used for reference data. Figure 6.19 shows the comparison for the subsonic shell, with the reference data in the upper graph and the simulated data in the lower graph. The shape of the simulated data graph is much flatter than the reference data graph, with the simulate data being lower than the reference data at 20% of the length while being higher at 70 % of the length. However, the point of minimum friction is correctly predicted at 70% of the length and the values of the local skin friction are in the correct range, with the worst deviation being around the point of minimum

	Subsonic	Supersonic
Mach number	0.597	1.7
p	73,227 Pa	48,201 Pa
ρ	0.6377 kg/m^3	0.8897 kg/m^3
T_∞	400 K	188.72 K
T_{wall}	289 K	289 K
L	1.524 m	0.3048 m
Timestep	0.01 s	0.01 s

Table 6.5: Simulation settings for the subsonic and supersonic momentum thickness & skin friction validation

	Subsonic	Supersonic
Increased pressure	80,549 Pa	-
Increased density	0.7015 kg/m^3	0.9787 kg/m^3
Increased wall temperature	440 K	389.16 K
Smaller timestep	0.001 s	0.001 s

Table 6.6: Simulation settings for the subsonic and supersonic momentum thickness & skin friction sensitivity analysis.

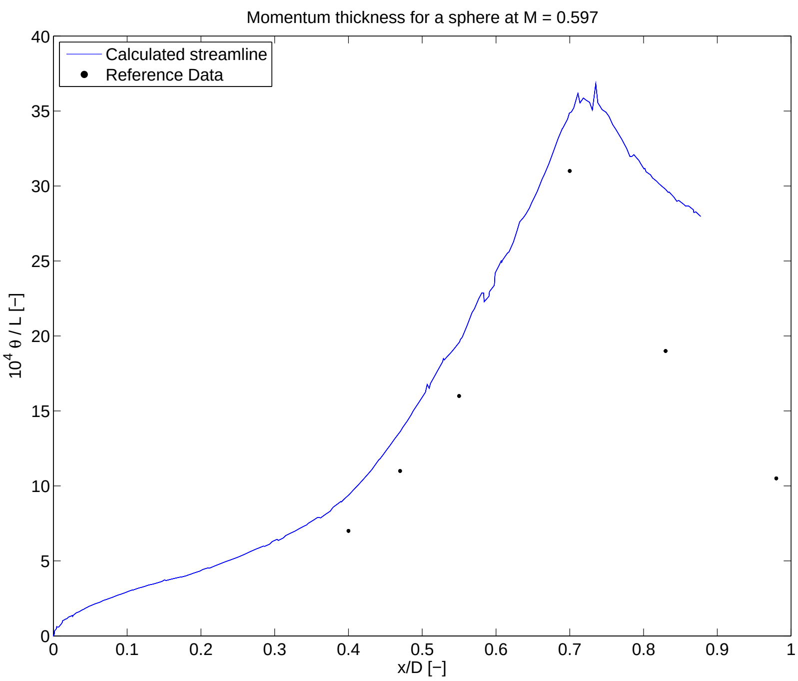

Figure 6.16: Comparison of the momentum thickness from the simulation with experimental data from [Winter *et al.* , 1970] for M = 0.597.

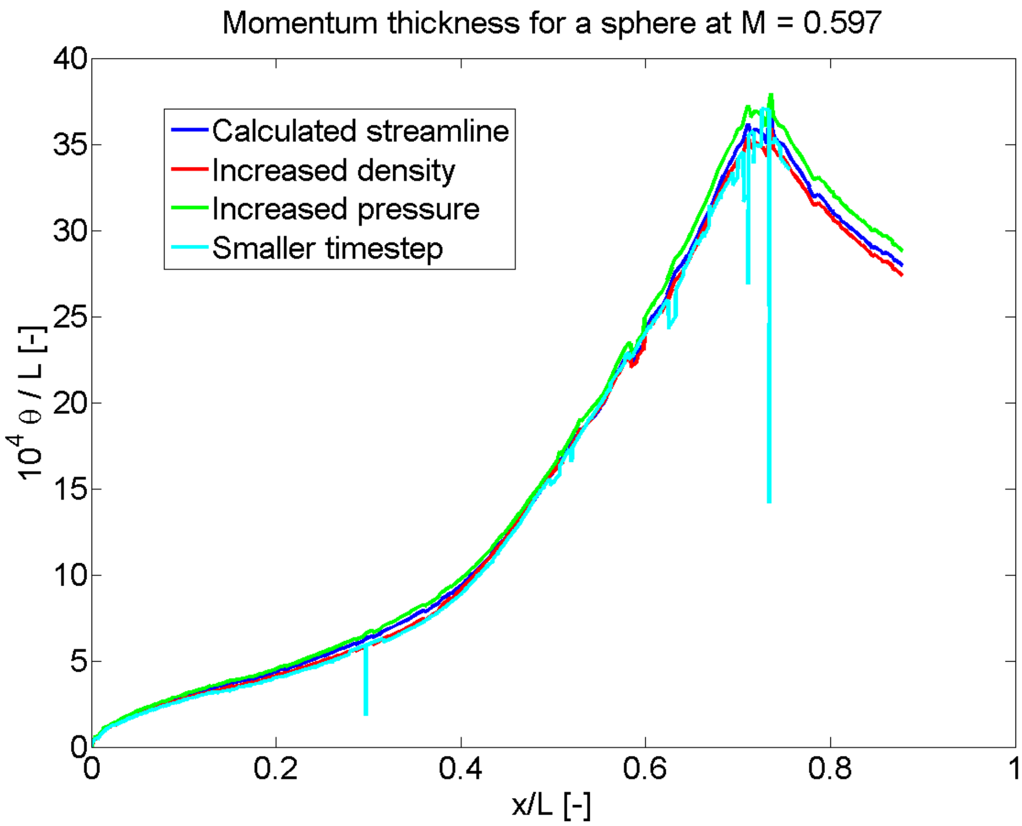

Figure 6.17: Sensitivity of momentum thickness to changes in variables.

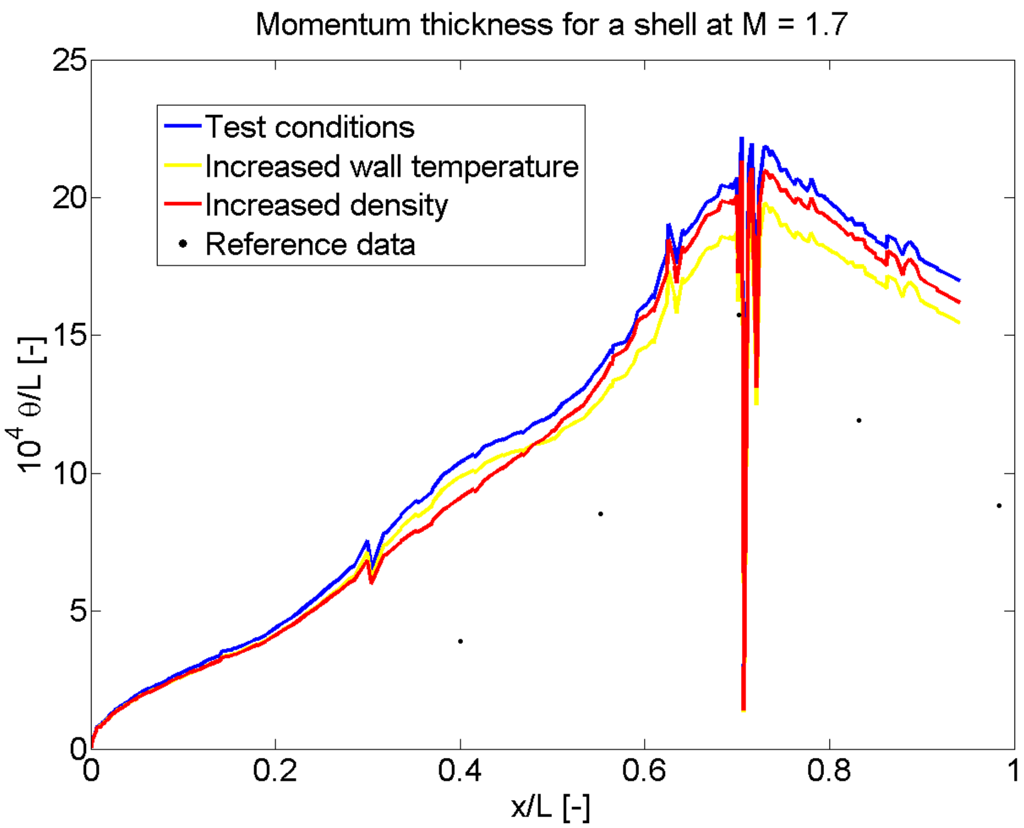

Figure 6.18: Comparison of the momentum thickness from the simulation with experimental data from [Harris, 1971] for M = 1.7.

skin friction where the simulated value is 50% higher than the reference value.

The comparison between the reference skin friction and the simulated skin friction for the supersonic case is shown in Figure 6.20. The initial slope downward of the simulated data is steeper than that of the reference data which has the effect that for the first 40% of the model the simulated skin friction is lower than the reference skin friction. After the 40% mark the simulated skin friction more or less levels levels off while the reference skin friction keeps decreasing. The maximum deviation occurs again at 70% of the length, where the reference skin friction is 50% lower than the simulated skin friction. The conclusion is that the match between the simulated and reference skin friction is not great but that it is sufficient for a first approximation of the total skin friction on a model.

The figures also shows the influence of changes in the input variables on the outcome. The changes made to the input variables are the same as for the momentum thickness, see Table 6.6. The changes also have the same effect on the output; increases in density and wall temperature decrease the skin friction, an increase in pressure increases the skin friction and a smaller time step does not change the values but exacerbates oscillations. One big difference is that the output is much smoother compared to the momentum thickness with a much smaller amplitude for deviations. This is because in the calculation of the skin friction the logarithm of the momentum thickness Reynolds number is taken, which dampens the errors.

6.3. COMPARISON OF SIMULATED DATA TO EXISTING HORUS DATA

The final section in this chapter is concerned with the validation of code calculating the aerodynamic and stability coefficients from the output of the aerodynamic simulation. To do this the simulated results will be compared to reference data from [Cucinelii & Müller, 1988]. Because of the large number of coefficients that have been simulated the tables have been placed in Appendix 10. In these tables the abbreviation "Sim" indicates a simulated value while the abbreviation "Ref" indicates reference data. The input values shown in Table 7.1 were used to determine the coefficients. It should be noted that these coefficients were simulated using older versions of the code, but this is not expected to influence the values much.

6.3.1. CLEAN CONFIGURATION COEFFICIENT COMPARISON

From a first overview of the coefficients tabulated in Appendix 10 a few things become clear. First of all, the simulated symmetric coefficients (C_L, C_D, C_m) are much closer to the reference symmetric coefficients than the asymmetric coefficients. The simulated lift coefficient is very close to the reference lift coefficient, while the drag coefficient and pitch-moment coefficient have larger differences but follow the trend and are at certain angles of attack also close to the reference data. This shows that there are differences in the slope of the coefficients for drag and pitch.

The asymmetric coefficients are not replicated successfully. While the sign is correct and the correct order of magnitude is achieved, there are still differences of more than 50% between the reference and simulated data. This is most apparent in the roll-moment derivative where the simulated data gives an almost zero coefficient at M = 2, while the reference value is not insignificant. A reason could be that errors do not always scale with the value of the parameter, in some cases the error has a nearly fixed value, which has a larger influence on small coefficients such as the asymmetric coefficients. Another possible cause is that sideslip angles created wake effects around the fuselage, which are less straightforward to simulate that the wake at the back of the vehicle for symmetric flight.

The degree of matching of the data is not as good for the Mach 1.2 case as for the Mach 2 case. Especially the lift coefficient value is off more than for the Mach 2 case, underreporting it over the whole range. The drag and pitch coefficients are fair, but similar to the lift coefficient the value of the pitch coefficient is now lower than the reference data, where for Mach 2 it was higher. It seems

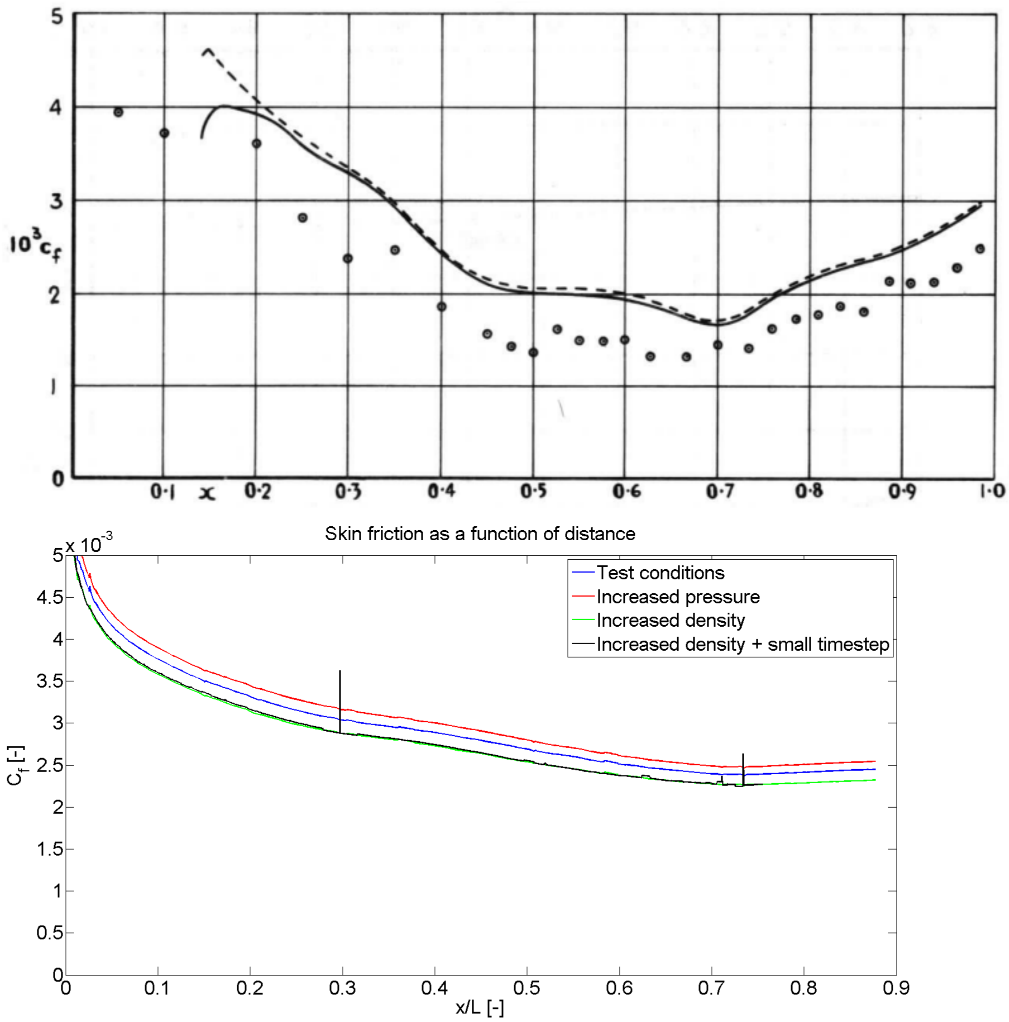

Figure 6.19: Comparison of the skin friction from the simulation with experimental data from [Winter *et al.* , 1970] for M = 0.597. For the upper figure the reference length used in $\frac{1}{5}$ of the total length.

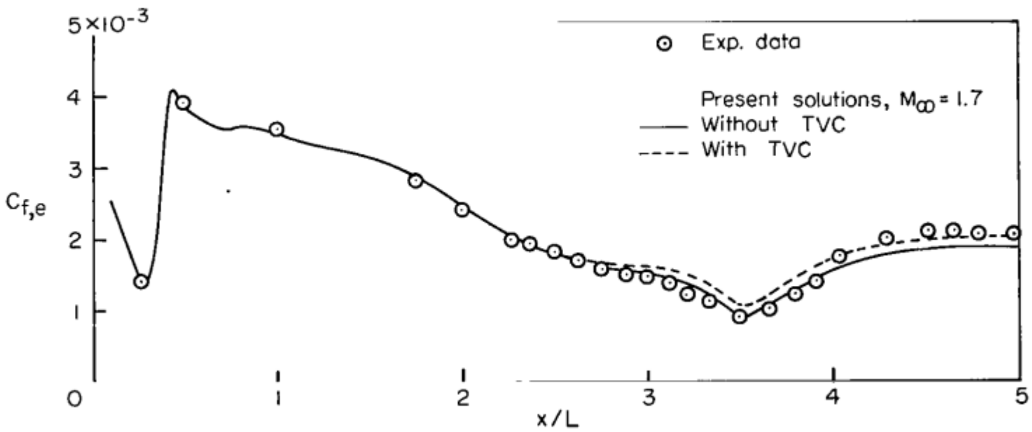

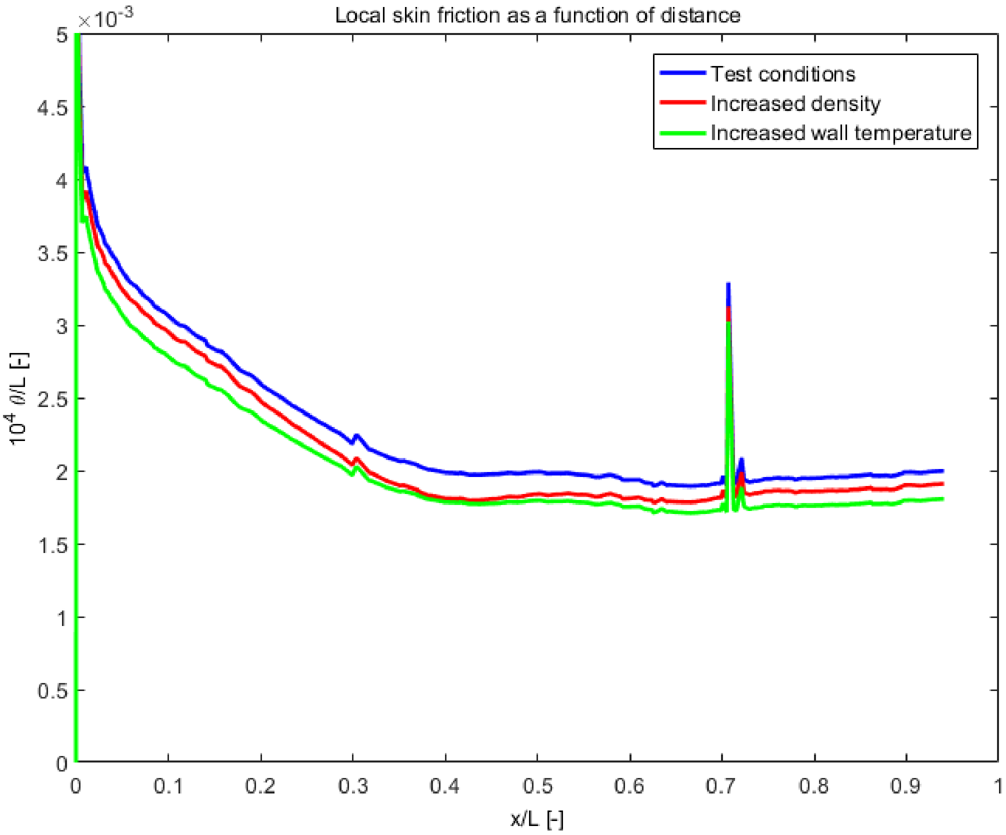

Figure 6.20: Comparison of the skin friction from the simulation with experimental data from [Harris, 1971] for M = 1.7. For the upper figure the reference length used in $\frac{1}{5}$ of the total length.

to indicate that the effects of changes in Mach number influence the simulation more than the reference data.

6.3.2. BODY FLAP ANALYSIS

Because all coefficients regarding the body flap are symmetric, a good reproduction of the reference data is expected. However, this is not the case for the drag coefficient and parts of the lift coefficient. The fit for the drag coefficient is not good and the simulation under reports the value by a factor of 4. The lift coefficient fit is off by a factor of 2 for lower angles of attack, but comes close to the reference value at higher angles of attack. It should be noted that some coefficients also have the opposite trend compared to the reference data. For example, for the drag coefficient increment the simulated data goes down first and then up significantly, while the reference data is monotonously decreasing. It is important to remember that the bodyflap is deflected away from the airflow, which could have effects as it will reside in a lower pressure area. Regarding the body flap influence the M = 1.2 cases performs similar or even better than the supersonic M = 2 case, contrary to the clean vehicle analysis.

6.3.3. ELEVON DEFLECTION ANALYSIS

The elevon has the most data associated with it, as it influences all the force and moment coefficients. The drag, lift and pitch-moment coefficient increments are predicted well, while the roll-moment and side force predictions are also fair. This breaks with the earlier trend that the asymmetric coefficients are not predicted well. The likeliest explanation is that because an elevon deflection introduces significant asymmetric forces and moments, the trouble with the small absolute values of those coefficients vanishes. An extra clue pointing to this argument is the yaw-moment coefficient; because the influence of the elevon on the yaw-moment will be small, the prediction is not very good. The elevon cases show again that the predictions for the supersonic Mach number are better than those for the transonic Mach number.

6.3.4. RUDDER DEFLECTION ANALYSIS

The rudder deflection only has significant effects on the yaw-moment and the side force. The yaw moment is reproduced well for the transonic case and fair for the supersonic case. The side force is off by quite a bit. That the primary effect of the rudder is reproduced rather well lends credence again to the hypothesis that large effects are reproduced much more faithfully than small effects.

6.3.5. DYNAMIC STABILITY CALCULATIONS

As a final step the software that calculates the eigenvalues and eigenvectors from the stability coefficients needs to be validated. This is done by using coefficients from [Cucinelii & Müller, 1988] as input and comparing the output to [Mooij, 1997]. The input data and coefficients are given in Table 6.7. The output eigenvalues (Table 6.8) and eigenvectors (Table 6.10) can be compared to the reference eigenvalues and eigenvectors in Table 6.9. From this comparison it follows that the simulation reproduces all the eigenmodes that are present in the reference table, though in a slightly different order (in Table 6.8 $\lambda_{3,4}$ is lateral oscillation, λ_5 is pitch/roll divergence and $\lambda_{6,7}$ is periodic pitch/roll). The difference in eigenvalues between simulation and reference is generally 10% or less, except for the really small eigenvalues, where the simulated eigenvalue is twice as high as the reference eigenvalue.

The differences between the reference eigenvectors and simulated eigenvectors are generally larger than the differences in eigenvalues. The maximum difference between the moduli (z) is approximately 30%. While this difference is quite significant, it does not interfere with the ability to identify the major components of the eigenvectors, which means the difference is acceptable. The difference between the reference and simulated arguments (θ) are often very large. The reason is that this is dependent upon the ratio between the real and imaginary part of the eigenvector entry, which in turn is very sensitive to the exact value of the coefficients. As the arguments play no role in determining the major contributors to a certain motion, these deviations are acceptable.

Mach	2.5
h	26.7
rho	0.0301677
T	223.35
bref	13
cref	23
alpha	16.6
gamma	-8.4
mu	55

C_{D_α}	0.019
C_{L_α}	0.033
C_{S_β}	-0.017556
C_{m_α}	0.00072
C_{l_β}	-0.0013594
C_{n_β}	-0.000484
$C_{D_{Mach}}$	-0.04
$C_{L_{Mach}}$	-0.1
$C_{m_{Mach}}$	0.012
C_{D_0}	0.1954
C_{L_0}	0.4014

Table 6.7: Input for the dynamic stability validation.

	λ_1	λ_2	$\lambda_{3,4}$	λ_5	$\lambda_{6,7}$	λ_8	λ_9
Re	-1.1815	1.0533	0.0394	0.0353	-0.0227	-8.47E-05	-1.86E-15
Im	0	0	±1.3612	0	±0.0133	0	0
P [s]	0	0	4.6157	0	471.8938	0	0
$T_{1/2}$ [s]	0.5867	-0.6581	-17.5969	-19.6328	30.485	8.18E+03	3.73E+14
ζ [-]	1	-1	-0.0289	-1	0.8629	1	1
ω_n [rad/s]	1.1815	1.0533	1.3618	0.0353	0.0263	8.47E-05	1.86E-15

Table 6.8: Simulated eigenvalues and motion characteristics for the validation case at Mach 2.5 an altitude of 26.7 km.

		former short-period oscillation		periodic pitch/roll mode		lateral oscillation		pitch/roll divergence	spiral mode	
λ_i	Re	-1.0884	0.9518	-0.0213		0.0392		0.0401	$-0.1059 \cdot 10^{-3}$	$-0.9138 \cdot 10^{-15}$
	Im	-	-	±0.0146		±1.343		-	-	-
P (s)		∞	∞	430.4		4.7		∞	∞	∞
$T_{1/2}$ (s)		0.6	-0.7	32.6		-17.7		-17.3	6,544.1	$0.759 \cdot 10^{15}$
ζ (-)		-	-	0.825		-0.029		-	-	-
ω_n (rad/s)		-	-	0.026		1.343		-	-	-
μ_i		z	z	z	θ (°)	z	θ (°)	z	z	z
ΔV		0.9895	0.8871	$0.6586 \cdot 10^{-2}$	52.8	0.0268	339.8	0.0419	$0.3379 \cdot 10^{-4}$	$0.1613 \cdot 10^{-4}$
$\Delta \gamma$		$0.1275 \cdot 10^{-2}$	$0.1111 \cdot 10^{-2}$	$0.3613 \cdot 10^{-4}$	68.9	$0.1815 \cdot 10^{-2}$	72.9	$0.4591 \cdot 10^{-4}$	$0.1498 \cdot 10^{-6}$	$0.3187 \cdot 10^{-8}$
ΔR		1.0000	1.0000	1.0000	35.0	1.0000	341.4	1.0000	1.0000	1.0000
Δp		$0.3547 \cdot 10^{-4}$	$0.3566 \cdot 10^{-4}$	$0.1380 \cdot 10^{-5}$	305.5	0.1259	74.5	$0.1785 \cdot 10^{-5}$	$0.3427 \cdot 10^{-8}$	$0.6985 \cdot 10^{-9}$
Δq		0.0266	0.0220	$0.5895 \cdot 10^{-6}$	343.9	$0.3583 \cdot 10^{-3}$	336.1	$0.4785 \cdot 10^{-5}$	$0.8551 \cdot 10^{-8}$	$0.3164 \cdot 10^{-8}$
Δr		$0.1701 \cdot 10^{-5}$	$0.1710 \cdot 10^{-5}$	$0.6617 \cdot 10^{-7}$	305.5	$0.6041 \cdot 10^{-2}$	74.5	$0.8561 \cdot 10^{-7}$	$0.1644 \cdot 10^{-9}$	$0.1977 \cdot 10^{-8}$
$\Delta \alpha$		0.0267	0.0210	$0.7066 \cdot 10^{-5}$	52.8	$0.4624 \cdot 10^{-3}$	71.3	$0.4525 \cdot 10^{-4}$	$0.3632 \cdot 10^{-7}$	$0.1734 \cdot 10^{-7}$
$\Delta \beta$		$0.5123 \cdot 10^{-5}$	$0.4504 \cdot 10^{-5}$	$0.4726 \cdot 10^{-8}$	339.9	0.0225	346.2	$0.9498 \cdot 10^{-8}$	$0.4817 \cdot 10^{-13}$	$0.1735 \cdot 10^{-22}$
$\Delta \sigma$		$0.2715 \cdot 10^{-3}$	$0.2695 \cdot 10^{-3}$	$0.4661 \cdot 10^{-4}$	298.7	0.0911	342.9	$0.3464 \cdot 10^{-4}$	$0.3238 \cdot 10^{-6}$	$0.2104 \cdot 10^{-6}$

Table 6.9: Reference Eigenvalues and corresponding characteristic values for time point 314, approximately Mach 2.5 [Mooij, 1997].

	Former short-period oscillation				Lateral oscillation		Pitch/roll divergence		Periodic pitch/roll mode		Spiral mode			
	λ_1		λ_2		$\lambda_{3,4}$		λ_5		$\lambda_{6,7}$		λ_8		λ_9	
	z	θ(°)	**z**	θ(°)	**z**	θ(°)	**z**	θ(°)	**z**	θ(°)	**z**	θ(°)	**z**	θ(°)
ΔV	7.185E-01	180	6.849E-01	180	2.592E-02	-179	3.504E-02	180	7.389E-03	166	2.998E-05	180	2.034E-05	180
$\Delta \gamma$	9.662E-04	0	8.999E-04	0	1.810E-03	89	4.071E-05	0	3.696E-05	150	1.203E-07	180	4.010E-09	180
ΔR	6.948E-01	180	7.281E-01	0	9.851E-01	0	9.994E-01	0	1.000E+00	0	1.000E+00	0	1.000E+00	180
Δp	2.444E-05	0	2.603E-05	0	1.368E-01	-93	1.436E-06	0	1.554E-06	98	2.747E-09	180	6.597E-10	0
Δq	2.376E-02	0	2.120E-02	0	4.179E-04	5	3.242E-06	0	5.613E-07	64	7.965E-09	0	3.241E-09	180
Δr	1.292E-06	0	1.376E-06	0	7.231E-03	-93	7.595E-08	0	8.217E-08	98	1.453E-10	180	1.869E-09	180
$\Delta \alpha$	2.179E-02	180	1.855E-02	0	4.558E-04	90	3.411E-05	0	7.166E-06	-14	2.911E-08	0	1.975E-08	0
$\Delta \beta$	3.664E-06	0	3.479E-06	180	2.364E-02	175	6.435E-09	180	5.197E-09	68	2.954E-14	180	2.492E-23	0
$\Delta \sigma$	1.950E-04	180	2.019E-04	180	9.777E-02	-1	2.953E-05	180	4.999E-05	105	3.273E-07	0	2.175E-07	180

Table 6.10: Simulated eigenvectors for the validation case at Mach 2.5 an altitude of 26.7 km.

7

Results & Analysis

In this chapter the results of the simulations will be discussed and an analysis of the stability of the HORUS will be made. This chapter will thus satisfy the requirements regarding the analysis of the static stability, the analysis of the dynamic stability and the analysis of the total stability picture of the HORUS. The first section will give the settings that were used for the simulation. The second section discusses the inviscid simulation results as well as issues arising from these simulations. The third section treats the stability analysis of the HORUS, including the trim condition, influence of the skin friction on stability, static stability and dynamic stability. The fourth section deals with a sensitivity analysis of the results which aims to show how robust the stability results are.

7.1. Experimental setup

For a correct understanding of the results and the simulation conditions some terminology much be defined first. The nominal simulation cases are the simulations that are used as a baseline for the difference calculations that determine the coefficient derivatives. These nominal settings are shown in Table 7.1. The values are based on the altitudes given in [Jiang & Yang, 2014], using the altitudes of 5 km for Mach 0.8, 12 km for Mach 1.2 and 20 km for Mach 2. The corresponding atmospheric parameter values were obtained from the U.S. Standard Atmosphere Model ([U.S. Government Printing Office, 1976]). Whenever the term 'reference values' or 'reference data' is used, the data about HORUS in either [Cucinelii & Müller, 1988] (for static stability) or [Mooij, 1997] (for dynamic stability is meant.

M	Mach number	0.8	1.2	2
h_{alt}	Altitude [m]	5,000	12,000	20,000
ρ_∞	Free-stream density [kg/m^3]	0.736116	0.310828	0.0880
p_∞	Free-stream pressure [N/m^2]	54,020	19,330	5,475
T_∞	Free-stream temperature [K]	255.7	216.7	216.7
T_w	Wall temperature [K]	T_{aw}	T_{aw}	T_{aw}
α	Angle of attack [°]	10	10	10
β	Sideslip angle [°]	0	0	0
σ	Bank angle [°]	0	0	0

Table 7.1: Reference values for the nominal simulation cases of the HORUS.

The Mach number, center of mass and altitude deviations used for the dynamic stability calculations were given in the simulation plan. The only thing missing is a more detailed overview of the settings for the altitude deviation, for which a number of flow variables change. The settings for the altitude deviation can be found in Table 7.2.

M	Mach number	2
h	Altitude $[m]$	19,000
ρ_∞	Free-stream density [kg/m^3]	0.103071
p_∞	Free-stream pressure [N/m^2]	6,410
T_∞	Free-stream temperature [K]	216.7
T_w	Wall temperature [K]	T_{aw}
α	Angle of attack [°]	10
β	Sideslip angle [°]	0
σ	Bank angle [°]	0

Table 7.2: Reference values for the altitude deviation simulation at 19 km.

7.2. HORUS AERODYNAMIC ANALYSIS

The first step in the analysis is to define what is happening in the inviscid flow field and what conclusions can be drawn from that. In this section the interesting features will be shown and issues that came up will be discussed.

7.2.1. HIGH SUPERSONIC FLOW FIELD

Figure 7.1 shows the side view of the flow field in the symmetry plane. The bow shock in front is clearly visible (demarcated by the sharp change in color from orange to yellow) as are the stagnation region and the wake where the Mach number is below 1 (shown as the dark blue areas). An interesting feature is that due to the body flap being deflected upwards an expansion fan occurs and the flow accelerates to the highest Mach number around the vehicle, around Mach 2.5. This creates an extra low pressure area originating from the base of the body flap, which is visible as the dark blue area extending downwards from the body flap in Figure 7.2. This means that due to the upwards deflection of the body flap the wake drag changes, which is the mechanism through which upwards deflections act on the pitch coefficient and drag coefficient.

The most interesting feature in the top view in Figure 7.3 is that the Mach number is highest over the wings. Due to the angle of attack of 10° there is a low pressure area on top of the wing planform which accelerates the flow. This low pressure area can be seen in Figure 7.4. Another thing to note in the latter figure is that the pressure coefficient on top of the fuselage is a lot higher than the pressure coefficient on the wing. This means that for the upper side of the vehicle the wings are the major player in creating lift, which is expected. The bottom view in Figure 7.5 shows that except for leading edges most of the lift on the lower side is created by the fuselage and the wings combined. The elevon and body flap have very low pressure coefficients, showing that they are out of the flow at this angle of attack and this flow regime.

7.2.2. LOW SUPERSONIC / TRANSONIC FLOW FIELD

Throughout this thesis the case for Mach 1.2 has been called the transonic case, on the assumption that this is the upper limit of the range of Mach numbers between 0.8 and 1.2 that is generally considered transonic. Checking Figure 7.6 there is no subsonic flow on the vehicle except for the stagnation region, the wing leading edge and the wake of the vehicle. This means that the flow can be considered fully supersonic, albeit being near the lower limit of the supersonic range.

The most interesting feature is that there is a lower speed region at the root of the elevons spanning their length. Figure 7.6 gives a more detailed look and changes the variable to the pressure

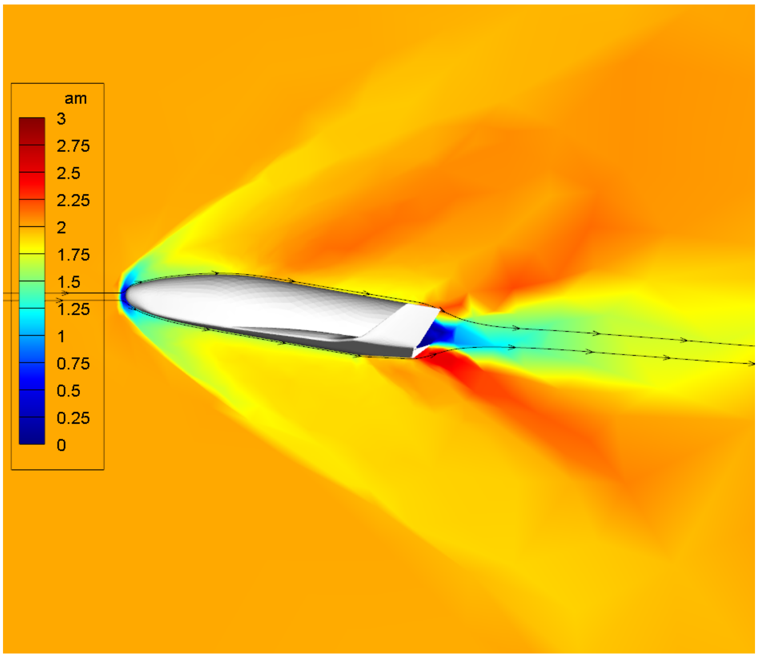

Figure 7.1: Side view of the Mach number around HORUS at a Mach number of 2, angle of attack of 10°, $\delta_{bf} = -20°$ and $\delta_{el} = 0°$.

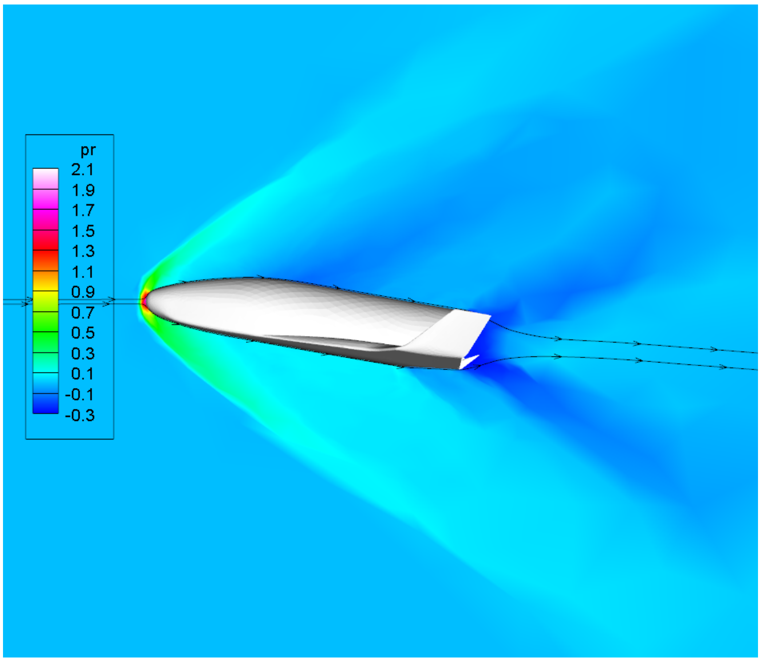

Figure 7.2: Side view of the pressure coefficient around HORUS at a Mach number of 2, angle of attack of 10°, $\delta_{bf} = -20°$ and $\delta_{el} = 0°$.

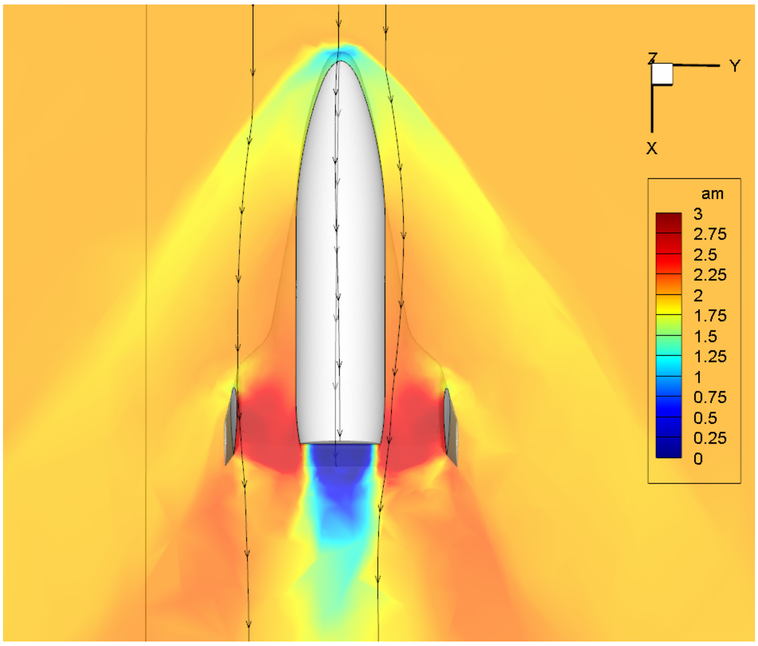

Figure 7.3: Top view of the Mach number around HORUS at a Mach number of 2, angle of attack of 10°, $\delta_{bf} = -20°$ and $\delta_{el} = -16°$.

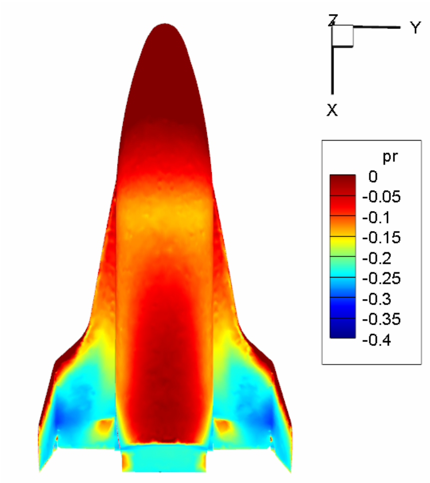

Figure 7.4: Top view of the pressure coefficient around HORUS at a Mach number of 2, angle of attack of 10°, $\delta_{bf} = -20°$ and $\delta_{el} = -16°$.

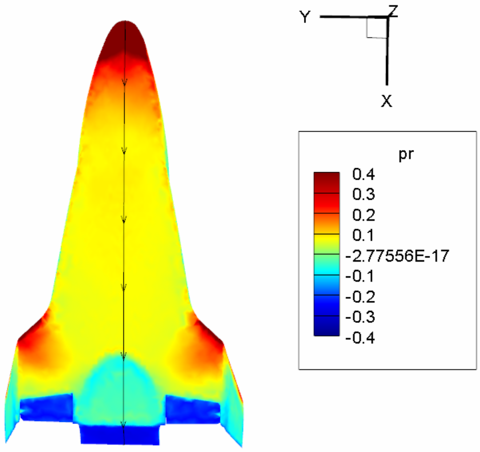

Figure 7.5: Bottom view of the pressure coefficient around HORUS at a Mach number of 2, angle of attack of 10°, $\delta_{bf} = -20°$ and $\delta_{el} = -16°$.

coefficient. The region is again clearly visible due to a higher pressure coefficient. This means that the upper side of the elevon now has an effect on the flow, which means it gains in usefulness for trim and control. Whether this is only due to the larger elevon deflection or also because of the lower Mach number will become clear when discussing the case at a Mach number of 0.8.

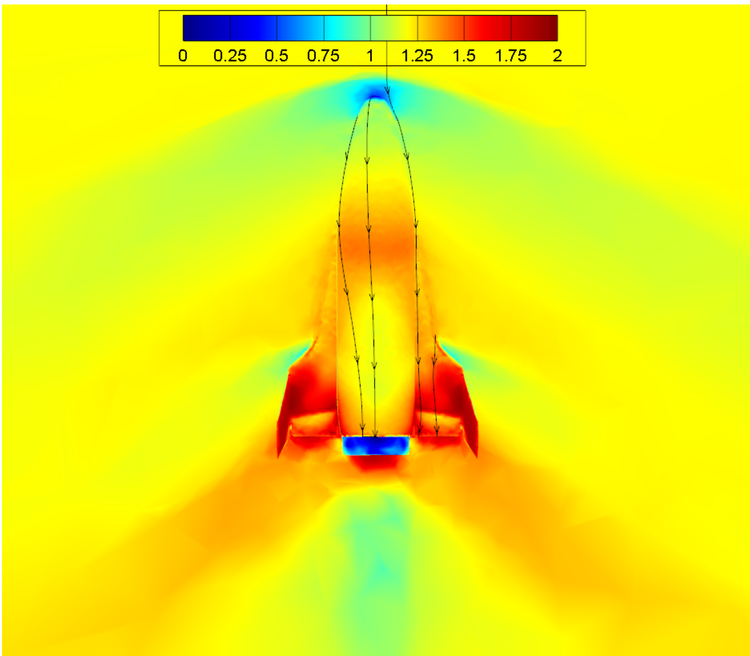

Figure 7.6: Top view of the Mach number around HORUS at a Mach number of 1.2, angle of attack of 10°, $\delta_{bf} = -20°$ and $\delta_{el} = -16°$.

7.2.3. HIGH SUBSONIC FLOW FIELD

Finally the case for Mach number of 0.8 will be discussed. This case has been referred to as the subsonic case, but Figure 7.8 shows that this is actually not the case. Over the wings the flow becomes supersonic, making this a transonic case. Around the base of the elevon a rapid decrease of the Mach number can be observed. Due to the supersonic Mach number and the upwards deflected

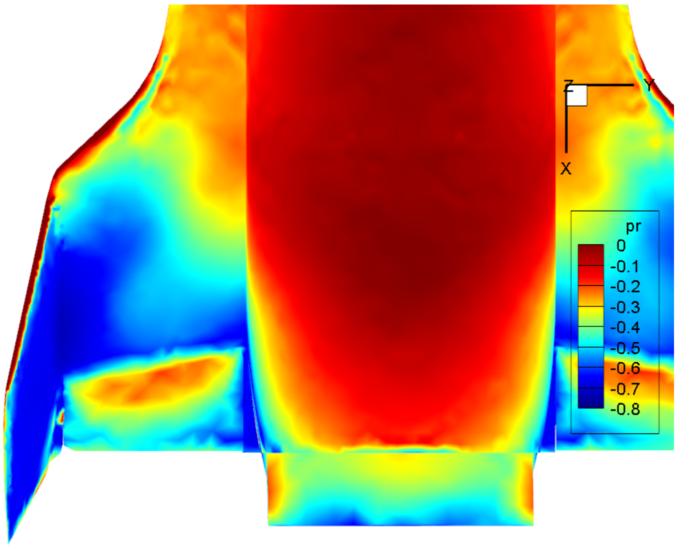

Figure 7.7: Top view of the pressure coefficient on the wing, elevon and body flap at a Mach number of 1.2, angle of attack of 10°, $\delta_{bf} = -20°$ and $\delta_{el} = -16°$.

elevon a shock wave occurs at this point. This is further evidenced by Figure 7.9, which shows the pressure coefficient on the surface and in a slice of the flow field. The rapid rise in pressure both on the surface and in the flow field (close to the elevon) is a clear indication that the flow goes subsonic here. This may have a large effect on the stability of the vehicle as slight changes in the Mach number and angle of attack will change the position of the shock or even the presence.

7.2.4. ERRORS IN THE FLOW FIELD SOLUTION

During the final analysis of the stability of the vehicle, it was noticed that for some cases certain moment coefficients were quite different from what would be expected based on the values in [Cucinelii & Müller, 1988]. In the subsequent investigation it became apparent that some of the Euler solutions contained artifacts that possibly influenced some of the aerodynamic coefficients. The affected cases are the 2° sideslip angle for both Mach 0.8 and Mach 1.2, as well as the 5° angle of attack for Mach 0.8. Figure 7.10 shows the issue at 2° sideslip angle and a Mach number of 0.8. The problem arises on only 1 side near the root of the wing. A detailed look shows mesh errors at this location which were not present in the input mesh. However, it was observed that there were some convex sections ('dimples') at the leading edge in the input mesh. The case at 2° sideslip angle and a Mach number of 1.2 shows the same issue, except that it occurs on the leading edge much further from the root of the wing. The cause seems to be the same however.

Figure 7.11 shows the issue at 5° angle of attack and a Mach number of 0.8. In this case there are localized high Mach number spots (with Mach numbers of up to 80) on the front of the winglets on both sides of the vehicle. There is no apparent mesh fault in the surface mesh and the flowfield mesh shows that the issue extends some way outside the vehicle too. While the direct cause is not known, these issue may be prevent by rerunning the Euler simulation with different settings.

7.3. STABILITY RESULTS

In this section the results for the stability of the HORUS will be discussed. Topics included are the trim condition, static stability and dynamic stability.

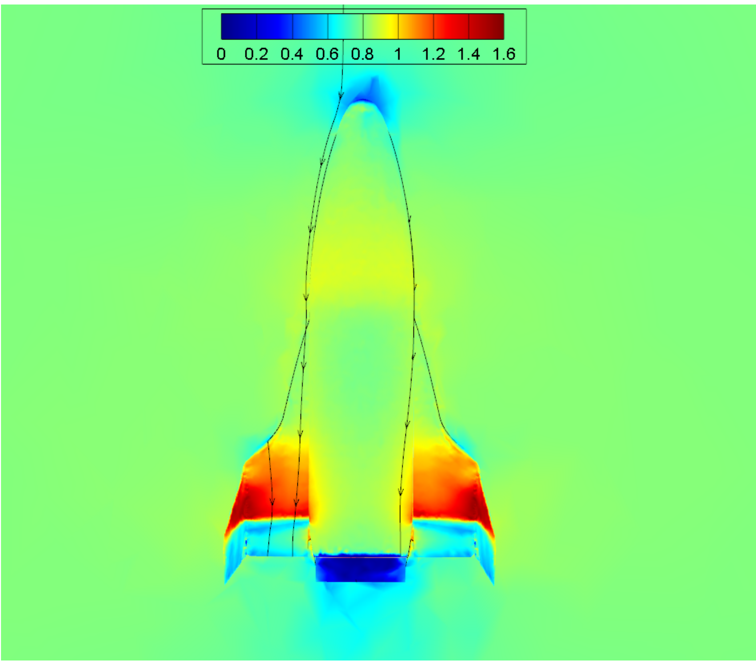

Figure 7.8: Top view of the Mach number around HORUS at a Mach number of 0.8, angle of attack of 10°, $\delta_{bf} = -20°$ and $\delta_{el} = -16°$.

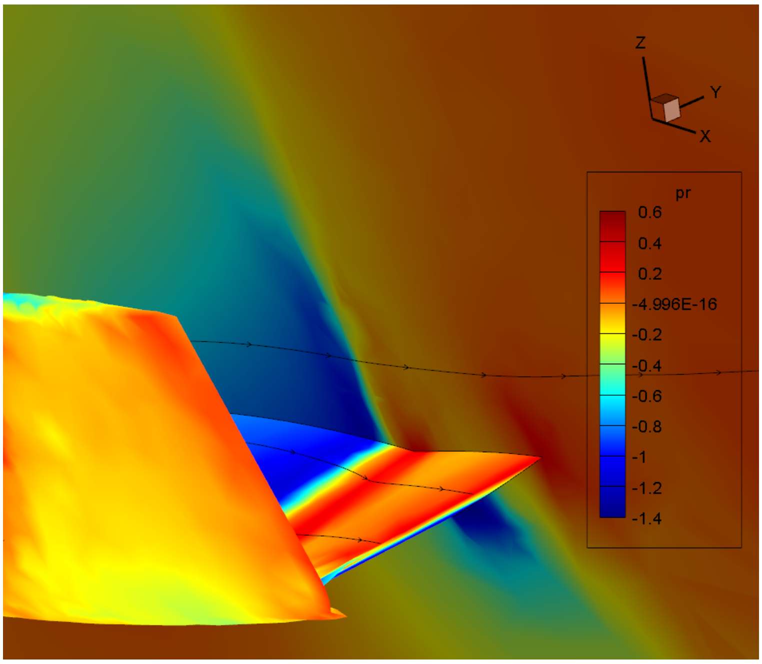

Figure 7.9: Pressure coefficient on the wing, elevon and a slice of the flow field going over the elevon at a Mach number of 0.8, angle of attack of 10°, $\delta_{bf} = -20°$ and $\delta_{el} = -16°$.

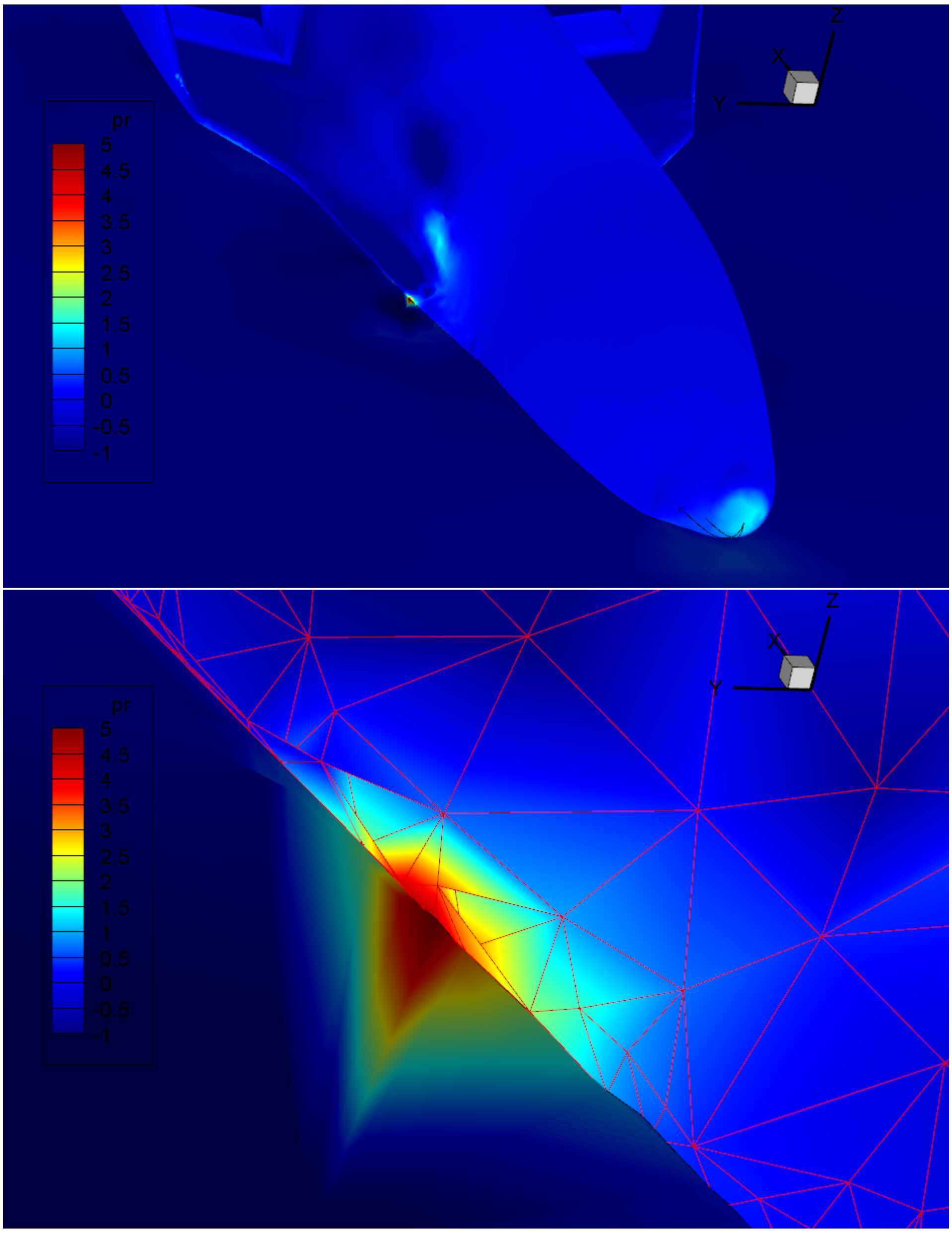

Figure 7.10: Pressure error in the 2° sideslip Mach 0.8 case. Upper graph shows the overview, lower graph shows a zoomed-in version with mesh.

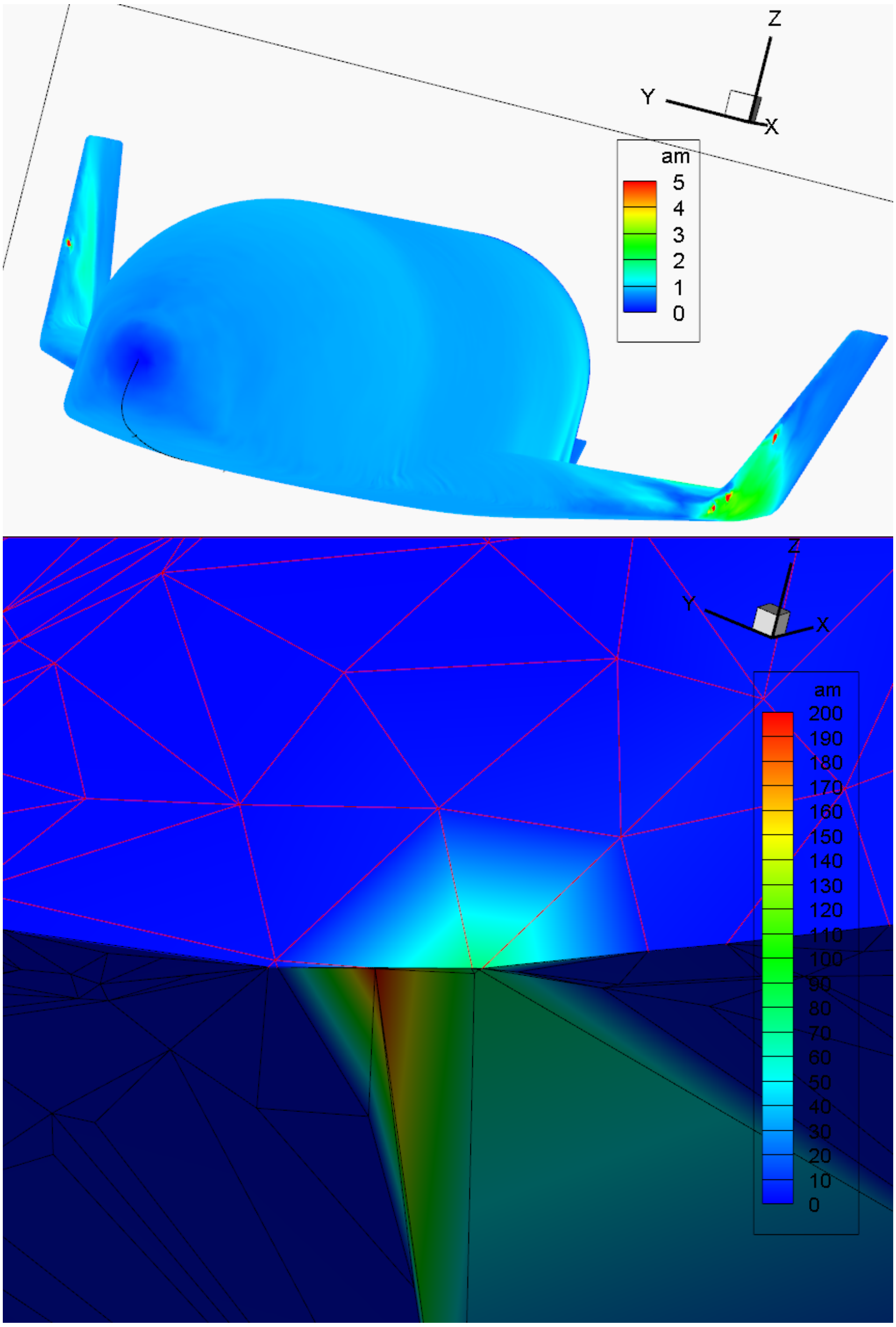

Figure 7.11: Mach number error in the 5° angle of attack, Mach 0.8 case. Upper graph shows the overview, lower graph shows a zoomed-in version with mesh.

7.3.1. TRIM

For the dynamic stability to be valid the vehicle needs to be trimmed, i.e. the moment coefficients should be zero. As the vehicle and flow are supposed to be symmetric barring errors, the moment coefficients around the X-axis and Z-axis can be assumed to be zero. This leaves the pitch coefficient to be investigated for trim. Figure 7.12 shows the pitch coefficient as a function of Mach number and angle of attack. For a Mach number of 2 the pitch coefficient is close to zero for the nominal angle of attack of 10°, though at 5° angle of attack it is even closer to zero. The trim angle of attack is thus lower than 5° according to the simulated results, assuming C_{L_α} remains positive. For Mach 1.2 the pitch coefficient at the nominal angle of attack of 10° is further from zero but still relatively close to trim condition. The trim angle of attack is between 5° and 10°. Finally, for Mach 0.8 the pitch coefficient is far from zero, indicating that the trim condition is not satisfied. As the trim condition is not satisfied for all angle of attack shown at Mach 0.8, it is unlikely to be due to errors in the simulation (unless it is a systemic error). A new trim deflection of the elevons needs to be found for this case.

In conclusion, for both Mach 1.2 and Mach 2 the pitch coefficient is close enough to zero to be considered in trim condition. For Mach 0.8 this is not the case, which means the outcomes of the dynamic stability analysis should be treated carefully.

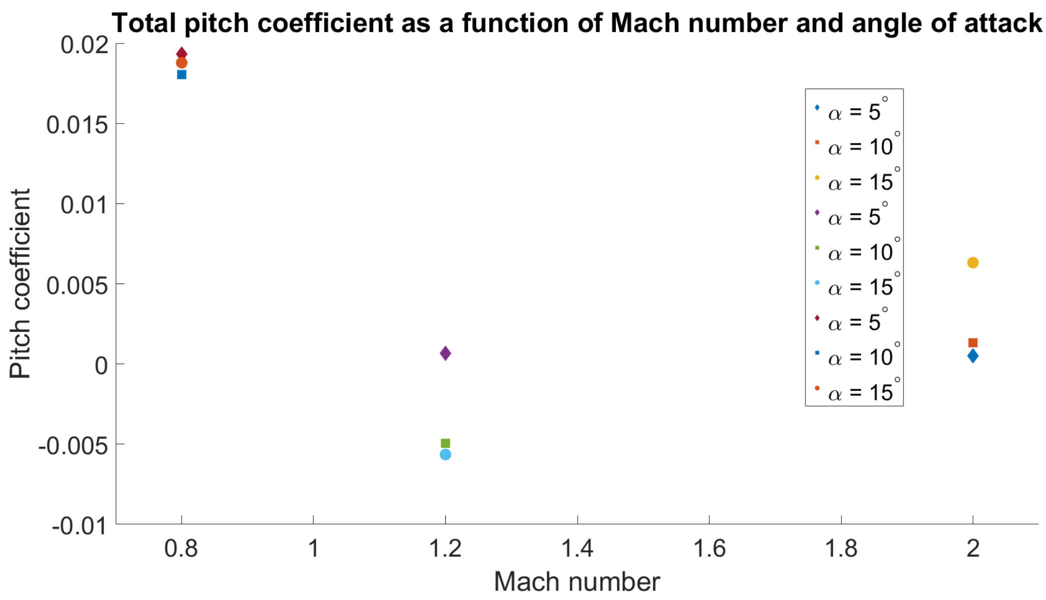

Figure 7.12: Total pitch coefficient for the nominal test cases.

7.3.2. INFLUENCE OF THE SKIN FRICTION

A major part of this thesis has been the addition of friction calculations to the total aerodynamic simulation. The question now remains whether that skin friction plays a significant role in the aerodynamics and stability of the vehicle. To answer this question the fraction that the skin friction drag contributes to the lift coefficient, drag coefficient and pitch coefficient is shown in Figures 7.13 through 7.15. Figure 7.13 shows that the contribution of the skin friction to the total drag is not very significant for all the Mach numbers tested, with a maximum contribution of about 6% for Mach 0.8. Due to the errors in the Euler solution for $\alpha = 5°$ at Mach 0.8 the total drag may be an overestimation, which would mean the skin friction fraction is an underestimation.

Figure 7.16, which shows the total drag coefficient as a function of Mach number and angle of attack, gives an idea of the possible drag overestimation. For Mach 1.2 and Mach 2 the distance between the drag coefficient for $\alpha = 5°$ and $\alpha = 10°$ is approximately half the distance between $\alpha =$

10° and $\alpha = 15°$. Assuming the trend holds for Mach 0.8, this would mean that the drag coefficient is overestimated by about 50%. This means the skin friction fraction would rise to 10%-15% for $\alpha = 5°$ and M = 0.8, which is not insignificant but neither a major contribution.

The skin friction contribution to the lift coefficient is shown in Figure 7.14 and is below 1% for all cases. This means the skin friction drag is not significant for the lift coefficient. Finally the skin friction contribution to the pitch coefficient is shown in Figure 7.15 and it is large, up to 80% of the total pitch coefficient. The reason for this is twofold: First, the skin friction has a much smaller variation with angle of attack compared to the pressure drag. Second, the spaceplane is at or near trim condition, meaning that the total pitch coefficient is small. In essence, it is not the pitch coefficient due to skin friction that becomes much larger but the pitch coefficient due to the pressure distribution that becomes much smaller, which also increases the fraction of the skin friction contribution to the total coefficient.

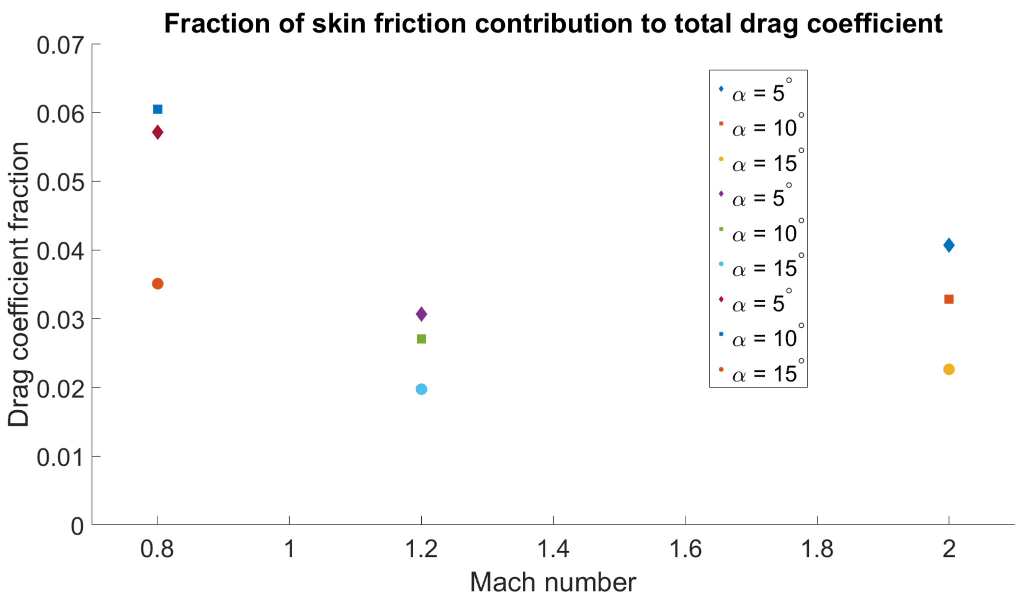

Figure 7.13: Skin friction contribution to total drag coefficient for the nominal test cases.

7.3.3. STATIC STABILITY

The next step in the stability analysis is to investigate the static stability. The static stability coefficients have been calculated for the nominal settings for the three Mach numbers, as well as as a different c.o.m. position for the simulation at Mach 2.

HIGH SUPERSONIC REGIME (MACH 2)

For the supersonic static stability analysis two cases will be presented, the nominal case with a c.o.m. at 61% of the total vehicle length and an alternative case for a c.o.m. at 56% of the total vehicle length. This is based on the given center of mass position at 14 meters from the tip of the nose with respect to the reference length of 23 meters (61% CoM) and the total length of 25 meters (56% CoM).

Only a subset of the coefficients will be shown, as only the moment coefficients matter for the static stability and some of the coefficients can normally be assumed to be zero because of a decoupling between lateral moments and longitudinal angle changes. This means that C_{l_α} and C_{n_α} should be zero or at least insignificant.

Table 7.3 shows the coefficients for the nominal case at Mach 2 and a c.o.m. position of 61% of the vehicle length. The sideslip derivative C_{l_β} has the preferred sign and is thus statically stable. The

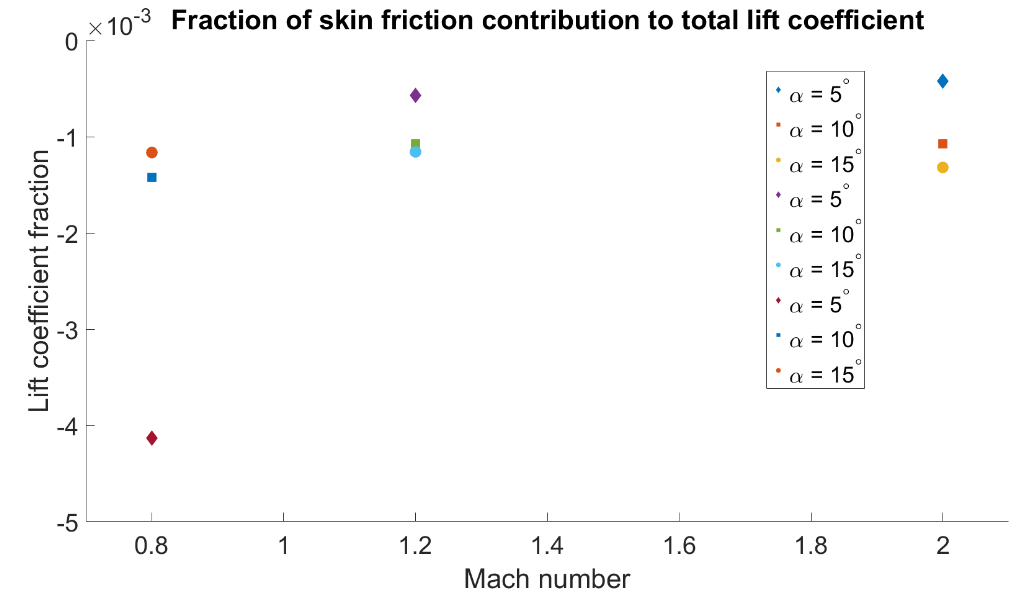

Figure 7.14: Skin friction contribution to total lift coefficient for the nominal test cases.

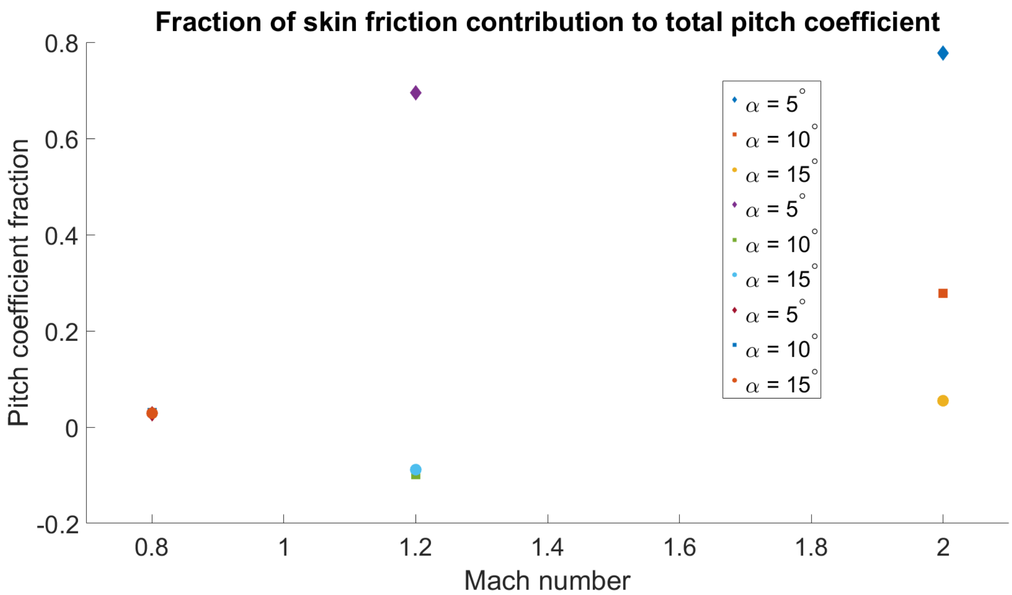

Figure 7.15: Skin friction contribution to total pitch coefficient for the nominal test cases.

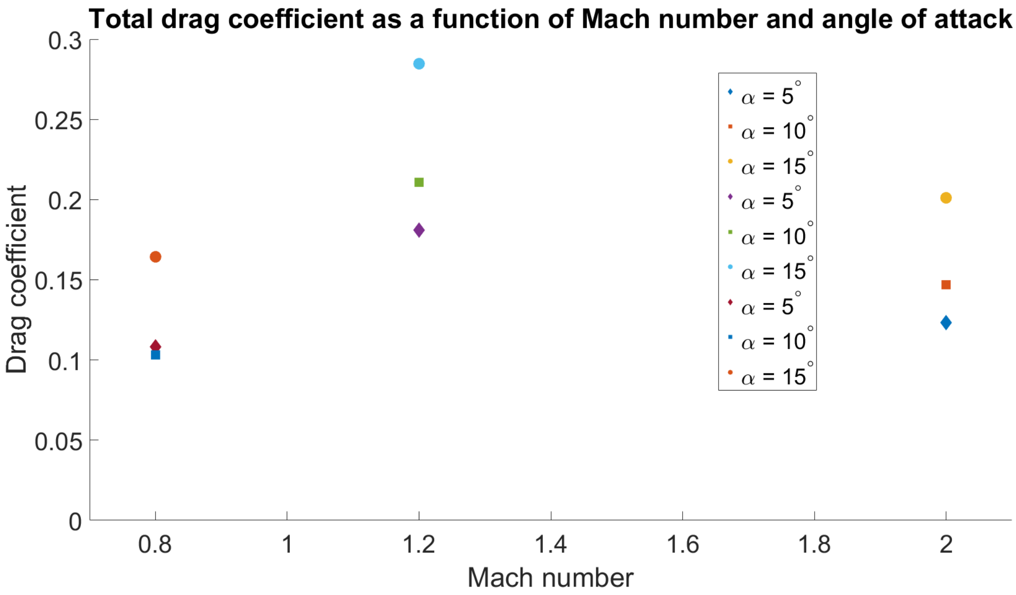

Figure 7.16: Total drag coefficient for the nominal test cases.

pitch coefficient derivative with respect to the angle of attack (C_{m_α}) is positive but small. This means there is no static stability, but the instability is small. The instability of C_{m_α} is not unexpected as this derivative is also positive or only slightly negative at Mach 2 and $\alpha = 10°$ in [Cucinelii & Müller, 1988]. The weathercock stability C_{n_β} is negative and not small, contradicting the data in [Cucinelii & Müller, 1988] where it is positive and close to zero.

As will be clear from the discussion of the coefficients at lower Mach numbers, the coefficient C_{n_β} has the correct trend as it becomes more positive for lower Mach numbers. The change of side force with increasing sideslip angle is very similar in the reference data and simulated data, so this can be eliminated as a cause for the mismatch in C_{n_β}. Moving the center of mass forwards does make the derivative more positive as expected.

Table 7.4 shows the results for alternative case with c.o.m. at 56%. The major difference with the previous case is that C_{m_α} changed sign, making it stable. Because C_{m_α} has changed sign and became negative the center of mass must now be in front of the aerodynamic center. The other coefficients all become closer to zero, which means C_{m_β} and C_{n_β} become less unstable and C_{l_β} becomes less stable. The effects of the change in center of mass on the eigenmotions of HORUS will be investigated in the section on dynamic stability.

The final supersonic case is at a lower altitude to investigate what influence a change in atmospheric variables has. The resulting coefficients are shown in Table 7.5. Crucially, the same Euler solution was used for the simulation at 19 km as the simulation at 20 km, the differences were only inserted at the start of the boundary layer simulation. This ensures there are no differences due to small variations in the Euler simulation. Comparing the coefficients in Table 7.5 to those in Table 7.5 it turns out the influence of altitude is very small. The maximum change is in C_{l_β}, where the change in altitude results in a change of coefficient of less than 1%.

LOW SUPERSONIC REGIME (MACH 1.2)

The low supersonic static stability coefficients are shown in Table 7.6 for a center of mass at 61% of the length and Table 7.7 for a center of mass at 56% of the length. For both cases all coefficients have the required sign for static stability, which improves the changes that the HORUS is also dynamically stable for this regime. For the forward center of mass C_{m_α} and C_{n_β} are further from zero, which generally improves stability. C_{l_β} on the other hand becomes closer to zero and thus less stable.

Coefficient	Value	Preferred sign	Stable?
C_{m_α}	$6.7277{\cdot}10^{-4}$	-	No
C_{l_β}	$-1.0064{\cdot}10^{-3}$	-	Yes
C_{m_β}	$6.8950{\cdot}10^{-5}$	0	-
C_{n_β}	$-3.9752{\cdot}10^{-3}$	+	No

Table 7.3: Primary supersonic static stability coefficients for c.o.m. at 61% and an altitude of 20 km. Coefficients have units [deg^{-1}].

Coefficient	Value	Preferred sign	Stable?
C_{m_α}	$-8.561{\cdot}10^{-4}$	-	Yes
C_{l_β}	$-4.1035{\cdot}10^{-4}$	-	Yes
C_{m_β}	$4.5809{\cdot}10^{-5}$	0	-
C_{n_β}	$-3.4115{\cdot}10^{-3}$	+	No

Table 7.4: Primary supersonic static stability coefficients for c.o.m. at 56% and an altitude of 20 km. Coefficients have units [deg^{-1}].

Coefficient	Value	Preferred sign	Stable?
C_{m_α}	$6.7486{\cdot}10^{-4}$	-	No
C_{l_β}	$-1.0072{\cdot}10^{-3}$	-	Yes
C_{m_β}	$6.9489{\cdot}10^{-5}$	0	-
C_{n_β}	$-3.9884{\cdot}10^{-3}$	+	No

Table 7.5: Primary supersonic static stability coefficients for c.o.m. at 61% and an altitude of 19 km. Coefficients have units [deg^{-1}].

Finally, C_{m_β} has grown and is thus less stable. In summary, compared to the Mach 2 case at Mach 1.2 the HORUS is statically more stable, as all coefficients that have a preferred sign for stability have that sign. The dynamic stability analysis will reveal whether the dynamic motions are also stable in these cases.

Coefficient	Value	Preferred sign	Stable?
C_{m_α}	-2.3823·10^{-4}	-	Yes
C_{l_β}	-2.2623·10^{-3}	-	Yes
C_{m_β}	2.5704·10^{-3}	0	-
C_{n_β}	5.7252·10^{-4}	+	Yes

Table 7.6: Primary transonic static stability coefficients for c.o.m. at 61% and an altitude of 12 km. Coefficients have units [deg^{-1}].

Coefficient	Value	Preferred sign	Stable?
C_{m_α}	-2.5321·10^{-3}	-	Yes
C_{l_β}	-1.7553·10^{-3}	-	Yes
C_{m_β}	3.1693·10^{-3}	0	-
C_{n_β}	1.6913·10^{-3}	+	Yes

Table 7.7: Primary transonic static stability coefficients for c.o.m. at 56% and an altitude of 12 km. Coefficients have units [deg^{-1}].

TRANSONIC (MACH 0.8)

The subsonic static stability coefficients are shown in Table 7.8 for the center of mass at 61% length and in Table 7.9 for the center of mass at 56% length. Compared to the Mach 1.2 case the longitudinal coefficient C_{m_α} has become unstable (positive) again for the aft center of mass. The other coefficients are all stable, with improved stability for all (C_{l_β} more negative, C_{m_β} closer to zero, C_{n_β} more positive. For the forward center of mass case all coefficients have their preferred sign again, indicating they are all stable. Because C_{m_α} changes sign due to this shift this indicated that the aerodynamic center lies between 56% and 61% of the length. The other 3 coefficients have moved further from zero, making C_{l_β} and C_{n_β} more stable and C_{m_β} more unstable.

Coefficient	Value	Preferred sign	Stable?
C_{m_α}	5.5519·10^{-4}	-	No
C_{l_β}	-9.2684·10^{-3}	-	Yes
C_{m_β}	2.6899·10^{-3}	0	-
C_{n_β}	3.1480·10^{-3}	+	Yes

Table 7.8: Primary subsonic static stability coefficients for c.o.m. at 61% and an altitude of 5 km. Coefficients have units [deg^{-1}].

7.3.4. DYNAMIC STABILITY

The dynamic stability will be treated in this section. This includes investigating the stability and nature of the eigenmotions as well as the influence of a different altitude or center of mass on the eigenmotion. The analysis will be in two directions: a more in-depth analysis for Mach 2 (analyzing the influence of changing parameters on the dynamic stability) and a shallower analysis of the Mach sweep through Mach 1.2 and Mach 0.8. This is done to limit the scope of the analysis, as well as the

Coefficient	Value	Preferred sign	Stable?
C_{m_α}	-1.7310·10^{-3}	-	Yes
C_{l_β}	-9.9913·10^{-3}	-	Yes
C_{m_β}	5.1267·10^{-3}	0	-
C_{n_β}	4.7558·10^{-3}	+	Yes

Table 7.9: Primary subsonic static stability coefficients for c.o.m. at 56% and an altitude of 5 km. Coefficients have units [deg^{-1}].

fact that it is not unreasonable to assume that the changes in parameters have similar effects for all Mach numbers. Whether this is true should be investigated in follow-up research.

HIGH SUPERSONIC (MACH 2)

Nominal case

The nominal case will be discussed first, simulated using the conditions in Table 7.1 for an altitude of 20 km. Figure 7.17 shows a plot of the eigenvalues with the real parts on the horizontal axis and the imaginary parts on the vertical axis. All the eigenvalues in the figure are on a line at an imaginary part value of 0, which means that all motions are aperiodic. Furthermore, 2 motions have clear negative eigenvalues (stable) and 2 motions have clear positive eigenvalues (unstable). The remaining 5 motions are close to zero, making it hard to discern whether they are positive or negative. For a more detailed look Table 7.10 can be used, which lists all the eigenvalues, their corresponding eigenvectors and motion characteristics.

The characteristics are the period (P), half or doubling time ($T_{1/2}$, a minus sign means it is a doubling time instead), damping ratio (ζ) and natural frequency (ω_n). The eigenvector components are the changes in velocity V, flight path angle γ, radius/altitude R, roll rate p, pitch rate q, yaw rate r, angle of attack α, sideslip angle β and bank angle σ.

In the table, as well as further tables in this chapter, certain abbreviations are used for the motions described in more detail in Chapter Flight Mechanics, Stability & Control. They are listed below:

- Short-Period Oscillation (SPO), identified by the velocity, altitude, pitch rate and angles of attack being major components. This motion is periodic.
- Former Short-Period Oscillation (FSPO), the aperiodic version of the SPO.
- Phugoid Motion (PM), identified by the velocity and altitude being major components.
- Lateral Oscillation (LO), identified by the roll rate, yaw rate, sideslip angle and bank angle being major components.
- Former Lateral Oscillation (FLO), the aperiodic version of the LO.
- Aperiodic Roll Motion (ARM), identified by the bank angle being the sole major component.
- Height Mode (HM), identified by the altitude being the sole major component.

Table 7.10 shows that for Mach 2 and the c.o.m. at 61% of the length of the vehicle none of the motions are periodic. The motions that stood out in Figure 7.17 are the FSPO and LO because of their large eigenvalues. For both these modes there is one stable and one unstable motion. For the FSPO the half/doubling time is on the order of half a second, meaning that the unstable motion will very rapidly diverge. For the LO the same is true, but $T_{1/2}$ is even shorter at approximately 0.3 seconds. Again, the unstable motion diverges rapidly and can be dangerous if not checked timely.

The phugoid is the third mode to have both a stable and unstable motion. However, because of the longer doubling time for the unstable motion (19 seconds), this motion is much easier to keep under control. Both aperiodic roll motions are unstable, with one having a doubling time of 17 seconds and the other having a doubling time of over 5 million years. Clearly the latter motion will not present problems and also the former motion is slow enough to be corrigible. The final mode, the height mode, is table and has a long half time. While a short half time would be preferable, this motion is at least stable.

The general picture is that for the situation simulated here the HORUS is far from stable, with two unstable modes that rapidly diverge. Comparing the motions to those found at the final time point in [Mooij, 1997], clear differences arise. According to this source (relevant data shown in Table 6.9) at Mach 2.5 there should be two aperiodic short period oscillations, a periodic pitch/roll mode, a periodic lateral oscillation, an aperiodic pitch/roll divergence and two aperiodic spiral modes. The spiral mode does not turn up in the simulated data, while some motions that should be aperiodic are periodic and vice versa. While the Mach number is lower for the simulation, one would not expect such large differences at first glance. However, there are some good reasons that explain the differences.

The first reason is that for the simulation the bank angle is set to zero, while for the reference data it is set at 55°. As can be seen from the bank angle graph in [Mooij, 1997], the spiral motion and roll motions only occur when the bank angle is non-zero. The second reason is that a value for C_{n_β} was found that had a sign opposite from the reference data, influencing the lateral motions. The third reason is the exact location of the center of mass. Depending on the location of the aerodynamic center, the stability of the motions of the vehicle can be very sensitive to a shift in the center of mass. Furthermore, there is some uncertainty about the exact location of the center of mass for the HORUS. While the location is given at 14 meter, there are three lengths to work with: the reference length (23 meter), drawing length (23.5 meter) and total length (25 meter). This means the center of mass location of the HORUS can be somewhere between 56% and 61% of the total length, which has large implications on the stability. Therefore the stability for a center of mass at 56% of the length will be analyzed now.

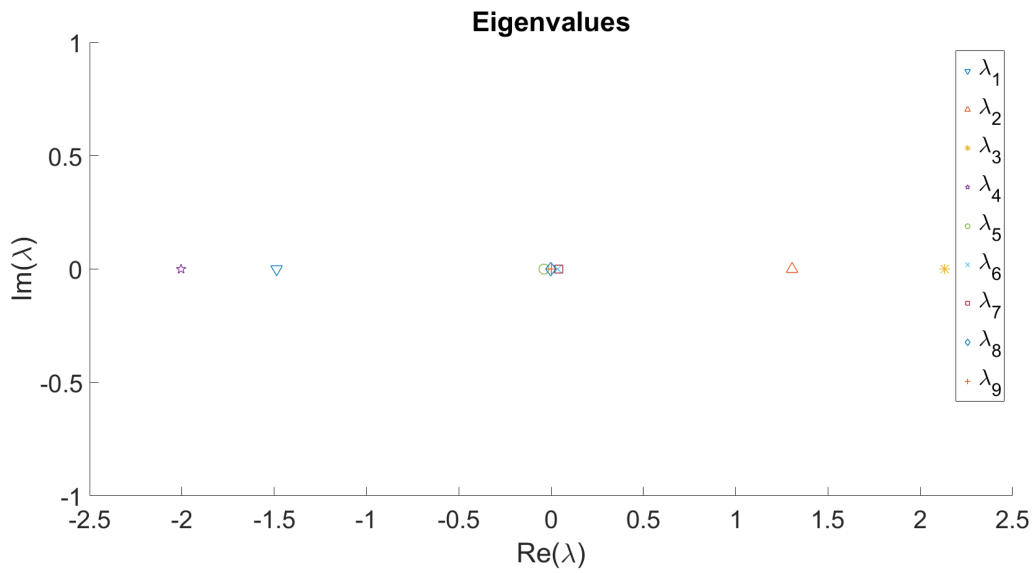

Figure 7.17: Eigenvalues at Mach 2 for a c.o.m. position at 61% of the vehicle length at an altitude of 20 km.

	FSPO		PM		FLO		ARM		HM
	λ_1	λ_2	λ_3	λ_4	λ_5	λ_6	λ_7	λ_8	λ_9
Re	-1.4872	1.3049	-0.0382	0.0360	2.1329	-2.0045	0.0411	3.8024E-15	-3.0846E-05
Im	0.0000	0.0000	0.0000	0.0000	0.0000	0.0000	0.0000	0.0000	0.0000
P [s]	0.0000	0.0000	0.0000	0.0000	0.0000	0.0000	0.0000	0.0000	0.0000
$T_{1/2}$ [s]	0.4661	-0.5312	18.1589	-19.2529	-0.3250	0.3458	-16.8666	-1.8229E+14	2.2471E+04
ζ [-]	1.0000	-1.0000	1.0000	-1.0000	-1.0000	1.0000	-1.0000	-1.0000	1.0000
ω_n [rad/s]	1.4872	1.3049	0.0382	0.0360	2.1329	2.0045	0.0411	3.8024E-15	3.0846E-05
	z	**z**	**z**	**z**	**z**	**z**	**z**	**z**	**z**
ΔV	2.0351E-01	2.0501E-01	1.7714E-02	1.5636E-02	1.9130E-15	3.1603E-15	1.9569E-15	5.4379E-14	3.7131E-05
$\Delta\gamma$	2.4414E-03	2.1355E-03	6.9525E-05	5.7874E-05	2.5763E-17	1.1263E-17	2.0984E-17	4.6580E-17	4.3939E-08
ΔR	9.7841E-01	9.7830E-01	9.9984E-01	9.9988E-01	2.8173E-12	4.1676E-12	4.3443E-13	1.3236E-09	1.0000E+00
Δp	2.1176E-19	1.2257E-18	6.0983E-20	3.3992E-19	7.7959E-01	7.7314E-01	4.0646E-02	2.1918E-04	4.2622E-21
Δq	2.8686E-02	2.4720E-02	2.1223E-06	2.8361E-06	2.1926E-18	5.3942E-18	4.9231E-19	1.1814E-18	3.5746E-10
Δr	1.3600E-19	7.3115E-19	3.9741E-20	2.7477E-19	4.5730E-01	4.5351E-01	2.3843E-02	1.6752E-02	1.1905E-18
$\Delta\alpha$	2.1729E-02	1.6807E-02	1.8633E-05	1.6536E-05	1.9372E-18	3.6784E-18	2.1710E-18	5.7257E-17	3.9144E-08
$\Delta\beta$	7.9938E-20	3.3437E-19	8.0903E-20	1.0264E-19	1.5733E-01	1.4664E-01	1.5805E-04	2.8943E-18	2.0661E-21
$\Delta\sigma$	1.9959E-19	8.3066E-19	7.9908E-19	8.1813E-18	3.9796E-01	4.1842E-01	9.9889E-01	9.9986E-01	7.1497E-17

Table 7.10: Motion characteristics and eigenvectors for all eigenvalues at a c.o.m. at 61% of the vehicle, a Mach number of 2 and an altitude of 20 km.

Forward c.o.m.

Moving the center of mass forward will change the moments around the Y-axis and Z-axis and the corresponding moment coefficients. As was already shown in Table 7.3 and Table 7.4, this makes C_{m_α} negative (static stability) and brings the other coefficients closer to zero.

Figure 7.18 shows the eigenvalues for the case with the c.o.m. moved forward. The first thing to notice is that two motions have become periodic, indicated by their non-zero imaginary parts. Because of this periodicity, there are only 7 motions instead of the previous 9. For a closer look Table 7.11 and 7.12 can be used. Compared to the aft center of mass the short period oscillation and phugoid are now periodic and stable. This means that the longitudinal motions are stable except for the height mode, which is not an issue due to the long doubling time. The slow aperiodic roll motion has also become stable, while the fast aperiodic roll motion's doubling time has increased from 17 seconds to 55 seconds. In other words, the modes have become (more) stable.

The only motion that has not changed significantly and will continue to cause stability problems is the unstable lateral oscillation. One major cause is that the yaw derivative still has a negative value: $C_{n_\beta} = -0.0034$. For reference, [Mooij, 1997] gives a positive value of $C_{n_\beta} = 0.0004$. According to this same source, the simulated value is expected to be found around Mach 10, while the sign of C_{n_β} should switch from negative (unstable) to positive (stable) between Mach 2 and Mach 3. This means that it is paramount that the value of C_{n_β} is investigated further as it is quite critical in the stability of the HORUS at Mach 2.

The next question is how much the Mach dependency influences the stability. The reason this is investigated is because it has a significant influence on a number of stability matrix coefficients and it may be less accurate in the transonic regime.

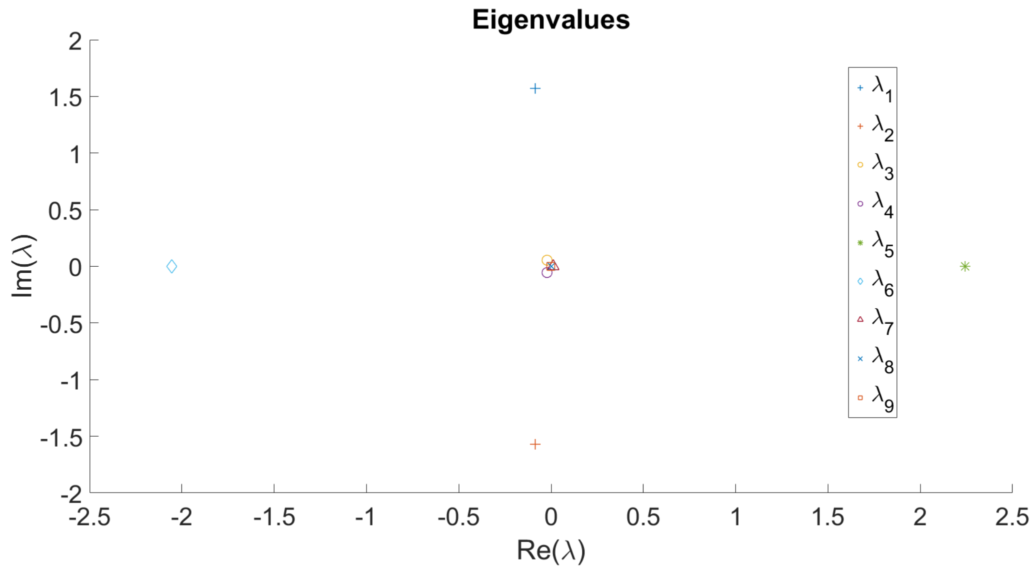

Figure 7.18: Eigenvalues at Mach 2 for a c.o.m. position at 56% of the vehicle length at an altitude of 20 km.

	SPO	PM	LO		ARM		HM
	$\lambda_{1,2}$	$\lambda_{3,4}$	λ_5	λ_6	λ_7	λ_8	λ_9
Re	-0.0858	-0.0230	2.2434	-2.0559	0.0127	-5.9422E-15	1.7910E-05
Im	±1.5682	±0.0520	0.0000	0.0000	0.0000	0.0000	0.0000
P [s]	4.0067	120.7515	0.0000	0.0000	0.0000	0.0000	0.0000
$T_{1/2}$ [s]	8.0742	30.1934	-0.3090	0.3372	-54.6753	1.1665E+14	-3.8703E+04
ζ [-]	0.0547	0.4037	-1.0000	1.0000	-1.0000	1.0000	-1.0000
ω_n [rad/s]	1.5705	0.0569	2.2434	2.0559	0.0127	5.9422E-15	1.7910E-05

Table 7.11: Motion characteristics and eigenvectors for all eigenvalues at a c.o.m. at 56% of the vehicle, a Mach number of 2 and an altitude of 20 km.

	SPO		PM		LO		ARM		HM
	$\lambda_{1,2}$		$\lambda_{3,4}$		λ_5	λ_6	λ_7	λ_8	λ_9
	z	$\theta(°)$	**z**	$\theta(°)$	**z**	**z**	**z**	**z**	**z**
ΔV	2.285E-01	270	1.662E-02	228	2.900E-16	8.457E-17	1.106E-15	5.723E-13	1.575E-05
$\Delta\gamma$	2.560E-03	93	9.577E-05	116	3.733E-17	3.910E-17	4.076E-18	9.757E-16	2.690E-08
ΔR	9.728E-01	0	9.999E-01	0	6.217E-11	5.618E-11	6.343E-11	3.635E-08	1.000E+00
Δp	6.539E-21	180	5.653E-21	172	5.175E-01	5.182E-01	1.326E-02	7.776E-04	1.694E-20
Δq	3.213E-02	272	4.837E-06	245	1.064E-18	6.590E-19	1.858E-20	1.026E-17	2.807E-10
Δr	1.042E-21	173	1.611E-21	106	7.431E-01	7.441E-01	1.904E-02	1.685E-02	3.699E-19
$\Delta\alpha$	2.043E-02	186	2.382E-05	228	1.788E-19	1.045E-19	1.572E-18	8.174E-16	2.249E-08
$\Delta\beta$	3.066E-22	86	1.765E-23	43	3.125E-01	2.867E-01	4.524E-05	1.896E-17	4.377E-23
$\Delta\sigma$	4.088E-21	267	9.938E-20	238	2.869E-01	3.090E-01	9.997E-01	9.999E-01	2.192E-17

Table 7.12: Motion characteristics and eigenvectors for all eigenvalues at a c.o.m. at 56% of the vehicle, a Mach number of 2 and an altitude of 20 km.

Neglecting Mach effects

Variations in the Mach number can have a large effect on the pressure and drag on a vehicle, for example due to changing shocks and effects on the control surfaces. This could therefore be expected to be one of the most inaccurate derivatives. This can be investigated by setting all derivatives with respect to the Mach number equal to zero, which has been done for this case. Figure 7.19 shows that again there are 8 eigenmotions of which 1 is periodic. This means that one of the motions has turned from aperiodic to periodic. The other eigenvalues seem to not have changed much. Table 7.13 and Table 7.14 show that the only motions that are noticeably impacted are the phugoid and the height mode. The phugoid is the mode that has become periodic and is now stable. The height mode has changed from stable to unstable, but the doubling time is large so it is corrigible by a controller or pilot. Concluding, the inclusion of Mach effects makes 1 mode stable. However, the critical motions at Mach 2, the short period oscillation and the lateral oscillation still have an unstable motion with a short doubling time, so the stability picture is equally critical for both cases.

The final in-depth analysis is what the effects of a different altitude is. This is important in case the reference trajectory is not exactly followed, which is a real risk if the entry conditions are different than expected.

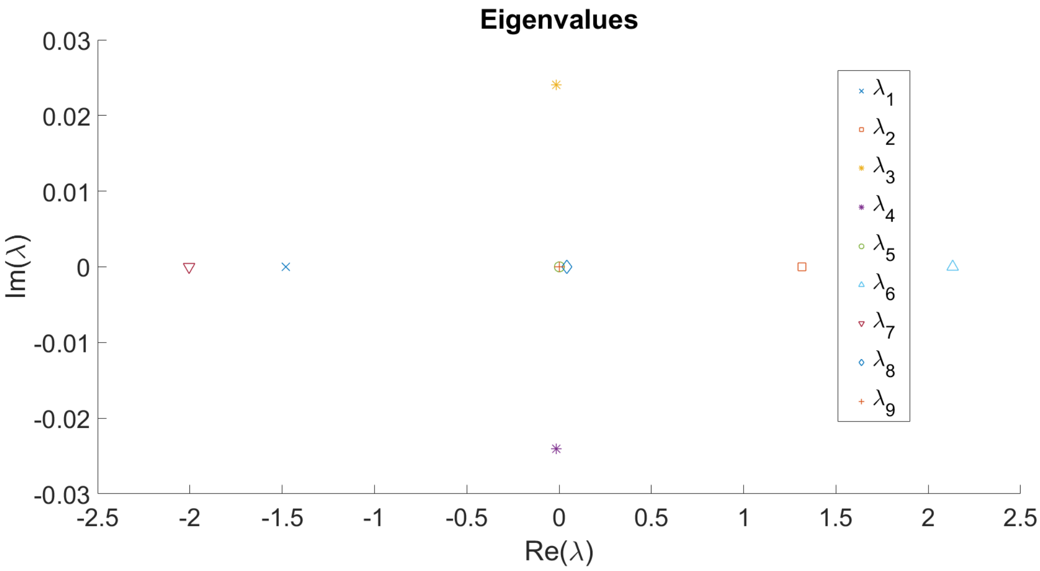

Figure 7.19: Eigenvalues at Mach 2 for a c.o.m. position at 61% of the vehicle length at an altitude of 20 km, neglecting Mach effects.

	FSPO		PM	LO		ARM		HM
	λ_1	λ_2	$\lambda_{3,4}$	λ_5	λ_6	λ_7	λ_8	λ_9
Re	-1.4805	1.3141	-0.0147	2.1329	-2.0045	0.0411	2.1079E-16	8.7001E-05
Im	0.0000	0.0000	±0.0241	0.0000	0.0000	0.0000	0.0000	0.0000
P [s]	0.0000	0.0000	261.1129	0.0000	0.0000	0.0000	0.0000	0.0000
$T_{1/2}$ [s]	0.4682	-0.5275	47.0278	-0.3250	0.3458	-16.8666	-3.2883E+15	-7.9671E+03
ζ [-]	1.0000	-1.0000	0.5223	-1.0000	1.0000	-1.0000	-1.0000	-1.0000
ω_n [rad/s]	1.4805	1.3141	0.0282	2.1329	2.0045	0.0411	2.1079E-16	8.7001E-05

Table 7.13: Motion characteristics and eigenvectors for all eigenvalues at a c.o.m. at 61% of the vehicle, a Mach number of 2 and an altitude of 20 km, neglecting Mach effects.

	FSPO		PM		LO		ARM		HM
	λ_1	λ_2	$\lambda_{3,4}$		λ_5	λ_6	λ_7	λ_8	λ_9
	z	**z**	**z**	θ(°)	**z**	**z**	**z**	**z**	**z**
ΔV	2.036E-01	2.052E-01	1.664E-02	243	1.039E-17	1.338E-17	2.294E-17	6.518E-19	6.359E-05
$\Delta\gamma$	2.430E-03	2.151E-03	4.635E-05	126	5.935E-18	5.996E-18	2.675E-19	3.791E-19	1.337E-07
ΔR	9.784E-01	9.782E-01	9.999E-01	0	1.358E-14	1.602E-14	1.473E-15	5.236E-15	1.000E+00
Δp	2.576E-20	2.934E-20	2.849E-21	184	7.796E-01	7.731E-01	4.065E-02	2.192E-04	2.992E-21
Δq	2.821E-02	2.529E-02	1.141E-06	248	4.034E-19	8.710E-19	7.566E-22	1.273E-21	6.662E-10
Δr	0.000E+00	0.000E+00	0.000E+00	0	4.573E-01	4.535E-01	2.384E-02	1.675E-02	0.000E+00
$\Delta\alpha$	2.148E-02	1.710E-02	1.655E-08	9	1.613E-18	1.155E-18	1.186E-19	1.098E-19	2.981E-14
$\Delta\beta$	0.000E+00	0.000E+00	0.000E+00	0	1.573E-01	1.466E-01	1.581E-04	8.683E-18	0.000E+00
$\Delta\sigma$	0.000E+00	0.000E+00	0.000E+00	0	3.980E-01	4.184E-01	9.989E-01	9.999E-01	0.000E+00

Table 7.14: Norms and arguments of the eigenvectors at a c.o.m. at 61% of the vehicle, a Mach number of 2 and an altitude of 20 km, neglecting Mach effects.

Effect of altitude

The final case that will be investigated for Mach 2 will be for a lower altitude. This can help to provide clarity on what effects deviations from the reference trajectory have on the dynamic stability. Comparing Figure 7.20 (19 km) to Figure 7.19 (20 km), the main observation is that the differences are very small, with the largest effects for the motions with eigenvalue real parts close to zero. No motions have changed from aperiodic to periodic. Table 7.15 allows for a more detailed investigation. The largest difference can be found in the phugoid motion, which has become worse from a stability point of view. The doubling time for the unstable phugoid motion has decreased significantly to 7 seconds while the half time for the stable phugoid motion has increased to 41 seconds. The unstable motions have generally become worse with shorter doubling times. Finally, the height mode has become unstable, though the doubling time is still large.

In conclusion, lowering the altitude decreases stability. As the general picture of the stability with the center of mass at 61% length at Mach 2 was not good at the original altitude, undershooting the reference trajectory makes it worse.

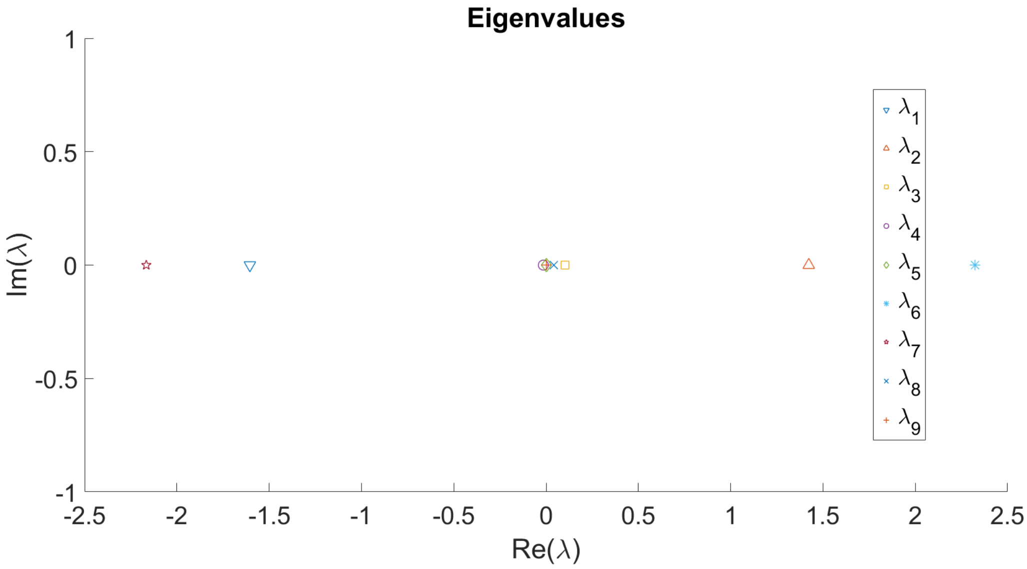

Figure 7.20: Eigenvalues at Mach 2 for a c.o.m. position at 61% of the vehicle length at an altitude of 19 km.

	FSPO		PM		LO		ARM		HM
	λ_1	λ_2	λ_3	λ_4	λ_5	λ_6	λ_7	λ_8	λ_9
Re	-1.6053	1.4222	0.1020	-0.0167	2.3230	-2.1645	0.0404	7.1679E-15	1.2742E-04
Im	0.0000	0.0000	0.0000	0.0000	0.0000	0.0000	0.0000	0.0000	0.0000
P [s]	0.0000	0.0000	0.0000	0.0000	0.0000	0.0000	0.0000	0.0000	0.0000
$T_{1/2}$ [s]	0.4318	-0.4874	-6.7962	41.4613	-0.2984	0.3202	-17.1523	-9.6701E+13	-5.4398E+03
ζ [-]	1.0000	-1.0000	-1.0000	1.0000	-1.0000	1.0000	-1.0000	-1.0000	-1.0000
ω_n [rad/s]	1.6053	1.4222	0.1020	0.0167	2.3230	2.1645	0.0404	7.1679E-15	1.2742E-04
	z	**z**	**z**	**z**	**z**	**z**	**z**	**z**	**z**
ΔV	2.0907E-01	2.3422E-01	1.0112E-01	2.7224E-03	2.7715E-17	3.7350E-17	4.5339E-17	6.4267E-19	2.9905E-05
$\Delta\gamma$	2.6343E-03	2.3090E-03	1.4955E-04	2.9255E-05	1.3784E-18	1.3997E-18	1.0745E-19	1.1448E-21	2.2516E-07
ΔR	9.7716E-01	9.7167E-01	9.9487E-01	1.0000E+00	3.8525E-12	3.8188E-12	1.9667E-13	2.5062E-14	1.0000E+00
Δp	2.8674E-21	4.9402E-21	2.9358E-21	3.4795E-21	7.9040E-01	7.8378E-01	4.0498E-02	7.4418E-04	3.3874E-21
Δq	3.1049E-02	2.6796E-02	9.8209E-06	5.6606E-07	1.0341E-18	8.3801E-19	2.4517E-20	5.5941E-22	4.5144E-10
Δr	0.0000E+00	0.0000E+00	0.0000E+00	0.0000E+00	4.6481E-01	4.6092E-01	2.3816E-02	1.6844E-02	0.0000E+00
$\Delta\alpha$	2.1974E-02	1.6529E-02	6.9618E-05	1.8903E-06	6.5390E-19	6.8262E-19	3.8734E-20	5.6711E-22	2.0718E-08
$\Delta\beta$	0.0000E+00	0.0000E+00	0.0000E+00	0.0000E+00	1.4827E-01	1.3700E-01	1.3216E-04	3.1355E-17	0.0000E+00
$\Delta\sigma$	0.0000E+00	0.0000E+00	0.0000E+00	0.0000E+00	3.7045E-01	3.9304E-01	9.9890E-01	9.9986E-01	0.0000E+00

Table 7.15: Motion characteristics and eigenvectors for all eigenvalues at a c.o.m. at 61% of the vehicle, a Mach number of 2 and an altitude of 19 km.

LOW SUPERSONIC (MACH 1.2)

After analyzing a range of different conditions for Mach 2, now the case for Mach 1.2 will be discussed. Figure 7.21 paints a different picture of the stability at Mach 1.2 compared to Mach 2. Three of the motions have become periodic, meaning there are only 6 separate motions. Furthermore, there is only 1 motion that is clearly unstable because it has a significant positive eigenvalue real part. Table 7.16 and 7.17 can be used for more detail.

Both the short period oscillation and the phugoid motion are now stable and periodic, with half times of 3 seconds and 16 seconds respectively. The only longitudinal motion that is not stable is the height mode, but similar to all the previous cases the doubling time is large (on the order of hours). The lateral stability situation has improved compared to Mach 2 and a center of mass at 61% length, as the fast aperiodic roll motion is now stable with a half time of only 5 seconds. The largest stability problem is still caused by the lateral oscillation. This motion is aperiodic and unstable for this Mach number, with a doubling time on the order of 3 seconds. This doubling time is an improvement compared to the Mach 2 case as a doubling time of 3 seconds is within the realm of human corrigibility and entirely possible for an automated controller. In general, at Mach 1.2 seems quite stable with the most critical motion being the lateral oscillation.

Checking back with Table 7.6 regarding the static stability coefficients, the improvements in stability are likely due to the now negative pitch moment coefficient C_{m_α} and the positive value of C_{n_β}. Why not all motions are stable is not completely clear. The lateral oscillation eigenvalues at higher Mach number from [Mooij, 1997] show that all lateral oscillations are unstable, so it is not unexpected that it stays unstable at lower Mach numbers.

For this Mach number it will also be investigated what influence a forward shift of the center of mass, in the same way as for Mach 2.

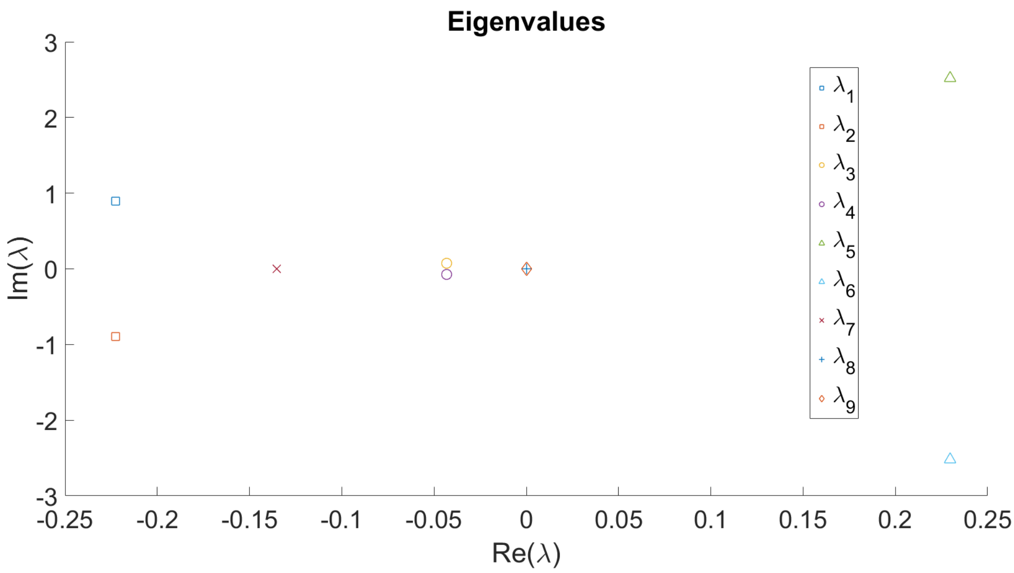

Figure 7.21: Eigenvalues at Mach 1.2 for a c.o.m. position at 61% of the vehicle length at an altitude of 12 km.

	SPO	PM	LO	ARM		HM
	$\lambda_{1,2}$	$\lambda_{3,4}$	$\lambda_{5,6}$	λ_7	λ_8	λ_9
Re	-0.2225	-0.0432	0.2298	-0.1353	1.2148E-16	2.0964E-05
Im	±0.8981	±0.0755	±2.5235	0.0000	0.0000	0.0000
P [s]	6.9957	83.2163	2.4899	0.0000	0.0000	0.0000
$T_{1/2}$ [s]	3.1156	16.0335	-3.0161	5.1246	-5.7058E+15	-3.3063E+04
ζ [-]	0.2404	0.4969	-0.0907	1.0000	-1.0000	-1.0000
ω_n [rad/s]	0.9253	0.0870	2.5339	0.1353	1.2148E-16	2.0964E-05

Table 7.16: Motion characteristics and eigenvectors for all eigenvalues at a c.o.m. at 61% of the vehicle, a Mach number of 1.2 and an altitude of 12 km.

	SPO		PM		LO		ARM		HM
	$\lambda_{1,2}$		$\lambda_{3,4}$		$\lambda_{5,6}$		λ_7	λ_8	λ_9
	z	θ(°)	**z**	θ(°)	**z**	θ(°) **z**	**z**	**z**	**z**
ΔV	1.291E-01	275	2.764E-02	61	7.521E-17	72	1.124E-16	1.295E-14	1.147E-05
$\Delta\gamma$	2.566E-03	104	2.425E-04	302	1.707E-17	1	1.235E-18	6.394E-17	5.524E-08
ΔR	9.916E-01	0	9.996E-01	180	6.728E-12	19	1.136E-13	1.131E-09	1.000E+00
Δp	2.245E-20	266	8.480E-21	294	9.295E-01	0	1.279E-01	4.210E-03	2.571E-21
Δq	4.732E-03	282	1.722E-05	69	1.325E-18	173	1.052E-19	1.270E-18	1.225E-09
Δr	6.692E-21	16	4.494E-21	178	3.493E-02	180	4.806E-03	2.859E-02	4.042E-20
$\Delta\alpha$	5.050E-03	207	2.823E-05	59	7.680E-19	60	1.283E-19	1.268E-17	1.127E-08
$\Delta\beta$	5.456E-21	120	3.262E-22	295	7.800E-02	265	5.729E-04	2.462E-17	7.468E-22
$\Delta\sigma$	2.369E-20	6	9.808E-20	320	3.588E-01	95	9.918E-01	9.996E-01	1.348E-18

Table 7.17: Motion characteristics and eigenvectors for all eigenvalues at a c.o.m. at 61% of the vehicle, a Mach number of 1.2 and an altitude of 12 km.

Forward c.o.m.

Figure 7.22 shows the eigenvalues for the motions at Mach 1.2 and a c.o.m. at 56% of the length of HORUS. The general picture of the stability does not change much, but there are some differences. First of all, the imaginary values of the left-most and right-most conjugate pairs have increased (shorter periods), while that of the middle pair has decreased (longer periods). The range of the real parts has also increased, with the left-most eigenvalue pair becoming more negative and the right-most pair becoming more positive.

Table 7.18 and 7.19 show that the effects of these changes on the general stability picture is minor. The half time of the short period oscillation has become smaller, while those of the phugoid and fast aperiodic roll motion have become larger. The slow aperiodic roll motion has become stable, but this is still irrelevant to the general stability situation due to its large half/doubling time. Because the doubling time of the lateral oscillation has slightly decreased the overall stability situation has worsened slightly, but the impact is limited.

The forward shift in c.o.m. does not produce such a significant effect compared to the Mach 2 case. The difference is that the aerodynamic center was already behind the center of mass for the c.o.m. position at 61% of the length, as evidenced by the negative value of C_{m_α}. Because of this a forward shift in center of mass will only make a small difference, while a shift of the center of mass to the back might make certain motions unstable again.

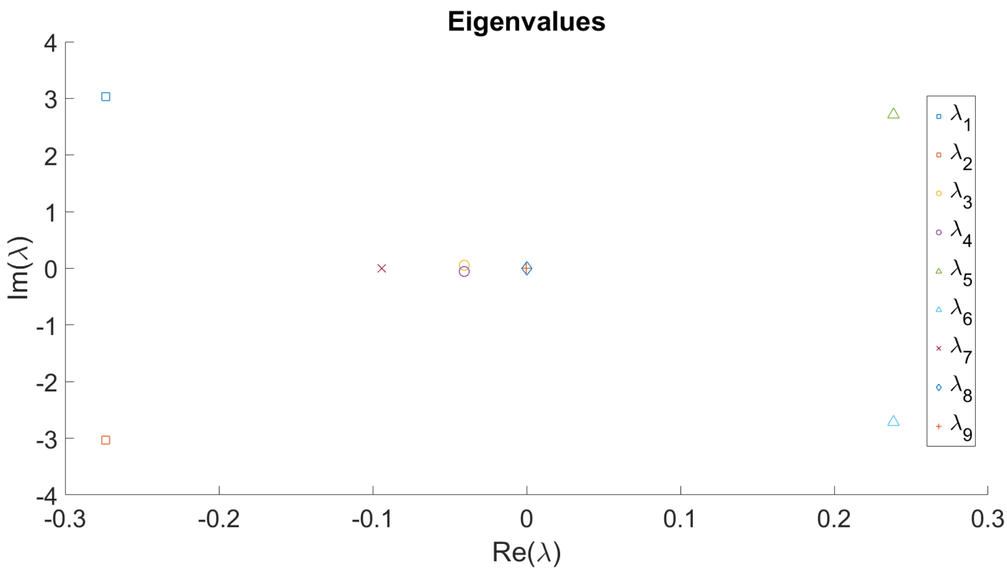

Figure 7.22: Eigenvalues at Mach 1.2 for a c.o.m. position at 56% of the vehicle length at an altitude of 12 km.

	SPO	Phugoid	LO	APR		HM
	$\lambda_{1,2}$	$\lambda_{3,4}$	$\lambda_{5,6}$	λ_7	λ_8	λ_9
Re	-0.2736	-0.0404	0.2386	-0.0940	-1.0186E-16	4.2425E-05
Im	±3.0357	±0.0516	±2.7118	0.0000	0.0000	0.0000
P [s]	2.0698	121.8531	2.3170	0.0000	0.0000	0.0000
$T_{1/2}$ [s]	2.5335	17.1660	-2.9050	7.3759	6.8047E+15	-1.6338E+04
ζ [-]	0.0898	0.6165	-0.0876	1.0000	1.0000	-1.0000
ω_n [rad/s]	3.0480	0.0655	2.7223	0.0940	1.0186E-16	4.2425E-05

Table 7.18: Motion characteristics and eigenvectors for all eigenvalues at a c.o.m. at 56% of the vehicle, a Mach number of 1.2 and an altitude of 12 km.

	SPO		Phugoid		LO		ARM		HM
	$\lambda_{1,2}$		$\lambda_{3,4}$		$\lambda_{5,6}$		λ_7	λ_8	λ_9
	z	$\theta(°)$	**z**	$\theta(°)$	**z**	$\theta(°)$ **z**	**z**	**z**	**z**
ΔV	3.950E-01	93	2.768E-02	256	2.871E-16	162	4.644E-15	8.216E-13	1.982E-05
$\Delta\gamma$	7.739E-03	275	1.801E-04	131	3.250E-17	353	1.215E-17	4.672E-15	1.131E-07
ΔR	9.084E-01	180	9.996E-01	0	8.431E-12	200	2.135E-11	4.176E-08	1.000E+00
Δp	1.102E-19	1	6.504E-21	262	9.292E-01	0	8.635E-02	5.838E-03	4.252E-21
Δq	1.303E-01	95	7.787E-06	262	3.542E-17	273	1.096E-18	1.179E-16	2.772E-09
Δr	7.816E-21	161	2.392E-21	158	1.330E-01	180	1.236E-02	2.888E-02	6.708E-21
$\Delta\alpha$	4.272E-02	10	4.623E-06	256	1.178E-17	193	8.202E-19	1.361E-16	3.283E-09
$\Delta\beta$	8.315E-21	256	1.652E-23	77	1.080E-01	265	3.463E-04	1.431E-18	2.729E-23
$\Delta\sigma$	3.628E-20	90	1.183E-19	319	3.276E-01	95	9.962E-01	9.996E-01	2.309E-19

Table 7.19: Motion characteristics and eigenvectors for all eigenvalues at a c.o.m. at 56% of the vehicle, a Mach number of 1.2 and an altitude of 12 km.

TRANSONIC (MACH 0.8)

The eigenvalues for Mach 0.8 are shown in Figure 7.23. The picture is quite different compared to Mach 2 or Mach 1.2. There are 2 conjugate pairs of eigenvalues and thus periodic motions, bringing the number of separate motions to 7. Of the periodic motions one is clearly unstable (with a significant positive eigenvalue real part) and the other one has an eigenvalue real part just below zero and is thus stable.

Table 7.20 and 7.21 give more insight into the motions. Compared to Mach 1.2, the former short period oscillation has become aperiodic again with one stable and one unstable motion, with the latter having a doubling time of 0.3 seconds. The cause of the aperiodic FSPO is that C_{m_α} has become positive again, implicating that the center of mass is behind the aerodynamic center. The aperiodic roll motion has become stable in this situation, while the lateral oscillation is still unstable with a doubling time of around 2 seconds.

The general stability situation has worsened compared to the low supersonic case at Mach 1.2. The unstable motion of the former short period oscillation diverges rapidly and is thus hard to correct. As discussed in the aerodynamic analysis, there is a shock on the vehicle, specifically the wing. This shock and corresponding rapid pressure change the pressure distribution on the wing, leading to the positive value of C_{m_α} and thus the unstable motion in the FSPO. Whether the FSPO becomes stable again for a more forward center of mass will be investigated next.

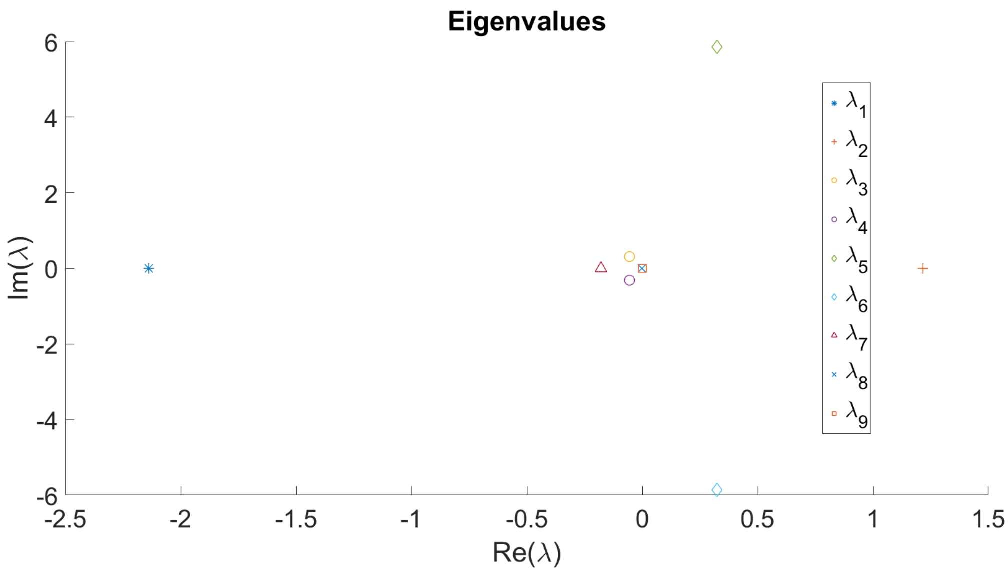

Figure 7.23: Eigenvalues at Mach 0.8 for a c.o.m. position at 61% of the vehicle length at an altitude of 5 km.

	FSPO		PM	LO	ARM		HM
	λ_1	λ_2	$\lambda_{3,4}$	$\lambda_{5,6}$	λ_7	λ_8	λ_9
Re	-2.1374	1.2165	-0.0553	0.3244	-0.1786	-5.5723E-16	-8.6935E-06
Im	0.0000	0.0000	±0.3043	±5.8583	0.0000	0.0000	0.0000
P [s]	0.0000	0.0000	20.6446	1.0725	0.0000	0.0000	0.0000
$T_{1/2}$ [s]	0.3243	-0.5698	12.5315	-2.1370	3.8803	1.2439E+15	7.9732E+04
ζ [-]	1.0000	-1.0000	0.1788	-0.0553	1.0000	1.0000	1.0000
ω_n [rad/s]	2.1374	1.2165	0.3093	5.8673	0.1786	5.5723E-16	8.6935E-06

Table 7.20: Motion characteristics and eigenvectors for all eigenvalues at a c.o.m. at 61% of the vehicle, a Mach number of 0.8 and an altitude of 5 km.

	FSPO		PM		LO		ARM		HM
	λ_1	λ_2	$\lambda_{3,4}$		$\lambda_{5,6}$		λ_7	λ_8	λ_9
	z	**z**	**z**	$\theta(°)$	**z**	$\theta(°)$	**z**	**z**	**z**
ΔV	9.070E-02	1.031E-02	3.930E-02	196	3.098E-17	90	4.859E-17	1.941E-14	1.196E-06
$\Delta\gamma$	8.428E-03	4.784E-03	1.215E-03	101	2.158E-17	0	1.046E-18	5.667E-16	3.489E-08
ΔR	9.953E-01	9.998E-01	9.992E-01	0	1.458E-12	20	1.590E-13	1.622E-08	1.000E+00
Δp	2.358E-19	1.258E-19	5.741E-20	87	9.845E-01	180	1.667E-01	6.836E-03	8.841E-20
Δq	2.477E-02	1.371E-02	3.644E-04	219	1.022E-18	0	5.548E-19	4.548E-18	2.828E-10
Δr	1.771E-20	1.888E-20	2.289E-20	354	4.966E-02	0	8.408E-03	3.964E-02	4.488E-19
$\Delta\alpha$	2.003E-02	6.488E-03	3.577E-04	201	2.635E-19	186	4.165E-19	1.880E-16	1.159E-08
$\Delta\beta$	4.884E-21	2.963E-21	3.065E-21	23	3.759E-02	87	1.938E-04	7.719E-18	5.770E-23
$\Delta\sigma$	1.171E-19	1.125E-19	4.072E-19	114	1.638E-01	273	9.860E-01	9.992E-01	1.149E-17

Table 7.21: Norms and arguments of the eigenvectors at a c.o.m. at 61% of the vehicle length, a Mach number of 0.8 and an altitude of 5 km

Forward c.o.m.

Figure 7.24 shows the effect of the forward shift in center of mass on the eigenvalues. The eigenvalues have become much more spread out, with 3 motions that are clearly stable (negative real part), 2 motions that are clearly unstable (positive real part) and only 2 motions with eigenvalue real parts around zero. Table 7.22 and Table 7.23 give more insight in the motions. Regarding the longitudinal stability, the short period oscillation has become periodic and stable due to the now negative C_{m_α}, while the phugoid motion has become aperiodic with one stable and one unstable motion. This is an improvement of the stability because the doubling time is longer for this motion and the phugoid does not include large changes in angle of attack, which could be hazardous due to stall condition considerations.

The lateral motions have not changed significantly, with the lateral oscillation still being unstable with a doubling time of around 2 seconds. This means that while the forward shift in the center of mass does aid the stability of HORUS somewhat, it does not provide complete stability. It is possible that when the flow around the vehicle is completely subsonic again at lower Mach numbers that the motions are more stable again, but this investigation is outside the scope of this thesis.

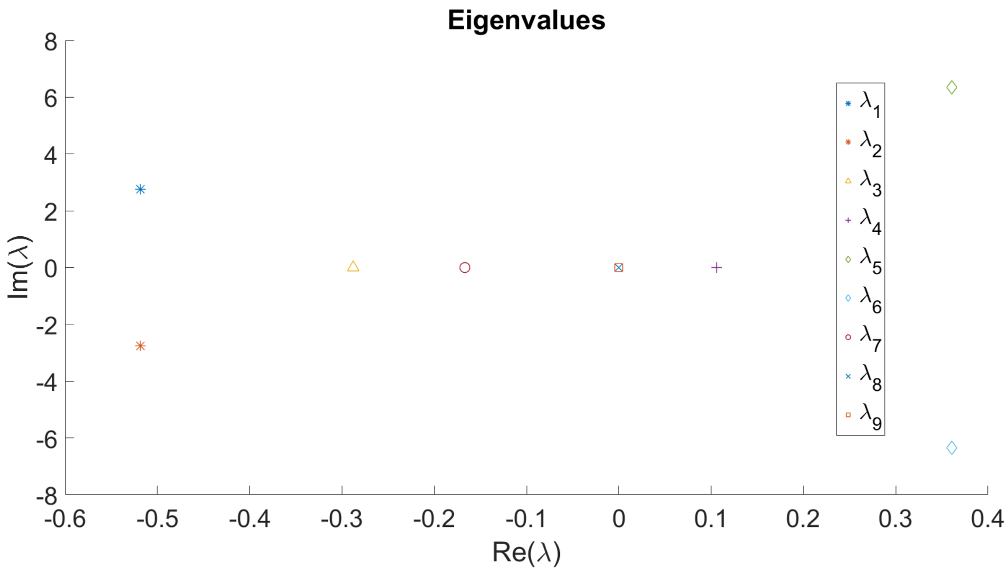

Figure 7.24: Eigenvalues at Mach 0.8 for a c.o.m. position at 56% of the vehicle length at an altitude of 5 km.

	SPO	PM		LO	ARM		HM
	$\lambda_{1,2}$	λ_3	λ_4	$\lambda_{5,6}$	λ_7	λ_8	λ_9
Re	-0.5181	-0.2881	0.1062	0.3608	-0.1671	-4.8657E-16	-2.9011E-05
Im	±2.7658	0.0000	0.0000	±6.3463	0.0000	0.0000	0.0000
P [s]	2.2717	0.0000	0.0000	0.9901	0.0000	0.0000	0.0000
$T_{1/2}$ [s]	1.3378	2.4058	-6.5278	-1.9210	4.1482	1.4246E+15	2.3893E+04
ζ [-]	0.1841	1.0000	-1.0000	-0.0568	1.0000	1.0000	1.0000
ω_n [rad/s]	2.8139	0.2881	0.1062	6.3566	0.1671	4.8657E-16	2.9011E-05

Table 7.22: Motion characteristics and eigenvectors for all eigenvalues at a c.o.m. at 56% of the vehicle, a Mach number of 0.8 and an altitude of 5 km.

	SPO		PM		LO		ARM		HM
	λ_1	λ_2	$\lambda_{3,4}$		$\lambda_{5,6}$		λ_7	λ_8	λ_9
	z	$\theta(°)$	**z**	**z**	**z**	$\theta(°)$	**z**	**z**	**z**
ΔV	7.873E-02	312	1.001E-01	1.431E-02	1.109E-17	280	4.660E-17	1.355E-14	3.831E-06
$\Delta\gamma$	1.104E-02	281	1.184E-03	4.103E-04	1.538E-19	191	1.139E-18	3.963E-16	1.121E-07
ΔR	9.930E-01	180	9.950E-01	9.999E-01	2.771E-13	39	7.376E-13	3.537E-09	1.000E+00
Δp	2.471E-20	345	1.212E-19	9.214E-21	9.854E-01	0	1.534E-01	9.268E-03	3.247E-20
Δq	8.193E-02	100	2.383E-04	5.462E-05	3.312E-19	222	3.937E-20	3.907E-18	1.136E-09
Δr	3.187E-21	360	1.052E-21	7.041E-21	6.965E-02	180	1.084E-02	4.007E-02	1.137E-20
$\Delta\alpha$	2.907E-02	21	4.605E-04	6.384E-05	1.947E-19	114	1.953E-19	6.116E-17	1.729E-08
$\Delta\beta$	7.660E-22	100	2.844E-23	4.387E-22	3.781E-02	267	1.548E-04	3.936E-18	1.050E-21
$\Delta\sigma$	1.084E-20	67	4.697E-19	1.940E-19	1.507E-01	93	9.881E-01	9.992E-01	3.351E-19

Table 7.23: Norms and arguments of the eigenvectors at a c.o.m. at 56% of the vehicle length, a Mach number of 0.8 and an altitude of 5 km

7.3.5. SUMMARY OF STABILITY SITUATION FOR ALL SIMULATED CASES.

The results showed that the most critical stability situations at Mach 2 occur for the short period oscillation and/or lateral oscillation, depending on the center of mass location. Moving the center of mass forward improved the stability of the HORUS, as one unstable mode disappeared (SPO) and the other unstable mode (LO) got a longer doubling time. At Mach 1.2 the lateral oscillation was the critical motion for the general stability as it was the only unstable motion with a doubling time on the order of seconds. For the Mach 0.8 case the critical motion was the former short period oscillation and the lateral oscillation for the aft center of mass (61% of length), while for the forward center of mass the lateral oscillation and phugoid motion are most critical with doubling times on the order of seconds.

7.4. SENSITIVITY ANALYSIS

As already shown in Chapter 6, the accuracy of the coefficient predictions varies with the type of coefficient that is calculated. For example, the longitudinal coefficients are generally predicted better than the lateral coefficients. In order to investigate the impact of these uncertainties a sensitivity analysis is performed. For this a Monte Carlo simulation will be used, with a range of values for each coefficient between the simulated value and the reference values. These reference values for the coefficients were obtained from the tables in [Mooij, 1995] for the corresponding Mach number and angle of attack.

For each Monte Carlo iteration motion characteristics such as the period, half time, damping coefficient and natural frequency will be calculated and a histogram of all the outcomes is made. Because the sensitivity of the motions to the coefficients is the area of interest, the outcomes will be grouped by the type of motion and not by the eigenvalue. For modes that have an unstable and a stable motion such as the former short-period oscillation, aperiodic phugoid motion and aperiodic lateral oscillation, the unstable motion will appear in the histograms. This choice is made because the unstable motion determines the total stability of the mode. For periodic modes this does not matter because it will be either stable or unstable.

The histograms shown are those for the half/doubling time and the damping ratio. From the damping ratio histogram it can be determined whether the motions are stable (positive) or unstable (negative) and whether the motions are periodic (damping ratio between -1 and 1) or aperiodic (damping ratio of -1 or 1). The half/doubling time histogram allows for an assessment of the seriousness of instabilities, where short doubling times are a serious issue for the stability.

There will be no sensitivity analysis for Mach 0.8 because there is no reference data available, making the uncertainty large and the conclusions from a sensitivity analysis not very useful. For the sensitivity analyses at Mach 2 and 1.2 the Monte Carlo simulation was performed with 1,000 iterations.

7.4.1. HIGH SUPERSONIC (MACH 2)

The case that was used for this sensitivity analysis is the case with a Mach number of 2 and the center of mass at 61% of the length of the vehicle. The range of the input coefficients is shown in Table 7.24. The histograms corresponding to the longitudinal motions are shown in Figure 7.25 through 7.27. The histograms for the damping ratio of the FSPO and the PM both show that these motions are aperiodic unstable for all inputs. There is some variance in the half times, for the FSPO they are quite close together between 0.43 seconds and 0.54 seconds, while for the PM they are between 14 and 26 seconds with an average of 18 seconds. This increases the confidence that these motions were simulated correctly and that the FSPO is quite critical to the stability. The phugoid motion is not as critical as in all cases the doubling time is 14 seconds or more.

The half time histogram for the height mode in Figure 7.27 does not contain the complete range of values due to some extreme outliers. What is shown is the range between the 5% and 95% quantile. Approximately three-quarters of the half times are lower than 100,000 seconds, while the outliers reach up to 10,000,000 seconds. The damping ratio histogram shows that approximately 90% of the iterations the motion is aperiodic stable, with the remaining 10% being aperiodic unstable. The doubling times for the unstable motion are long for all the iterations, so this is not critical for stability.

Coefficient	Simulated value	Reference value
C_L	0.2026	0.2100
C_D	0.1232	0.0840
C_{L_α}	1.5168	1.8472
C_{D_α}	0.2296	0.4183
C_{m_α}	0.0385	0.0573
C_{S_β}	-1.5720	-1.3121
C_{n_β}	-0.2278	0.0229

Table 7.24: Range of values used for the Monte Carlo simulation.

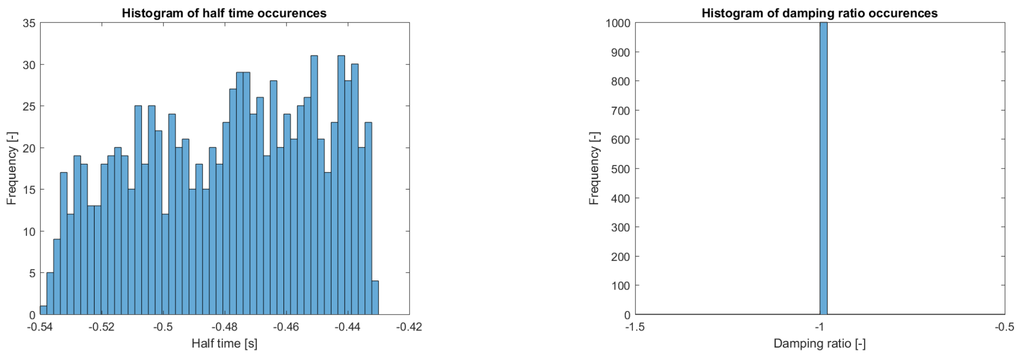

Figure 7.25: Histograms of the FSPO at Mach 2.

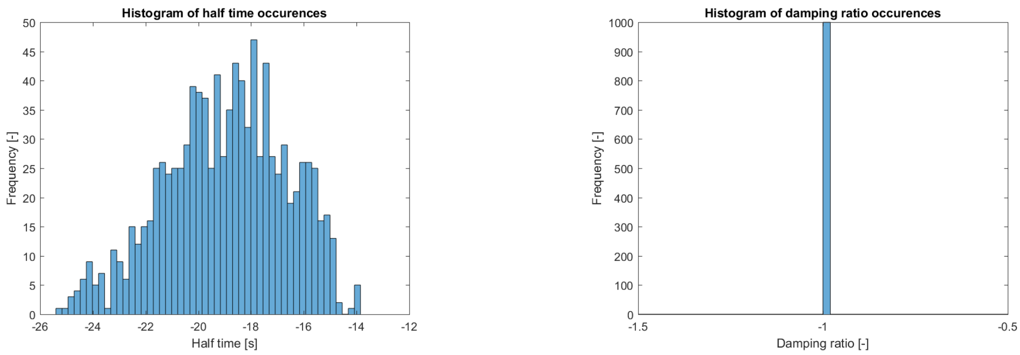

Figure 7.26: Histograms of the PM eigenvalue at Mach 2.

Figures 7.28 through 7.30 show the histograms for the lateral motions. The lateral oscillation damping ratio histogram shows that for all iterations there was an unstable motion present, which is periodic for half of the iterations. The half times vary between 0.3 seconds and 6.5 seconds, which is a rather large variance. The uncertainty in C_{n_β} manifests itself here and this uncertainty needs to be decreased in further research to be able to determine whether this motion is dangerously fast (below 1 second).

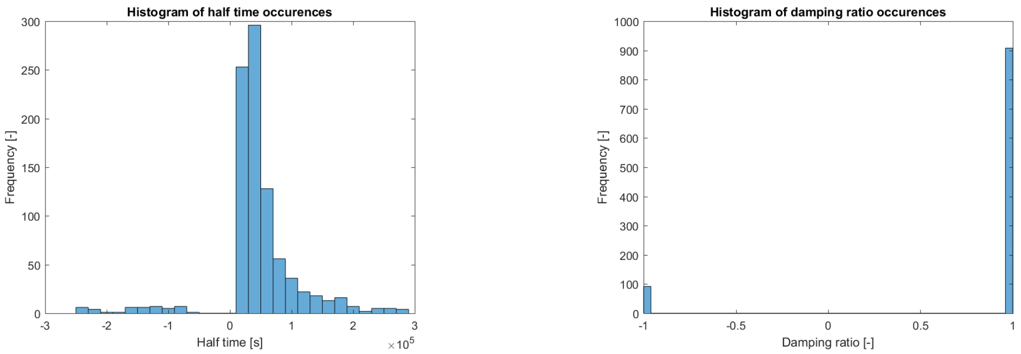

Figure 7.27: Histograms of the HM at Mach 2.

The uncertainty in C_{n_β} also shows itself in the histograms of the fast aperiodic roll motion. The damping ratio histogram shows that the motion can either be aperiodic stable or unstable. Notice that the frequencies combined do not count up to 1000, this is because of certain edge cases where the fast aperiodic roll motion is very similar to an aperiodic lateral oscillation and this motion is not captured by the software. The half/doubling time graph shows that for unstable motions the doubling time will almost always be more than 1 second and is most iteration above 5 seconds (the peak indicated short half times, thus a stable motion). While an improved estimate of C_{n_β} might be helpful here, there Monte Carlo simulation shows that generally this motion is stable or unstable and slow enough to be corrigible on human reaction timescales.

The final mode, the slow aperiodic roll motion is shown to be stable about half of the iterations and always aperiodic according to the damping ratios. The half/doubling time graph shows a large variance, but all half/doubling times are very large (more than 10^{14} seconds). This motion will thus not pose a problem for the stability of the HORUS for any input.

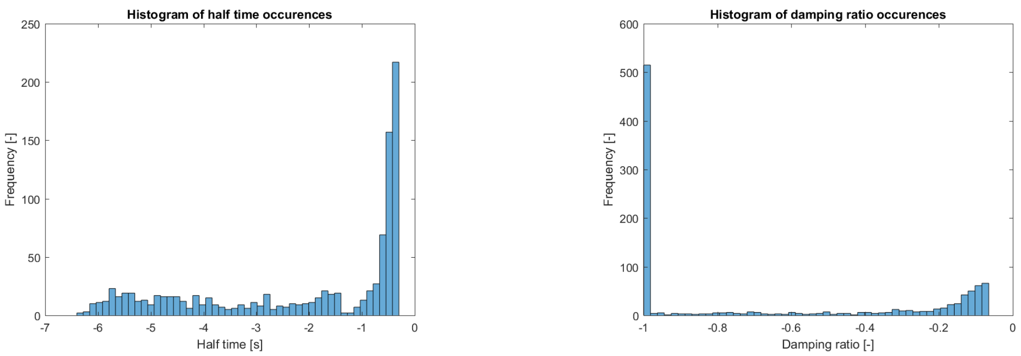

Figure 7.28: Histograms of the LO at Mach 2.

7.4.2. LOW SUPERSONIC (MACH 1.2)

The case that was used for this sensitivity analysis is the case with a Mach number of 1.2 and the center of mass at 61% of the length of the vehicle. The range of the input coefficients is shown in Table 7.25. It is immediately clear that the range is much higher for many coefficients, meaning there is more uncertainty. Three likely causes are the location of the center of mass (at 56% of the length the coefficients are much closer), errors in the estimated altitude at Mach 1.2 and the fact that drag variations with altitude may be significant below Mach 1.5.

The histograms corresponding to the longitudinal motions are shown in Figure 7.31 through 7.33. The histograms for the damping ratio of the SPO and the PM both show that these motions are

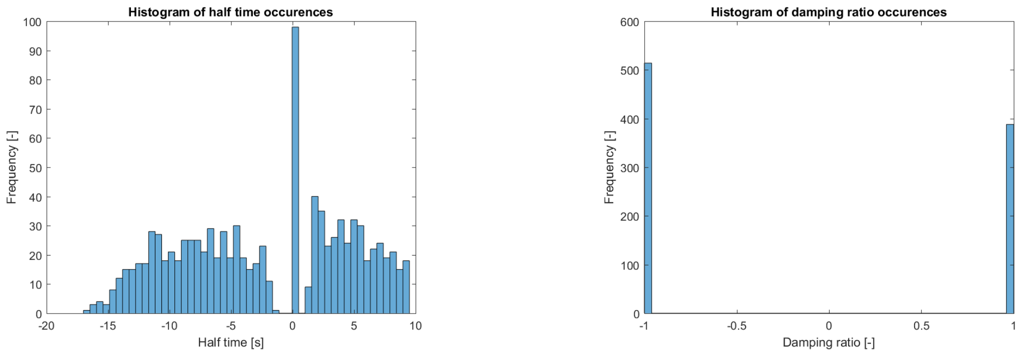

Figure 7.29: Histograms of the fast ARM at Mach 2.

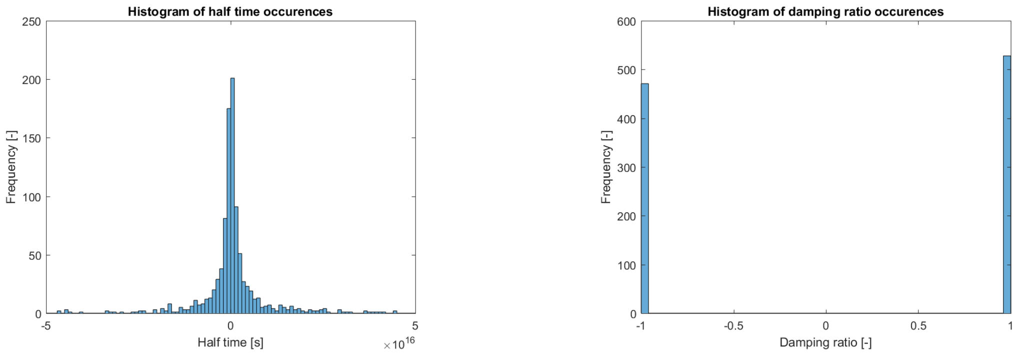

Figure 7.30: Histograms of the slow ARM at Mach 2.

periodic and stable for all inputs. As expected the range of half/doubling times and damping ratios for the short-period oscillation and the phugoid motion are a bit more spread out due to the larger range of Monte Carlo input values. However, for all inputs both of these motions are stable with half times not larger than 3.5 seconds for the short-period oscillation and not larger than 21 seconds for the phugoid motion, so the uncertainty in input does not lead to stability uncertainties.

The height mode in Figure 7.33 is now unstable for the whole input range with half times larger than 10,000 seconds. The type of motion is not very sensitive to the input values, but the doubling time is, with a wide peak of occurrences between 15,000 and 20,000 seconds. Due to the large doubling times, the stability is not affected.

Coefficient	Simulated value	Reference value
C_L	0.2789	0.3500
C_D	0.1786	0.2040
C_{L_α}	2.0082	3.7242
C_{D_α}	0.2906	0.8594
C_{m_α}	-0.0136	-0.1461
C_{S_β}	-1.4340	-2.8648
C_{n_β}	0.0328	0.4985

Table 7.25: Range of values used for the Monte Carlo simulation at Mach 1.2.

Figures 7.34 through 7.36 show the histograms for the lateral motions. Even thought the input range of the lateral stability coefficients (regarding β) is large, the variability in half/doubling time and damping ratio of the lateral oscillation (Figure 7.34) is limited. This means that the sensitivity

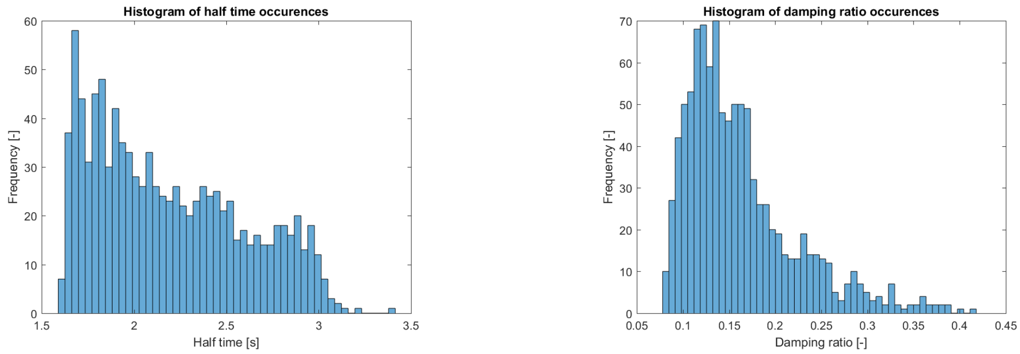

Figure 7.31: Histograms of the FSPO at Mach 1.2.

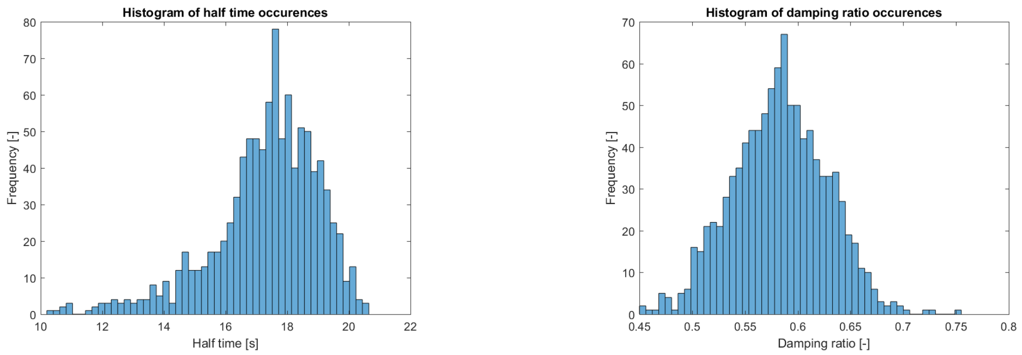

Figure 7.32: Histograms of the PM eigenvalue at Mach 1.2.

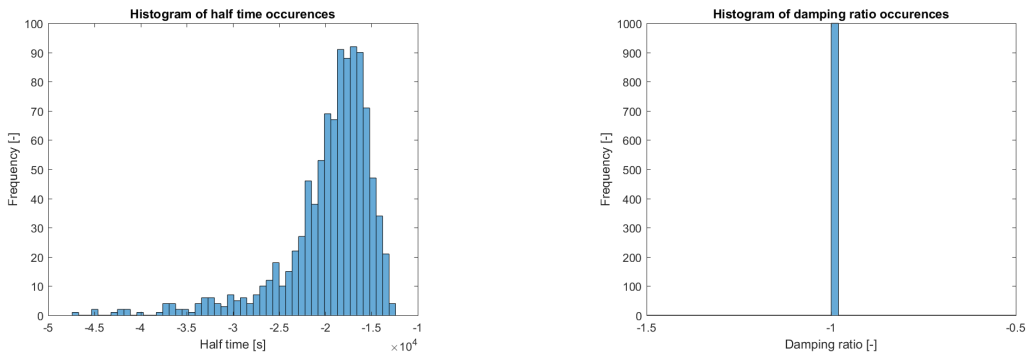

Figure 7.33: Histograms of the HM at Mach 1.2.

of this motion is rather low. The lack of a clearly defined peak can be contributed to the large input range. As the doubling times are between 1.8 seconds and 3.8 seconds this unstable periodic motion is hazardous, but not as critical as was the case at Mach 2.

The fast aperiodic roll motion in Figure 7.35 is aperiodic and stable for all inputs meaning the sensitivity of the stability to the uncertainty range is low. The half time histogram is rather flat due to the large input range and has a range between 5 seconds and 16 seconds. These half times are low enough to stabilize the motion rather quickly. Because the motion is stable for the whole input range the fast ARM is not critical for the overall stability.

The slow aperiodic roll motion is shown in Figure 7.36. According to the damping ratio histogram the motion is stable half of the iterations and aperiodic in all cases. Similar to the slow aperiodic roll modes for Mach 2 the spread of half/doubling times is large, with a peak for lower values. As the half/doubling time is large for all input values this motion will not be critical if it is unstable.

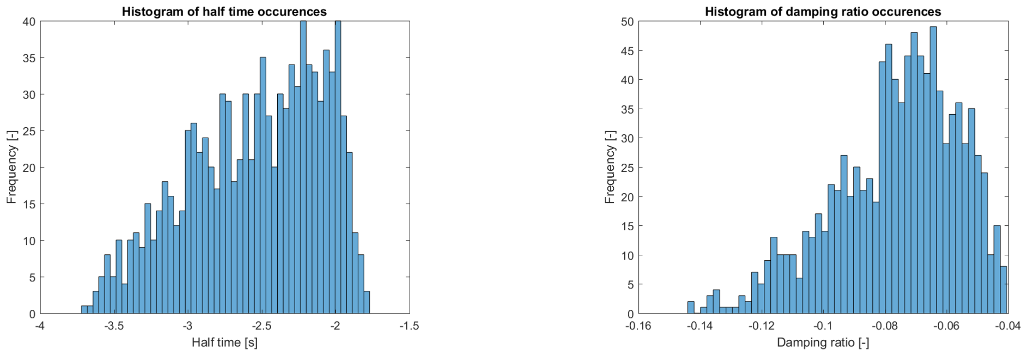

Figure 7.34: Histograms of the LO at Mach 1.2.

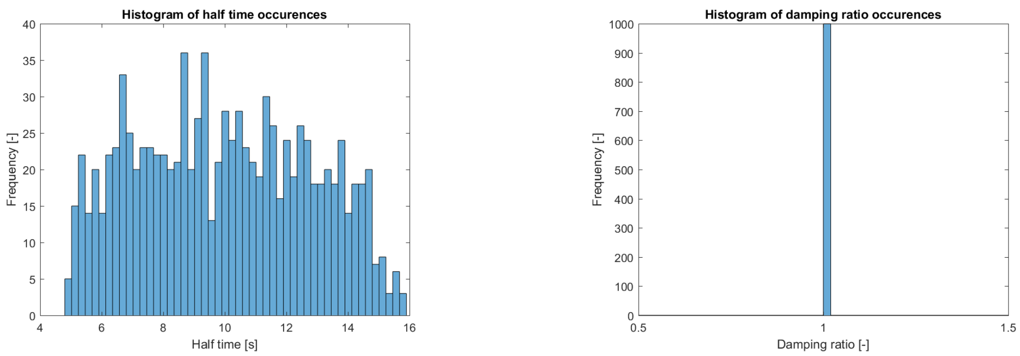

Figure 7.35: Histograms of the fast ARM at Mach 1.2.

The sensitivity analysis showed that for most modes the sensitivity to the input values is low enough to be able to determine whether the motion is stable or unstable and whether the unstable motion represents a problem. The exceptions are the lateral oscillation and the fast aperiodic roll motion for Mach 2. The former is always unstable, but because of the large variance in doubling times it is uncertain whether this will present issues during flight. For the fast aperiodic roll motion at Mach 2 it cannot be determined whether the motion will be stable or unstable. For both these motions the derivative C_{n_β} plays a significant role, so this should be the first coefficient to be investigated further. Furthermore, based on this analysis and the coefficient comparison in Chapter Verification and Validation it can be said that the confidence in the longitudinal motions and coefficients is higher than in the lateral motions and coefficients. Further research should focus on

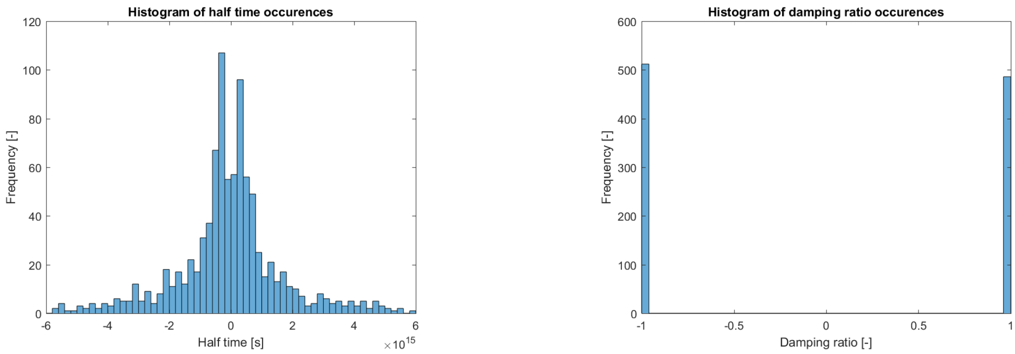

Figure 7.36: Histograms of the slow ARM at Mach 1.2.

improving the simulation of these coefficients, possibly supplemented by wind tunnel data.

8

Conclusions & Recommendations

In the previous chapters the different aspects of this study were treated in order to answer the main research questions. In this final chapter the conclusions will be drawn from all the previous chapters. The subquestions will be answered first, after which the main question is answered. Finally, a number of recommendations for follow-up research are given.

The main research question is restated below:

8.1. Conclusions

Can a method based on the axisymmetric analogue predict the performance and stability coefficients of the HORUS spaceplane accurately enough to determine which motions are stable and unstable in the supersonic regime?

The subquestions for this main question are:

1. Can boundary layer development be accurately predicted using the axisymmetric analogue?
2. Can the boundary layer skin friction be successfully determined from the boundary layer development?
3. Can a complex model like the HORUS spaceplane be treated as a model for the axisymmetric analogue?
4. Using a combined inviscid flow field and viscous boundary layer model, can predictions for performance and stability be made outside the known range and if yes, what do these predictions show?
5. Is the skin friction contribution to the performance and stability coefficients significant?
6. Can predictions for performance and stability be made outside the known range and if yes, what do these predictions show?
7. What motions can be identified for the HORUS-2B, which of those motions are stable in the TAEM and what does this mean for the overall stability?

These subquestions will now be answered separately, after which the main question will be answered.

Can boundary layer development be accurately predicted using the axisymmetric analogue?
According to the theory, a body can be represented using the axisymmetric analogue if the cross-flow between streamlines is small, which is the case for small angles of attack. The validation process on different models showed that the boundary layer thickness development can be reasonably predicted using methods based on the axisymmetric analogue. The match up between simulated and experimental data is fair; the shape and location of maximum momentum thickness is predicted well while the values may deviate by up to 25%. The answer to this question is thus a qualified yes.

Can the boundary layer skin friction be successfully determined from the boundary layer development?
The validation process has shown that with the engineering methods for the skin friction that are used in the current version of the simulation a fair estimate of the friction value can be found. While not very accurate for a single point on the model, by considering the whole model the errors tend to cancel out. This means the total skin friction will not deviate much, but the distribution may be different which may be important in moment calculations. The largest errors are on the order of 50%, but this is only at a single point where the largest momentum thickness occurs, the errors at other locations along the streamline are on the order of 10%-30%.

Can the flow around a complex model like the HORUS be modeled accurately using the axisymmetric analogue in combination with an inviscid flow field solution?
There is no clear answer to this question. On the one hand the simulation reproduced the boundary layer behavior well, as well as the reference values for the HORUS. However, because these reference values are in a regime where the pressure-based coefficients dominate the total value of the coefficients, this only shows the accuracy of the inviscid Euler code for such a complex model. The boundary layer validation was done on the most complex model for which boundary layer data was available, but because all these models are axisymmetric themselves it can not be said with certainty this also works for models which are far from axisymmetric.

The results do give some insight into the correctness of the axisymmetric transformation for the HORUS. Most of the observed behaviors of the contributions caused by friction coefficients are in line with expected behavior. For example, the reduction of skin friction for increased angle of attack. Another is the growth of relative importance of the skin friction in the total coefficient values for lower Mach numbers. These trends indicate that the treatment of the vehicle through the axisymmetric analogue is sound. Because of the relation between skin friction and friction heating a wind tunnel test measuring the temperature changes around the model for supersonic Mach numbers could be used to calculate the actual skin friction. This measured skin friction can then be used to ensure the validity of the skin friction calculations in the simulation.

Is the skin friction contribution to the performance and stability coefficients significant?
As already touched upon in the answer to the previous question, in most cases (especially the supersonic ones) the skin friction only plays a minor role for the majority of the performance and stability coefficients. The exception is the skin friction coefficient contribution to the pitch moment coefficient near or at the trim condition, where it can contribute up to 80% of the total pitch coefficient. For the simulation at Mach 0.8 the influence of the skin friction on the pitch coefficient is only minimal because the trim condition was not satisfied. However, because the skin friction drag's contribution increases with decreasing Mach number due to the decrease of the pressure drag coefficient, it can be expected to stay important close to the trim condition.

Can predictions for performance and stability be made outside the known range and if yes, what do these predictions show?
Predictions for the stability coefficients have been made for Mach numbers of 2, 1.2 and 0.8, which are all below the lowest Mach number of 2.5 for which stability characteristics have been determined in the reference data set. The coefficients have been validated against known coefficients for HORUS, which showed that the signs of the coefficients were generally correctly predicted. Furthermore the values for longitudinal coefficients have been reproduced with a maximum deviation of 20% to 30%. The derivatives with respect to the sideslip angle were much less accurate, in some cases the difference between the reference value and the simulated value was more than 75%. The answer to this question is a cautious yes for most coefficients and longitudinal motions, with validation using a different method recommended.

What motions can be identified for the HORUS-2B, which of those motions are stable in the TAEM and what does this mean for the overall stability? The simulations showed that for level flight for all Mach numbers the same motions exist: the short period oscillation, the phugoid motion, the lateral oscillation, the aperiodic roll mode and the height mode. The case simulated for the purpose of validation showed that when HORUS is flying with a non-zero bank angle, some other motions appear, namely the pitch/roll divergence, the periodic pitch/roll mode and the spiral mode.

The stability of the motions depended on the simulation settings. The short-period oscillation is generally stable when the coefficient C_{m_α} is negative. The phugoid motion was generally stable except for the Mach 2 case at the aft center of mass and the forward center of mass at Mach 0.8. The lateral oscillation was unstable in all cases with small doubling times. Similar to the phugoid motion, the fast aperiodic roll motion was stable except for the Mach 2 case at the aft center of mass. The stability of the slow aperiodic roll motion and the height mode varied between stable and unstable, but in all cases the doubling times were very high.

The two most problematic motions for the TAEM are the short-period oscillation when it is unstable and the lateral oscillation. Both generally have short doubling times when unstable, which in certain cases are below 1 second. According to the results and sensitivity analysis, at Mach 2 the HORUS is dangerously unstable with at least one likely two and in extreme cases even three unstable motions with doubling times below 1 second (former short-period oscillation, lateral oscillation and fast aperiodic roll motion respectively). The stability picture at Mach 1.2 is much better, with the only fast, unstable mode being the lateral oscillation. As the doubling time has increased to approximately 3 seconds, this instability has becomes a lot less crucial. The picture for Mach 0.8 is mixed. For the aft center of mass the former short period oscillation has an unstable motion that has a doubling time of 0.5 seconds, which means the stability is critical. At the forward center of mass however the lateral oscillation is the unstable motion with the shortest doubling time, and because this doubling time is around 2 seconds it is hazardous but not critical for the overall stability.

Concluding, for Mach 2 the stability has at least 1 critically fast motion for all cases, for Mach 1.2 the most unstable motion is not critical and for Mach 0.8 the most unstable motion is critical for the aft center of mass but not critical for the forward center of mass.

With all the subquestions answered, the main question can be tackled, repeated here for convenience:

Can a method based on the axisymmetric analogue predict the performance and stability coefficients of the HORUS spaceplane accurately enough to determine which motions are stable and unstable in the supersonic regime?

The simulated HORUS data has been matched to reference HORUS data within 25% for many of the coefficients, though not for smaller coefficients or secondary effects. The boundary layer parameter have been successfully simulated. The calculated coefficients conform to expectations regarding sign and behaviour. The stability of the HORUS has been assessed for the planned range of Mach numbers and it has been shown that at Mach 2 there are always critically unstable motions, at Mach 1.2 there are no critically unstable motions and at Mach 0.8 the existence of a critically unstable motion depends on the location of the center of mass. This leads to the conclusion that a method based on the axisymmetric analogue shows potential to reasonably predict a limited set of performance and stability coefficients of the HORUS spaceplane and that the overall stability of the HORUS can generally be predicted successfully.

8.2. RECOMMENDATIONS

Runge-Kutta integration for streamlines

Euler integration is used for the tracing of the streamlines in the current version of the software. Upgrading the integration to Runge-Kutta4 integration or similar improved methods will allow accurate streamline tracing with a larger timestep.

Improve stagnation line detection & calculation

While the current version of the stagnation line detection gives a good impression of the areas in which a stagnation line is present, it is not fully accurate. Furthermore, it requires manual calibration to not over- or underestimate the number of elements through which a stagnation line flows. This will improve skin friction prediction as the streamlines start from the correct position. Furthermore, the current code assumes an element is either part of a stagnation line or an element through with streamlines can flow. In reality, there is often a mix between streamlines and stagnation lines working in different direction.

More stability and performance coefficients

At the moment only a subset of the symmetric coefficients has been determined, which in itself is a subset again of the total number of performance and stability coefficients. A much better picture could be obtained by simulation asymmetric disturbance such a sideslip, as well as asymmetric contributions of control surface deflections.

Improved skin friction methods

There is a set of more complex methods that might yield better results for the skin friction. One of these methods is described in [Winter *et al.* , 1970] and is based on the Kármán integral. In the process, both the kinetic energy thickness and the displacement thickness are determined, which might be useful in their own right. The major limitation on this method is that it only works for adiabatic walls, limiting the applicability. A major part of the method is already in the software but needs some attention to get it to work properly.

Investigate validity of model in transonic flow
The transonic flow regime is very interesting for both ascent and reentry. Interactions between shock waves and partially supersonic flow can lead to unexpected behaviour of the stability and control coefficients. It is unknown whether the current boundary layer model is equipped to handle this flow regime.

Extended validation of boundary layer code for complex models
The boundary layer code has mostly been validated against axisymmetric models, which is the type of model that is most often used for wind tunnel experiments. The comparison with reference results for HORUS also could not give a clear answer on the validity because the influence of the skin friction is very small. An extended validation would put trust in the capabilities of the code and allow a wider range of applications. A good start would be total drag estimations of model vehicles at high subsonic Mach numbers, where the influence of the skin friction is more pronounced.

Extended validation of the stability coefficients with respect to the sideslip angle
The stability coefficients with respect to the sideslip angle showed the largest difference between simulated and reference data. As the lateral motions are often critical for the stability of the vehicle, it is important to have a more accurate value for these coefficients, especially for C_{l_β} and C_{n_β}

Use of other inviscid simulations
While the Euler code gives great results for the most relevant flow regimes in this thesis, it is inaccurate below a Mach number of 0.6 and slow to converge for many subsonic flows. Given the right format, other methods such as Newton's method for hypersonic flows could be used to investigate other flow regimes.

Simulate a larger set of configurations
For this thesis the set of configurations that was simulated had to be kept limited. Interesting questions remain regarding the behaviour of the body flap for positive deflections and for the rudder for negative deflections. A reproduction of the complete control curves would be a great addition too.

Automate choice of the value of ϵ, the stagnation line limit etc.
At the moment it is up to the user using trial & error to find good values for some of the parameters in the streamsettings.dat file. Many of these should be possible to automate, which would improve the user experience.

Bibliography

Aftosmis, M., Berger, M., & Adomavicius, G. 2000. A parallel multilevel method for adaptively refined Cartesian grids with embedded boundaries. *38th Aerospace Sciences Meeting and Exhibit.*

Anderson, W Kyle, & Bonhaus, Daryl L. 1994. An Implicit Upwind Algorithm for Computing Turbulent Flows on Unstructured Grids. **23**(1), 1–21.

Bibb, K.L., Peraire, J., & Riley, C.J. 1997. *HYPERSONIC FLOW COMPUTATIONS ON UNSTRUCTURED MESHES.* Tech. rept.

Blasius, H. 1950. *The boundary layers in fluids with little friction (Translation).* Tech. rept. NACA, Washington.

Boeing. 2017. *X-20 Dyna-Soar Space Vehicle.*

Bonner, E., Clever, W., Divan, P., Dunn, K., & Kojima, J. 1981. Aerodynamic preliminary analysis.

Bonner, E., Clever, W, & Dunn, K. 1991. Aerodynamic Preliminary Analysis System II, Part I-Theory. **182076**.

Bornemann, W.E., & Surber, T.E. 1978. *Aerodynamic Design of the Space Shuttle Orbiter.* Tech. rept. Rockwell International Corporation, Downey.

Buning, P G, Chiu, I T, Obayashi, S, Rizk, Y M, & Steger, J L. 1988. Numerical simulation of the integrated space shuttle vehicle in ascent. *AIAA Atmospheric Flight Mechanics Conference, Minneapolis, MN*, 265–283.

Cimbala, John M., & Cengel, Yunus A. 2012. The Turbulent Flat Plate Boundary Layer. *In: Fluid Mechanics: Fundamentals and Applications.*

Cohen, By Clarence B, & Reshotko, E L I. 1956. The Compressible Laminar Boundary Layer With Heat Transfer and Arbitrary Pressure Gradient.

Cooke, J.C. 1961. *An Axially Symmetric Analogue for General Three-Dimensional Boundary Layers.* Tech. rept. 3200. Ministry of aviation, aeronautical research council.

Coué, Philippe. 2003. The beginning of Hermes spaceplane (1976 – 1985).

Cucinelii, G., & Müller, W. 1988. *Study on re-entry guidance and control.* Tech. rept. MBB Space Communication and Propulsion Systems Division.

Deveikis, William D., & Walker, Robert W. 1961. *LOCAL AERODYNAMIC HEAT TRANSFER AND BOUNDARY -LAYER TRANSITION ON ROUGHENED SPHERE-ELLIPSOID BODIES AT MACH NUMBER 3.0.* Tech. rept. August. Langley Research Center.

ESA. 2011. *History Hermes spaceplane.*

Etkin, Bernard. 1996. *Dynamics of Flight - Stability and Control.*

Frink, N.T. 1998. Tetrahedral unstructured Navier-Stokes method for turbulent flows. *AIAA Journal*, **36**(11), 1975–1982.

Gadd, G. E. 1962. Interactions between Normal Shock Waves and Turbulent Boundary Layers. 1–69.

Geuzaine, Christophe, & Remacle, Jean-Francois. 2009. Gmsh: a three-dimensional finite element mesh generator with built-in pre- and post-processing facilities. *International Journal for Numerical Methods in Engineering*, 1–24.

Glenn Research Center. 2013. *AtmosModeler Simulator - Version 1*.

Gong, Leslie, Ko, William L., & Quinn, Robert D. 1984. *Thermal Response of Space Shuttle Wing During Reentry Heating*. Tech. rept.

Hamilton, H H, Weilmuenster, K J, & Dejarnette, F R. 2006. Improved Approximate Method for Computing Convective Heating on Hypersonic Vehicles Using Unstructured Grids. *Pages 1–21 of: Proceedings of the 9th AIAA/ASME Joint Thermophysics and Heat Transfer Conference*. San Francisco: AIAA.

Hamilton, H H, Weilmuenster, K J, & DeJarnette, F R. 2009. Approximate Method for Computing Laminar and Turbulent Convective Heating on Hypersonic Vehicles Using Unstructured Grids. *Pages 1–26 of: Proceedings of the 41st AIAA Thermophysics Conference*. San Antonio: AIAA.

Harris, J E. 1971. Numerical Solution of the equations for compressible laminar, transitional and turbulent boundary layers and comparisons with experimental data. *Report*, 89.

Harwood, William. 2006. *STS-121 Entry Timeline*.

Hirschel, E.H., & Weiland, C. 2009. *Selected Aero-thermodynamic Design Problems of Hypersonic Flight Vehicles*. Heidelberg: Springer, AIAA.

Hosman, Ruud, & Stassen, Henk. 1999. Pilot's perception in the control of aircraft motions. **7**, 1421–1428.

J.Erickson. 1986. *Report of the PRESIDENTIAL COMMISSION on the Space Shuttle Challenger Accident*. Tech. rept.

Jiang, Wen, & Yang, Zhaohua. 2014. Guidance Law Design for Terminal Area Energy Management of Reusable Launch Vehicle by Energy-to-Range Ratio. **2014**.

John W. Slater. 1999. *Laminar Flat Plate Study #1*. Tech. rept. NPARC Alliance Validation Archive.

Kawato, Hiroshi, Watanabe, Shigeya, Yamamoto, Yukimitsu, & Fujii, Kenji. 2002. A Study on Aerodynamic Performances of Lifting-body Configurations for a Reentry Vehicle. *AIAA/AAAF 11th International Space Planes and Hypersonic Systems and Technologies Conference*.

Kenwright, David N., Henze, Chris, & Levit, Creon. 1999. Feature extraction of separation and attachment lines. *IEEE Transactions on Visualization and Computer Graphics*, **5**(2), 135–144.

Kenwright, D.N. 1998. Automatic detection of open and closed separation and attachment lines. *Proceedings Visualization '98 (Cat. No.98CB36276)*.

Kinney, David J. 2011. Approximate Entropy Layer Swallowing Model for the Engineering Level Aerothermodynamics Code CBAERO. *49th AIAA Aerospace Sciences Meeting including the New Horizons Forum and Aerospace Exposition*.

Koelle, Dietrich E., & Kuczera, Heribert. 1992. Sänger Space Transportation System - Progress Report. *Space Technology*, **12**(4), 353–367.

Lam, S.S.W., & Pollock, N. 1989. *An Experimental Study of Transonic Flow Past a Sphere.*

Marzocca, Pier. 2003. *AE 430 - Stability and Control of Aerospace Vehicles Directional Stability Directional (Weathercock) stability Stable / unstable aircraft.*

McGraw-Hill Concise Encyclopedia of Physics. 2002. *McGraw-Hill Concise Encyclopedia of Physics.*

Molina, Rafael. 2014. *Meeting concerning the workings of the Euler code.*

Mooij, E. 1995. *The HORUS-2B Reference Vehicle.*

Mooij, E. 1997. *Linear quadratic regulator design for an unpowered winged re-entry vehicle.* Tech. rept. Faculty of Aerospace Engineering, TU Delft.

Moore, T. 1991. Space shuttle entry terminal area energy management.

Moser, Robert. 2013. *Direct Numerical Simulations of High Reynolds Number Turbulent Channel Flow.*

Mulder, J. A., van Staveren, W. H. J. J., van der Vaart, J. C., de Weerdt, E., Veld, A. C. in 't, & Mooij, E. 2013. *Flight Dynamics.* Delft: Delft University of Technology.

NASA. 1976. *U.S. Standard Atmosphere, 1976.* Tech. rept. NASA, NOAA.

NASA. 2002. *HSF - The Shuttle Mission Profile.*

NASA. 2005. *Landing the Space Shuttle Orbiter.*

NASA. 2014. *Normal Shock Wave Equations.*

NOAA. 2013. *NWS JetStream - Average temperature profile of the atmosphere.*

Parhizkar, H., & Karimian, S.M.H. 2009. Application of axisymmetric analog to unstructured grid for aeroheating prediction of hypersonic vehicles. *International Journal of Numerical Methods for Heat & Fluid Flow*, **19**(3/4), 501–520.

Potturi, Amarnatha Sarma, & Peroomian, Oshin. 2016. Dynamic Stability Analysis of the Orion Crew Module through Computational Fluid Dynamics. *46th AIAA Fluid Dynamics Conference*, 1–12.

Powers, Bruce G. 1986. Space Shuttle Longitudinal Landing Flying Qualities. *Journal of Guidance, Control, and Dynamics*, **9**(5), 566–572.

Raillon, E, Parnis, P., & Devaux, N. 1992. Flying Qualities of the Hermes Spaceplane and Shape Definition Process. *Acta Astronautica*, **26**(8), 621–632.

Schuster, David M. 2008. NASA Perspective on Requirements for Development of Advanced Methods Predicting Unsteady Aerodynamics and Aeroelasticity.

Slater, John W. 2015. *Mach 5 Shock Wave Boundary Layer Interaction.*

Struzak, Ryszard. 2003. *Mobile telecommunications via stratosphere.*

Teramoto, Susumu, Hiraki, Kouju, & Fujii, Kozo. 2001. Numerical analysis of dynamic stability of a reentry capsule at transonic speeds. *AIAA journal*, **39**(4), 646–653.

Thwaites, B. 1949. Approximate Calculation of the Laminar Boundary Layer. *Aeronautical Quarterly*, **1**, 245–280.

UCAR. 2003. *Air Composition - What's in the Air?*

Umeda, Masaki, Takenaka, Keizo, Hatanaka, Keita, Hirayama, Daisuke, Yamazaki, Wataru, Matsushima, Kisa, & Nakahashi, Kazuhiro. 2007. Validation of CFD Capability for Supersonic Transport Analysis Using NEXST-1 Flight Test Results.

U.S. Government Printing Office. 1976. *U.S. Standard Atmosphere*.

van Driest, E.R. 1956. On Turbulent Flow Near a Wall. *Journal of the Aeronautical Sciences*, **23**(11), 1007–1011.

Vassberg, John C, Tinoco, Edward N, Rider, Ben, Company, The Boeing, Beach, Huntington, Louis, St, Zickuhr, Tom, Levy, David W, Wahls, Richard A, Morrison, Joseph H, & Mavriplis, Dimitri J. 2010. Summary of the Fourth AIAA CFD Drag Prediction Workshop.

Vinh, Nguyen X. 1981. *Optimal Trajectories in Atmospheric Flight*.

Wade, Mark. 2016. *Astronautix - Saenger*.

Wazzan, A., Gazley, A.M.O., & Smith, C.R. 1981a. *H-Rx Method For Predicting Transition*.

Wazzan, A.R., Gazley, C., & Smith, A.M.O. 1981b. H-Rx Method for Predicting Transition. *AIAA Journal*, **19**(6), 810–812.

White, Frank M. 2005. *Viscous Fluid Flow*. 3rd edn. New York: McGraw Hill.

Williamson, Ray A. 1996. *Developing the Space Shuttle*. Vol. 1.

Winter, K. G., Rotta, J.C., & Smith, K.G. 1970. Studies of the Turbulent Boundary Layer on Waisted Body of Revolution in Subsonic and Supersonic Flow.

Zoby, E V, Moss, J N, & Sutton, K. 1981. Approximate Convective-Heating Equations for Hypersonic Flows. *Journal of Spacecraft and Rockets*, **18**(1), 64–70.

9

APPENDIX A: STABILITY MATRIX COEFFICIENTS

$$a_{VV} = -\frac{1}{mV_0}\left(M_0\frac{\partial C_D}{\partial M}\bar{q}_0 S_{ref} + 2D_0\right)$$

$$a_{V\gamma} = -g_0\cos\gamma_0$$

$$a_{VR} = 2\frac{g_0}{R_0}\sin\gamma_0$$

$$a_{V\alpha} = -\frac{1}{m}\frac{\partial C_D}{\partial \alpha}\bar{q}_0 S_{ref}$$

$$a_{Vp} = a_{Vq} = a_{Vr} = a_{V\beta} = a_{V\sigma} = 0$$

$$a_{\gamma V} = \frac{1}{V_0}\left(-\dot{\gamma}_0 + \frac{2V_0}{R_0}\cos\gamma_0\right) + \frac{\cos\sigma_0}{mV_0^2}\left(M_0\frac{\partial C_L}{\partial M}\bar{q}_0 S_{ref} + 2L_0\right)$$

$$a_{\gamma\gamma} = -\left(\frac{V_0}{R_0} - \frac{g_0}{V_0}\right)\sin\gamma_0$$

$$a_{\gamma R} = \left(\frac{2g_0}{V_0} - \frac{V_0}{R_0}\right)\frac{\cos\gamma_0}{R_0}$$

$$a_{\gamma\alpha} = \frac{\cos\sigma_0}{mV_0}\frac{\partial C_L}{\partial \alpha}\bar{q}_0 S_{ref}$$

$$a_{\gamma\beta} = -\frac{\sin\sigma_0}{mV_0}\frac{\partial C_S}{\partial \beta}\bar{q}_0 S_{ref}$$

$$a_{\gamma\sigma} = -\frac{L_0}{mV_0}\sin\sigma_0$$

$$a_{\gamma p} = a_{\gamma q} = a_{\gamma r} = 0$$

$$a_{RV} = \sin\gamma_0$$

$$a_{R\gamma} = V_0\cos\gamma_0$$

$$a_{RR} = a_{Rp} = a_{Rq} = a_{Rr} = a_{R\alpha} = a_{R\beta} = a_{R\sigma} = 0$$

$$a_{p\beta} = \frac{1}{I_{xx}}\frac{\partial C_l}{\partial \beta}\bar{q}_0 S_{ref} b_{ref}$$

$$a_{pV} = a_{p\gamma} = a_{pR} = a_{pp} = a_{pq} = a_{pr} = a_{p\alpha} = a_{p\sigma} = 0$$

$$a_{qV} = \frac{M_0}{I_{yy}V_0}\frac{\partial C_m}{\partial M}\bar{q}_0 S_{ref} c_{ref}$$

$$a_{q\alpha} = \frac{1}{I_{yy}}\frac{\partial C_m}{\partial \alpha}\bar{q}_0 S_{ref} c_{ref}$$

$$a_{q\gamma} = a_{qR} = a_{qp} = a_{qq} = a_{qr} = a_{q\beta} = a_{q\sigma} = 0$$

$$a_{r\beta} = \frac{1}{I_{zz}} \frac{\partial C_n}{\partial \beta} \bar{q}_0 S_{ref} b_{ref}$$

$$a_{rV} = a_{r\gamma} = a_{rR} = a_{rp} = a_{rq} = a_{rr} = a_{r\alpha} = a_{r\sigma} = 0$$

$$a_{\alpha V} = -\frac{g_0}{V_0^2} \cos\gamma_0 \cos\sigma_0 - \frac{1}{mV_0^2} \left(M_0 \frac{\partial C_L}{\partial M} + C_L \right) \bar{q}_0 S_{ref}$$

$$a_{\alpha\gamma} = -\frac{g_0}{V_0} \sin\gamma_0 \cos\sigma_0$$

$$a_{\alpha R} = -\frac{2g_0}{R_0 V_0} \cos\gamma_0 \cos\sigma_0$$

$$a_{\alpha q} = 1$$

$$a_{\alpha\alpha} = -\frac{1}{mV_0} \frac{\partial C_L}{\partial \alpha} \bar{q}_0 S_{ref}$$

$$a_{\alpha\sigma} = -\frac{g_0}{V_0} \cos\gamma_0 \sin\sigma_0$$

$$a_{\alpha p} = a_{\alpha r} = a_{\alpha\beta} = 0$$

$$a_{\beta V} = \frac{g_0}{V_0^2} \cos\gamma_0 \sin\sigma_0$$

$$a_{\beta\gamma} = \frac{g_0}{V_0} \sin\gamma_0 \sin\sigma_0$$

$$a_{\beta R} = \frac{2g_0}{R_0 V_0} \cos\gamma_0 \sin\sigma_0$$

$$a_{\beta p} = \sin\alpha_0$$

$$a_{\beta r} = -\cos\alpha_0$$

$$a_{\beta\beta} = -\frac{1}{mV_0} \frac{\partial C_S}{\partial \beta} \bar{q}_0 S_{ref}$$

$$a_{\beta\sigma} = -\frac{g_0}{V_0} \cos\gamma_0 \cos\sigma_0$$

$$a_{\beta q} = a_{\beta\alpha} = 0$$

$$a_{\sigma V} = \frac{\tan\gamma_0 \sin\sigma_0}{mV_0^2}\left(M_0\frac{\partial C_L}{\partial M} + C_L\right)\bar{q}_0 S_{ref}$$

$$a_{\sigma\gamma} = \frac{L_0}{mV_0}\sin\sigma_0$$

$$a_{\sigma p} = -\cos\alpha_0$$

$$a_{\sigma r} = -\sin\alpha_0$$

$$a_{\sigma\alpha} = \frac{\tan\gamma_0 \sin\sigma_0}{mV_0}\frac{\partial C_L}{\partial\alpha}\bar{q}_0 S_{ref}$$

$$a_{\sigma\beta} = \frac{\tan\gamma_0 \cos\sigma_0}{mV_0}\frac{\partial C_S}{\partial\beta}\bar{q}_0 S_{ref} - \frac{L_0}{mV_0} + \frac{g_0}{V_0}\cos\gamma_0\cos\sigma_0$$

$$a_{\sigma\sigma} = \tan\gamma_0\cos\sigma_0\frac{L_0}{mV_0}$$

$$a_{\sigma R} = a_{\sigma q} = 0$$

$$b_{Ve} = b_{Va} = b_{Vr} = b_{Vx} = b_{Vy} = b_{Vz} = 0$$

$$b_{\gamma e} = b_{\gamma a} = b_{\gamma r} = b_{\gamma x} = b_{\gamma y} = b_{\gamma z} = 0$$

$$b_{Re} = b_{Ra} = b_{Rr} = b_{Rx} = b_{Ry} = b_{Rz} = 0$$

$$b_{pa} = \frac{1}{I_{xx}}\frac{\partial C_l}{\partial\delta_a}\bar{q}_0 S_{ref} b_{ref}$$

$$b_{px} = \frac{1}{I_{xx}}$$

$$b_{pe} = b_{pr} = b_{py} = b_{pz} = 0$$

$$b_{qe} = \frac{1}{I_{yy}}\frac{\partial C_m}{\partial\delta_e}\bar{q}_0 S_{ref} c_{ref}$$

$$b_{qy} = \frac{1}{I_{yy}}$$

$$b_{qa} = b_{qr} = b_{qx} = b_{qz} = 0$$

$$b_{ra} = \frac{1}{I_{zz}}\frac{\partial C_n}{\partial\delta_a}\bar{q}_0 S_{ref} b_{ref}$$

$$b_{rr} = \frac{1}{I_{zz}} \frac{\partial C_n}{\partial \delta_r} \bar{q}_0 S_{ref} b_{ref}$$

$$b_{rz} = \frac{1}{I_{zz}}$$

$$b_{re} = b_{rx} = b_{ry} = 0$$

$$b_{\alpha e} = b_{\alpha a} = b_{\alpha r} = b_{\alpha x} = b_{\alpha y} = b_{\alpha z} = 0$$

$$b_{\beta e} = b_{\beta a} = b_{\beta r} = b_{\beta x} = b_{\beta y} = b_{\beta z} = 0$$

$$b_{\sigma e} = b_{\sigma a} = b_{\sigma r} = b_{\sigma x} = b_{\sigma y} = b_{\sigma z} = 0$$

10

Appendix B: validation stability and control coefficients

Clean configuration data

α	Ref	Sim (old model)	Sim (new model)
0°	-0.03	-0.0471	-
5°	0.10	-	0.1222
10°	0.26	0.3184	0.2832
15°	0.42	-	0.4428
20°	0.60	0.6636	-
30°	0.94	0.9853	-
40°	1.20	1.2182	-

Table 10.1: Lift coefficient comparison for clean configuration at M = 2

Angle of attack	Ref	Sim
5°	0.27	0.2212
10°	0.56	0.4343
15°	0.86	0.6501

Table 10.2: Lift coefficient comparison for clean configuration at M = 1.2

Mach number	Ref	Sim
2	-0.0229	-0.0098
1.2	-0.0500	-0.0079

Table 10.3: Side force derivative per degree comparison for clean configuration

α	Ref	Sim (old model)	Sim (new model)
0°	0.08	0.1383	-
5°	0.09	-	0.1340
10°	0.12	0.1699	0.1641
15°	0.18	-	0.2252
20°	0.29	0.3190	-
30°	0.60	0.6139	-
40°	1.07	1.0352	-

Table 10.4: Drag coefficient comparison for clean configuration at M = 2

Angle of attack	Ref	Sim
5°	0.12	0.1841
10°	0.20	0.2292
15°	0.33	0.3070

Table 10.5: Drag coefficient comparison for clean configuration at M = 1.2

Mach number	Ref	Sim
2	-0.00128	-3.41072e-05
1.2	-0.00283	-8.4788e-04

Table 10.6: Roll moment derivative per degree comparison for clean configuration

α	Ref	Sim (old model)	Sim (new model)
0°	-0.013	-0.0089	-
5°	-0.016	-	-0.0159
10°	-0.016	-0.020	-0.0211
15°	-0.014	-	-0.0237
20°	-0.012	-0.0272	-
30°	-0.011	-0.0368	-
40°	-0.014	-0.0496	-

Table 10.7: Pitch coefficient comparison for clean configuration at M = 2

Angle of attack	Ref	Sim
5°	-0.051	-0.0379
10°	-0.067	-0.0513
15°	-0.079	-0.0630

Table 10.8: Pitch coefficient comparison for clean configuration at M = 1.2

Mach number	Ref	Sim
2	0.0004	0.0018
1.2	0.0093	0.0020

Table 10.9: Yaw moment derivative per degree comparison for clean configuration.

BODY FLAP DATA

δ_b	-20°	
Angle of attack	Ref	Sim
5°	0.03	0.0092
10°	0.018	0.0046
15°	0.008	1.9812e-03

Table 10.10: Drag coefficient increment due to bodyflap at M = 1.2

δ_b	-20°	
Angle of attack	Ref	Sim
5°	0.009	1.22184e-03
10°	0.006	2.2214e-04
15°	0.002	0.0072

Table 10.11: Drag coefficient increment due to bodyflap at M = 2

δ_b	-20°	
Angle of attack	Ref	Sim
5°	-0.070	-0.0392
10°	-0.067	-0.0352
15°	-0.053	-0.0422

Table 10.12: Lift coefficient increment due to bodyflap at M = 1.2

δ_b	-20°	
Angle of attack	Ref	Sim
5°	-0.021	-0.0117
10°	-0.022	-0.0141
15°	-0.021	-0.0186

Table 10.13: Lift coefficient increment due to bodyflap at M = 2

δ_b	-20°	
Angle of attack	Ref	Sim
5°	0.0179	0.0140
10°	0.0167	0.0130
15°	0.0154	0.0138

Table 10.14: Pitch-moment coefficient increment due to bodyflap at M = 1.2

δ_b	-20°	
Angle of attack	Ref	Sim
5°	0.0058	0.0052
10°	0.0065	0.0056
15°	0.0060	0.0064

Table 10.15: Pitch-moment coefficient increment due to bodyflap at M = 2

ELEVON TABULATED DATA

δ_e	5°		27.5°	
Angle of attack	Ref	Sim	Ref	Sim
5°	0.007	0.0066	0.053	0.0298
10°	0.0085	0.0060	0.0585	0.0357
15°	0.01	0.0069	0.065	-

Table 10.16: Drag coefficient increment due to elevon at M = 1.2

δ_e	5°		16°	
Angle of attack	Ref	Sim	Ref	Sim
5°	0.002	0.0022	0.0088	0.0061
10°	0.003	0.0025	0.0114	0.0072
15°	0.0035	0.0040	0.0142	-

Table 10.17: Drag coefficient increment due to elevon at M = 2

δ_e	5°	
Angle of attack	Ref	Sim
5°	0.0023	0.0035
10°	0.0025	0.0045
15°	0.00265	0.0057

Table 10.18: Side force coefficient increment due to elevon at M = 1.2

δ_e	5°	
Angle of attack	Ref	Sim
5°	0.00075	0.0013
10°	0.0011	0.0017
15°	0.0013	0.0014

Table 10.19: Side force coefficient increment due to elevon at M = 2

δ_e	5°		27.5°	
Angle of attack	Ref	Sim	Ref	Sim
5°	0.0075	0.0101	0.03125	0.0572
10°	0.007	0.0089	0.026	0.0540
15°	0.006	0.0084	0.019	-

Table 10.20: Lift coefficient increment due to elevon at M = 1.2

δ_e	5°		16°	
Angle of attack	Ref	Sim	Ref	Sim
5°	0.003	0.0038	0.0108	0.0137
10°	0.0035	0.0034	0.013	0.0129
15°	0.004	0.0036	0.01325	-

Table 10.21: Lift coefficient increment due to elevon at M = 2

δ_e	5°	
Angle of attack	Ref	Sim
5°	0.00235	0.0014
10°	0.00235	0.0014
15°	0.00235	0.0013

Table 10.22: Roll moment coefficient increment due to elevon at M = 1.2

δ_e	5°	
Angle of attack	Ref	Sim
5°	0.0010	7.31441e-04
10°	0.0011	7.53572e-04
15°	0.0013	6.58704e-04

Table 10.23: Roll moment coefficient increment due to elevon at M = 2

δ_e	5°		27.5°	
Angle of attack	Ref	Sim	Ref	Sim
5°	-0.0029	-0.0041	-0.014525	-0.0207
10°	-0.0031	-0.0039	-0.01465	-0.0201
15°	-0.00315	-0.0035	-0.0146	-0.0147

Table 10.24: Pitch moment coefficient increment due to elevon at M = 1.2

δ_e	5°		16°	
Angle of attack	Ref	Sim	Ref	Sim
5°	-0.0012	-0.0017	-0.0048	-0.0057
10°	-0.00145	-0.0014	-0.005375	-0.0053
15°	-0.00165	-0.0012	-0.006075	-

Table 10.25: Pitch moment coefficient increment due to elevon at M = 2

δ_e	5°	
Angle of attack	Ref	Sim
5°	-0.0036	-4.3772e-04
10°	-0.00375	-6.5356e-04
15°	-0.0043	5.0595e-04

Table 10.26: Yaw-moment coefficient increment due to elevon at M = 1.2

δ_e	5°	
Angle of attack	Ref	Sim
5°	-0.0012	-8.2373e-04
10°	-0.00135	-8.5648e-04
15°	-0.0017	-6.8985e-04

Table 10.27: Yaw-moment coefficient increment due to elevon at M = 2

RUDDER TABULATED DATA

δ_r	5°	
Angle of attack	Ref	Sim
5°	0.0040	0.0091
10°	0.0030	0.0097
15°	0.0018	0.0092

Table 10.28: Side force coefficient increment due to rudder at M = 1.2

δ_r	5°	
Angle of attack	Ref	Sim
5°	0.00245	0.0031
10°	0.00195	0.0043
15°	0.00145	0.0032

Table 10.29: Side force coefficient increment due to rudder at M = 2

δ_r	5°	
Angle of attack	Ref	Sim
5°	-0.00255	-0.0028
10°	-0.00205	-0.0020
15°	-0.00135	-0.0013

Table 10.30: Yaw-moment coefficient increment due to rudder at M = 1.2

δ_r	5°	
Angle of attack	Ref	Sim
5°	-0.0012	-0.0020
10°	-0.00105	-0.0018
15°	-0.00085	-0.0019

Table 10.31: Yaw-moment coefficient increment due to rudder at M = 2